A NOVEL FAST REMESH-FREE FINITE ELEMENT METHOD FOR OPTIMAL DESIGN OF ELECTRIC MACHINES

YANPU ZHAO

Ph.D

The Hong Kong Polytechnic University

2015

The Hong Kong Polytechnic University

Department of Electrical Engineering

A NOVEL FAST REMESH-FREE FINITE ELEMENT METHOD FOR OPTIMAL DESIGN OF ELECTRIC MACHINES

Yanpu ZHAO

A thesis submitted in partial fulfillment of the requirements for the degree of Doctor of Philosophy

November 2014

Certificate of Originality

I hereby declare that this thesis is my own work and that, to the best of my knowledge and belief, it reproduces no previously published or written, nor material that has been accepted for the award of any other degree or diploma, except where due acknowledgement has been made in the text.

_____

Name: Yanpu ZHAO

Abstract of thesis entitled

"A Novel Fast Remesh-Free Finite Element Method for Optimal Design of Electric Machines"

Submitted by
Yanpu ZHAO
for the degree of Doctor of Philosophy
at The Hong Kong Polytechnic University
in November 2014

In this thesis, a novel fast remesh-free finite element method (FEM) for optimal design of electric machines and other electromagnetic (EM) devices is investigated to accelerate the process of optimal design of EM devices. Both two-dimensional (2D) and three-dimensional (3D) engineering optimal design problems can be solved using the proposed algorithms which are also developed into software packages in C++. This work is aiming to accelerate the solution of optimal shape design problems of EM devices, and the contribution of this work includes fast remesh-free mesh deformation techniques for 2D and 3D meshes, a novel adaptive degrees-of-freedom (DoFs) finite element algorithm and a low-frequency approximation to the Maxwell equations simultaneously considering inductive and capacitive effects. The remesh-free mesh deformation method, FEM and global optimization algorithms are combined to tackle several engineering optimal shape design problems.

In this research of accelerating the optimal design process of EM devices, the 2D Delaunay parameterized mesh generation and refinement method and 3D remesh-free mesh deformation method are first proposed and applied to practical problems. To solve the magnetic field accurately with minimal effort, a novel error estimator is proposed to obtain the numerical error of the computed magnetic field with multiple materials in the problem domain. Besides, an adaptive DoFs FEM is proposed and applied to static nonlinear problems and transient field computation in time-domain. To solve the quasi-magneto-static field inside high-speed moving conductors presenting thin eddy-current layers accurately, the

adaptive discontinuous Galerkin method (DGM), characteristic Galerkin method (CGM) and operator splitting method (OSM) are proposed and proved to be effective in use. For 3D EM field computation, a low-frequency approximation to the Maxwell equations simultaneously considering inductive and capacitive effects is proposed. All the proposed algorithms are implemented into computer code in C++, which is then applied to optimize the performance of several EM devices, such as electromagnet, permanent magnet motor, and magnetic gear.

In this thesis, the following work has been done:

(1) 2D parameterized mesh generation and mesh refinement algorithms, including edge bisection, element trisection and regular mesh refinement methods; 2D parameterized mesh deformation technique for small shape modification and large mesh deformation; 3D fast remesh-free mesh deformation technique and its application to practical optimal design problems.

(2) 2D finite element solver with second-order triangular finite element basis functions for the approximation of the magnetic vector potential (MVP); To analyze the EM fields in electric machines, nonlinear material, rotational movement and circuit-coupling are all taken into account. Adaptive mesh refinement is allowed using several optional error estimators. The Newton-Raphson iteration method is adopted for handling nonlinear magnetic material. For transient eddy-current field analysis, the backward-Euler time stepping scheme with slave-master technique for handling of rotational movement is adopted.

(3) A novel adaptive DoFs FEM and its application to each Newton iteration step for nonlinear problems and each time-step for transient eddy-current field analysis. Only one set of mesh is needed in the method, the DoFs can be dynamically adjusted to adapt to the variation of the solution, both mesh refinement and mesh coarsening are processed implicitly.

(4) 3D finite element solver with Whitney edge element to discretize the MVP and first-order nodal element to discretize the electric scalar potential (ESP). A low-frequency approximation to the Maxwell equations simultaneously considering inductive and capacitive effects is

proposed. The magnetostatic, transient eddy-current, and nearly full-wave EM fields with external circuit-coupling can be solved with the developed code. Benchmark TEAM Workshop problems are used to validate the accuracy of the developed program.

(5) An adaptive DGM, CGM and OSM are applied to eddy-current problems with high-speed moving conductors which present thin eddy-current layers. The advantages of these proposed methods are compared with traditional FEM.

The major contributions of this work can be summarized as:

- A novel parameterized mesh generation, refinement and deformation method for 2D and 3D optimal design problems.
- A novel adaptive DoFs FEM which can reduce the computational time for both static and transient problems. A novel error estimator which is convenient to be used to estimate the local error distribution of the finite element solution.
- The DGM, CGM and OSM are used to capture the thin eddy-current layers for problems with high-speed moving conductors.
- Second-order 2D finite element and first-order 3D edge element programs are developed to solve EM field computation problems with nonlinear material, mechanical movement and external circuit.
- A low-frequency approximation to the Maxwell equations simultaneously considering inductive and capacitive effects in the time-domain is proposed and validated using a numerical example.
- Practical engineering optimal design problems are solved using the proposed methods and evolutionary optimization algorithms for several types of EM devices.

List of Published Journal Papers

1. Yanpu Zhao, Shuangxia Niu, S. L. Ho, W. N. Fu, and Jianguo Zhu, "A parameterized mesh generation and refinement method for finite element parameter sweeping analysis of electromagnetic devices," *IEEE Trans. Magn.*, vol. 48, no. 2, Feb. 2012, pp. 239-242.
2. Yanpu Zhao, Xiu Zhang, S. L. Ho, and W. N. Fu, "A local discontinuous Galerkin method for eddy current field analysis in high-speed moving conductors," *IEEE Trans. Magn.*, vol. 48, no. 2, Feb. 2012, pp. 251-254.
3. Yanpu Zhao, Xiu Zhang, S. L. Ho, and W. N. Fu, "An adaptive mesh method in transient finite element analysis of magnetic field using a novel error estimator," *IEEE Trans. Magn.*, vol. 48, no. 11, Nov. 2012, pp. 4160-4163.
4. Yanpu Zhao, S. L. Ho, and W. N. Fu, "A novel adaptive mesh finite element method for nonlinear magnetic field analysis," *IEEE Trans. Magn.*, vol. 49, no. 5, May 2013, pp. 1777-1780.
5. Yanpu Zhao, S. L. Ho, and W. N. Fu, "An operator splitting finite element method for eddy-current field analysis in high-speed rotating solid conductors," *IEEE Trans. Magn.*, Jul. 2013, pp. 3171-3174.
6. Yanpu Zhao, S. L. Ho, and W. N. Fu, "An adaptive degrees-of-freedom finite-element method for transient magnetic field analysis," *IEEE Trans. Magn.*, vol. 49, no. 12, Dec. 2013, pp. 5724-5729.
7. Shuangxia Niu, Yanpu Zhao, S. L. Ho, and W. N. Fu, "A parameterized mesh technique for finite element magnetic field computation and its application to optimal designs of electromagnetic devices," *IEEE Trans. Magn.*, vol. 47, no. 10, Oct. 2011, pp. 2943-2946.
8. S. L. Ho, Yanpu Zhao, and W. N. Fu, "A local discontinuous Galerkin method for numerical computation of waveguide eigenvalue problems in polar coordinates," *IEEE Trans. Magn.*, vol. 48, no. 2, Feb. 2012, pp. 255-258.
9. Xiu Zhang, Yanpu Zhao, S. L. Ho and W. N. Fu, "Analysis of wireless energy transfer system based on 3-D finite element method including displacement current," *IEEE Trans. Magn.*, vol. 48, no. 11, Nov. 2012, pp. 3692-3695.
10. S. L. Ho, Yanpu Zhao, and W. N. Fu, "An efficient parameterized mesh method for large shape variation in optimal designs of electromagnetic devices," *IEEE Trans. Magn.*, vol. 48, no. 11, Nov. 2012, pp. 4507-4510.
11. S. L. Ho, Yanpu Zhao, and W. N. Fu, "A characteristic Galerkin method for eddy-current field analysis in high-speed rotating solid conductors," *IEEE Trans. Magn.*, vol. 48, no. 11, Nov. 2012, pp. 4634-4637.
12. S. L. Ho, Yanpu Zhao, W. N. Fu, and Xiu Zhang, "A novel mesh morphing technique for large shape deformation and its application to optimal design problems," *IEEE Trans. Magn.*, vol. 49, no. 5, May 2013, pp. 2165-2168.
13. S. L. Ho, Yanpu Zhao, and W. N. Fu, "Adaptive discontinuous Galerkin method for transient analysis of eddy current fields in high-speed rotating solid rotors," *IEEE Trans. Magn.*,vol. 50, no. 2, Feb. 2014, pp. 7014504.

ACKNOWLEGEMENTS

I would like to express my sincere gratitude to my chief supervisor, Dr. W. N. FU for his invaluable guidance, endless support and generous encourage in the past four years. It is my great honor to study and work with Dr. Fu. I have learn a lot from my supervisor his attitude towards life, devotion to research and endeavor in his career and this experience will benefit me for my whole life.

I would also like to acknowledge my co-supervisor, Prof. S. L. HO. I have learnt lots of knowledge from him. Thanks him for his valuable suggestion and encouragement in my research.

I also wish to express my appreciation to all the group members in our Computational Electromagnetics Lab, especially Dr. Shuangxia NIU, Dr. Xiu ZHANG and Dr. Ningning CHEN who was a former group member.

Finally, special recognition and thanks goes out to my family, for their support, sacrifice, encouragement and patience during my pursuit of the Doctorate in Electrical Engineering. To my lovely wife Mrs Na XU, my ever loving companion and supporter of 5 years, who inspired me and provided constant encouragement during the entire process. To my little boy, Kevin ZHAO, who missed out on a lot of Daddy time while I sought intellectual enlightenment. I thank both of you for your patience and love you more than you will ever know.

This work was supported by the Hong Kong PhD Fellowship of the Research Grants Council and the Tuition Scholarship of The Hong Kong Polytechnic University.

Table of Contents

List of Figures

Chapter 1:

Chapter 2:

Chapter 3:

Chapter 4:

Chapter 5:

Chapter 7:

List of Tables

CHAPTER 1

INTRODUCTION

1.1. Computational Challenges of Optimal Design Problems and Motivation of the Thesis

In today's fiercely competitive world, companies manufacturing electromagnetic (EM) devices, such as electric machines and transformers, have to continually improve the quality and reduce the cost of their products. For electric machines, which are the major constituent for electromechanical energy conversion, even a small efficiency increment in the energy conversion process can produce very substantial savings in the global energy resources because of large number of electric machines are running in daily life. It is hence of paramount importance to investigate novel optimal design methods.

Good designs of EM devices should be cost-saving, with high power density, high performance, optimal efficiency and high level of reliability. Optimal machine designs by accurate performance prediction can effectively maximize their energy conversion efficiency and minimize their cost. In practice, there may be multiple objective functions to be optimized and there are constraints for the design variables (for example, the electrical machines used in the hub of a wheel have strict volume constraints), to find the optimal design is usually a complicated task. Nowadays, optimal design algorithms coupled with numerical methods that can search automatically the optimal solution under given constraints, are very useful and widely used in practice [A1]. Finding the best design quickly by just clicking a mouse on the computer is indeed the ultimate dream of many electrical engineers.

To accurately predict the performance parameters of the EM devices, finite element method (FEM) is a good choice which is one of the most widely used numerical methods in engineering. Nowadays, with the development of computer aided design (CAD) system, even the design process of new EM devices can be accomplished with EM numerical software packages by parameter sweeping

analysis[A2-A4]. Based on the numerical simulation results, designers can calculate the parameters they are interested in and have a quantitative knowledge of the design and improve it.

However, finding the best design within reasonable time is a big challenge for researchers. Firstly, the inverse problems of finding the design parameters which are solved using FEM are very time-consuming, because magnetic field problem needs to be solved thousands of times in optimization studies. Secondly, an associated FEM mesh needs to be generated again for each set of updated geometric parameters during the optimization process. Such remeshing procedure usually needs to be executed thousands of times, which is very time-consuming and is also not very robust, especially for complicated 3D applications, where the mesh-making process may take up to 90% of the total simulation time [A5]. Furthermore, since there are usually too many design parameters, the computational time needed for finding the optimal design is still too long although the computing ability of computers increases very fast. Due to the limited time allowed for the design process, there is still a great need to reduce the computational time when finding the optimal design, especially for 3D optimal design problems.

1.2. Contributions and Research Objectives

Considering the importance of optimal design problems and the computational challenges, this research work focuses on reducing the computational time and accelerating the optimal design process. To achieve this goal, two respects requiring intensive computation can be improved to tackle this issue. On is to reduce each finite element computation time by improving the algorithm, the other is to reduce the time needed to make meshes when design parameters change. The contributions and research objectives of this research work are

(1) Computer implementation of 2D and 3D FEM using objective-oriented programming technique for numerical computation of EM fields. The developed software packages are used to analyze the forward problem in optimal design of EM devices;

(2) 2D parameterized and remesh-free mesh generation, refinement and deformation methods for geometric shape variations;

(3) 3D remesh-free mesh deformation method for geometric shape variations;

(4) 2D adaptive DoFs FEM for nonlinear static and transient eddy-current field computation;

(5) A 3D MVP formulation of the Maxwell equations simultaneously considering inductive and capacitive effects in the time-domain;

(6) Application of the developed optimal design package to 2D and 3D optimal design problems, including benchmark examples and engineering design examples.

1.3. Literature Review of FEM in Electromagnetics

In electrical engineering analysis and design, many phenomena have to be considered in order to fully predict a device's behavior. Commonly physical processes involved are of electromagnetic, thermal, mechanical, or other type. Mathematically, these physical phenomena can be described by partial differential equations (PDEs) with proper boundary conditions (BCs) and initial conditions (ICs), which forms the so-called initial boundary value problems (BVPs). The availability of immense and cheap computing power on desktop or laptop computers has provided a solid hardware platform for the numerical solution of these problems. Today numerical simulations are commonly used to analyze and design devices, though often only one field phenomenon is studied in detail. In this thesis, the electromagnetic field computation is mainly concerned and investigated in detail.

There are mainly two categories of numerical methods that can be used to solve the BVPs, including PDE-based methods and integral equation based methods which works with the integral forms of the PDEs. Integral equation solvers are mainly used in linear high-frequency regime to analyze the EM wave phenomena [A6]. Differential BVP solvers are derived from the PDEs directly or their weak forms, they can treat nonlinearity conveniently and the resultant matrices are sparse which can be solved efficiently by iterative linear solvers or parallel sparse direct linear solvers [A7, A8].

Commonly used PDE-based numerical methods for the solution of EM BVPs are finite difference method (FDM) [A9, A10], FEM [A7, A8, A11], finite volume method (FVM, also called the generalized FDM) [A12, A13], discontinuous Galerkin method (DGM) [A14-A16]and so on. All these methods have their own popularity, depending on the applications and the underlying nature of the problems. Of these numerical methods the first two methods are the most popular ones.

The FDM which uses difference quotient to approximate derivatives on finite Cartesian grids is simple in nature and relatively easier to be parallelized. It is widely used in high-frequency EM field analysis. The FEM, where unstructured mesh are usually used, can approximate the geometry outlines much more accurately and hence remove the staircase problems encountered when using FDM. It is more widely used to solve low-frequency EM BVPs defined on complex geometric domains usually containing different types of materials, such as air, permanent magnets, nonlinear iron materials, and stranded or solid conductors.

The FEM was introduced and applied to computational mechanics in 1950s [A17]. It was applied to computational electromagnetics since 1960s [A18]. It is now a well-established technique in electromagnetics and still generates considerable research. To perform finite element analysis (FEA), three processes are generally included [A19], namely the preprocessing where the finite element mesh is generated; the solution process where the discrete matrix equation is built and solved; and the post post-processing where the quantities or parameters of interest are calculated from the field solution and numerical results are displayed in figures. It is noted that usually the mesh generation in the preprocessing phase and the solution of the resultant linear matrix equation takes up most of the computational time.

FEM has become a powerful and routine tool to simulate the magnetic fields and eddy current fields in EM devices, especially in electric motors. Different formulations are widely used by people, including the magnetic vector potential (MVP) formulation (usually also called the $\vec{A}-\varphi$ formulation) [A20-A25], and the magnetic scalar potential (MSP) formulation (usually also called the $\vec{T}-\Omega$ or $\vec{T}-\vec{T}_0-\psi$ formulation) [A26-A32]. The MSP formulation uses a scalar potential in the non-conducting region, so the total number of unknowns can be reduced greatly,

compared with the MVP formulation where a vector potential is used in the non-conducting region. However there are immense difficulties when implementing the MSP formulation for eddy-current problems containing multiply-connected conductors [A31-A34] in the solution domain. Because of its elegant treatment of conductors with arbitrary geometric topology, the MVP formulation is implemented in C++ in this thesis.

For 2D finite element field analysis, the scalar dependent variable are usually the z-component of the MVP. In such a case the divergence of the MVP is zero and thus the Coulomb gauge is satisfied automatically [A35], which indicating the resultant linear system has unique solution. Thus the MVP formulation is mostly adopted for 2D magnetic field analysis. Traditional nodal element works well for this case. The Newton-Raphson iteration can be applied to deal with nonlinear regions in the problem domain conveniently [A36]. For transient eddy-current field analysis of the motor with rotational movement, the slave-master technique can be applied to the sliding surface connecting the rotor and stator meshes [A37]. Since the EM devices are usually driven by external circuit, the strong field-circuit coupling can be also accomplished using FEM conveniently [A11, A37].

Although 2D instead of 3D FEA is more commonly used because of its lower computational complexity, it has several limitations and is generally not possible to model the skewing effect, variation of material properties along the axial direction, and the flux leakage in the end-winding regions of radial-flux motors (RFMs). 2D FEA can't be used to analyze the axial-flux modulated motors (AFMMs) either. A complete 3D FEA that fully resolves these shortcomings is necessary when one desires an accurate prediction of performances of electric machines[A38-A40].

For 3D finite element field analysis, the MVP $\vec{A}$ is a vector field with three components. Traditional nodal element can be applied to each component without considering the underlying continuity constraints [A41]. However, the nodal element presents unacceptable numerical errors at geometry corners or interfaces between iron and air [A42]. These problems can be cured by using Whiney edge element [A20-A23] basis functions to approximate the MVP $\vec{A}$. For eddy-current field problems, an

additional potential called the electric scalar potential (ESP) φ is needed and useful to describe the induced eddy currents in conductors.

By introducing the ESP in conducting regions, the continuity equation of the current can be explicitly imposed which is also computationally advantageous [A22, A43, A44]. Although the resultant PDE system of $\vec{A} - \varphi$ formulation is singular, if the right hand side is consistent, the resultant linear matrix can be solved by iteration method with suitable preconditioning matrix and converges fast. The consistency of the linear matrix equation can be accomplished using a current vector potential (CVP) representation of the source excitation current [A45]. For simple circular or racetrack-shaped coil, analytical expressions of the CVP are also available [A28, A36]. For coils of general shape, the source field CVP can be computed numerically [A46].The pre-computed source field can be also used for circuit-coupling in case of external circuit excitations [A32].

1.4. Review of Global Optimal Design Methods

In the optimal design process of EM devices, their performance parameters are usually taken as the design objectives which will be continuously improved by selecting better design parameters under the requirement of given constraints. The evolution of the design parameters or the optimization variables is determined by calling the optimization solvers. In practice, global stochastic optimization methods are more suitable for the inverse EM design problems because they are capable of finding global optimal solution under complex constraints of design variables.

Popular global optimization methods includes genetic algorithm (GA) [A47], taboo search algorithm (TSA) [A48], particle swarm optimization (PSO) [A49] and differential evolution algorithm(DEA) [A50]. These heuristic algorithms are invented by analyzing and animating natural phenomena and society activities. They usually starts with an arbitrary feasible solution and continually improve it by different stochastic evolution operations. Such optimization methods are good at finding the globally optimal solution and is widely used in the optimization of EM devices.

In the evaluation of the performance of a design of EM devices, the FEM can be applied to compute the objective function values under a set of design parameters. Since it is impossible to sweep every set of design parameters as there are infinitely many choices, the response surface methodology (RSM) is a good choice to describe the relationship between design parameters and the response values, so that the inverse problem can be replaced with direct ones. A number of user-specified sample points determined by optimization solvers and the response values obtained finite element analysis were combined together to build a response surface model. Then the optimal solution is solved through the reconstructed model. The objective function values are calculated from the response surface model instead of calling the computation intensive finite element program. It is now widely used in engineering optimization problems [A51-A55].

1.5. Layout of the Thesis

The scope of this thesis covers a review study of the potential formulations for the Maxwell's system used in low-frequency computational electromagnetics. 2D and 3D FEM with nodal and edge basis functions are studied for both static and transient eddy-current problems. Field-motion-circuit coupling method for dynamical simulation of EM devices is investigated. Several global optimization algorithms are discussed and the integration of global optimization algorithms with FEA is applied to several optimal design examples.

The next chapters are organized as follows: Chapter 2 gives the detailed potential formulations of the Maxwell system for low-frequency problems. Several global optimization methods and the RSM are briefly presented. Chapter 3 mainly discusses the parameterized mesh generation, refinement and deformation methods, for both 2D and 3D applications. Two techniques for large shape deformation are also presented. Chapter 4 deals with the implementation details of the 2D nodal FEM and 3D edge element method with nonlinear material, mechanical motion and circuit-coupling. In Chapter 5, a novel adaptive DoFs FEM is applied to nonlinear static problems and transient eddy-current filed computation. In Chapter 6, three numerical methods for

the solution of eddy-current problem with high-speed moving conductors are investigated. In Chapter 7, optimal design examples, including benchmark examples and practical examples, are solved by combining FEA and optimization solvers. Finally, conclusions are drawn and future work is identified in Chapter 8. To make it clear, the flowchart of this thesis is shown below:

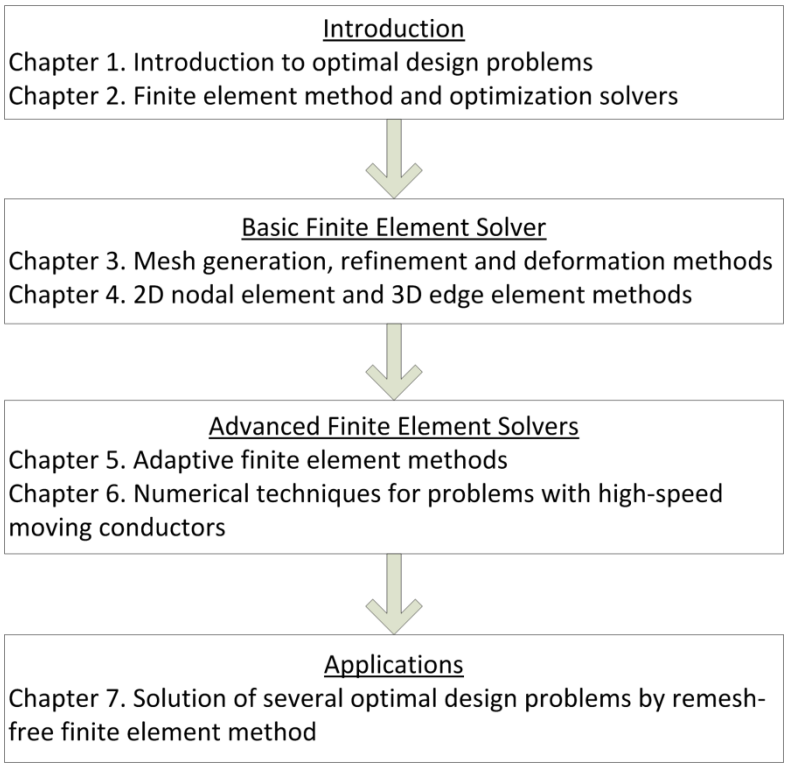

Fig. 1.1. Flowchart of this thesis.

1.6. References-Part A

[A1] J. K. Sykulski, "Computational electromagnetics for design optimisation: the state of the art and conjectures for the future," *Bull. Pol. Ac.: Tech.*, vol. 57, no. 2, pp. 123-131, 2009.

[A2] Lecture 8: Optimetrics Analysis, *ANSYS Maxwell V16 Training Manual*, 2013.

[A3] D. Stevenson, and H. Schaub, "Multi-sphere method for modeling space craft electrostatic forces and torques," *Advances in Space Research*, vol. 51, pp. 10-20, 2013.

[A4] D. C. Meeker, Finite Element Method Magnetics, Version 4.2 (02 Nov 2009 Build), http://www.femm.info/wiki/Documentation/.

[A5] C. Lu, Generalized finite element method for electromagnetic analysis, PhD thesis, Michigan State University, 2008.

[A6] W. C. Chew, M. S. Tong, and B. Hu, Integral Equation Methods for Electromagnetic and Elastic Waves, Morgan and Claypool, San Rafael, Calif, 2009.

[A7] T. Rylander, P. Ingelstrom, and A. Bondeson, Computational Electromagnetics, Second Edition, Springer-Verlag, 2013.

[A8] G. Meunier, The Finite Element Method for Electromagnetic Modeling, ISTE Ltd, 2008.

[A9] N. A. Demerdash, and T. W. Nehl, "Flexibility and economics of implementation of the finite element and difference techniques in nonlinear magnetic fields of power devices," *IEEE Trans. Magn.*, volume12, no. 6, pp. 1036-1038, Nov. 1976.

[A10] K. Venkataratnam, and M. S. Abdul Kadu, "Normalized force-speed curves of eddy current brakes with ferromagnetic loss drums," *IEEE Transactions on Power Apparatus and Systems*, vol. PAS-104, no. 7, pp. 1789-1796, Jul. 1985.

[A11] W. N. Fu, P. Zhou, D. Lin, S. Stanton, and Z. J. Cendes, "Modeling of solid conductors in two-dimensional transient finite-element analysis and its application to electric machines," *IEEE Trans*. *Magn.*, vol. 40, no. 2, pp. 426-434, Mar. 2004.

[A12] J. Zou, Y. Q. Xie, J. S. Yuan, X. S. Ma, X. Cui, S. M. Chen, and J. L. He, "Analysis of the thin plate eddy-current problem by finite volume method," *IEEE Trans*. *Magn.*, vol. 40, no. 2, pp. 1370-1373, Mar. 2004.

[A13] G. Dong, J. Zou, R. H. Bayford, X. Ma, S. Gao, W. Yan, and M. Ge, "The comparison between FVM and FEM for EIT forward problem," *IEEE Trans*. *Magn.*, vol. 41, no. 5, pp. 1468-1471, May 2005.

[A14] P. Alotto, A. Bertoni, I. Perugia, and D. Schötzau, "Efficient use of the local discontinuous Galerkin method for meshes sliding on a circular boundary," *IEEE Trans*. *Magn.*, vol. 38, no. 2, pp. 405-408, Mar. 2002.

[A15] S. Außerhofer, O. Bíró, and K. Preis, "Discontinuous Galerkin finite elements in time domain eddy-current problems," *IEEE Trans*. *Magn.*, vol. 45, no. 3, pp. 1300-1303, Mar. 2009.

[A16] S. Außerhofer, O. Bíró, and K. Preis, “Discontinuous Galerkin formulation for eddy-current problems,” *COMPEL*, vol. 28, no. 4, pp. 1081-1090, 2009.

[A17] M. J. Tuner, R. W. Clough, H. C. Matin, and L. J. Topp, “Stiffness and deflection analysis of complex structures,” *Journal of Aeronautical Science*, vol. 23, pp. 805-824, 1956.

[A18] A. M. Winslow, “Magnetic field calculation in an irregular triangular mesh,” Lawrence Radiation Laboratory Report, UCRL-7784-T, Rev. 1, 1965.

[A19] J. E. Flaherty, Finite Element Analysis Lecture Notes, Spring, 2000.

[A20] O. Biro, K. Preis, and K. R. Richter, “On the use of the magnetic vector potential in the nodal and edge finite element analysis of 3D magnetostatic problems,” *IEEE Trans*. *Magn.*, vol. 32, no. 3, pp. 651-654, May 1996.

[A21] H. Igarashi, and T. Honma, “On convergence of ICCG applied to finite-element equation for quasi-static fields,” *IEEE Trans*. *Magn.*, vol. 38, no. 2, pp. 565-568, Mar. 2002.

[A22] B. Weiß, and O. Bíró, “On the convergence of transient eddy-current problems,” *IEEE Trans*. *Magn.*, vol. 40, no. 2, pp. 957-960, Mar. 2004.

[A23] B. Weiß, and O. Bíró, “Multigrid for time-harmonic 3-D eddy-current analysis with edge elements,” *IEEE Trans*. *Magn.*, vol. 41, no. 5, pp. 1712-1715, May 2005.

[A24] J. Gyselinck, P. Dular, C. Geuzaine, and R. V. Sabariego, “Surface-impedance boundary conditions in time-domain finite-element calculations using the magnetic-vector-potential formulation,” *IEEE Trans*. *Magn.*, vol. 45, no. 3, pp. 1280-1283, Mar. 2009.

[A25] P. Dular, N. Sadowski, J. P. A. Bastos, and W. Legros, “Dual complete procedures to take stranded inductors into account in magnetic vector potential formulations,” *IEEE Trans*. *Magn.*, vol. 36, no. 4, pp. 1600-1605, Jul. 2000.

[A26] J. P. Webb, and B. Forghani, “A single scalar potential method for 3D magnetostatics using edge elements,” *IEEE Trans*. *Magn.*, vol. 25, no. 5, pp. 4126-4128, Sep. 1989.

[A27] J. P. Webb, and B. Forghani, “T-Ω method using hierarchal edge elements,” *IEE Proc.-Sci. Meas. Technol.*, vol. 142, no. 2, pp. 133-141, Mar. 1995.

[A28] A. G. Kladas, and J. A. Tegopoulos, “A new scalar potential formulation for 3-D magnetostatics necessitating no source field calculation,” *IEEE Trans. Magn.*, vol. 28, no.2, pp. 1103-1106, Mar. 1992.

[A29] H. T. Luong, Y. Marechal, and G. Meunier, “Computation of 3-D current driven eddy current problemsusing cutting surfaces,” *IEEE Trans*. *Magn.*, vol. 33, no. 2, pp. 1314-1317, Mar. 1997.

[A30] A. T. Phung, O. Chadebec, P. Labie, Y. L. Floch, and G. Meunier, “Automatic cuts for magnetic scalar potential formulations,” *IEEE Trans*. *Magn.*, vol. 41, no. 5, pp. 1668-1671, May 2005.

[A31] Z. Ren, “T-Ω formulation for eddy-current problems in multiply connected regions,” *IEEE Trans*. *Magn.*, vol. 38, no. 2, pp. 557-560, Mar. 2002.

[A32] P. Zhou, Z. Badics, D. Lin, and Z. J. Cendes, “Nonlinear T-Ω formulation including motion for multiply connected3-D problems,” *IEEE Trans*. *Magn.*, vol. 44, no. 6, pp. 718-721, Jun. 2008.

[A33] P. Dłotko, R. Specogna, and F. Trevisan, “Automatic generation of cuts on large-sized meshes for the T-Ω geometric eddy-current formulation,” *Comput. Methods Appl. Mech. Engrg.*, vol. 198, pp. 3765-3781, 2009.

[A34] R. Specogna, “Optimal cohomology generators for 2-D eddy-current problems in linear time,” *IEEE Trans. Magn.*, vol. 49, no. 4, pp. 1299-1304, Apr. 2013.

[A35] D. Marcsa, “Induction motors simulation by finite element method and different potential formulations with motion voltage term,” B.Sc. thesis, Széchenyi István Univ., Györ, Hungary, 2008.

[A36] W. Yao, Finite Element Analysis Of 3D Electric Machine Problems, Master thesis, University of Illinois at Urbana-Champaign, 2010.

[A37] W. N. Fu, and S. L. Ho, “Elimination of nonphysical solutions and implementation of adaptive step size algorithm in time-stepping finite-element method for magnetic field-circuit-motion coupled problems,” *IEEE Trans. Magn*., vol. 46, no. 1, pp.29-38, Jan. 2010.

[A38] C. Kaehler, and G. Henneberger, “Transient 3-D FEM computation of eddy-current losses in the rotor of a claw-pole alternator,” *IEEE Trans. Magn*., vol. 40, no. 2, pp. 1362-1365, Mar. 2004.

[A39] Huo Feiyang, Han Jichao, Li Weili, Zhou Xingfu, Zhang Yihuang, Li Yong, and Guan Chunwei, "Influence of copper shield structure on 3-D electromagnetic field, fluid and temperature fields in end region of large turbo generator," *IEEE Trans. Energy Convers.*, vol. 28, no. 4, pp. 832-840, Dec. 2013.

[A40] H. Shin, J. Choi, S. Jang, and K. Lim, "Design and analysis of axial permanent magnet couplings based on 3D FEM," *IEEE Trans. Magn*., vol. 49, no. 7, pp. 3985-3988, Jul. 2013.

[A41] O. Biro, and K. Preis, "On the use of the magnetic vector potential in the finite element analysis of 3D eddy currents," *IEEE Trans. Magn*., vol. 25, no. 4, pp. 3145-3159, Jul. 1989.

[A42] K. Preis, I. Bardi, O. Biro, C. Magele, G. Vrisk, and K.R. Richter, "Different finite element formulations of 3D magnetostatic fields," *IEEE Trans. Magn.*, vol. 28, no. 2, pp. 1056-1059, Mar. 1992.

[A43] K. Fujiwara, T. Nakata, and H. Ohashi, "Improvement of convergence characteristic of ICCG method for the $\vec{A}-\varphi$ method using edge elements," *IEEE Trans. Magn.*, vol. 32, no. 3, pp. 804-807, May 1996.

[A44] H. Igarashi, and N. Yamamoto, "Effect of preconditioning in edge-based finite-element method," *IEEE Trans. Magn.*, vol. 44, no. 6, pp. 942-945, Jun. 2008.

[A45] Z. Ren, "Auto gauging of vector potential by iterative solver-numerical evidence", *3rd Int. Workshop on Electric and Magnetic Fields*, Liège, 6-9 May 1996, pp. 119-124.

[A46] Z. Ren, P. Zhou, and Z. Cendes, "Computation of current vector potential due to excitation currents in multiply connected conductor," in *Proc. ICEF*, Tianjin, China, Sep. 2000.

[A47] S. L. Ho, N. N. Chen, and W. N. Fu, "An optimal design method for the minimization of cogging torques of a permanent magnet motor using FEM and genetic algorithm," *IEEE Trans. Applied Superconductivity*, vol. 20, no. 3, pp. 861-864, Jun. 2010.

[A48] S. L. Ho, S. Y. Yang, G. Z. Ni, and H. C. Wong, "An improved Tabu search for the global optimizations of electromagnetic devices," *IEEE Trans. Magn.*, vol. 37, no. 5, pp. 3570-3573, Sep. 2001.

[A49] W. Wang, Y. Lu, J.S. Fu, and Y. Z. Xiong, "Particle swarm optimization and finite-element based approach for microwave filter design," *IEEE Trans. Magn.*, vol. 41, no. 5, pp. 1800-1803, May 2005.

[A50] A. Ketabi, and M. J. Navardi, "Optimization shape of variable capacitance micromotor using differential evolution algorithm," *Mathematical Problems in Engineering*, vol. 2010, Article ID 909240, 15 pages, 2010.

[A51] M. Jeon, D. Kim, and C. Kim, "Optimum design of BLDC motor for cogging torque minimization using genetic algorithm and response surface method," *Journal of Electrical Engineering & Technology*, vol. 1, no. 4, pp. 466-471, 2006.

[A52] B. Lee, K. Kim, J. Hong, and J. Lee, "Optimum shape design of single-sided linear induction motors using response surface methodology and finite-element method," *IEEE Trans. Magn.*, vol. 47, no. 10, pp. 3657-3660, Oct. 2011.

[A53] L. Jian, G. Xu, J. Song, H. Xue, D. Zhao, and J. Liang, "Optimum design for improving modulating-effect of coaxial magnetic gear using response surface methodology and genetic algorithm," *Progress In Electromagnetics Research*, vol. 116, pp. 297-312, 2011.

[A54] S. L. Ho, S. Y. Yang, G. Z. Ni, and H. C. Wong, "A response surface methodology based on improved compactly supported radial basis function and its application to rapid optimizations of EM devices," *IEEE Trans. Magn.*, vol. 41, no. 6, pp. 2111-2117, Jun. 2005.

[A55] S. L. Ho, S. Y. Yang, P. H. Ni, and K. F. Wong, "An adaptive interpolating MLS based response surface model applied to design optimizations of EM devices," *IEEE Trans. Magn.*, vol. 43, no. 4, pp. 1593-1596, Apr. 2007.

CHAPTER 2

LOW-FREQUENCY FEM AND OPTIMAL DESIGN METHODS

2.1. Introduction to Low-frequency Maxwell Problems

The differential form of full-wave Maxwell equations reads

$$\nabla \times \vec{H} = \vec{J} + \frac{\partial \vec{D}}{\partial t}, \tag{2.1}$$

$$\nabla \times \vec{E} = -\frac{\partial \vec{B}}{\partial t}, \tag{2.2}$$

$$\nabla \cdot \vec{B} = 0, \tag{2.3}$$

$$\nabla \cdot \vec{D} = \rho, \tag{2.4}$$

with constitutive relations

$$\vec{B} = \mu \vec{H}, \tag{2.5}$$

$$\vec{J} = \sigma \vec{E}, \tag{2.6}$$

$$\vec{D} = \varepsilon \vec{E}, \tag{2.7}$$

where $\vec{E}$ and $\vec{H}$ are the electric and magnetic field, $\vec{D}$ and $\vec{B}$ the electric and magnetic induction, respectively, $\vec{J}$ is the density of the electric current and ρ the electric charge density; μ is the magnetic permeability, σ is the electric conductivity and ε is the permittivity, generally they are tensors for anisotropic materials, depending on the spatial variable $\vec{x} = (x, y, z)$. Physically, (2.1) is Ampere's circuital law, (2.2) is Faradays' law of induction, (2.3) and (2.4) are Gauss's law for the magnetic field and electric field respectively.

For low-frequency EM field computation problems, the frequency of the source varies slowly with time such that the wavelength is immensely longer than the characteristic size of geometry in the domain considered. Thus the field varies instantaneously with the change of the source other than lagging behind it. This assumption is the case for most of low-frequency EM devices, such as electric

machines, power transformers, induction heating devices, non-destructive testing devices EM brakes, sensors and so on. Thus the displacement current is much smaller than the conduction current and hence can be neglected from (2.1).

The low-frequency approximation of the Maxwell system without displacement current is also called the quasistatic approximation. The problems to be solved are usually called eddy-current or magneto-quasistatic problems. Typically the computational domain of an eddy-current problem V can be split into two parts as shown in Fig. 2.1. One part is the eddy current region V_1 with $\sigma > 0$, which includes the passive conductors or solid source conductors with skin effect. The other is the remaining eddy-current free region V_2 with $\sigma = 0$, which includes the stranded source conductors, the nonconducting ferromagnetic cores and the air region. The boundary of the domain ∂V is decomposed into S_B where the normal component of the magnetic flux density is prescribed, and S_H where the tangential component of the magnetic field intensity is prescribed. Without loss of generality, in this thesis the conducting and nonconducting material interface S_{12} also denotes the magnetic and non-magnetic material interface. In the nonconducting region, the field instantaneously adapts to the excitation (quasi-stationary behavior), while, in the conducting region, this adaptation takes some time (due to eddy currents induced by the varying magnetic fields).

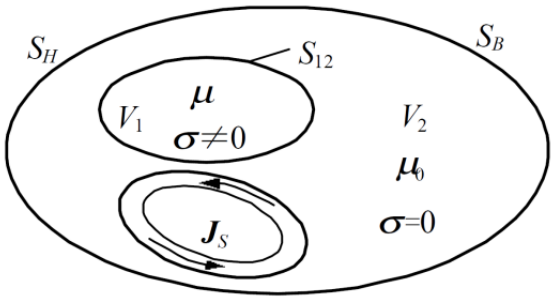

Fig. 2.1. Illustration of typical eddy-current problems.

Dropping the displacement current term of (2.1), the eddy-current problem in V_1 is given by

$$\nabla \times \vec{H} = \sigma \vec{E}, \tag{2.8}$$

$$\nabla \times \vec{E} = -\frac{\partial \vec{B}}{\partial t}, \tag{2.9}$$

$$\nabla \cdot \vec{B} = 0, \tag{2.10}$$

and in V_2

$$\nabla \times \vec{H} = \vec{J}_s, \tag{2.11}$$

$$\nabla \cdot \vec{B} = 0. \tag{2.12}$$

Usually the BCs are homogenous Dirichlet ones

$$\vec{B} \cdot \vec{n} = 0, \text{ on } S_B, \tag{2.13}$$

$$\vec{H} \times \vec{n} = 0, \text{on } S_H. \tag{2.14}$$

And on the material interface S_{12}, there holds

$$\vec{B}_1 \cdot \vec{n}_{12} = \vec{B}_2 \cdot \vec{n}_{12}, \tag{2.15}$$

$$\vec{H}_1 \times \vec{n}_{12} = \vec{H}_2 \times \vec{n}_{12}, \tag{2.16}$$

where $\vec{J}_s$ is the known impressed current density, $\vec{J}_e = \sigma \vec{E}$ is the unknown induced eddy-current density, $\vec{n}$ is the unit outward vector on surface ∂V and $\vec{n}_{12}$ is the unit normal vector pointing from region V_1 to V_2. (2.8) and (2.11) can be also unified as

$$\nabla \times \vec{H} = \vec{J} = \vec{J}_e + \vec{J}_s. \tag{2.17}$$

Note that the intersection of V_1 and V_2 maybe not empty, which is the case for solid excitation coils where the skin effect and proximity effect can't be neglected. Since $\vec{J}_s$ is known and appears to the right hand side of (2.11), the solid excitation coil can be then removed from the study domain and leaves the solid excitation coils region as a part of the eddy-current region. It is also noted that in eddy-current free region V_2, the problem is of magnetostatic type. So only formulations for eddy-current problems are given in the following sections.

2.1.1. Potential Formulations for Magnetoquasistatics

For very simple problems, analytical solutions to the Maxwell equations and prescribed BCs and ICs are available. In general, the Maxwell problems have to be tackled numerically and the BVPs to be solved can be formulated by field quantities or potentials. Field formulations work directly with the physical variables while potential formulations work with some auxiliary variables from which the physical field variables can be derived.

To reduce the number of components of the unknown dependent variables (there are totally six components of $\vec{E}$ and $\vec{H}$) and to make it convenient for considering nonlinear effects of ferromagnetic materials or coupling with external circuits, the potential formulations [B1-B4] rather than the field formulations [B5, B6] are widely used in low-frequency static and transient eddy current solvers. Another reason of using potentials lies in the fact that (2.8) and (2.9) only contain first order spatial derivative of the unknown variables and this type of PDEs is not suitable for directly applying traditional FEM to find the numerical solutions. Furthermore, the required physical discontinuities of field variables, namely (2.15) and (2.16), can be modeled by differentiating the continuous potentials which can be discretized with usual finite elements. There are mainly two types of potential formulations, including the MSP formulations and the MVP formulations, which are dual to each other [B7-B11].

The merit of the MSP formulation is that it uses scalar potentials in current-free regions and hence greatly reduces the total number of DoFs. While if the current-carrying regions are multiply-connected, which is very common to see, surface cuts or volume cuts have to be introduced [A30-A34] to make these regions simply-connected and Ampere's law is satisfied by assigning suitable jump discontinuities to the MSP [A30] or put the required jump of the MSP to the CVP [A31, A32]. However, this cut-making process is very complicated and the resultant scalar potential solver is very difficult to develop.

On the other hand, there is more DoFs in the MVP formulation but it doesn't need to care much about the topological properties of the conducting regions of the problem domain [B13]. For BVPs defined in complicated multiply-connected domains, the MVP also works just as the case in simply-connected problem domains, thus it is widely used in the solution of static and eddy-current problems. These two types of potential formulations are presented in the following sections.

2.1.2. Magnetic Scalar Potential Formulation

From the continuity of the given source current $\vec{J}_s$ and induced eddy-current $\vec{J}_e$,

$$\nabla \cdot \vec{J}_s = 0, \tag{2.18}$$

$$\nabla \cdot \vec{J}_e = 0, \tag{2.19}$$

two CVPs $\vec{T}_0$ and $\vec{T}$ can be introduced such that

$$\vec{J}_s = \nabla \times \vec{T}_0, \tag{2.20}$$

$$\vec{J}_e = \nabla \times \vec{T}. \tag{2.21}$$

From (2.17), the MSP ψ can be introduced in V_1

$$\vec{H} = \vec{T} - \nabla\psi + \vec{T}_0, \tag{2.22}$$

and in V_2

$$\vec{H} = \vec{T}_0 - \nabla\psi. \tag{2.23}$$

Applying Faradays' law and Gauss's law for the solenoidality of the magnetic flux density, the MSP formulation in conducting region V_1 is

$$\begin{cases} \nabla \times (\frac{1}{\sigma} \nabla \times \vec{T}) + \frac{\partial}{\partial t}(\mu\vec{T} - \mu\nabla\psi) = -\frac{\partial}{\partial t}(\mu\vec{T}_0) \\ \nabla \cdot (\mu\vec{T} - \mu\nabla\psi) = -\nabla \cdot (\mu\vec{T}_0) \end{cases}, \tag{2.24}$$

and in nonconducting region V_2

$$\nabla \cdot (-\mu\nabla\psi) = -\nabla \cdot (\mu\vec{T}_0). \tag{2.25}$$

In the MSP formulation, both vector potential $\vec{T}$ and scalar potential ψ exist in conducting region while only scalar potential ψ exists in nonconducting region, which greatly reduces the total number of DoFs. However, nothing comes for free and the MSP formulation encounters difficulties in case of multiply-connected current-carrying conductor loops.

The difficulty when implementing the MSP method is mainly due to the fact that the curl-free function space can't be represented by purely gradient fields on general geometric domains with nontrivial topologies [A31, B13]. An example is shown in Fig. 2.2, where the coil loop carries a nonzero net current I and the closed path C passed through the hole of the loop. Suppose the purely gradient function ψ is used to approximate the magnetic field in the multiply-connected air region, since there is no conduction current and $\nabla \times \vec{H} = \vec{J} = 0$. As a result, there holds

$$\vec{H} = -\nabla\psi \Rightarrow \oint_C \vec{H} \cdot \mathrm{d}\vec{s} = 0. \tag{2.26}$$

On the other hand, from Ampere's law, there holds

$$\oint_C \vec{H} \cdot \mathrm{d}\vec{s} = I \neq 0. \tag{2.27}$$

This contradiction is due to the fact that the curl-free function space can't be represented by purely gradient fields in case of multiply-connected conducting regions.

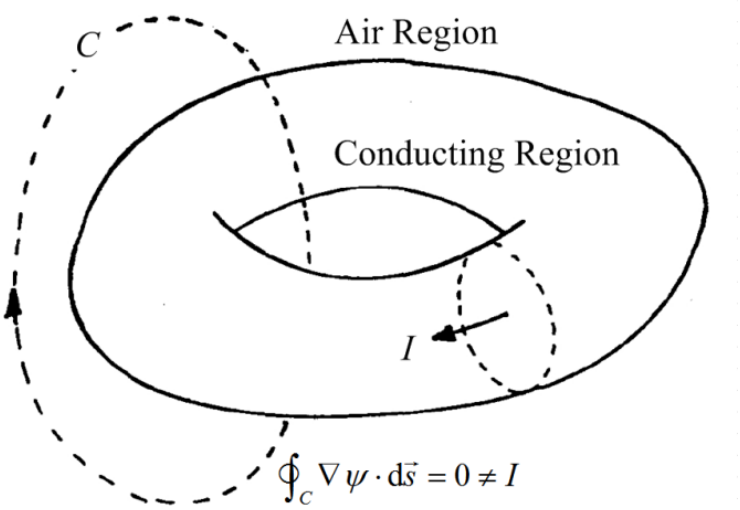

Fig. 2.2. Typical multiply-connected eddy current problems.

One way to conquer this difficulty is to introduce a cutting surface in the conducting region and set double scalar potential values for each node on this surface. The potential jump is set to be the net current flowing in the conductor loop to make the magnetic field satisfy Ampere's law [A30]. However, when there are multiple conductors with holes in the domain, the cuts introduced may intersect with each other which is quite complicated to deal with [A34].

Another method is to use thick cuts constructed from the thin surface cuts [A31, A32], which removes the additional difficulties both in the theory and in the implementation. The thick cuts can be one layer of elements and the required jump of the MSP is absorbed by the CVP, leaving the MSP single-valued in the entire domain. However, these cut-making process is not trivial and the desired MSP finite element solver is very difficult to develop and test. For illustration, a multiply-connected conductor is shown in Fig. 2.3, the conductor mesh with a cutting surface blocking the hole is shown in Fig. 2.4 and the conductor mesh with thick cut which is composed one layer of elements is shown in Fig. 2.5.

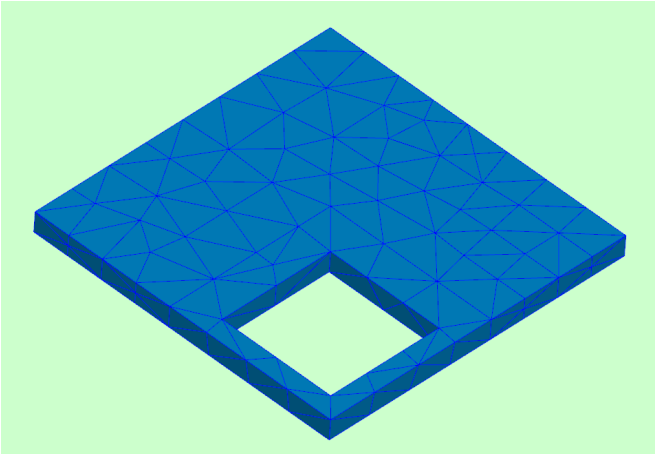

Fig. 2.3. A multiply-connected conductor with a hole inside it.

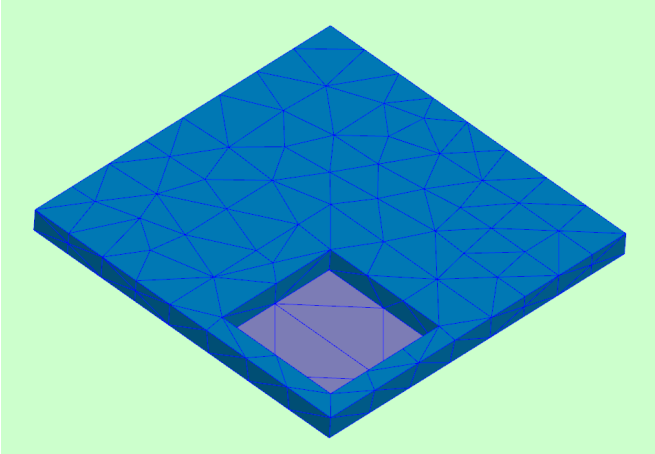

Fig. 2.4. The conductor becomes simply-connected by introducing a cutting surface blocking the hole.

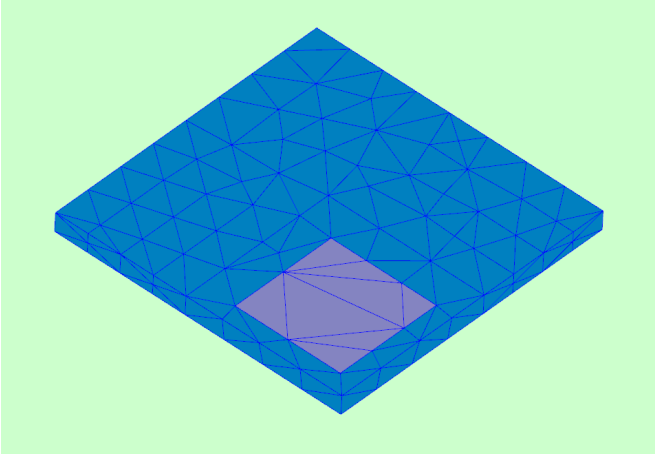

Fig. 2.5. The conductor becomes simply-connected by a cutting domain composed of one layer of tetrahedral elements.

2.1.3. Magnetic Vector Potential Formulation

From the solenoidality of the magnetic flux density, the MVP $\vec{A}$ can be introduced such that

$$\vec{B} = \nabla \times \vec{A}, \tag{2.28}$$

and the use of the MVP makes sure that the Gauss's law for magnetic field (2.10) is satisfied automatically. Then the Faraday's law (2.9) can be rewritten as

$$\nabla \times (\vec{E} + \frac{\partial \vec{A}}{\partial t}) = 0. \tag{2.29}$$

Thus a scalar potential φ can be introduced such that

$$\vec{E} = -\frac{\partial \vec{A}}{\partial t} - \nabla \varphi. \tag{2.30}$$

Then the MVP formulation of the eddy-current problem (2.8)-(2.16) reads

$$\begin{cases} \nabla \times (\nu \nabla \times \vec{A}) = -\sigma \dfrac{\partial \vec{A}}{\partial t} - \sigma \nabla \varphi \\ \nabla \cdot (-\sigma \dfrac{\partial \vec{A}}{\partial t} - \sigma \nabla \varphi) = 0 \end{cases}, \tag{2.31}$$

in conducting region V_1 and

$$\nabla \times (\nu \nabla \times \vec{A}) = \vec{J}_s. \tag{2.32}$$

in nonconducting region V_2, where $\nu = 1/\mu$ is the magnetic reluctivity. Note that the ESP φ exists only in conductors. Furthermore, in practice the eddy-current region is always surrounded by an sufficiently large air layer to model infinitely large space. So on the boundary of the problem domain there is only $\vec{A}$. And the BCs of the potential $\vec{A}$ are

$$\vec{n} \times \vec{A} = 0, \text{ on } S_B, \tag{2.33}$$

$$(\nu \nabla \times \vec{A}) \times \vec{n} = 0, \text{ on } S_H. \tag{2.34}$$

On the material interface S_{12} of V_1 and V_2, there holds

$$\vec{A}_1 \times \vec{n}_{12} = \vec{A}_2 \times \vec{n}_{12}, \text{ on } S_{12}, \tag{2.35}$$

$$(-\sigma \frac{\partial \vec{A}}{\partial t} - \sigma \nabla \varphi) \cdot \vec{n}_{12} = 0, \text{ on } S_{12}. \tag{2.36}$$

Equation (2.35) can be obtained by

$$\begin{aligned}&\vec{B}_1\cdot\vec{n}_{12}=\vec{B}_2\cdot\vec{n}_{12}\Rightarrow(\nabla\times\vec{A}_1)\cdot\vec{n}_{12}=(\nabla\times\vec{A}_2)\cdot\vec{n}_{12}\\&\Rightarrow\nabla\cdot(\vec{A}_1\times\vec{n}_{12})=\nabla\cdot(\vec{A}_2\times\vec{n}_{12}),\ \text{on}\ \ S_{12},\end{aligned}\tag{2.37}$$

and

$$\nabla\cdot(\vec{a}\times\vec{b})=(\nabla\times\vec{a})\cdot\vec{b}-\vec{a}\cdot(\nabla\times\vec{b}),\tag{2.38}$$

which indicated that the continuity of the tangential component of the MVP $\vec{A}$ on the interface S_{12} can guarantee the continuity of the normal component of the magnetic flux density $\vec{B}$. Condition (2.35) can also be obtained using the fact that

$$\vec{B}_1\cdot\vec{n}_{12}=\vec{B}_2\cdot\vec{n}_{12}\Rightarrow[[\vec{B}]]\cdot\vec{n}_{12}=0,\ \text{on}\ \ S_{12},\tag{2.39}$$

and Stokes' theorem

$$\iint_{S_{12}}[[\vec{B}]]\cdot\mathrm{d}\vec{S}=\oint_C[[\vec{A}]]\cdot\mathrm{d}\vec{l}.\tag{2.40}$$

Equation (2.36) means that the induced eddy-current flows tangentially along the interface of conducting and non-conducting interface.

Although there are three components of $\vec{A}$ in nonconducting region which incurs more DoFs the magnetic scalar formulation, it is the duality and complementary of the MSP formulation. For the MSP formulation the Ampere's equation is rigorously satisfied while for the MVP formulation the Faraday's equation is rigorously satisfied. Furthermore, if the edge element is used, the continuity of the normal component of $\vec{B}$ is rigorously satisfied in the MVP formulation, leaving the tangential component of $\vec{H}$ weakly imposed by the variational form. And for the MSP formulation, the tangential component of $\vec{H}$ is rigorously satisfied, leaving the normal component of $\vec{B}$ weakly imposed. There are several computational advantages of the $\vec{A}-\varphi$ formulation:

(1) The formulation is much easier to implement than the MSP formulation and it is very elegant for arbitrary geometry topologies, multiply-connected conductors are convenient to deal with;

(2) The BCs on internal interfaces are natural boundary conditions which are automatically satisfied when the FEM is applied to discretize the BVPs;

(3) The resultant discrete algebraic equation is better-conditioned and easier to be solved than that from the MSP formulation, especially for nonlinear problems.

Actually, the ungauged $\vec{A}-\varphi$ formulation converged fast using iterative solvers if the matrix equation is consistent, which can be accomplished using a CVP representation of the source current densities.

(4) The circuit-coupling with the MVP formulation is also easier to implement than that of the MSP formulation. The expression of the back electromotive force (EMF), which is the bridge to link the magnetic field domain with the electric circuit domain, depends on the MVP $\vec{A}$ directly.

2.1.4. On the Uniqueness of the MVP

It is well known that the solution of the MVP formulation (2.31)-(2.32) for analyzing eddy-currents is not unique. Although the curl of the MVP $\vec{A}$ is specified by (2.28), there is no equation to specify its divergence. So from Helmholtz's theorem, the solution of $\vec{A}$ is not unique. Actually, for arbitrary scalar field ξ, the following vector field and scalar field

$$\begin{cases} \vec{A}_1 = \vec{A} + \nabla\xi \\ \varphi_1 = \varphi - \dfrac{\partial\xi}{\partial t} \end{cases}, \tag{2.41}$$

also satisfy

$$\begin{cases} \vec{B} = \nabla \times \vec{A}_1 \\ \vec{E} = -\dfrac{\partial\vec{A}_1}{\partial t} - \nabla\varphi_1 \end{cases}. \tag{2.42}$$

The function ξ is called the gauge function.

In literature, there are many choices to treat this problem. One is to specify the divergence of the MVP $\vec{A}$ to make the problem has unique solution. A popular choice in low-frequency computational electromagnetics is to adopt the Coulomb gauge

$$\nabla \cdot \vec{A} = 0. \tag{2.43}$$

Another gauge condition which is usually used in high-frequency case is the Lorentz gauge

$$\nabla \cdot \vec{A} = -\mu\varepsilon\frac{\partial\varphi}{\partial t}. \tag{2.44}$$

While it is also feasible not to specify the divergence of $\vec{A}$, just solving the discretized eddy-current equation (2.31)-(2.32) by Krylov space iterative solvers, provided that the right-hand-side (RHS) vector is consistent. An explanation of this method is that in the iteration process, the divergence of $\vec{A}$ is auto-determined or $\vec{A}$ is auto-gauged [A45]. This is the state-of-the-art and popular technique in contemporary low-frequency computational electromagnetics. Because there are some difficulties to adopt the gauged formulation, as can be seen below.

Take the Coulomb gauge for example, one method to specify this gauge condition is to use the penalty technique, where the gauged formulation reads

$$\begin{cases} \nabla\times(\nu\nabla\times\vec{A})-\nabla(\lambda\nabla\cdot\vec{A})=-\sigma\dfrac{\partial\vec{A}}{\partial t}-\sigma\nabla\varphi \\ \nabla\cdot(-\sigma\dfrac{\partial\vec{A}}{\partial t}-\sigma\nabla\varphi)=0 \end{cases}, \tag{2.45}$$

in conducting region V_1 and

$$\nabla\times(\nu\nabla\times\vec{A})-\nabla(\lambda\nabla\cdot\vec{A})=\vec{J}_s. \tag{2.46}$$

in nonconducting region V_2, where λ is a penalty parameter [A41]. Taking the divergence of the first equation in (2.45) and (2.46), it can be observed that $-\Delta(\lambda\nabla\cdot\vec{A})=0$ is implicitly imposed in the whole problem domain where Δ is the Laplace operator. So if the boundary condition $\nabla\cdot\vec{A}=0$ is applied, the Coulomb gauge condition $\nabla\cdot\vec{A}=0$ is also satisfied in the whole domain. The Coulomb-gauged formulation (2.45)-(2.46) can be solved using nodal finite elements. Unfortunately, large numerical error are observed at sharp geometry corners or iron and air interfaces [A42].

Edge elements can be used to remove the numerical error at interfaces when there are materials with different parameters of large ratios. However for edge elements, since $\nabla\cdot\vec{A}=0$ is automatically satisfied locally in each element, it is impossible to use to penalty method to impose the Coulomb gauge globally. To make the resultant matrix equation discretized from edge elements have a unique solution, the tree-cotree method can be used to remove the redundant DoFs by setting the tree-DoFs to be zero. Unfortunately, this way the reduced linear system becomes ill-conditioned and the iterative linear solvers lose their effectiveness [A36].

Another method to apply the Coulomb gauge is to introduce a Lagrange multiplier p to apply this constraint of divergence of the MVP $\vec{A}$

$$\begin{cases} \nabla \times (\nu \nabla \times \vec{A}) - \lambda \nabla p = -\sigma \partial \vec{A} / \partial t - \sigma \nabla \varphi \\ \nabla \cdot (-\sigma \dfrac{\partial \vec{A}}{\partial t} - \sigma \nabla \varphi) = 0 \\ \nabla \cdot \vec{A} = 0 \end{cases}, \tag{2.47}$$

in conducting region V_1 and

$$\begin{cases} \nabla \times (\nu \nabla \times \vec{A}) - \lambda \nabla p = \vec{J}_s \\ \nabla \cdot \vec{A} = 0 \end{cases}. \tag{2.48}$$

in nonconducting region V_2. Homogeneous Dirichlet boundary condition is applied to the multiplier p. Taking the divergence of the first equation in (2.47) and (2.48), it can be observed that $-\lambda \Delta p = 0$ is implicitly imposed in the whole problem domain. So if the boundary condition $p = 0$ is applied, the multiplier p is zero in the whole domain. The problem now is a mixed saddle point problem, the linear system discretized from this method is indefinite for which the effective linear solver should be carefully designed preconditioner [B14-B16].

Considering the above mentioned difficulties, and the necessity to adopt iterative linear solvers in large-scale 3D EM field computation, the ungauged formulation (2.31)-(2.32) with edge elements for the MSP $\vec{A}$ and nodal elements for the ESP φ is really a good choice in practice [A21-A23].

2.2. Optimal Design Methods

In the world of EM design, state-of-the-art finite element simulation, which can be used to compute the performance parameters of each design, is critical to the virtual testing of new concepts and optimization of existing designs. This enables a reduction in the number of costly prototypes and offers the engineer an insight into the behavior of the magnetic field which complements, rather than competes with, test and measurement.

To find the optimal design parameters of a device by using finite element computation, there are usually two kinds of methods widely used, including the gradient based methods and the stochastic optimization methods. For the solution of optimal design or inverse design problems, deterministic gradient based methods use design sensitivity analysis, such as direct differentiation or adjoint method, to search

the optimal solution successively. Since the gradient based algorithms are known to lack design space exploration and are easily trapped by local optima [B17] and by the fact that the optimal design problems is highly complicated with nonlinearity or non-convexity in practical design of EM devices, stochastic optimization methods which avoid the complicated derivation and computation of the sensitivity and can easily get rid of arbitrary variable constraints, has become very popular nowadays [A54, A55, B18-B20].

2.3. Review of Evolutionary Global Optimization Solvers

Since there may be multiple local extremums of the objective function, classic gradient-based optimization solvers such as the conjugate gradient method (also called the steepest descent method) are effective in finding a single local extremum using the gradient information and searching in the steepest descent direction successively. To find the global extremum of complicated optimal design problems in electrical engineering, it is much better to adopt the global or evolutionary optimization solvers.

Generally speaking, the evolutionary optimization solvers are heuristic in that they gradually update the population of individuals by some principle similar to the evolution process of species in nature and try to find better solution in the iteration process. In this section, four frequently used global optimization solvers are briefly reviewed, including the Genetic Algorithm (GA), the Tabu Search Algorithm (TSA), the Particle Swarm Optimization (PSO) Algorithm and the Differential Evolution Algorithm (DEA).

Without loss of generality, suppose the single object function is $f(X)$ and the problem under consideration is a minimal optimization problem. For all the four algorithms, suppose the number of the design parameters is d, the population size is Np, and the i-th individual in the G-th generation is denoted by $X_{i,G}$ (i=1,2,...,Np, G=0,1,2,...,G_{max}), where G_{max} denotes the maximum generation number in the optimization process. The design parameters' lower and upper limits are denoted by X_{min} and X_{max} respectively.

2.3.1. Genetic Algorithm (GA)

GA is a directed search algorithm based on the mechanics of biological evolution, which is widely used in engineering optimization problems since its invention in 1975 [B21]. The essence of GA involves the encoding of the design variables as arrays of binary bits or character strings to represent the chromosomes, the selection, crossover and mutation operations according to their fitness to find a global optimal solution to the problem concerned. This is often done by the following procedure:

(1) Encoding of the objectives or optimization functions;

(2) Creating an initial population of individuals;

(3) Doing iterations by evaluating the fitness of each individuals in the population, generating a new population by performing selection, crossover, and mutation, and replacing the old population with the new population;

(4) Decoding the results to obtain the solution to the problem.

The design variables is usually coded in the form of binary arrays or real-valued arrays [B22]. For simplicity, the binary string with fixed string length L is adopted for coding to facilitate the genetic operators. The selection of individuals in a population is carried out by the evaluation of their fitness, and the selection probability is given by

$$P_{\text{select}}(X_{i,G}) = \frac{\tilde{f}(X_{i,G})}{\sum_{i=1}^{Np} \tilde{f}(X_{i,G})}, \tag{2.49}$$

where $\tilde{f}$ is called the fitness function, which is the corresponding maximum object function of $f(X)$. The crossover of two parent strings is the main operator with probability Pc (usually 0.6 to 1.0) and is carried out by switching one segment of one string with the corresponding segment on another string at a random position, as shown in Fig. 2.6. The mutation operation is achieved by the flopping of randomly selected bits, and the mutation probability Pm is usually taken to be small (0.001 to 0.05), as shown in Fig. 2.7. The whole process of GA can be briefly summarized as Fig. 2.8.

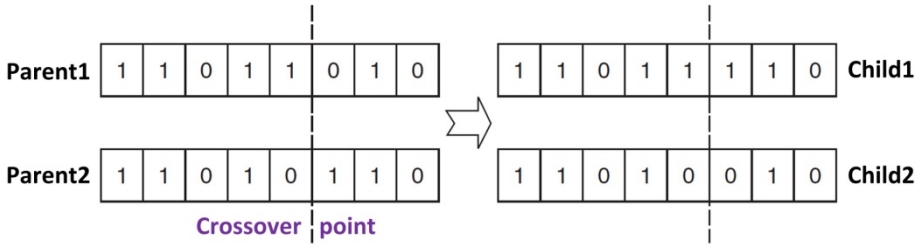

Fig. 2.6. Illustration of the crossover operation.

Fig. 2.7. Illustration of the mutation operation.

G=0;
Initialize The population;
Evaluate the fitness;
While (termination condition not met)
  G=*G*+1;
  selection;
  crossover;
  mutation;
end

Fig. 2.8. Structure of a GA.

2.3.2. Tabu Search Algorithm (TSA)

TSA is a heuristic optimization technique originally developed for combinatorial problems or integer programming [B23]. It has been widely used in optimization problems with continuous variables [B24-B26]. The idea of the TSA is very simple. It starts from an initial solution *s*, then a set of individuals *S*' are randomly generated in the neighbors of *s*. The objective function values are evaluated at each individual of *S*', and the best element *s*' in *S*' becomes the new current solution, even if it is worse than *s*. Hence it is possible to escape from the local minima of the objective function. Then a new iteration is performed: the previous procedure is repeated by starting from the new current point, until some given stopping condition is reached.

In computer implementation, the intervals of different variable directions $\{X^j_{\min}, X^j_{\max}\}^d_{j=1}$ are all transformed into [0,1] first. Then a series of subdomains

contained in the whole feasible domain is selected around the current best solution according to the predetermined step-lengths $\{h_i\}_{i=1}^{Np}$, and the population of the next generation is diversified in each of the subdomain. The step lengths can be taken as for each coordinate direction [B25]

$$\begin{cases} h_1 = 1, C = (\dfrac{1}{h_{\min}})^{\frac{1}{Np-1}}, \\ h_i = \dfrac{h_{i-1}}{C}, i = 2,3,...,Np. \end{cases}, \tag{2.50}$$

where $h_{\min}$ is the minimum step-length which usually taken to be 10^{-4} to meet the accuracy requirement of practical engineering problems. The following formula is used to update the population from the current best solution $\{X_G^j\}_{j=1}^d$

$$\begin{cases} X_{i,G+1}^j = X_G^j + r_{ij} \cdot P_j \cdot h_i \\ P_j = \dfrac{X_{\max}^j - X_{\min}^j}{2} \end{cases}, \tag{2.51}$$

where r_{ij} is a random number in the interval [-1,1].

2.3.3. Particle Swarm Optimization (PSO) Algorithm

The PSO method is a population based stochastic searching and optimization algorithm. It is inspired by social behavior of bird flocking or fish schooling. Individual swarm members can profit from the discoveries and previous experience of all other members of the school. These instructions help in the decision making process of individuals based on the following items [B27, B28]:

(1) experience of individual as its best results so far;

(2) outlay of experience of swarm as the best result among all individuals.

PSO algorithm use the swarm intelligence, which is the ability of each individual to use the experience of others guides the swarm toward its optimum goal, to successively attain the optimal solution.

In the PSO method, a potential solution is named as a particle. The trajectory of each particle is gradually adjusted towards its own best position and the global best position discovered by its neighbors, as well as the whole swarm. These particles try to converge to the optimal solution by coordinating and cooperating. The flowchart of the standard PSO algorithm can be illustrated as Fig. 2.9.

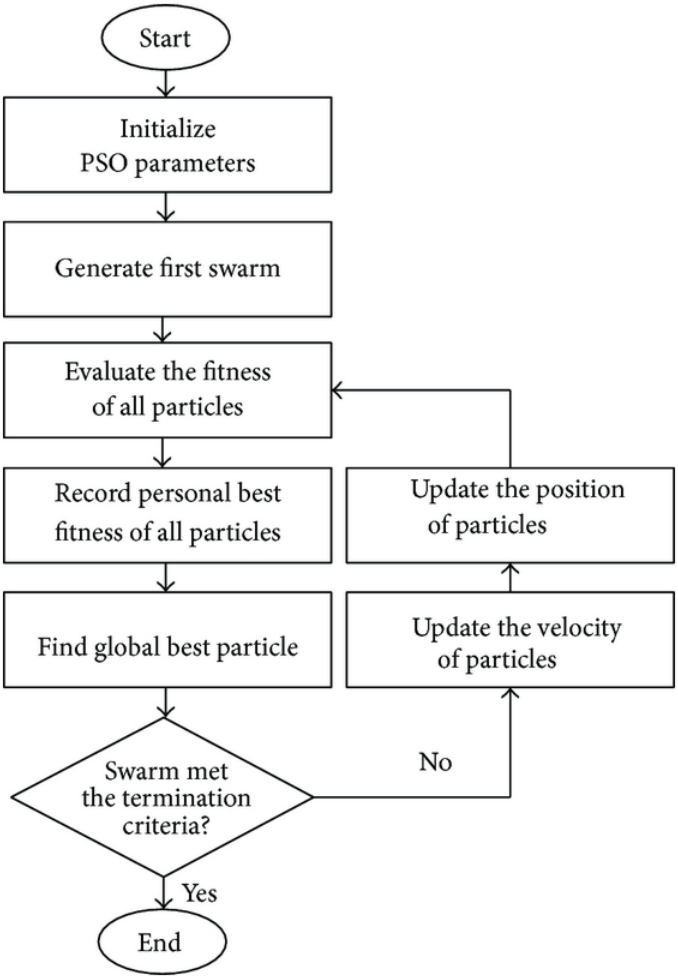

Fig. 2.9. Flowchart of the standard PSO algorithm.

The standard PSO method can be further improved by introducing some control parameters, including the inertial weight ω which is used to adjust the global and local optimization capability of the method, the acceleration parameters c_1 and c_2, and the positive maximum velocity in the j-th coordinate $v_{\max}^j$. The formula to update the population of particles read

$$\begin{cases} v_{i,G+1}^j = \omega v_{i,G}^j + c_1 r_1 (p_i^j - X_{i,G}^j) + c_2 r_2 (g_i^j - X_{i,G}^j) \\ v_{i,G+1}^j = \dfrac{v_{i,G+1}^j \cdot v_{\max}^j}{|v_{i,G+1}^j|}, \text{ if } |v_{i,G+1}^j| > v_{\max}^j \\ X_{i,G+1}^j = X_{i,G}^j + v_{i,G+1}^j \end{cases} . \tag{2.52}$$

where g_i^j represents the best particle position among the entire population and p_i^j is the previous best particle position. This iteration process terminates when the maximum generation number $G_{\max}$ is attained.

2.3.4. Differential Evolution Algorithm (DEA)

For the DEA, after initializing a population of the design variables according to their upper and lower limits as $\{X_{i,0}\}_{i=1}^{Np}$, the evaluation process is done to get the objective function values $\{f(X_{i,0})\}_{i=1}^{Np}$. The mutation (crossover, recombination) operation is executed to increase the diversity of the population. For each individual $X_{i,G}$ in the population, three random integers $r_1, r_2, r_3 \in \{1,2,...,Np\}$ which are mutually different to each other and a random integer $j_r \in \{1,2,...,d\}$ are used to generate a new individual $\tilde{X}_{i,G}$ with its j-th (j=1,2,...,d) component as

$$\tilde{X}_{i,G}^{j} = \begin{cases} X_{r_1,G}^{j} + F(X_{r_2,G}^{j} - X_{r_3,G}^{j}), \text{if rand}[0,1] < P_c \text{ or } j = j_r \\ X_{i,G}^{j}, \text{else.} \end{cases}, \tag{2.53}$$

where F is the crossover factor and P_c is the crossover probability. Then the selection process is executed to get the (G+1)-th population

$$X_{i,G+1}^{j} = \begin{cases} \tilde{X}_{i,G}^{j}, \text{if } f(\tilde{X}_{i,G}^{j}) < f(X_{i,G}^{j}), \\ X_{i,G}^{j}, \text{else.} \end{cases} \tag{2.54}$$

The whole process is terminated when some conditions are satisfied, for example, when the maximum generation number $G_{\max}$ is met and the optimal solution is taken as the one in the population with minimal objective function value. This algorithm can be realized within only about 20 lines in *C* code [B29].

2.4. Introduction to Response Surface Methodology

After sweeping all the sampling shape design parameters by FEM, a continuous optimization problem can be then reconstructed using the RSM [A54, A55]. RSM is an interpolation method to reconstruct a continuous multidimensional function from given discrete function values at the sample points. In the following, the RSM with radial basis functions is used as an example to illustrate the basic idea.

The construction of the response surface model using RBF can be briefly described as follows. Let $R^+ = \{x \in R, x \geq 0\}$ denote the set of non-negative real numbers and suppose a RBF $H : R^+ \to R$ is continuous with $H(0) \geq 0$. For example,

the RBF on R^d is defined in the form $H(\| X \|)$, where $X \in R^d$, $\| \cdot \|$ is the Euclidean norm of the point *X*.

In general, the reconstruction of an objective or constraint function $f(X): R^d \to R$ according to its value f_j at a given set of sample points $X_j \in R^d, j = 1,2,...,N,$ under the radial basis functions $\{H_j\}_{j=1}^N$ is

$$f(X) = \sum_{j=1}^{N} c_j H_j = \sum_{j=1}^{N} c_j H(\| X - X_j \|). \tag{2.55}$$

The unknown expansion coefficients $C = \{c_j\}_{j=1}^N$ are determined by solving the following linear algebraic system:

$$C = H^{-1} F, \tag{2.56}$$

where *H* is the interpolation matrix with entries $H_{ij} = H(\| X_i - X_j \|)$, and $F = \{f_j\}_{j=1}^N$ is the right hand side vector with f_j computed from the FEA at each sample point of the design space.

2.5. Summary

In this chapter, the formulations for low-frequency EM field computation is reviewed. The MVP-based formulation is elegant and easy to implement for arbitrarily complicated 3D geometries. Although the MSP-based formulation is computationally efficient since there is less unknowns, this formulation is highly difficult to implement for complicated multiply-connected 3D geometries.

For practical engineering optimal design problems, there may be multiple local extremums of the objective function. To find the global extremum of complicated optimal design problems in electrical engineering, it is much better to adopt the global or evolutionary optimization solvers.

In this chapter, four classical global optimization algorithms are introduced, including the GA, TSA, PSO and DEA. They are all proved to be effective in practice. To reduce the number of forward finite element runs to get the objective function values, the RSM can be also utilized to reconstruct a surrogate model to replace the actual finite element computations.

2.6. References-Part B

[B1] O. Biro, "Edge element formulation of eddy current problems," *Comput. Methods Appl. Mech. Engrg.*, vol. 169, pp. 391-405, 1999.

[B2] P. Dular, C. Geuzaine, and W. Legros, "A natural method for coupling magnetodynamic H-formulations and circuit equations," *IEEE Trans. Mag.*, vol. 35, no. 3, pp. 1626-1629, May 1999.

[B3] P. Dular, F. Henrotte, and W. Legros, "A general and natural method to define circuit relations associated with magnetic vector potential formulations," *IEEE Trans. Mag.*, vol. 35, no. 3, pp. 1630-1633, May 1999.

[B4] P. Dular, "The benefits of nodal and edge elements coupling for discretizing global constraints in dual magnetodynamic formulations," *Journal of Computational and Applied Mathematics*, vol. 168, pp. 165-178, 2004.

[B5] N. A. Golias, C. S. Antonopoulos, T. D. Tsiboukis, and E. E. Kriezis, "3D eddy current computation with edge elements in terms of the electric intensity," *COMPEL*, vol. 17, no. 5/6, pp. 667-673, 1998.

[B6] R. Rieben, and D. A. White, "Verification of high-order mixed finite-element solution of transient magnetic diffusion problems," *IEEE Trans. Mag.*, vol. 42, no. 1, pp. 25-39, Jan. 2006.

[B7] P. Dular, P. Kuo-Peng, C. Geuzaine, N. Sadowski, and J. P. A. Bastos, "Dual magnetodynamic formulations and their source fields associated with massive and stranded inductors," *IEEE Trans. Mag.*, vol. 36, no. 4, pp. 1293-1299, Jul. 2000.

[B8] P. Dular, J. Gyselinck, T. Henneron, and F. Piriou, "Dual finite element formulations for lumped reluctances coupling," *IEEE Trans. Mag.*, vol. 41, no. 5, pp. 1396-1399, May 2005.

[B9] Z. Ren, and A. Razek, "Comparison of some 3D eddy current formulations in dual systems," *IEEE Trans*. *Magn.*, vol. 36, no. 4, pp. 751-755, Jul. 2000.

[B10] Z. Ren, "2-D dual finite-element formulations for the fast extraction of circuit parameters in VLSI," *IEEE Trans. Mag.*, vol. 39, no. 3, pp. 1590-1593, May 2003.

[B11] R. Specogna, “Extraction of VLSI multiconductor transmission line parameters by complementarity,” *IEEE Trans. Very Large Scale Integr. (VLSI) Syst.*, vol. 22, no. 1, pp. 146-154, Jan. 2014.

[B12] F. Henrotte, and K. Hameyer, “An algorithm to construct the discrete cohomology basis functions required for magnetic scalar potential formulations without cuts,” *IEEE Trans. Mag.*, vol. 39, no. 3, pp. 1167-1170, May 2003.

[B13] L. Kettunen, K. Forsman, and A. Bossavit, “Discrete spaces for div and curl-free fields,” *IEEE Trans. Mag.*, vol. 34, no. 5, pp. 2551-2554, Sep. 1998.

[B14] Q. Hu, and J. Zou, “Substructuring preconditioners for saddle-point problems arising from Maxwell’s equations in three dimensions,” *Math. Comput.*, vol. 73, no.245, pp. 35-61, Aug. 2003.

[B15] J. Q. Chen, Y. F. Xu, and J. Zou, “An adaptive edge element method and its convergence for a saddle-point problem from magnetostatics,” *Numerical Methods for Partial Differential Equations*, vol. 28, no. 5, pp. 1643-1666, Sep. 2012.

[B16] S. Wu, T. Huang, and Cui-Xia Li, “Modified block preconditioners for the discretized time-harmonic Maxwell equations in mixed form,” *Journal of Computational and Applied Mathematics*, vol. 237, pp. 419-431, 2013.

[B17] F. Fraternali, A. Marino, T. Sayed, and A. Cioppa, “On the structural shape optimization through variational methods and evolutionary algorithms,” *Mechanics of Advanced Materials and Structures*, vol. 18, pp. 225-243, 2011.

[B18] S. L. Ho, and S. Y. Yang, “A computationally efficient vector optimizer using ant colony optimizations algorithm for multi-objective designs,” *IEEE Trans. Magn.*, vol. 44, no. 6, pp. 1034-1037, Jun. 2008.

[B19] S. L. Ho, S. Y. Yang, and G. Z. Ni, “Incorporating a-priori preferences in a vector PSO algorithm to find arbitrary fractions of the Pareto front of multi-objective design problems,” *IEEE Trans. Magn.*, vol. 44, no. 6, pp. 1038-1041, Jun. 2008.

[B20] S. L. Ho, S. Y. Yang, G. Z. Ni, and K. F. Wong, “An efficient multiobjective optimizer based on genetic algorithm and approximation techniques for EM design,” *IEEE Trans. Magn.*, vol. 43, no. 4, pp. 1605-1608, Apr. 2007.

[B21] John H. Holland, Adaptation in Natural and Artificial Systems. University of Michigan Press, Ann Arbor, 1975.

[B22] F. Herrera, M. Lozano, and J. L. Verdegay, "Tackling real coded genetic algorithms: operators and tools for behavioral analysis," *Artificial Intelligence Review*, vol. 12, pp. 265-319, 1998.

[B23] F. Glover, "Future paths for integer programming and links to artificial intelligence," *Computers and Operations Research*, vol. 13, pp. 533-549, 1986.

[B24] P. Siarry, and G. Berthiau, "Fitting of Tabu search to optimize functions of continuous variables," *International Journal for Numerical Methods in Engineering*, vol. 40, pp. 2449-2457, 1997.

[B25] S. Y. Yang, G. Z. Ni, Y. Li, B. X. Tian, and R. L. Li, "An universal Tabu search algorithm for global optimization of multimodal functions with continuous variables in electromagnetics," *IEEE Trans. Magn.*, vol. 34, no. 5, pp. 2901-2904, Sep. 1998.

[B26] X. D. Chen, G. Z. Ni, and S. Y. Yang, "An improved Tabu algorithm applied to global optimizations of inverse problems in electromagnetics," *IEEE Trans. Magn.*, vol. 38, no. 2, pp. 1069-1072, Mar. 2002.

[B27] Kennedy, and R. Eberhart, "Particle swarm optimization," in Proceedings of the IEEE International Conference on Neural Networks, pp. 1942-1948, December 1995.

[B28] M. Clerc, and J. Kennedy, "The particle swarm-explosion, stability, and convergence in a multidimensional complex space," *IEEE Trans. Evol. Comput.*, vol. 6, no. 1, pp. 58-73, 2002.

[B29] R. Storn, and K. Price, "Differential evolution-A simple and efficient heuristic for global optimization over continuous spaces," *J. Global Opt.*, vol. 11, pp. 341-359, 1997.

CHAPTER 3

MESH GENERATION, REFINEMENT, AND DEFORMATION METHODS

3.1. Mesh Generation and Refinement Methods

To apply the mesh-based numerical methods especially the FEM for field computation, the first step is to prepare the mesh data, usually called preprocessing. For standard FEM, a mesh is a set of non-overlapping conforming simplex elements covering the computational domain, as shown in Fig. 3.1.

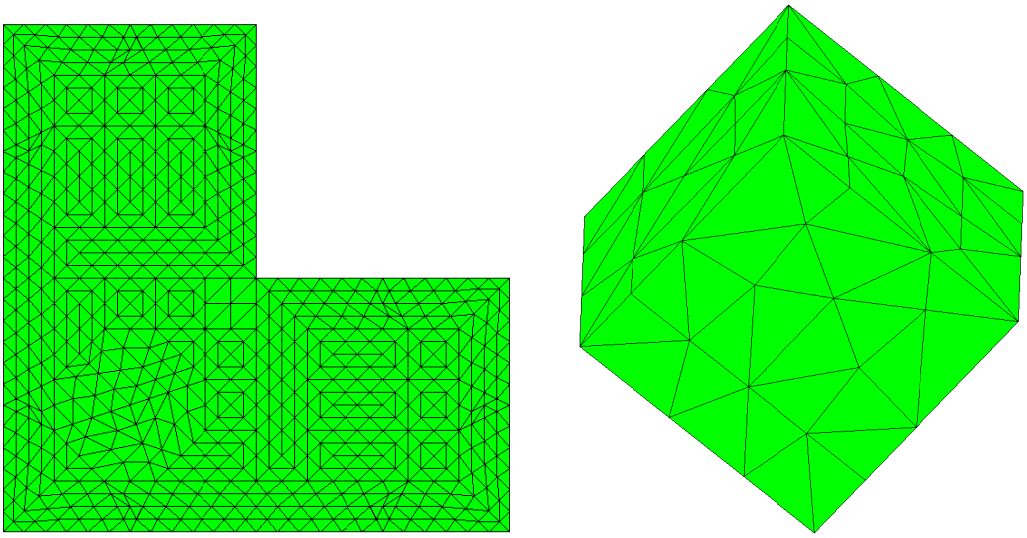

Fig. 3.1. A sample 2D triangular mesh and 3D tetrahedral mesh.

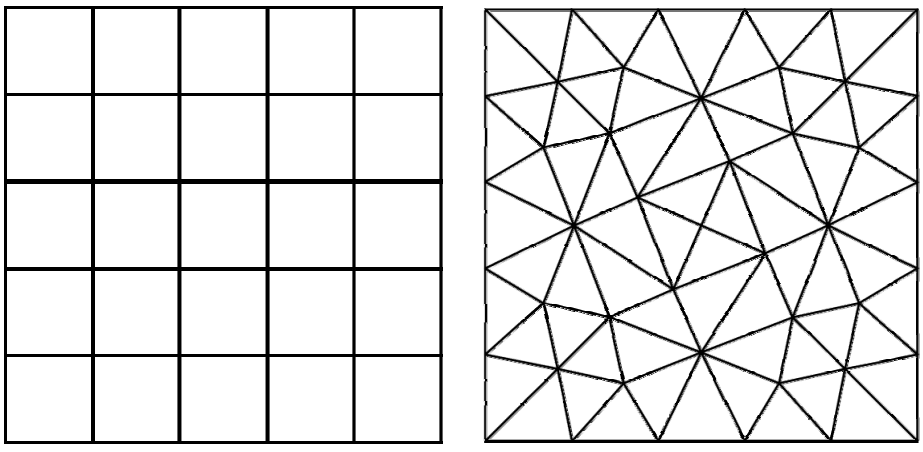

Fig. 3.2. A sample 2D structured mesh and unstructured mesh.

For simple geometries, structured meshes can be generated conveniently [C1]. A comparison between the structured mesh and unstructured mesh is given in Fig. 3.2. For general geometries with complicated object outlines, structured meshing is much more difficult to generate and unstructured mesh generation methods are more popular.

3.1.1. Delaunay Mesh Generation Methods

There are a lot of reported work on mesh generation methods for 2D domains and 3D domains, such as the advancing front or paving method [C1, C2], Delaunay method [C1, C3-C6], quadtree/octree methods [C7] and so on. Among these methods, the Delaunay mesh generation method has the advantage that the resultant triangles are optimal for the given set of points in that they usually do not contain many extremely skewed cells, which is a very desirable property from the viewpoint of computational accuracy when using the finite element method (FEM).

The Delaunay method has maximum minimal angles and empty circle properties, where no point of the forming node set can be contained inside the circum-circle of any triangle, as shown in Fig. 3.3. So the method can avoid generating long and thin triangular elements of bad shape/quality. In this thesis, the shape/quality of an element is evaluated by the quality factor (QF) defined as $Q = 4\sqrt{3}\Delta / (a^2 + b^2 + c^2)$, where a, b and c are the length of the three edges of the triangle being considered; Δ is its area. Clearly Q = 1.0 for an equiangular triangle, the smaller the value of Q, the worse the shape of an element. Typical elements with bad shape are illustrated in Fig. 3.4.

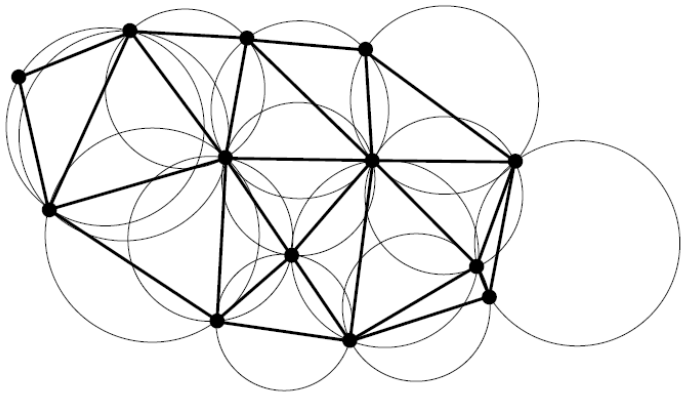

Fig. 3.3. Every triangle of a Delaunay triangulation has an empty circum-circle.

(a) (b)

Fig. 3.4. Triangular elements with bad shape: where small angles cause poor conditioning of the finite element matrix and large angles cause discretization error and big errors in interpolated derivatives.

To show the advantage of the Delaunay triangulation that it can avoid long and thin triangular elements with bad QFs, an arbitrary triangulation and the Delaunay one is given in Fig. 3.5 for comparison. From Fig. 3.5 one can easily observe that the QFs of the triangular elements in the Delaunay mesh are significantly improved.

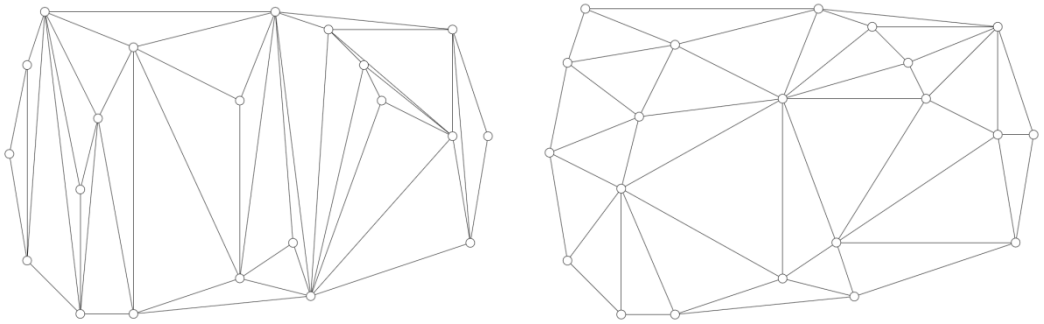

(a) (b)

Fig. 3.5. An arbitrary triangulation and the Delaunay mesh of the same domain with the same nodes.

There are mainly two algorithms to implement the Delaunay method, namely Lawson algorithm [C4] and Bowyer-Watson algorithm [C3, C8, C9]. In this thesis, the Delaunay method with Lawson algorithm is used to generate the initial mesh for the geometry of problem domain. To make sure that all input domain boundaries and material interface segments are present in the resultant initial mesh, a conforming Delaunay method adding stitch points or Steiner points is used [C5].

In Lawson's incremental insertion algorithm for Delaunay mesh generation, the nodes are inserted to the existing mesh one by one. For the insertion of a node *P*, firstly the triangular element *E* containing the node *P* is found using the algorithm illustrated in Fig. 3.6. Since the directed area of the triangle *PBC* is negative and the

neighboring element $E1$ on the right hand side of edge BC is non-empty, the search is moved to $E1$. This iteration will terminate when the element E containing P is found, in that case all the directed area of the triangle PAB, PBC and PCA are all positive.

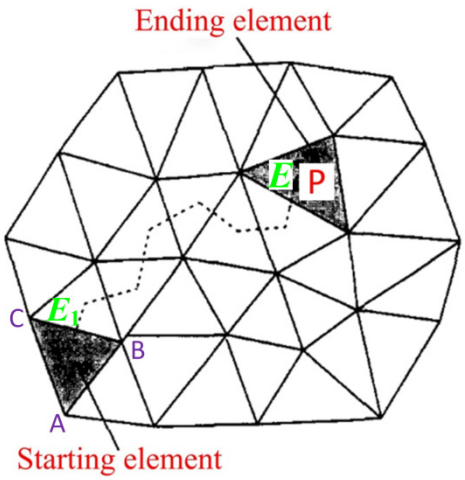

Fig. 3.6. Method to search the element containing P.

Then the element E is subdivided into three smaller triangles. This generally make the new mesh does not satisfy the Delaunay's empty circle property. To make the mesh satisfy Delaunay's principle, a key operation is to apply the edge swapping process, as shown in Fig. 3.7, to improve the quality of the mesh successively. The edge AC and BD is to be swapped if $\angle BAD + \angle BCD > \pi$.

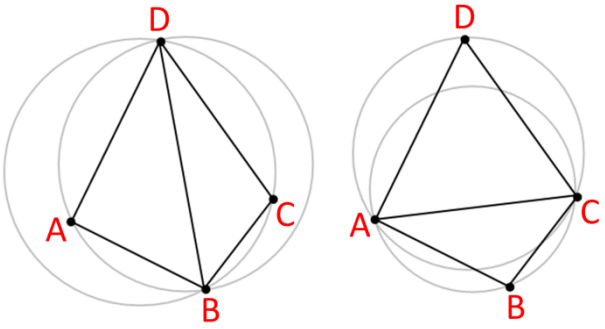

Fig. 3.7. Illustration of the edge swapping process. The left triangulation does not meet the Delaunay condition (the circumcircles contain more than three points). Flipping the common edge produces a Delaunay triangulation for the four points.

After the edge swapping operations to the mesh recursively after the insertion of the node P, every triangle in the mesh is now with good shape. This process is illustrated in Fig. 3.8.

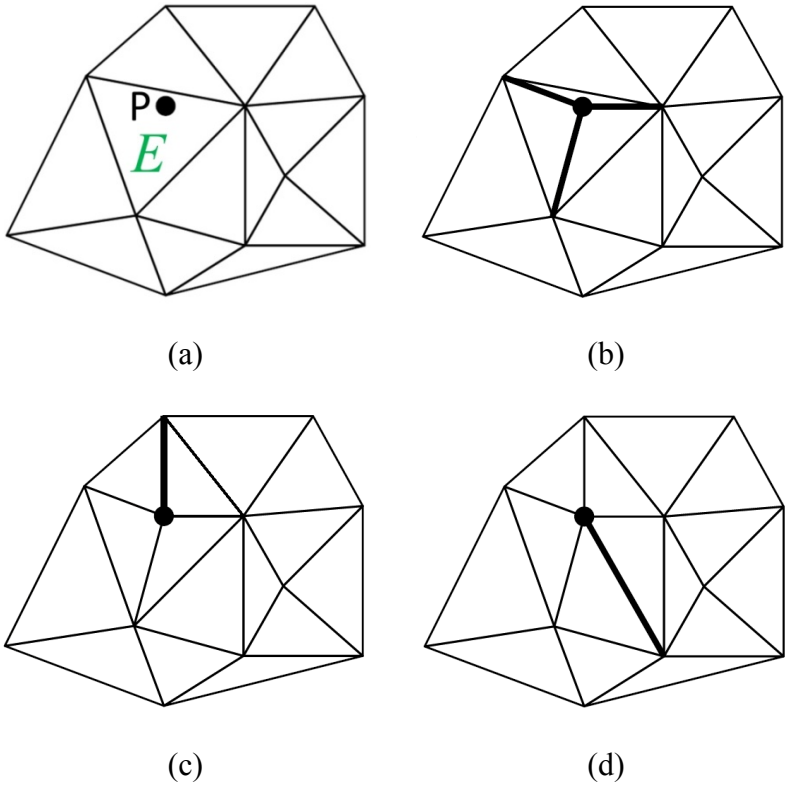

Fig. 3.8. (a) Insert a point *P* to the element *E*. (b) The element *E* is subdivided into three triangles with bad shapes. (c) The mesh after first edge swapping operation. (d) The mesh after second edge swapping operation.

It is noted that the result of mesh by Bowyer-Watson algorithm is the same as that of the Lawson algorithm. The difference lies in that in the Bowyer-Watson algorithm, instead of the tri-sectioning the element *E* containing the newly inserted point *P*, the cavity *ABCDFA* is first found, as shown in Fig. 3.9, and then *P* is connected to the vertices of the cavity to form the Delaunay mesh. The result is the same as what is shown in Fig. 3.8(d).

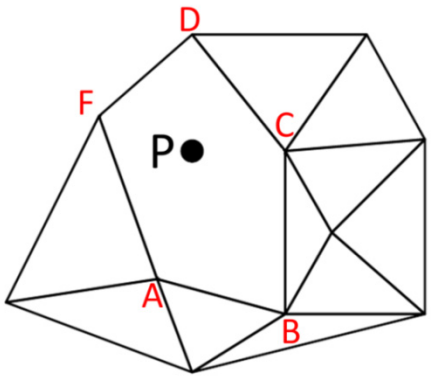

Fig. 3.9. Illustration of the Bowyer-Watson algorithm when inserting a point *P*.

3.1.2. Delaunay Mesh Refinement Methods

To assure the accuracy of the finite element solution, usually the mesh needs to be refined several times to achieve the desired accuracy [C10-C15]. The Delaunay method is also suitable for mesh refinement because the insertion of a vertex to a triangle is very local and only needs minor modification to existing mesh.

Three mesh refinement methods are widely used in FEM, namely the trisection method, (longest edge) bisection method [C16-C18] and the regular refinement method [C19, C20]. The trisection mesh refinement process is the same as the formerly mentioned node insertion process as shown in Fig. 3.8. In the regular mesh refinement method, also called the red-green refinement method, the element will be subdivided into four similar triangles by bisecting all the three edges. To make the mesh to be conforming, the three neighbor elements are bisected, as shown in Fig. 3.10. As can be seen from the figure, the mesh quality yet becomes worse than that of the original mesh.

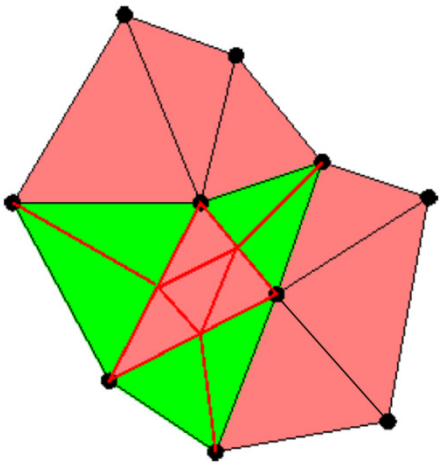

Fig. 3.10. Illustration of the red-green mesh refinement method.

A good choice is to adopt the bisection refinement method, which can improve the mesh quality at the same time when refining the mesh [C16]. In this thesis, the backward-longest-edge-bisection (BLEB) algorithm is adopted. Suppose the element t_0 is marked to be bisected, then the longest-edge propagation path (LEPP), which is composed of several elements, of t_0 is found to be $\{t_0, t_1, t_2, t_3\}$. The elements in the LEPP have strictly increasing longest edge. So it is easy to see that there are finite number of element in the LEPP. For the first iteration, the common longest edge of t_2

and t_3 AB is bisected and the LEPP is updated as $\{t_0, t_1, t_2\}$. In the second iteration, the common longest edge of t_1 and t_2 AC is bisected and the LEPP is updated to be $\{t_0, t_1, t_2, t_3, t_4\}$. In the third iteration, the common longest edge of t_3 and t_4 AD is bisected... This process will terminate if the element t_0 itself is bisected. The final result of the BLEB algorithm is shown in Fig. 3.11(d), where node 1 to node 6 are inserted into the mesh.

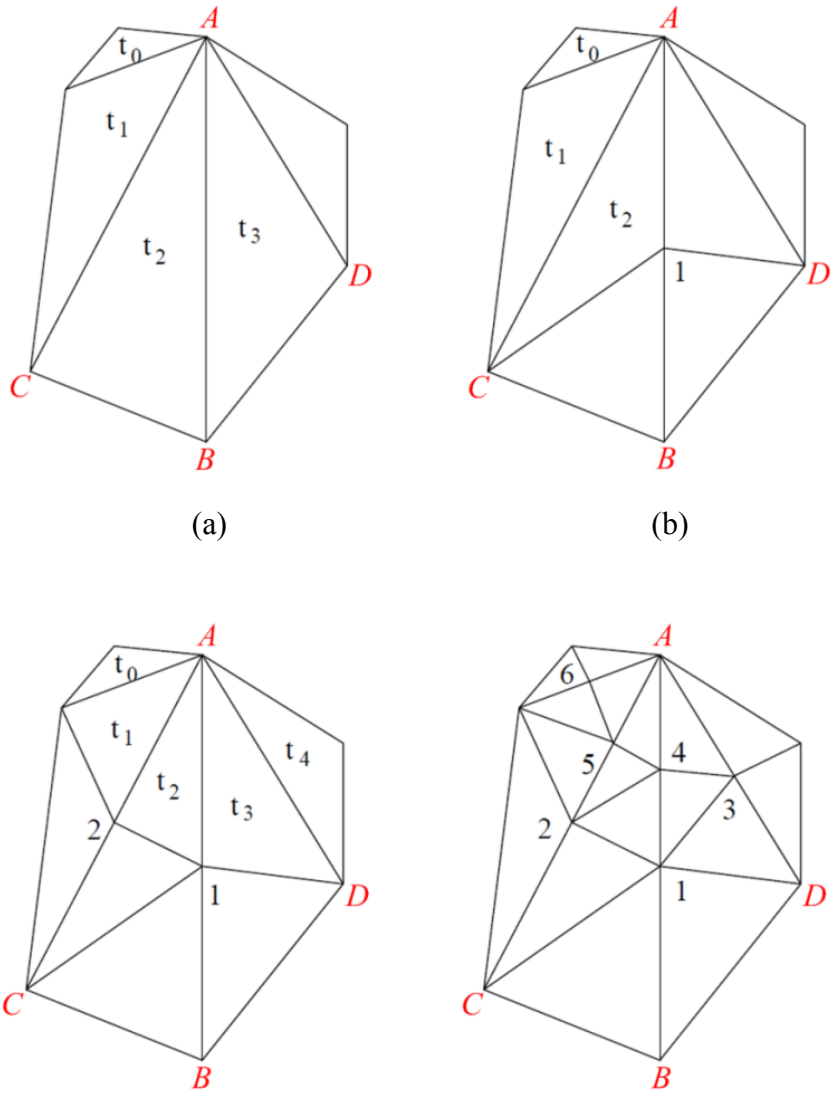

Fig. 3.11. (a) Initial triangulation, where the element t_0 is to be refined. (b) In the first step of the bisection refinement process, node 1 is inserted to the middle of AB. (c) In the second step, node 2 is inserted into the middle of AC. (d) Final triangulation after the insertion of node 1 to 6. In the last step, the insertion of node 6 bisects the element t_0 and the iteration terminates.

3.2. 2D Parameterized Mesh Deformation Method

To improve the performance of EM devices when designing new products, geometric shape optimization is a very important design objective. In practice, FEA is an indispensable tool for magnetic field computation in finding the sampling objective function values. In the optimization process, because there are frequent variations in geometric design parameters, the computational mesh has to be generated repeatedly before one can proceed to the finite element computations. However, the re-meshing process from scratch costs a lot of computing time, even if there is only very minor changes in the design parameters. Thus it is highly desirable to reduce the computing time required in mesh regeneration if there is no need to fully remesh the domain.

Several methods are available to update the mesh associated with the new design parameters from the previous mesh. One method is to partially remesh the domain by solving the equations of elasticity [C21] or the Laplace equation [C22] to calculate the new coordinates of the current mesh. However this type of partially remeshing method is still rather time consuming and not very robust and may even generate folding elements if there are large shape modifications. The method proposed in [C23] aims at alleviating the mesh overlapping problem in case of large shape deformations, however it is not automatic in that the whole domain must be manually decomposed into several convex sub-regions.

3.2.1. Parameterized Meshing Method

To overcome the drawbacks of the above mentioned method when making the meshes for new geometric parameters, a parameterized mesh technique is proposed for fast 2-D mesh deformation. In this method the coordinates of each node in the mesh is explicitly expressed as a set of expansion coefficients under a set of basis which includes all the shape design parameters. When the design parameter changes, the new coordinates of the nodes in the mesh can be calculated readily and the new mesh is obtained accordingly. Only arithmetic operations are all that required to deform the mesh without partially or fully remeshing the domain.

For simplicity but without losing generality, a 2D FEM with triangular element is used as an example to illustrate the basic idea of the proposed parameterized mesh method. Supposing there are geometry parameters p_1, p_2, …, p_N, which will vary during parameter sweeping, are expressed in a column matrix as:

$$\{p\} = \begin{Bmatrix} p_1 \\ p_2 \\ \vdots \\ p_N \end{Bmatrix}. \tag{3.1}$$

Suppose the coordinates (x_i,y_i) of a vertex i in a finite element mesh is expressed as linear functions of these parameters $p_1, p_2, \ldots, p_N$ by:

$$x_i = \begin{bmatrix} C_{x0}^i & C_{x1}^i & C_{x2}^i & \cdots & C_{xN}^i \end{bmatrix} \begin{Bmatrix} 1 \\ p_1 \\ p_2 \\ \vdots \\ p_N \end{Bmatrix} = \begin{bmatrix} C_x^i \end{bmatrix} \begin{Bmatrix} 1 \\ p \end{Bmatrix}, \tag{3.2}$$

$$y_i = \begin{bmatrix} C_{y0}^i & C_{y1}^i & C_{y2}^i & \cdots & C_{yN}^i \end{bmatrix} \begin{Bmatrix} 1 \\ p_1 \\ p_2 \\ \vdots \\ p_N \end{Bmatrix} = \begin{bmatrix} C_y^i \end{bmatrix} \begin{Bmatrix} 1 \\ p \end{Bmatrix}, \tag{3.3}$$

where $[C_x^i]$ and $[C_y^i]$ are real coefficient matrices for the vertices. For each vertex, not only the current coordinates (x_i,y_i) associated with current $\{p\}$ will be stored, the two coefficient matrices are also be stored in the class of vertex. When $\{p\}$ varies during the design process, the coordinates of all the vertices of the mesh will be changed accordingly and no remeshing process is needed.

During the meshing refinement, if a new vertex k is added at the barycenter of the triangular element with three vertices i, j, m, its coordinates (x_k, y_k) are governed by the following two formulas:

$$\begin{aligned} x_k &= \begin{bmatrix} \dfrac{C_{x0}^i + C_{x0}^j + C_{x0}^m}{3} & \dfrac{C_{x1}^i + C_{x1}^j + C_{x1}^m}{3} & \cdots & \dfrac{C_{xN}^i + C_{xN}^j + C_{xN}^m}{3} \end{bmatrix} \begin{Bmatrix} 1 \\ p \end{Bmatrix} \\ &= \frac{1}{3}[C_x^i + C_x^j + C_x^m] \begin{Bmatrix} 1 \\ p \end{Bmatrix} \end{aligned}, \tag{3.4}$$

$$y_k = \begin{bmatrix} \frac{C_{y0}^i + C_{y0}^j + C_{y0}^m}{3} & \frac{C_{y1}^i + C_{y1}^j + C_{y1}^m}{3} & \cdots & \frac{C_{yN}^i + C_{yN}^j + C_{yN}^m}{3} \end{bmatrix} \begin{Bmatrix} 1 \\ p \end{Bmatrix} = \frac{1}{3}[C_y^i + C_y^j + C_y^m] \begin{Bmatrix} 1 \\ p \end{Bmatrix}. \quad (3.5)$$

The expansion coefficients for vertex k with coordinates (x_k, y_k) under parameters $\{1, p_1, p_2, \ldots, p_N\}$ can be further expressed as $(\Sigma_{l=i,j,m}[C_x^l]/3, \Sigma_{l=i,j,m}[C_y^l]/3)$. For general cases, the coefficients of the newly added vertices are computed by:

$$[C_x^k] = \Sigma_{l=i,j,m} \lambda_l [C_x^l], \quad (3.6)$$

$$[C_y^k] = \Sigma_{l=i,j,m} \lambda_l [C_y^l], \quad (3.7)$$

where the weightings $\{\lambda_l\}$ are the area coordinates of the vertex k located in the triangle with vertices i, j and m. The definition of the area coordinates in 2D and the barycentric coordinates in 3D is illustrated in Fig. 3.12. To compute the area coordinate λ_i of a point $\vec{x} = (x, y)$ in the physical coordinates, first the area of the sub-triangle facing the vertex $\vec{x}_i = (x_i, y_i)$ is calculated as $\tau_i(\vec{x})$, then

$$\lambda_i(\vec{x}) = \frac{\tau_i(\vec{x})}{\tau}, \quad (3.8)$$

where τ is the area of the element considered. It is noted that the area coordinates have the following properties

$$\vec{x} = \sum_{i=1}^{d+1} \lambda_i(\vec{x}) \vec{x}_i, \quad (3.9)$$

$$1 = \sum_{i=1}^{d+1} \lambda_i(\vec{x}). \quad (3.10)$$

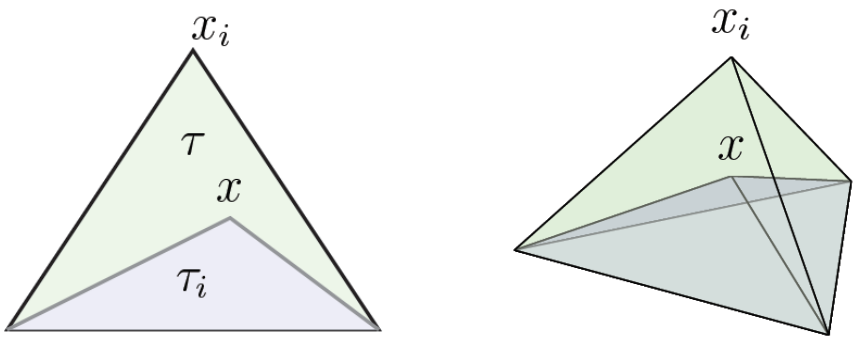

Fig. 3.12. Geometric explanation of barycentric coordinates for 2D and 3D element.

Note that, in general, the mesh parameters $\{p\}$ and the expansion coefficient matrices $[C_x]$ and $[C_y]$ (hereinafter referred as *C*-matrices) may depend on the coordinates of the vertices and as the geometry parameters $\{p\}$ are stored in the vertex class, some memory overhead is required. It can be seen however that if the initial mesh generation and mesh refinement methods are combined properly, this drawback can be successfully overcome.

With the *C*-matrices for each vertex, including the initial mesh vertices inputted by the user and the vertices adaptively added to the initial mesh in FEA, all coordinates of the vertices in the refined mesh will be changed automatically whenever the parameters $\{p\}$ vary. The shape of the refined mesh may change but its mesh quality will remain high by some mesh improvement methods. No mesh regeneration is required, thus the computing time for regeneration is greatly reduced. Furthermore, the solutions on each vertex can be carried over from previous mesh to the current mesh and no mapping of vertices is required.

For arbitrary vertex inserted to the mesh, it is necessary to have the information of the three vertices of the triangle in order to determine its vertex position. But if the insertion of new vertex is at the middle point of an edge of the triangle, then only two vertices' information suffice for determining the new vertex. To save memory for the parameterized mesh method, the bisection mesh refinement method, or the longest side bisection-Delaunay method [C16-C18] is used for adaptive mesh refinement. In this bisection method, whenever a triangular element is refined, its longest side will be bisected in a recursive way. During mesh refinement, for every vertex added into the initial mesh, the indices of the starting and ending points of the side where it is inserted are stored.

In practice, the procedures of the proposed parameterized mesh generation and refinement method is described as follows.

(1) Firstly input all the *C*-matrices for each key point (such as the four corners of a square) of the geometry under a set of design parameters $\{p\}$, then choose the initial values for these parameters and calculate the coordinates of all the key points by (2) and (3). Then input all the constrained sides' information (including the starting point and ending point of an edge and specify whether it is straight line edge, arc edge, etc.).

Specify the domain boundaries and material interface boundaries for the initial mesh generator. Send the parameterized geometry inputs to the initial mesh generator to generate the initial coarse mesh.

(2) Secondly, refine the initial parameterized mesh adaptively several times to get a relatively dense mesh for final FEM computation. Since the initial boundary mesh is composed of boundary vertices only, one can refine all the elements for the first time to make sure there exist certain interior vertices to define the unknowns for intermediate FEM computations and then compute the error indicators.

After obtaining the FEM solution during each refinement iteration, calculate the a posterior error for each triangle element according to some error estimator and refine adaptively certain percentage of the elements in the mesh. Each newly inserted vertex should be inserted at the middle point on the longest side of the triangle. These vertices are added one by one to the rear of the vertex list of the mesh, the last additional vertex is dependent totally on the two former ones in the mesh and they are referred as the "master vertices". This process is illustrated in Fig. 3.13(a)-(d), where the index (ID) *i* represents the vertex *i* in the plane for simplicity. It is not difficult to see that when the parameters change, one only needs to modify the coordinates of every vertex according to its master vertices in the natural order of all the vertices in the mesh. That is, the smaller the ID of a vertex, the more likely is its coordinates being modified. So in the proposed parameterized mesh method, only the ID numbers of the two master vertices for each vertex, instead of the two *C*-matrices, are stored. However this is equivalent to the method of storing all the *C*-matrices for each vertex.

(3) To generate high-quality computational mesh we also need to implement some mesh improvement operations using the longest edge bisection-Delaunay method. That is, the QF for each triangular element in the mesh is firstly calculated. With the calculated quality indicators, we will refine elements whose QF is less than the user-specified threshold value by the bisection method to improve the mesh.

(4) At last, the mesh is refined further to generate the final mesh for finite element analysis. With steps (2)-(3) done several times and all the coordinates of the vertices of the mesh resettled to new mesh parameters accordingly, the Delaunay diagonal swapping is realized for each edge first [C4] and then smart Laplacian mesh

smoothing is used to adjust the position of the vertices to enhance the mesh quality [C24].

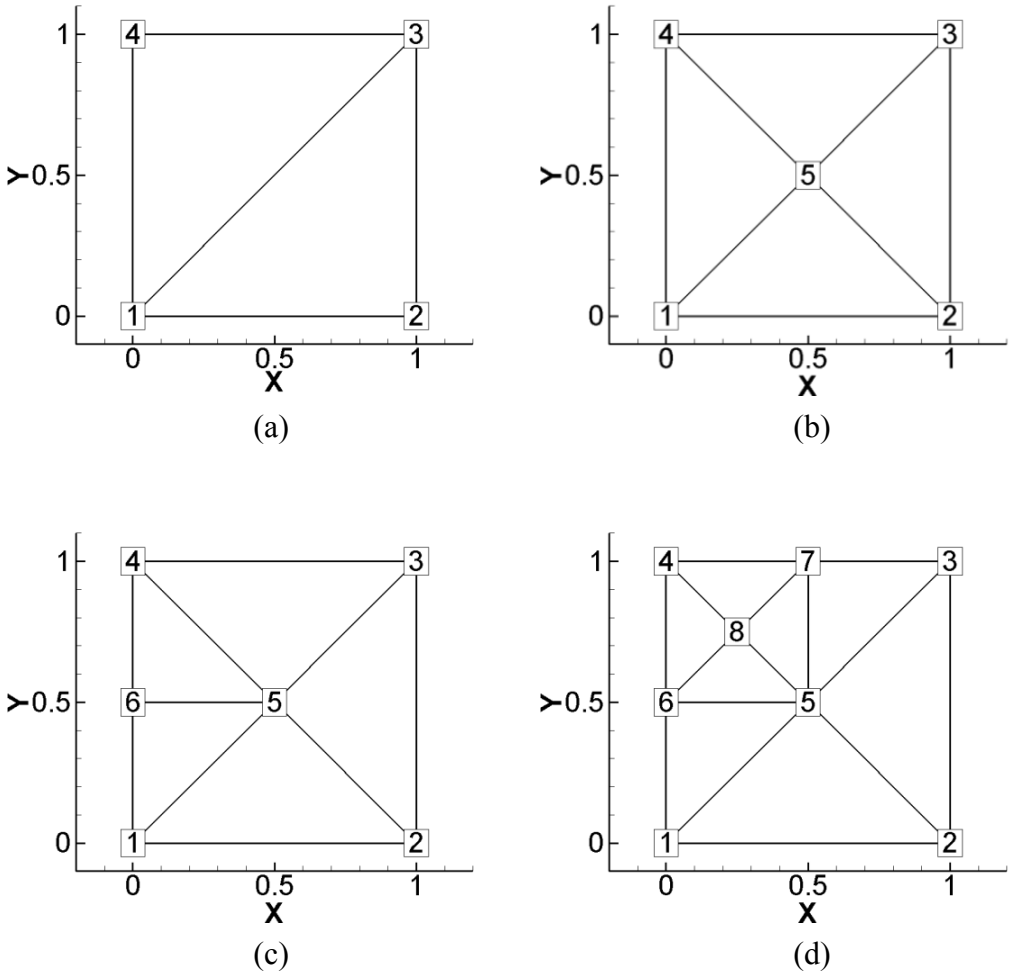

Fig. 3.13. (a) The initial mesh with vertex list {1, 2, 3, 4}. (b) The mesh after inserting vertex 5 in the middle of edge {1, 3}, the vertex list is {1, 2, 3, 4, 5}. (c) The mesh after inserting vertex 6 in the middle of edge {1, 4},the vertex list is {1, 2, 3, 4, 5, 6}. (d) The mesh after inserting vertex 7 at the middle of edge {3, 4} and vertex 8 in the middle of edge {4, 5}, the final mesh vertex list is {1, 2, 3, 4, 5, 6, 7, 8}.

3.2.2. 2D Small Shape Deformation Examples

The proposed parameterized mesh method works well in case of relatively small mesh deformations. The following are some examples. In the first example, a square with two circular holes is deformed, as shown in Fig. 3.14. For the second example, a

mesh with multiple objects are deformed, as shown in Fig. 3.15. For the last example, a practical motor mesh is deformed, as shown in Fig. 3.16.

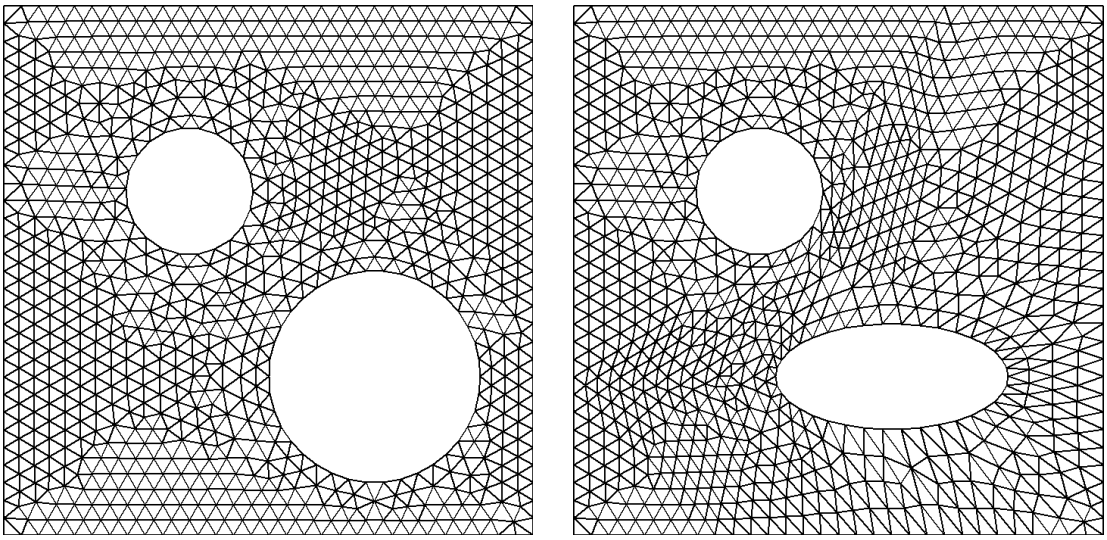

(a) (b)

Fig. 3.14. Left: mesh before deformation. Right: mesh after deformation.

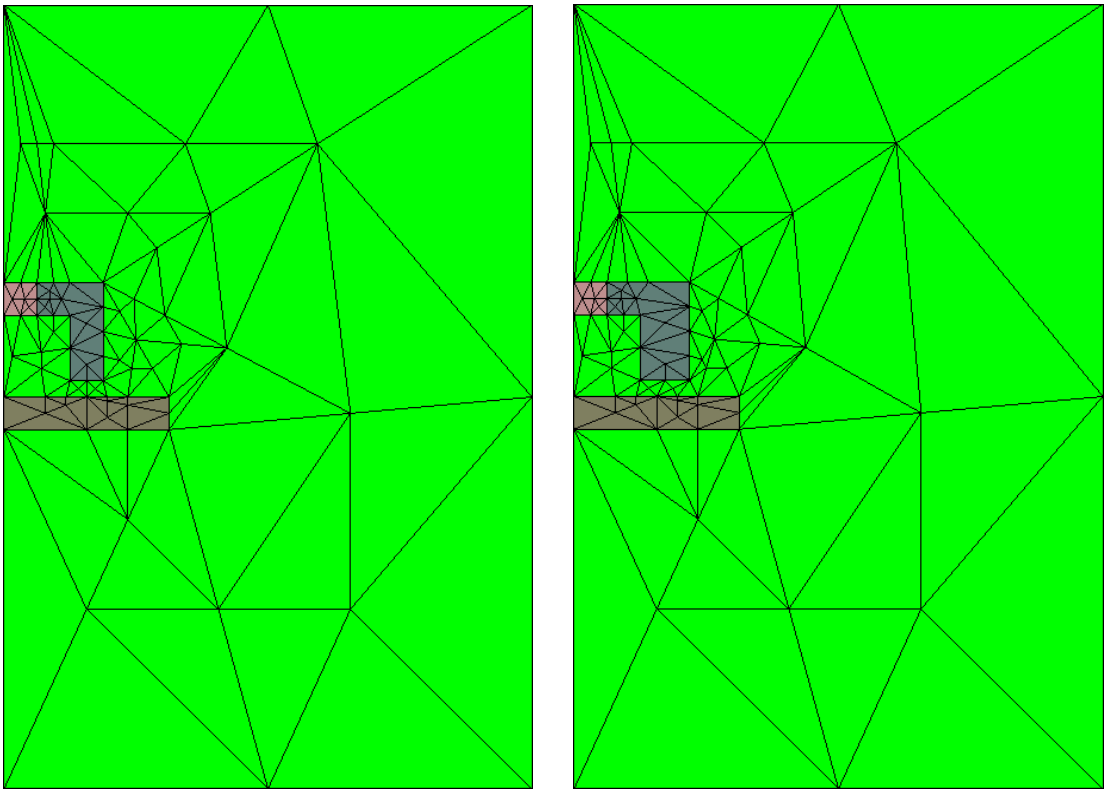

(a) (b)

Fig. 3.15. Left: mesh before deformation. Right: mesh after deformation.

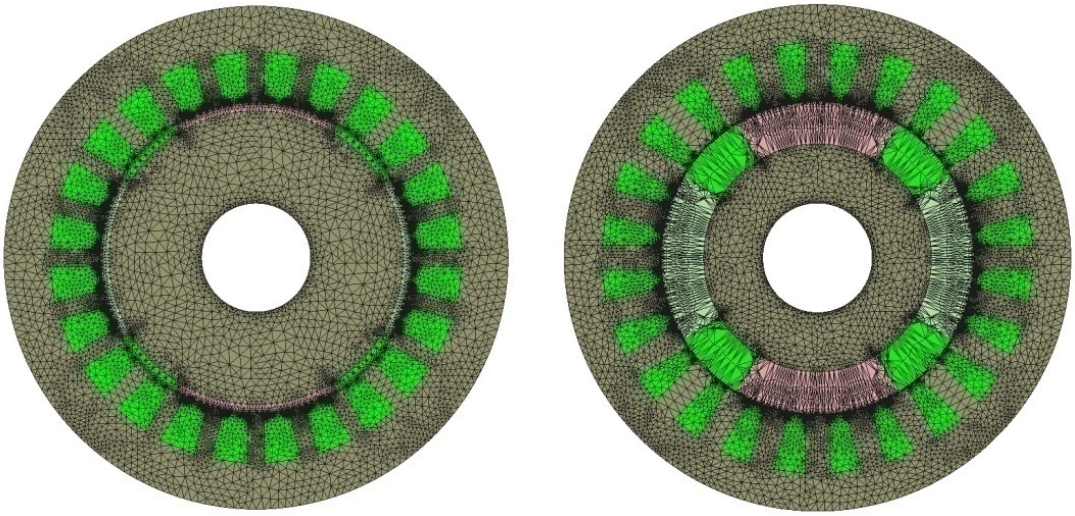

(a) (b)

Fig. 3.16. Left: mesh before deformation. Right: mesh after deformation.

3.2.3. 2D Large Shape Deformation Techniques

For the above proposed parameterized mesh method, in case of large variations of the design parameters $\{p\}$, the deformed mesh may also become overlapping which is invalid for FEA [C23]. How to generate the deformed mesh without overlapping in case of large shape deformations attracts much attention by researchers from different fields [C23, C25, C26]. In this thesis, two methods are proposed in regard to mesh folding due to large shape variation.

The first one is motivated by observing that the space available for the nodes to move freely when repositioning them is too limited, if it is based directly on the refined mesh. It is indeed more robust to work with an initial coarse mesh when updating the mesh. Note that all the elements in the initial coarse mesh also form a convex decomposition [C23, C25] of the geometry domain, so by keeping all the edges of elements of the initial coarse mesh un-swapped in subsequent mesh refinements (the refined meshes are nested) will ensure there is no inverted elements even in cases with large shape variation of the parameterized geometry.

For computer implementation, this can be realized easily by introducing an integer flag for each of the triangular element in the mesh. For the initial mesh, each triangle is assigned a unique integer for this flag and an edge is allowed to be swapped

only if its neighboring element has the same flag. An example of the effectiveness of this technique is shown in Figs. 3.17(a)- 3.17(f). Another example is also given in Figs. 3.18(a)-3.18(f).

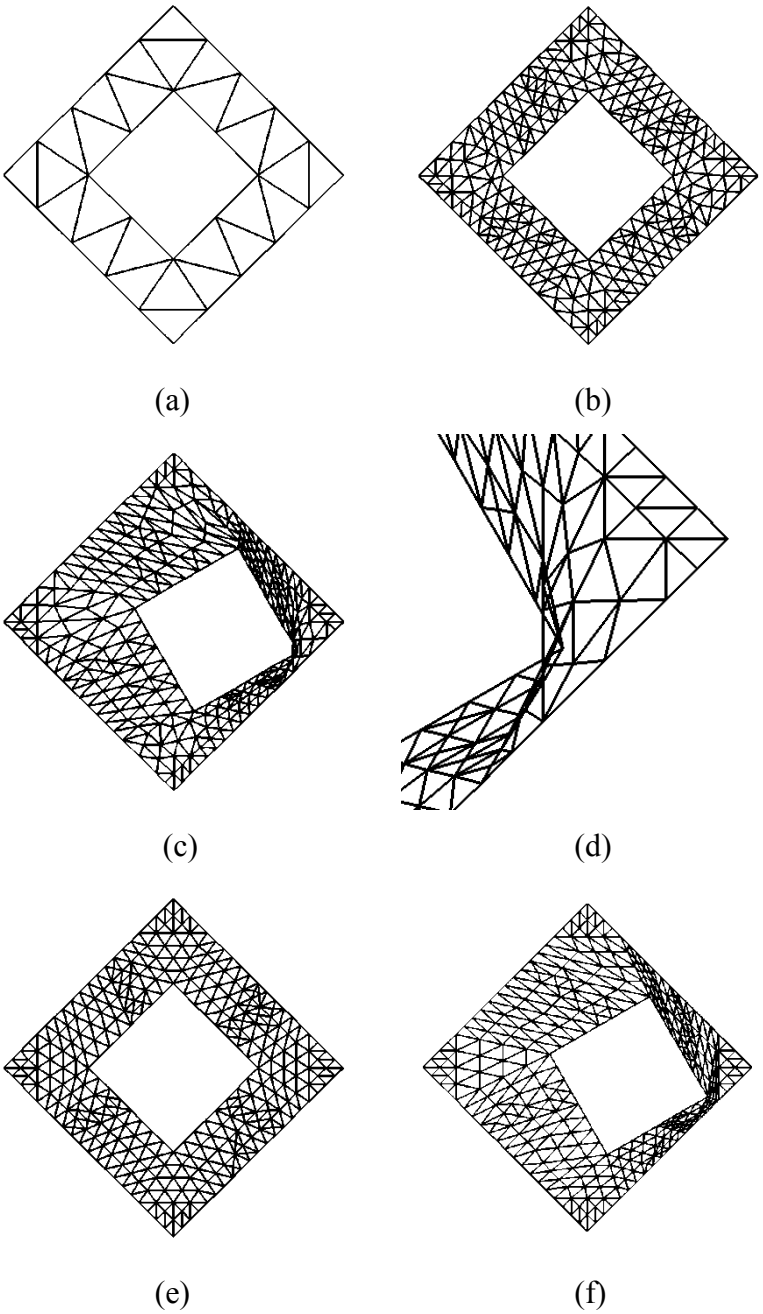

Fig. 3.17. (a) The initial coarse mesh. (b) Non-nested refined mesh of (a). (c) The invalid folding mesh obtained by resetting the parameterized mesh (b) for new design parameters. (d) Close view of the folding mesh. (e) Nested refined mesh of (a). (f) Valid mesh obtained by resetting the parameterized mesh (b) for the same parameters used in (c).

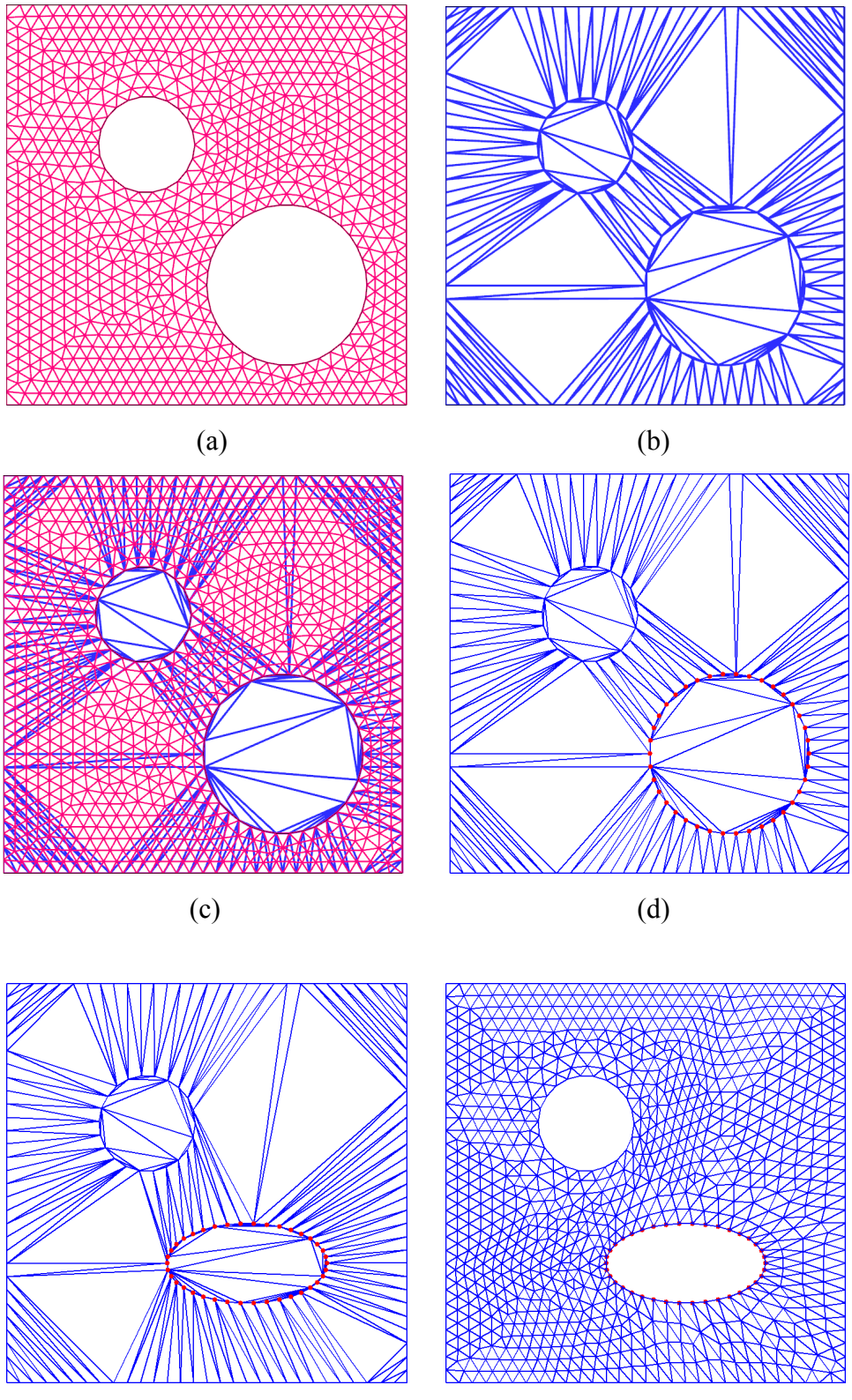

Fig. 3.18. (a) Original 2D finite element mesh. (b) Initial mesh. (c) Plot of both the fine mesh and the initial mesh. (d) The initial mesh with movable red nodes. (e) The deformed initial mesh. (f) The deformed finite element mesh.

The second method for large shape variation is based on a smart edge swapping algorithm. A simple mesh deformation problem is used to illustrate the basic idea. In Fig. 3.19(a), a mesh for the L-shaped domain is shown, where the coordinates of the corner point *O* is initially (0.5, 0.5). If *O* is repositioned to its new position (0.25, 0.25), the resultant mesh is overlapping with inverted elements as given in Fig. 3.19(b), if all the edges are the same as those in the original mesh.

To avoid the mesh overlapping problem, if the edge AB which is facing the displacement vector of corner *O* (in this case (-0.25,-0.25)) is swapped in a way as shown in Fig. 3.20(a), then the new mesh will be valid after deformation, which can be seen in Fig. 3.20(b). So it is not difficult to find that if all the edges are aligned along the nodal motion directions as much as possible, the resultant mesh is more resilient to mesh folding. The essence of the proposed smart edge swapping technique is to swap those edges hampering the nodal movement when the mesh is deformed.

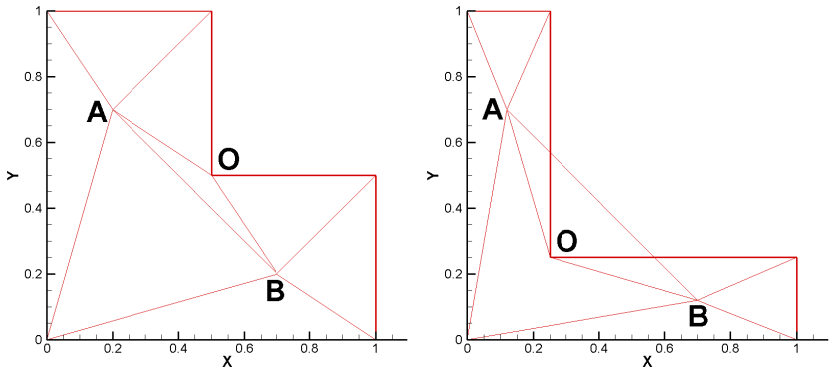

(a) (b)

Fig. 3.19. (a) Original mesh. (b) Deformed mesh with inverted elements.

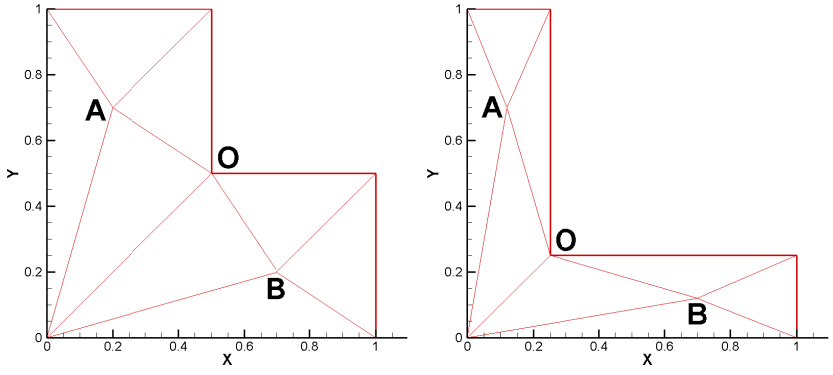

(a) (b)

Fig. 3.20. (a) The new mesh after swapping edge AB for the mesh shown in Fig. 3.19 (a). (b) Deformed mesh without inverted elements.

The above example is artificial and illustrative in that the edge *AB* in the mesh shown in Fig. 3.19(a) actually violates the Delaunay's empty circle property. However, even if all the triangular elements in the mesh observe Delaunay's property, the updated mesh for large shape deformation may still overlap. To explain it more clearly, the two-square mesh with a hole is taken as another example. The initial mesh for the geometry is a Delaunay triangulation, as shown in Fig. 3.21(a). Suppose the inner square is translated to a large extent, where the node *A* with coordinates (-1,0) in the initial mesh shown in Fig. 3.21(a) is repositioned to its new position (-1.7,0), as shown in Fig. 3.21(b), then one can observe there is obvious overlapping in the new mesh.

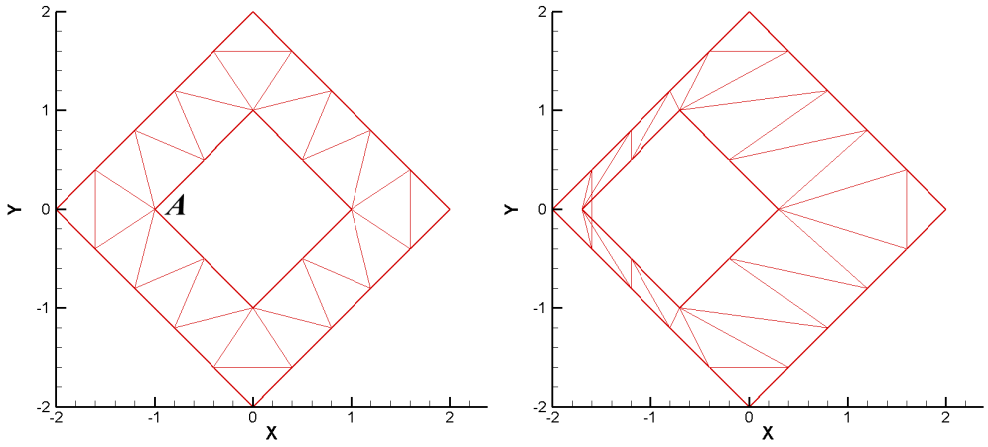

(a) (b)

Fig. 3.21. (a) Initial mesh for a two-square domain. (b) Deformed mesh with inverted elements.

To avoid the mesh overlapping problem, the smart edge swapping technique can be applied. The proposed smart edge swapping algorithm is very easy to implement. More specifically, for each triangle *e* in the mesh, the node with the maximum norm of displacement vector needs to be found first. If this node *P* is shifted a little along its motion vector and the new node *P*' is still located in the triangle *e* being considered, and then the edge in element *e* facing *P* is to be swapped.

Firstly the displacement vectors, which can be obtained instantly, of every node in the initial mesh shown in Fig. 3.21(a) are calculated, as indicated in Fig. 3.22(a).

Then the smart edge swapping algorithm is applied to those edges hampering the nodal movement and the resultant mesh is given in Fig. 3.22(b). It can be seen from Fig. 3.22(c) that there are no overlapping in the updated mesh, thus demonstrating the smart edge swapping algorithm is very effective. To further improve the quality of the mesh, the traditional edge swapping operation according to Delaunay's principle can be applied and the obtained mesh is shown in Fig. 3.22(d).

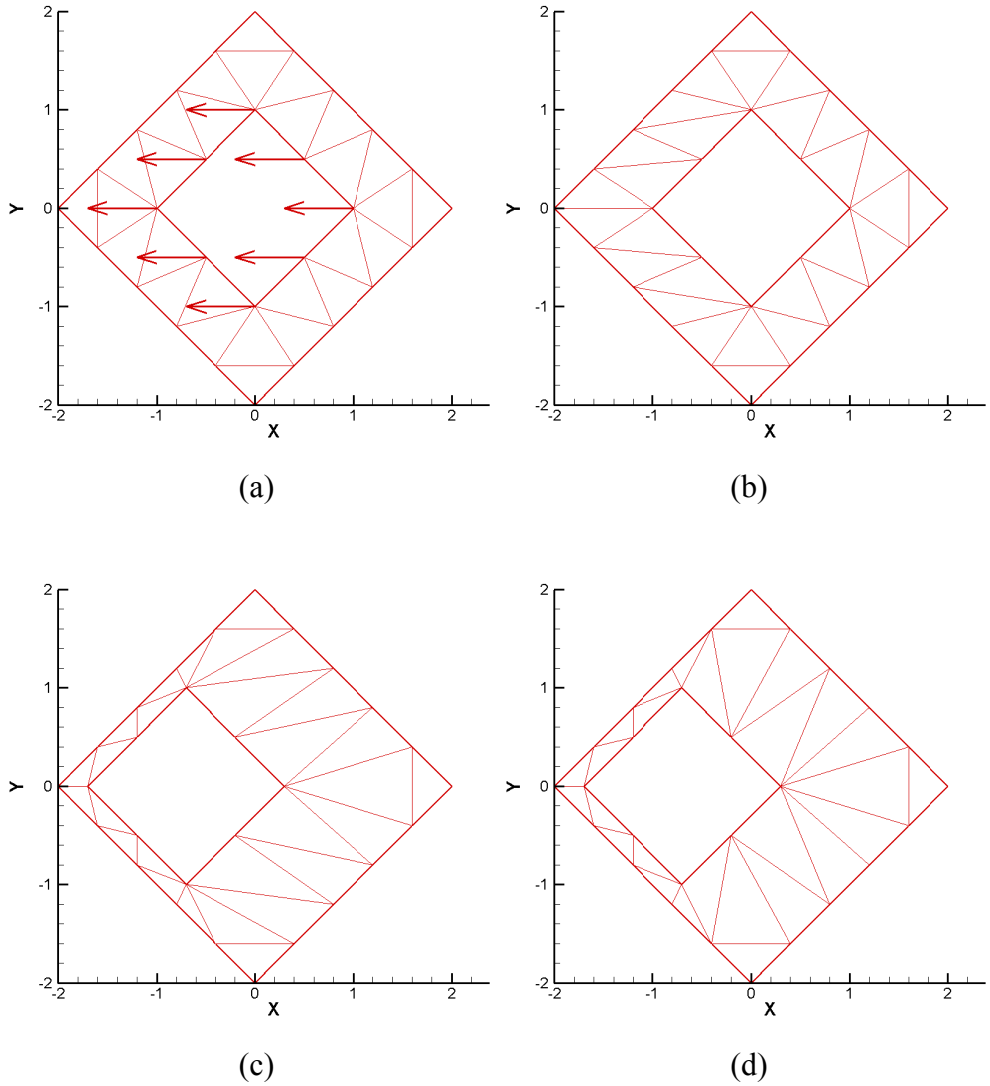

Fig. 3.22. (a) Displacement vectors for each node in the initial mesh. (b) Modified mesh obtained by using the proposed smart edge swapping algorithm, (c) Deformed mesh by resetting parameters. (d) Perform traditional Delaunay edge swapping operation to further improve the mesh quality.

3.3. 3D Remesh-free Mesh Deformation Method

In this section a novel fast remesh-free mesh deformation method for 3D problems is to be developed. Due to the complicated geometric input of the problem domain and difficult boundary conforming mesh generation process for 3D geometries [C6], a seamless generalization of the 2D parameterized mesh method to 3D is not straightforward. Nevertheless such remesh-free idea still provides a guideline for 3-D mesh deformation. A robust fast remesh-free mesh deformation technique is being proposed and can be applied for both 2D and 3D problems, aiming to reduce the time needed for generating the meshes for different design parameters to accelerate the optimal shape design process.

The proposed method requires only one set of fine finite element computational mesh and an initial mesh, which contains all the movable nodes in the fine mesh and yet they do not need to conform to the complicated outlines of the geometry. By using a coordinate mapping technique, the area coordinates of each node of the fine mesh in the initial mesh are first calculated and stored, and that needs to be done only once. By fixing these calculated area coordinates for each node, new meshes can be updated by providing the new positions of the nodes of the initial mesh and one can then map back the area coordinates to the Cartesian coordinates.

For the methods proposed in [C21, C22], the solution of some kind of equations to determine the interior nodal displacements are required to deform the mesh, and these may cost much time for complex 3-D geometries. In this work, such equation solution process is avoided using a coordinates mapping technique with the help of an initial coarse mesh, which contains all the movable nodes in the fine mesh.

To deform the fine mesh, firstly the area coordinates of each node in the fine mesh relative to its initial mesh is computed and stored for each node. This process needs to be done once and only once. When the geometry parameters are updated, the new initial mesh is first updated by resetting the movable nodes located on the geometry outlines. The formerly computed area coordinates of each node in the fine mesh are mapped back to the Cartesian coordinates under the basis of the newly updated initial mesh. In this way each node in the fine mesh is repositioned to form

the new fine mesh with its mesh connectivity unchanged. The flowchart of the proposed mesh deformation process is shown in Fig. 3.23.

This method is robust in that the deformed fine mesh is valid if and only if the deformed initial mesh is valid. Besides, the method can be applied to both 2-D and 3-D problems. For the first example, the original 3-D computation mesh is given in Fig. 3.24(a) and Fig. 3.24(b). In Fig. 3.24(c), the inner ball is enlarged and the deformed mesh is given. Fig. 3.24(d) is the 3-D view of the deformed mesh.

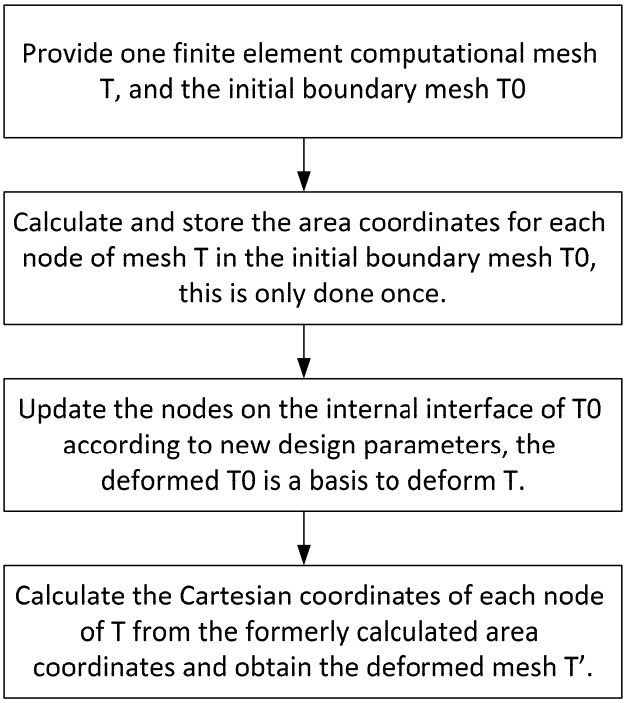

Fig . 3.23. Flowchart of the mesh deformation process.

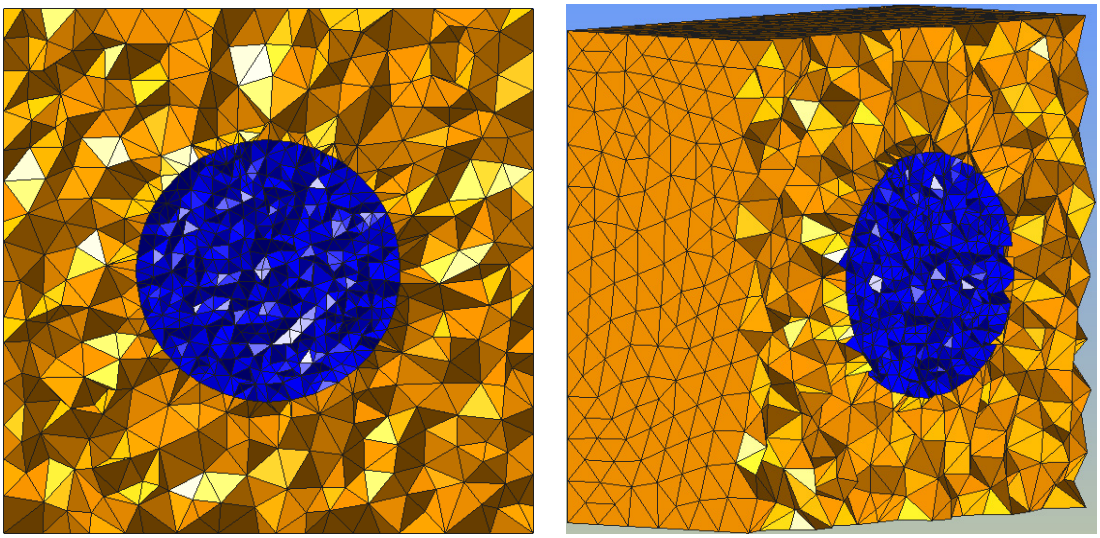

(a) (b)

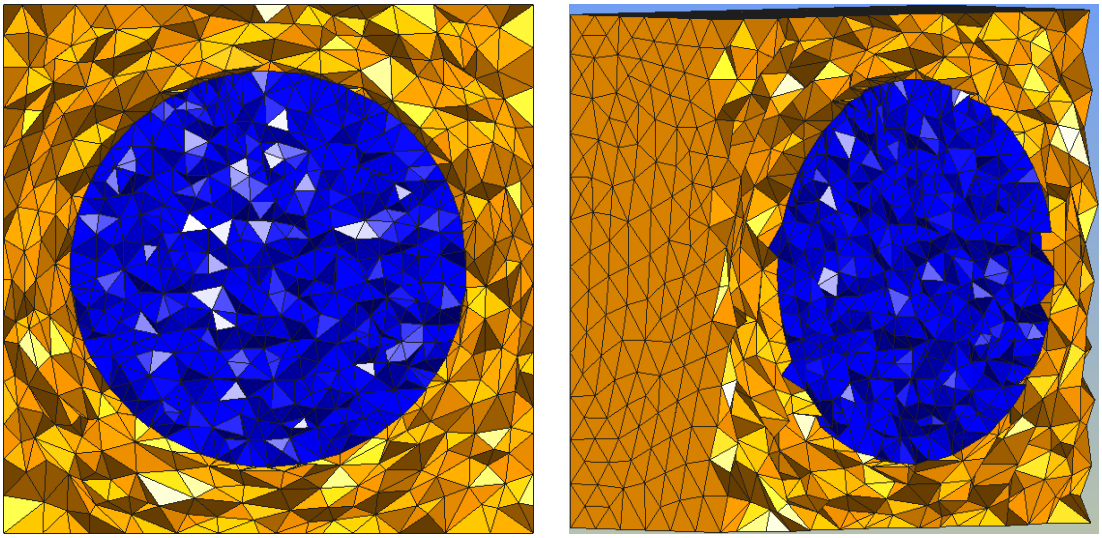

(c) (d)

Fig. 3.24. (a) Original 3D computational mesh, cut view. (b) Original 3D computational mesh, 3-D view. (c) Deformed mesh using the proposed method, cut view. (d) 3-D view of the deformed mesh.

In the second example, the 3D mesh of the three-phase induction motor of the TEAM Workshop Problem 30A [A35] is deformed using the proposed method. The original 2D problem domain is extruded along the axial direction to form the 3D problem domain. The initial shape of the induction motor with smooth solid rotor is shown in Fig. 3.25(a), where there are 202936 tetrahedral elements and 34923 nodes in the mesh.

The radius of the innermost cylinder shown in Fig. 3.25(a) is 2cm. The deformed mesh when the innermost cylinder is enlarged radially using the proposed remesh-free mesh deformation method is shown in Fig. 3.25(b), where the radius of the innermost cylinder is now 2.6cm. The mesh shown in Fig. 3.25(b) has exactly the same mesh topology as the one given in Fig. 3.25(a).

For this example, the CPU time needed to compute the area coordinates of all the nodes in the fine mesh is about 0.04s and the time for updating the mesh by mapping back these coordinates to Cartesian ones is about 0.003s. It costs about 140s for the generation of the geometry-conforming finite element mesh as shown in Fig. 3.25(a). One can clearly see that the proposed method cost relatively little time and hence the time needed for mesh deformation is reduced greatly.

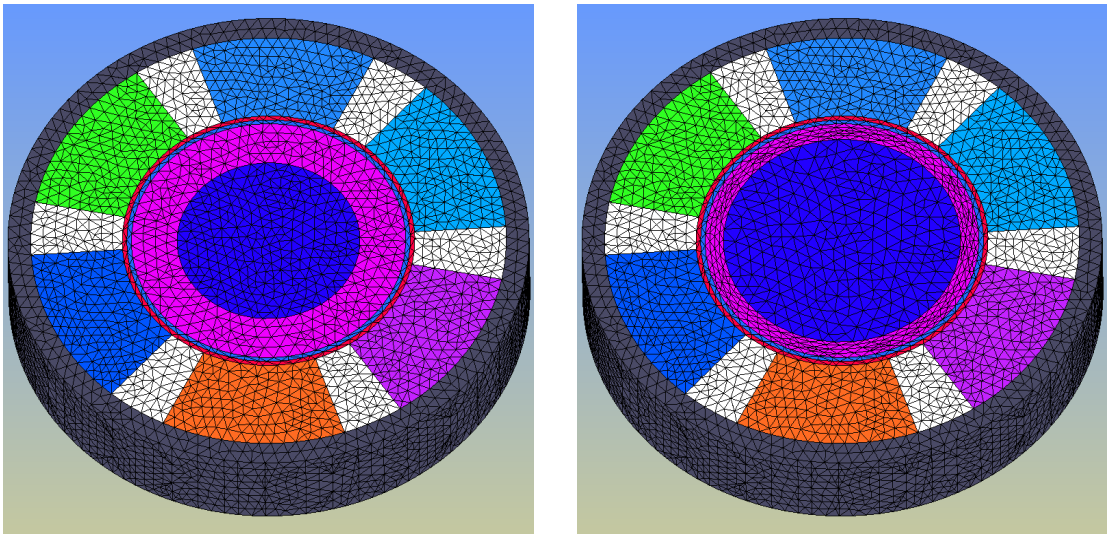

(a) (b)

Fig. 3.25. (a) The mesh for the initial shape of the motor. (b) Deformed mesh for the new shape when the innermost region is enlarged radially.

In the third example, an optimal shape design problem is studied using the proposed method. The device to be optimized is a magnet as shown in Fig. 3.26(a), and it is similar to the permanent magnet Magnetic Resonance Imaging (MRI) system in [C27]. The objective is to get a highly homogeneous magnetic field distribution in the working region. A sample view of the old mesh and the deformed mesh using the proposed method are shown in Figs. 3.26(b) and 3.26(c).

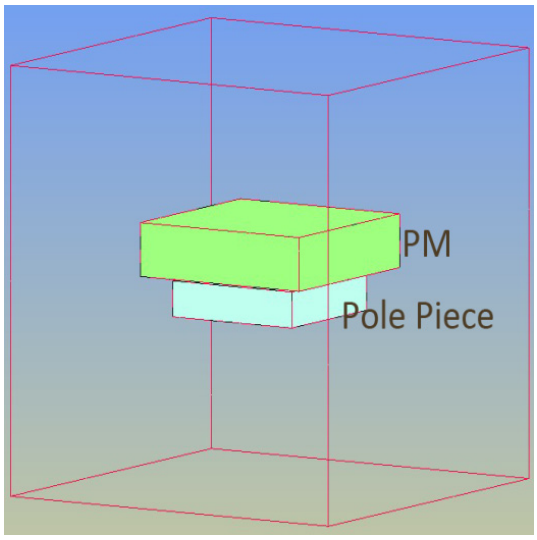

(a)

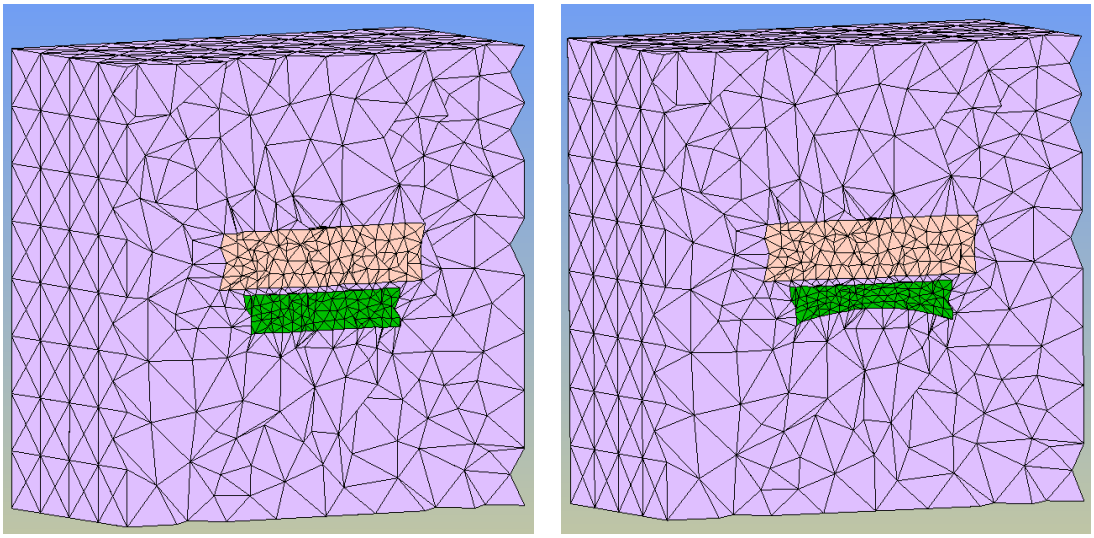

(b) (c)

Fig. 3.26. (a) The MRI device where the shape of the pole piece is to be optimized. (b) Finite element mesh of the initial shape of the device. (c) Finite element mesh of the new shape of the device.

3.4. Summary

In this chapter, the Delaunay mesh generation method is given in detail. Commonly used mesh refinement methods are also given, where the longest edge bisection method is highly recommended to use because it can simultaneously improve the quality of the mesh when refining it.

After reviewing the state-of-the-art mesh deformation methods, a novel 2D parameterized mesh deformation method is presented. For this method, the mesh vertex contains the information of the design variables. When these design variables are changed, new deformed meshes can be obtained very fast. Besides, two techniques to avoid inverted elements in case of relatively large mesh deformation are proposed and validated through practical examples. For 3D mesh deformation, a novel fast remesh-free mesh deformation technique is proposed using a coordinate mapping technique, Several examples are given to showcase the effectiveness of this method.

3.5. References-Part C

[C1] M. Farrashkhalvat, and J. P. Miles, Basic Structured Grid Generation: With an introduction to unstructured grid generation, Butterworth-Heinemann, 1st edition, Mar. 2003.

[C2] J. Schöberl, "NETGEN-An advancing front 2D/3D-mesh generator based on abstract rules," *Comput. Visual. Sci.*, vol. 1, pp. 41-52, 1997.

[C3] S. W. Sloan, and G. T. Houlsby, "An implementation of Watson's algorithm for computing 2-dimensional Delaunay triangulations," *Adv. Eng. Softw.*, vol. 6, no. 4, pp. 192-197, 1984.

[C4] S. W. Sloan, "A fast algorithm for constructing Delaunay triangulations in the plane," *Adv. Eng. Softw.*, vol. 9, no. 1, pp. 34-55, 1987.

[C5] J. F. Lee, and R. D. Edlinger, "Automatic mesh generation using a modified Delaunay tessellation," *IEEE Antennas Propag. Mag.*, vol. 39, no.1, pp. 34-45, 1997.

[C6] Hang Si, "Three dimensional boundary conforming Delaunay mesh generation," Ph. D. thesis, Technische Universität Berlin, Jul. 2008.

[C7] P. J. Frey, and Paul-Louis George, Mesh Generation: Application to Finite Elements, ISTE Ltd., 2008.

[C8] A. Bowyer, "Computing Dirichlet tessellations," *Computer Journal*, vol. 24, no. 2, pp. 162-166, 1981.

[C9] D. F. Watson, "Computing the *n*-dimensional Delaunay tessellation with application to Voronoi polytopes," *Computer Journal*, vol. 24, no. 2, pp. 167-172, 1981.

[C10] Z. J. Cendes, and D. N. Shenton, "Adaptive mesh refinement in the finite element computation of magnetic fields," *IEEE Trans. Magn.*, vol. MAG-21, no. 5, pp. 1811-1816, Sep. 1985.

[C11] A. Raizer, G.Meunier, and J. L. Coulomb, "An approach for automatic adaptive mesh refinement in finite element computation of magnetic fields," *IEEE Trans. Magn.*, vol. 25, no. 4, pp. 2965-2967, Jul. 1989.

[C12] J. O'Dwyer, and P. Evans, "Triangular element refinement in automatic adaptive mesh generation," *Trans. Magn.*, vol. 33, no. 2, pp. 1740-1743, Mar. 1997.

[C13] H. Choi, H. Kim, and S. Hahn, “An adaptive mesh generator based on nodal errors,” *IEEE Trans. Magn.*, vol. 36, no. 4, pp. 1619-1622, Jul. 2000.

[C14] D. P. Labridis, “Comparative presentation of criteria for adaptive finite element mesh generation in multiconductor eddy-current problems,” *IEEE Trans. Magn.*, vol. 36, no. 1, pp. 267-280, Jan. 2000.

[C15] D. Ladas, V. Mazauric, G. Meunier, O. Chadebec, M. Ebene-Ebene, Y. Marechal, and P. Wendling, “An energy based approach of electromagnetism applied to adaptive meshing and error criteria,” *IEEE Trans. Magn.*, vol. 44, no. 6, pp. 1246-1249, Jun. 2008.

[C16] M. C. Rivara, “New mathematical tools and techniques for the refinement and/or improvement of unstructured triangulations”, Proceedings 5th International Meshing Roundtable 96, Pittsburgh, pp. 77-86, 1996.

[C17] M. C. Rivara, “Review on longest edge nested algorithms,” *Numer. Math. Adv. Appl., G. Kreiss*, Ed. et al. Berlin Heidelberg: Springer-Verlag, pp. 763-770, 2010.

[C18] D. Azocar, M. Elgueta, and M. C. Rivara, “Automatic LEFM crack propagation method based on local Lepp-Delaunay mesh refinement,” *Adv. Eng. Softw.*, vol. 41, pp. 111-119, 2010.

[C19] R. E. Bank, and A. H. Sherman, “The use of adaptive grid refinement for badly behaved elliptic partial differential equations,” *Mathematics and Computers in Simulation*, vol. 22, no. 1, pp. 18-24, Mar. 1980.

[C20] X. Zhao, J. Hu, and Z. Shi, “Convergence analysis of the adaptive finite element method with the red-green refinement,” *Science China Mathematics*, vol. 53, no. 2, pp. 499-512, Feb. 2010.

[C21] Y. Y. Yao, J. S. Ryu, C. S. Koh, and D. X. Xie, “A novel mesh regeneration using structural deformation analysis for 3-D shape optimization of electromagnetic devices,” *IEEE Trans. Magn.*, vol. 40, no. 2, pp. 1009-1012, Mar. 2004.

[C22] K. Yamazaki, H. Ishigami, and A. Abe, “An adaptive finite element method for minor shape modification in optimization algorithms,” *IEEE Trans. Magn.*, vol. 44, no. 6, pp. 1202-1205, June 2008.

[C23] S. L. Ho, N. N. Chen, and W. N. Fu, “A moving mesh embedded algorithm in finite element method for optimal design of electromagnetic devices,” *IEEE Trans. Magn.*, vol. 47, no. 10, pp. 2947-2950, Oct. 2011.

[C24] L. A. Freitag, and P. M. Knupp, “Tetrahedral mesh improvement via optimization of the element condition number,” *Int. J. Numer. Meth. Eng.*, vol. 53, pp. 1377-1391, 2002.

[C25] E. Lefrancois, “A simple mesh deformation technique for fluid-structure interaction based on a submesh approach,” *Int. J. Numer. Meth. Engng.*, vol. 75, pp.1085-1101, 2008.

[C26] J. Kim, T. Panitanarak, and S. M. Shontz, “Multiobjective mesh optimization framework for mesh quality improvement and mesh untangling,” *Int. J. Numer. Meth. Engng.*, vol. 94, pp. 20-42, 2013.

[C27] J. S. Ryu, Y. Yao, C. S. Koh, and Y. J. Shin, “3-D optimal shape design of pole piece in permanent magnet MRI using parameterized nonlinear design sensitivity analysis,” *IEEE Trans. Magn.*, vol. 42, no. 4, pp. 1351-1354, Apr. 2006.

CHAPTER 4

2D AND 3D FINITE ELEMENT FIELD SOLVERS

4.1. 2D Nodal FEM for Magnetic Field Computation

Finite element method (FEM) has been widely used in 2D magnetic field analysis nowadays because its versatility and high accuracy [A8, A11, A35, A37, D1-D3]. The chapter discusses several aspects when applying the FEM to practical electromagnetic field analysis, including how to deal with nonlinear material and rotational movement. The field-circuit coupled formulation is later given in the 3D form.

4.1.1. 2D Finite Element MVP Formulation

For numerical modeling of most of the radial flux motors, by ignoring the end effect, the 3D problem reduces to 2D, supposing the field is the invariant at each section along the axial direction of the motor. In 2D FEA of magnetic fields, the MVP $\vec{A}$ is mostly used as the unknown variable, in such as case the MVP and the electric current are reduced to only one component (usually along the z direction in Cartesian coordinate system). Denote by A the unknown component to be solved, the 2D eddy-current problem reads [A11]

$$\sigma\frac{\partial A}{\partial t}-\frac{\partial}{\partial x}(\nu\frac{\partial A}{\partial x})-\frac{\partial}{\partial y}(\nu\frac{\partial A}{\partial y})=J_s+\nabla\times(\nu\mu_0\vec{M}_r)=J_s+\nu\mu_0(\frac{\partial M_y}{\partial x}-\frac{\partial M_x}{\partial y}), \quad (4.1)$$

where $\nu=\nu(B)=1/\mu$ is the magnetic reluctivity, J_s is the applied source current density, $\vec{M}_r$ is the magnetization vector with two components M_x and M_y. B is the magnitude of the magnetic flux density $\vec{B}=\nabla\times\vec{A}=[\frac{\partial A}{\partial y},-\frac{\partial A}{\partial x},0]$:

$$B=\|\vec{B}\|=\sqrt{(\frac{\partial A}{\partial x})^2+(\frac{\partial A}{\partial y})^2}=\sqrt{(\nabla\times\vec{A},\nabla\times\vec{A})}=\sqrt{(\nabla A,\nabla A)}, \quad (4.2)$$

where $\vec{A} = [0, 0, A]$. For 2D magnetostatic problem, the control equation is

$$-\frac{\partial}{\partial x}(\nu\frac{\partial A}{\partial x}) - \frac{\partial}{\partial y}(\nu\frac{\partial A}{\partial y}) = J_s + \nu\mu_0(\frac{\partial M_y}{\partial x} - \frac{\partial M_x}{\partial y}). \tag{4.3}$$

In low-frequency EM field analysis, two kinds of BCs are usually encountered, one is the homogenous Dirichlet BC

$$A = 0, \tag{4.4}$$

which models infinite BC where the magnetic flux density decreases to zero and the magnetic flux flows tangentially along the boundary of the problem domain. The other one is the homogenous Neumann BC

$$\frac{\partial A}{\partial n} = 0, \tag{4.5}$$

which is usually applied on symmetric planes where the magnetic flux is vertical to the boundary of the problem domain.

For problems with non-homogenous Dirichlet BC, the unknowns can be split into two parts, one part includes the non-homogenous Dirichlet boundary data and is zero on all other nodes, the remaining part to be solved is hence zero on the domain boundary. Note that the BC (4.4) has to be explicitly imposed on the finite element space while (4.5) is implicitly imposed by the weak form given as follows.

The FEM works with the weak form of the PDE (4.1), which can be obtained by multiplying both sides of (4.1) by an arbitrary test function N and integrating by parts:

$$\begin{aligned} &\iint_V \sigma N\frac{\partial A}{\partial t}\mathrm{d}x\mathrm{d}y + \iint_V \nu(\frac{\partial N}{\partial x}\frac{\partial A}{\partial x} + \frac{\partial N}{\partial y}\frac{\partial A}{\partial y})\mathrm{d}x\mathrm{d}y \\ &= \iint_V NJ_s\mathrm{d}x\mathrm{d}y + \iint_V \nabla\times N\cdot(\nu\mu_0\vec{M}_r)\mathrm{d}x\mathrm{d}y \\ &= \iint_V NJ_s\mathrm{d}x\mathrm{d}y + \iint_V \nu\mu_0(M_x\frac{\partial N}{\partial y} - M_y\frac{\partial N}{\partial x})\mathrm{d}x\mathrm{d}y. \end{aligned} \tag{4.6}$$

The problem domain V is then triangulated into a finite number of non-overlapping triangular elements $\{e\}$, called finite elements, whose union covers the whole domain. The unknowns to be solved, i.e., the DoFs, can be defined on the vertices, edges or interior of each element. The unknown potential function A is expanded under the finite element space spanned by finite element basis functions with the expansion coefficients to be the unknown DoFs. In this thesis, the second-order triangular finite element basis functions with six DoFs per element which are continuous across

elemental interfaces is adopted to approximate A. These elemental shape functions $\{N_i\}_{i=1}^{6}$ for each triangular element are shown in Fig. 4.1.

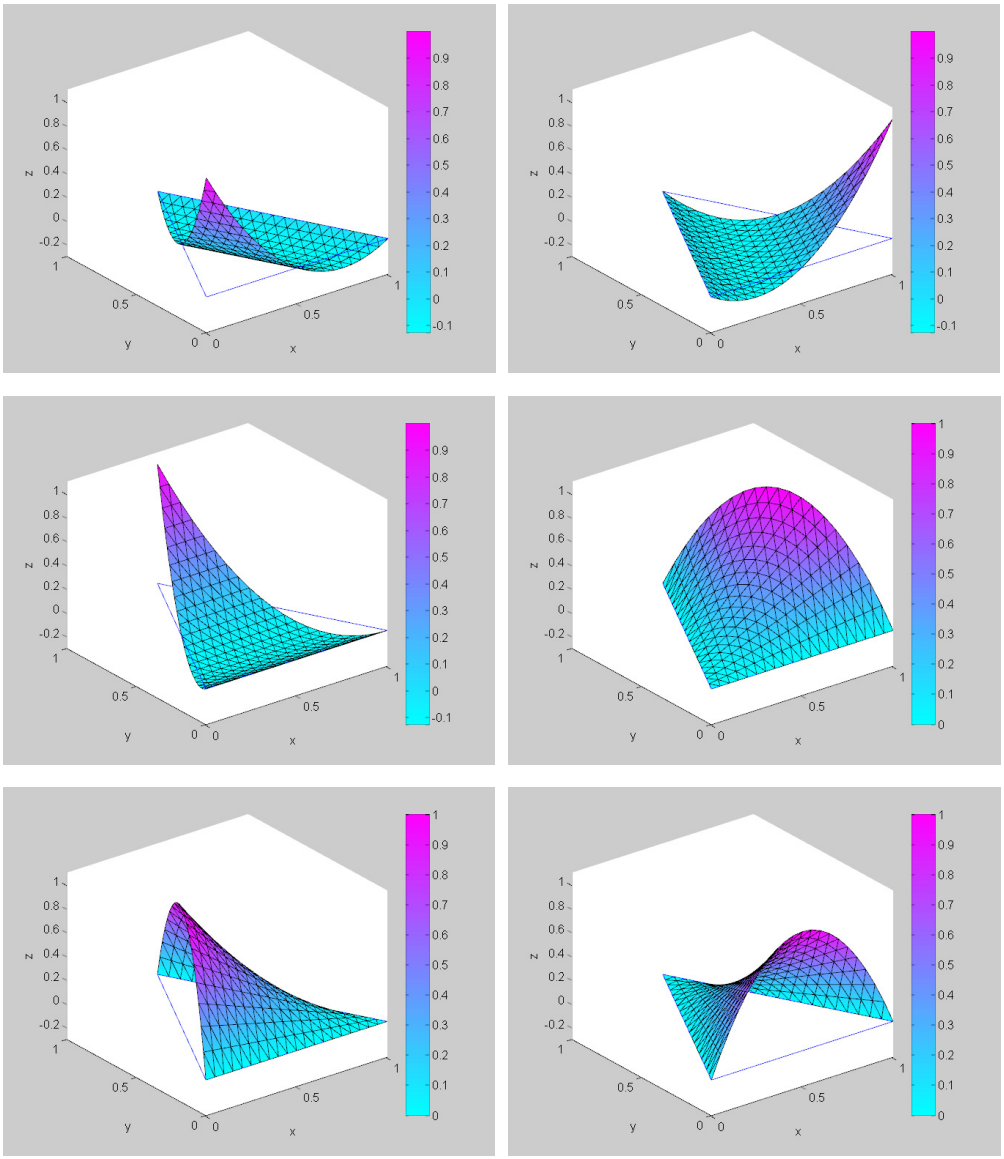

Fig. 4.1. Second order finite element shape functions $\{N_i\}_{i=1}^{6}$.

Within each element e, the MVP A can then be expanded as

$$A^e = \sum_{i=1}^{6} A_i^e N_i, \tag{4.7}$$

where $\{A_i^e\}$ are the elemental DoFs. Substitute (4.7) into (4.6) and perform integrals for an element e instead of the whole domain V, one can obtain the element matrices and element load vectors, this is the so-called element analysis process. These

computed element matrices and vectors are then assembled into the global ones in the subsequent global assembly process.

The main computational burden of the whole finite element solution process is in the element analysis process, where the integration of the multiplication of elemental shape functions and their spatial derivatives have to be calculated. To preserve the desired order of convergence for second-order elements, the seven point Gauss quadrature formula with fifth order of accuracy [A19] is adopted to numerically compute the integrals in (4.4). Under area coordinates, the formula reads

$$\iint_{V_0} f(\xi,\eta,\varsigma)\mathrm{d}V_0 = |V_0| \sum_{i=1}^{7} W_i f(\xi_i,\eta_i,\varsigma_i). \tag{4.8}$$

for a function $f(\xi,\eta,\varsigma)$ defined on V_0 with measure $|V_0|$, where (ξ,η,ς) is the area coordinates of a point (x,y) in the Cartesian or physical coordinates and the summation of the area coordinates is always unity:

$$\xi+\eta+\varsigma=1. \tag{4.9}$$

The weights and coordinates of the integration points of the seven-point Gauss quadrature are shown in Table 4.1. The positions of these integration points within a triangular element are shown in Fig. 4.2.

W_i	ξ_i	η_i	ς_i
0.1323941527885	0.0597158717897	0.4701420641051	0.4701420641051
0.1323941527885	0.4701420641051	0.0597158717897	0.4701420641051
0.1323941527885	0.4701420641051	0.4701420641051	0.0597158717897
0.1259391805448	0.7974269853530	0.1012865073234	0.1012865073234
0.1259391805448	0.1012865073234	0.7974269853530	0.1012865073234
0.1259391805448	0.1012865073234	0.1012865073234	0.7974269853530
0.225	1/3	1/3	1/3

Table 4.1. Weights and area coordinates of the seven point Gauss quadrature formula.

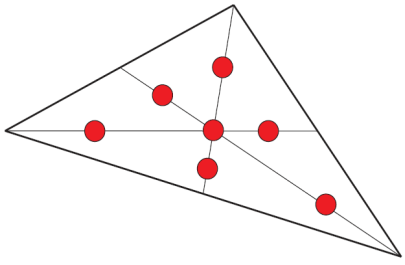

Fig. 4.2. Seven point Gauss quadrature points within a triangular element.

The final matrix form of (4.6) reads

$$[M]\frac{\mathrm{d}}{\mathrm{d}t}\{A\}+[K]\{A\}=\{P\}, \tag{4.10}$$

where $[M]$ is the mass matrix, $[K]$ is the stiffness matrix, $\{A\}$ denotes all the DoFs and the right hand side (RHS) vector $\{P\}$ includes the prescribed current density and the contribution from any permanent magnets (PMs). The entries of the element matrices $[M]$, $[K]$ on an element e can be written as

$$M_{ij}^{e}=\iint_{e}\sigma N_i N_j \mathrm{d}x\mathrm{d}y, \tag{4.11}$$

$$K_{ij}^{e}=\iint_{e}\nu\left(\frac{\partial N_i}{\partial x}\frac{\partial N_j}{\partial x}+\frac{\partial N_i}{\partial y}\frac{\partial N_j}{\partial y}\right)\mathrm{d}x\mathrm{d}y. \tag{4.12}$$

The last step before solving the linear matrix equation is to handle the BCs. The homogeneous Neumann BC is actually natural in that it is implicitly satisfied in (4.6) and it doesn't need any special treatment. While the Dirichlet BC must be handled explicitly which can be easily imposed using a TGV (tremendously great value) technique [D4, D5]. After setting all the BCs, the resultant matrix equation can be solved by calling direct linear solvers such as UMFPack [D6], PARDISO [D7]; or Krylov-space iterative solvers such as the conjugate gradient (CG) method [D8].

4.1.2. Handling Nonlinear Material

Ferromagnetic materials with high permeability such as iron, cobalt and nickel are usually used in EM devices to modify the magnetic field shape and conduction of flux to regions where it is requires. For electric machines, the iron materials can generate high magnetic field in air-gaps to further generate high-torque, which depends on the field intensity squared. Furthermore, the iron materials are usually characterized by nonlinear *B*-*H* relationship. As a result, the matrix $[K]$ generally depends on the unknowns $\{A\}$, because the magnetic reluctivity ν in (4.12) is a function of *B*.

The Newton-Raphson (NR) iteration, which uses first order derivative information of the nonlinear equations and has second order rate of convergence, can then be applied to linearize the problem successively. To show the NR iteration

scheme, the magnetostatic problem is enough for illustration because the electric conductivity is linear so that [M] is independent of $\{A\}$ in (4.10).

Suppose the resultant nonlinear algebraic equation system is

$$F(A) = [K(A)]\{A\} = \{P\}, \tag{4.13}$$

then the k-th equation reads ($e(i)$ is an element in the mesh and there are totally NE elements)

$$F_k = \sum_{i=1}^{NE} \iint_{e(i)} \nu \nabla N_k \cdot \nabla A \mathrm{d}x\mathrm{d}y, \tag{4.14}$$

which is obtained by testing with the k-th global nodal basis function. The element Jacobian matrix reads (g, h are integer indices)

$$\begin{aligned} J_{gh}^{e(i)} &= \frac{\partial F_g^{e(i)}}{\partial A_h} \\ &= \iint_{e(i)} \nu \frac{\partial}{\partial A_h}(\nabla N_g \cdot \nabla A)\mathrm{d}x\mathrm{d}y + \iint_{e(i)} \frac{\partial \nu}{\partial A_h}(\nabla N_g \cdot \nabla A)\mathrm{d}x\mathrm{d}y . \\ &= \iint_{e(i)} \nu(\nabla N_g \cdot \nabla N_h)\mathrm{d}x\mathrm{d}y + \iint_{e(i)} \frac{\partial \nu}{\partial A_h}(\nabla N_g \cdot \nabla A)\mathrm{d}x\mathrm{d}y \end{aligned} \tag{4.15}$$

The first term in the above equation is nothing but the stiffness matrix. The partial derivative $\frac{\partial \nu}{\partial A_h}$ in the second term can be further written as

$$\begin{aligned} \frac{\partial \nu}{\partial A_h} &= \frac{\partial \nu}{\partial B}\frac{\partial B}{\partial A_h} \\ &= \frac{\partial \nu}{\partial B}\frac{\partial \sqrt{(\nabla A, \nabla A)}}{\partial A_h} \\ &= \frac{\partial \nu}{\partial B}\frac{1}{2\sqrt{(\nabla A, \nabla A)}}\frac{\partial (\nabla A, \nabla A)}{\partial A_h} \\ &= \frac{\partial \nu}{\partial B}\frac{1}{2B}(2\nabla A, \frac{\partial (\nabla A)}{\partial A_h}) \\ &= \frac{\partial \nu}{\partial B}\frac{1}{B}(\nabla A, \frac{\partial (\nabla A)}{\partial A_h}) \\ &= \frac{\partial \nu}{\partial B}\frac{1}{B}(\nabla A, \nabla N_h) \end{aligned} , \tag{4.16}$$

where

$$\frac{\partial \nu}{\partial B} = \frac{\partial (H/B)}{\partial B} = \frac{\partial H / \partial B \cdot B - H}{B^2} . \tag{4.17}$$

In practice, the single-valued *B*-*H* curve is usually given by a set of discrete points. Then the derivative $\partial H / \partial B$ and H for given B can be approximated by spline function.

Just like the finite element global assembly process, the element Jacobian matrix $J^{e(i)}$ is then assembled into the global one called *J*. At last, the NR iteration scheme reads

$$J^{(l)}(A^{(l)})\Delta A^{(l+1)} = P - F(A^{(l)}) = P - K(A^{(l)})A^{(l)}, \tag{4.18}$$

where

$$A^{(l+1)} = \Delta A^{(l+1)} + A^{(l)}, l = 0,1,2,... \tag{4.19}$$

The iteration will terminate if the condition

$$\| P - F(A^{(l)}) \| < \varepsilon, \tag{4.20}$$

is met.

For transient FEA, the temporal variable in (4.10) is discretized using the absolutely stable backward Euler scheme. The fully-discrete finite element scheme for the 2D eddy-current equation (4.1) including nonlinearity reads

$$[M]\frac{\{A^{n+1}\} - \{A^n\}}{\Delta t} + [K(A^{n+1})]\{A^{n+1}\} = \{P^{n+1}\}, n = 0,1,2,... \tag{4.21}$$

$$[\frac{M}{\Delta t} + K(A^{n+1})]\{A^{n+1}\} = [\frac{M}{\Delta t}]\{A^n\} + \{P^{n+1}\}, n = 0,1,2,... \tag{4.22}$$

Then (4.22) is of the same form as (4.13) and $\{A^{n+1}\}$ can be iteratively found using NR scheme.

4.1.3. Numerical Examples

In this section, the NR iteration scheme is to be validated with two examples, including an artificial example with exact solution to test the accuracy of the developed 2D nodal FE program and a benchmark magnetostatic problem. It can be verified that

$$\begin{cases} A = e^{x+y} / \sqrt{2} \\ \nu(B) = A = e^{x+y} / \sqrt{2} \\ J_s = -2e^{2x+2y} \\ M_x = M_y = 0 \end{cases}, \tag{4.23}$$

is a solution to (4.3) with $B = 2^{1/4}\sqrt{H}$. The nonhomogeneous Dirichlet BC is applied on the boundary of the problem domain, which is a unit square, according to the exact solution of A. The mesh and numerical solution is shown in Fig. 4.3. And the L^2 error of A with different meshes are given in Table 4.2, where the optimal order of convergence is achieved using second order basis functions. In the computation, the NR scheme (4.18)-(4.19) terminates after about 10 iterations.

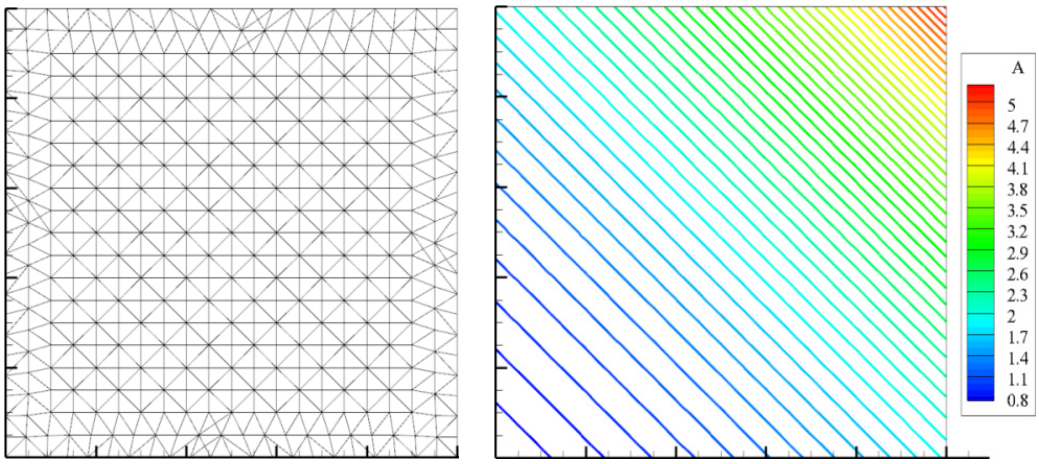

Fig. 4.3. Finite element mesh and numerical solution to the nonlinear magnetostatic problem with exact solution (4.23).

Number of DoFs	L^2 error of A	Order of convergence
869	1.16212E-005	-
1753	4.54488E-006	2.6757
3453	1.44055E-006	3.3897
6974	5.32957E-007	2.8291
13871	1.79521E-007	3.1650
27974	6.87687E-008	2.7358

Table 4.2. L^2 error of A versus different number of DoFs.

For the second example, the TEAM workshop problem 25 is solved using the NR iteration for handling material nonlinearity. This is a magneto-static problem, originally designed for testing optimization algorithms [D9]. Here we only take a set of fixed design parameters to check the developed computer program. The design parameters are given in Fig. 4.4 and the problem domain with R_1=7.2mm, L_2=15.3mm, L_3=29.5mm, L_4=11.5mm is shown in Fig. 4.5.

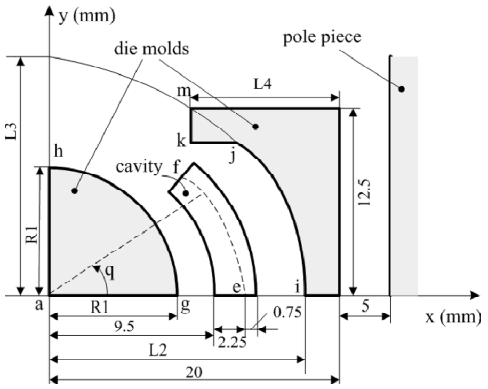

Fig. 4.4. Four geometric design parameters of the TEAM workshop problem 25.

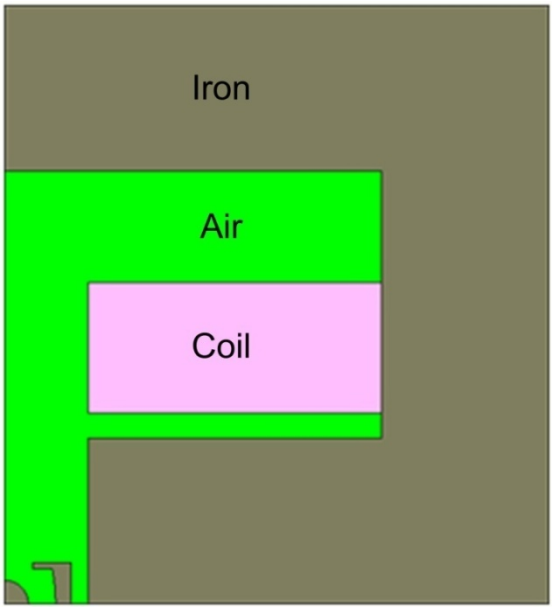

Fig. 4.5. Problem domain of the TEAM workshop problem 25, the size of the domain is 163mm × 180mm, where R_1=7.2mm, L_2=15.3mm, L_3=29.5mm, L_4=11.5mm. The excitation current in the coil region is 4253 ampere-turns (AT).

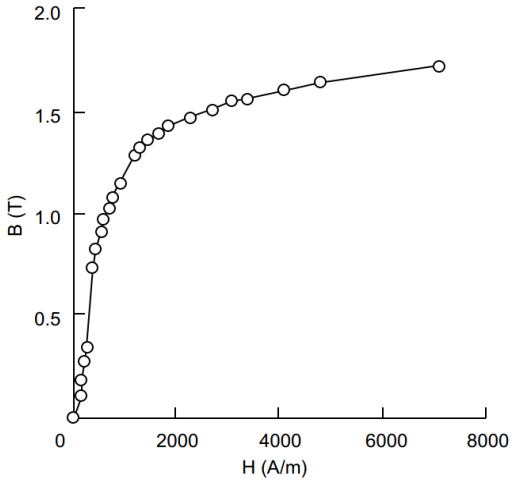

Fig. 4.6. Nonlinear *B-H* curve of the iron used in TEAM workshop problem 25.

The *B-H* curve for the nonlinear material is shown in Fig. 4.6. The computed mesh and the isopotential lines of the MVP *A* are shown in Fig. 4.7. For comparison, the mesh and numerical solution obtained by ANSYS Maxwell 2D are also given in Fig. 4.8. It can be observed that the two results are very close to each other.

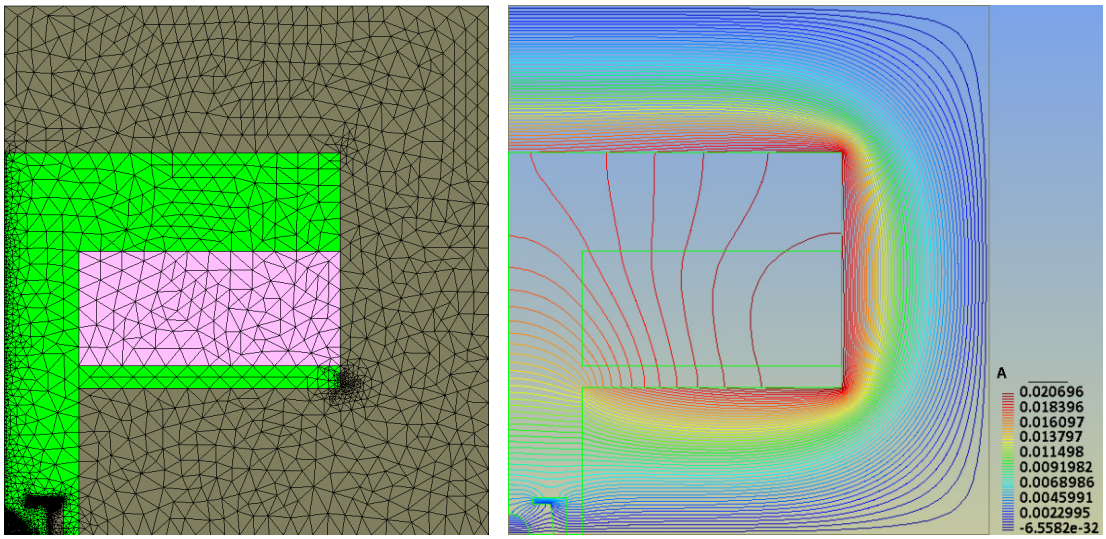

Fig. 4.7. Finite element mesh and the solution isopotential lines of the magnetic potential *A* of TEAM workshop problem 25.

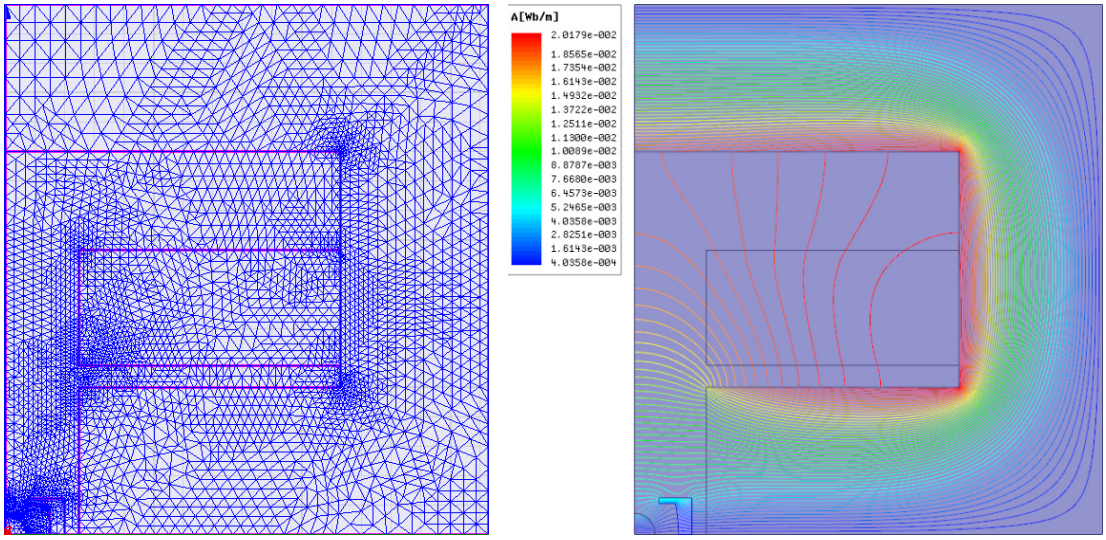

Fig. 4.8. Finite element mesh and the solution isopotential lines of the magnetic potential *A* of TEAM workshop problem 25, obtained by the software ANSYS Maxwell 2D.

4.1.4. Slave-master Technique for Rotational Movement

For dynamic simulation of electric machines, rotational movement must be taken into account in the transient finite element magnetic field analysis. If the rotor is solid, smooth and the material properties are invariant when it is rotating, one can simply add a convective term into the equation (4.1) to model the effect of velocity using Eulerian formulations [D10], where a fixed mesh is used throughout the time-stepping process. For most electric machines, the rotor is nonuniform when rotating, in such cases the Lagrangian formulations must be used to model the mechanical motion. In the Lagrangian formulations, the whole problem domain is divided into the rotor and stator parts, which are non-overlapping. The stationary part and the moving part are modeled in their own coordinate systems, only the matching condition is applied to the sliding interface to maintain the global continuity of the MVP A.

For computer implementation, the matching condition on the sliding surface can be fulfilled using the so-called slave-master technique. Take Fig. 4.9 for illustration, where the nodes 1, 2 , ..., 7, ... are master nodes on the master moving surface, while the nodes 1', 2', ..., 7', ... are slave nodes on the slave moving surface. All the DoFs associated with the slave nodes can be eliminated using the matching condition or the continuity condition.

$$\begin{aligned} A_{1'} &= w_1^{1'} A_1 + w_2^{1'} A_2 + w_3^{1'} A_3, \\ A_{2'} &= w_1^{2'} A_1 + w_2^{2'} A_2 + w_3^{2'} A_3, \\ &\cdots \\ A_{5'} &= w_1^{5'} A_5 + w_2^{5'} A_6 + w_3^{5'} A_7, \\ A_{6'} &= w_1^{6'} A_5 + w_2^{6'} A_6 + w_3^{6'} A_7, \\ &\cdots \end{aligned} \tag{4.24}$$

where the interpolation weights $\{w_1^{i'}, w_2^{i'}, w_3^{i'}\}, i = 1,2,...$ are calculated from the one-dimensional area coordinates of the node $P_{i'}$ relative to its three master nodes [Fu, Jan 2010]. It is noted that all the three weights are nonnegative and the sum of them equals to unity. A practical nonconforming mesh is also shown in Fig. 4.10, where the sliding surface is located between the blue and green region and is in the middle of the airgap region.

Fig. 4.9. Illustration of the matching condition on the sliding surface.

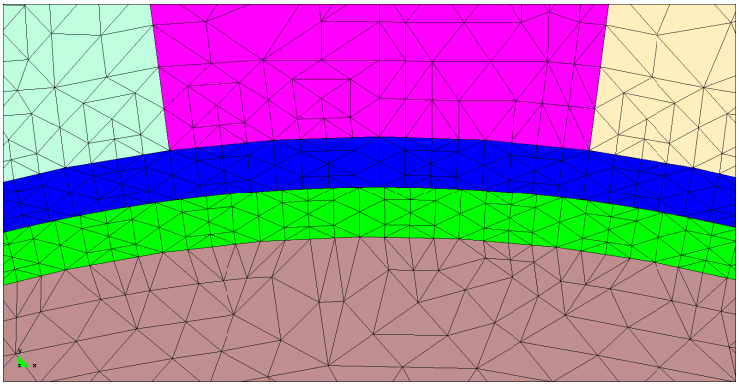

Fig. 4.10. Enlarged view of the stator mesh and rotor mesh are connected by the sliding surface, which lies between the green region and the blue region.

For each slave node, the associated contribution to the global matrix and global RHS vector are assembled into the corresponding master nodes. There is no unknowns defined on the slave nodes and the potential values on them are calculated from the solved ones on the master nodes. The slave-master technique can be easily realized with the help of a transformation matrix. Suppose the element e contains only one slave node S whose master nodes are M_0, M_1, and M_2, and the nodal potentials are related by

$$A_S = w_0 A_{M0} + w_1 A_{M1} + w_2 A_{M2}. \tag{4.25}$$

The DoFs $\{A_e\}$ within element e can be written as the union of two disjoint subsets, namely the master DoFs $\{A_M\}$ and the slave DoFs $\{A_S\}$:

$$\{A_e\} = \{A_M\} \cup \{A_S\}, \tag{4.26}$$

It is noted that all the DoFs associated with e include its own master DoFs $\{A_M\}$ and the master DoFs $\{A_S^M\}$, none of which belongs to $\{A_e\}$, of the slave DoFs $\{A_S\}$. The transformation matrix $[T]$ can be obtained by

$$\begin{Bmatrix} A_M \\ A_S \end{Bmatrix} = \begin{bmatrix} I & 0 \\ 0 & W \end{bmatrix} \begin{Bmatrix} A_M \\ A_S^M \end{Bmatrix} = [T] \begin{Bmatrix} A_M \\ A_S^M \end{Bmatrix}, \tag{4.27}$$

where $[I]$ is the identity matrix and $[W]$ is the interpolation weights matrix. The slave DoFs within element e can be eliminated by modifying the element matrix and element RHS vector using $[T]$ as

$$[\tilde{M}_e] = [T^T][M_e][T], \tag{4.28}$$

$$[\tilde{K}_e] = [T^T][K_e][T], \tag{4.29}$$

$$[\tilde{P}_e] = [T^T][P_e], \tag{4.30}$$

where $[T^T]$ is the transpose of $[T]$. It is not difficult to see from the above equations that by using this matrix transformation method, the symmetry property of the original matrix system can be upheld.

4.1.5. A Numerical Example

The slave-master technique for handling rotational movement is applied to the numerical solution of the TEAM workshop problems 30A [D11]. The TEAM problem 30A is to simulate a three-phase induction motor. The physical parameters are given in Fig. 4.11 [D11]. The winding in the stator is excited by an alternating current density at a frequency f=60 Hz. The rotor is made of steel (with electric conductivity σ=1.6×10^{6}S/m) and aluminum (with electric conductivity σ=3.72×10^{7}S/m), with the rotor steel surrounded by the rotor aluminum. The stator steel is laminated and its conductivity is set to be σ=0.

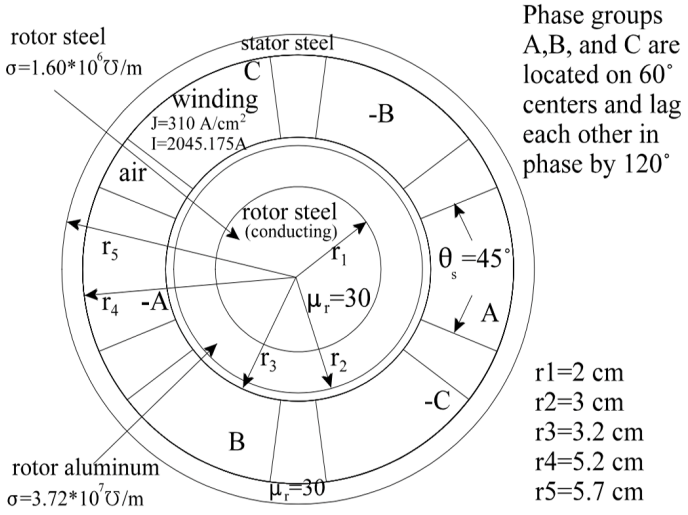

Fig. 4.11. The setting of TEAM workshop problem 30A.

In the computation, the time-dependent exciting source currents for phase $\pm$A, phase $\pm$B and phase $\pm$C are respectively set to be $\pm J_m \sin(2\pi f t)$, $\pm J_m \sin(2\pi f t + 2\pi/3)$ and $\pm J_m \sin(2\pi f t + 4\pi/3)$, where $J_m = \sqrt{2} \times 3.1 \times 10^6 \text{A/m}^2$. When the rotor rotates at an angular speed of $\omega = 200$rad/s counterclockwisely, the magnetic field is solved using two formulations, namely the Eulerian formulation and the Lagrangian one. It is due to the cylindrical shape of the solid rotor that the rotational motion can be described by both the Eulerian formulation and the Lagrangian one.

In Figs. 4.12(a)-4.12(e) the numerical solution contour lines are shown when the rotor rotates 0, 90, 180, 270 and 360 degrees counterclockwisely within the first period using the Lagrangian formulation. The numerical result obtained using ANSYS Maxwell 2D is given in Figs. 4.12(a')-4.12(e'). For comparison, numerical results obtained by the Eulerian formulation is also given in Figs. 4.12(a'')-4.12(e''). It can be observed that all the three sets of results are close to each other.

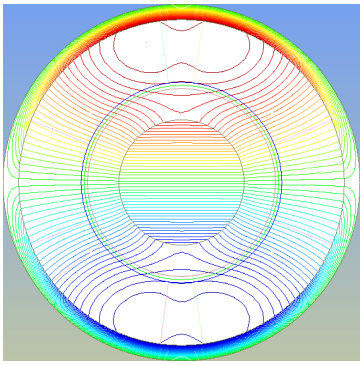

(a)

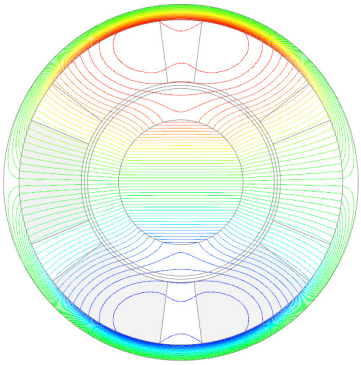

(a')

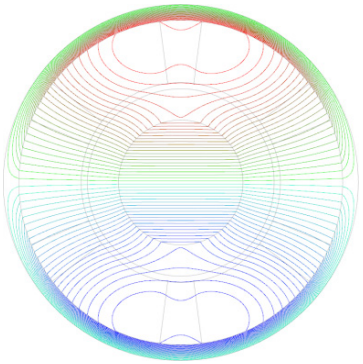

(a'')

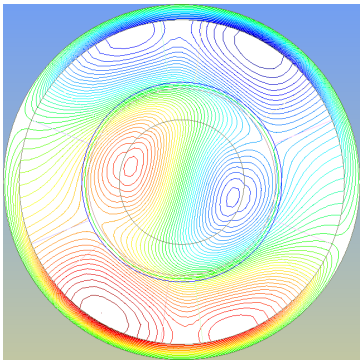

(b)

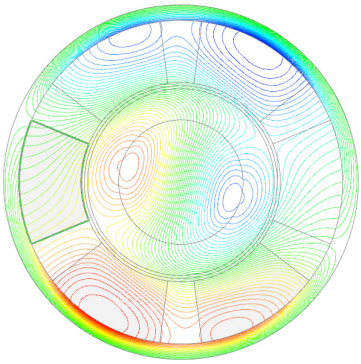

(b')

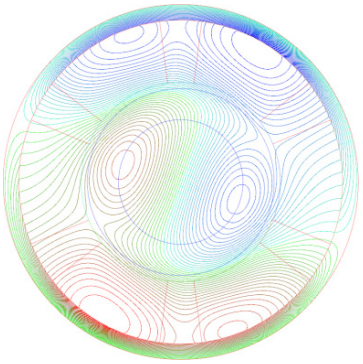

(b'')

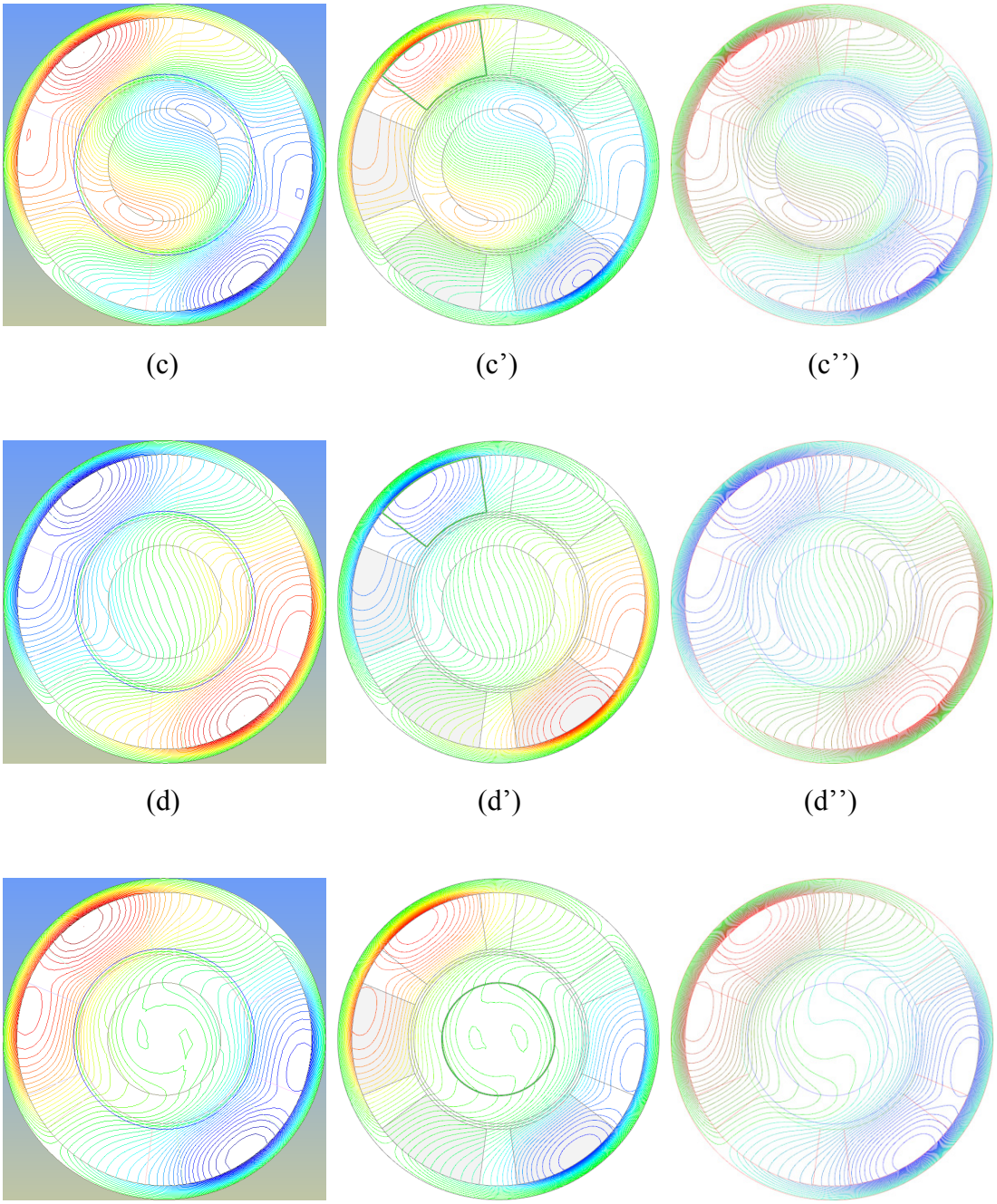

(c) (c') (c'')

(d) (d') (d'')

(e) (e') (e'')

Fig. 4.12. (a)-(e) The isopotential lines of the solution of A when the rotor rotates 0, 90, 180, 270 and 360 degrees using the slave-master technique. (a')-(e') The isopotential lines of the solution of A when the rotor rotates 0, 90, 180, 270 and 360 degrees using the commercial software ANSYS Maxwell 2D. (a'')-(e'') The isopotential lines of the solution of A when the rotor rotates 0, 90, 180, 270 and 360 degrees on a fixed mesh using Eulerian formulation.

4.2. 3D Edge-based FEM with MVP Formulation

The MVP formulation of the 3D eddy-current problem reads

$$\begin{cases} \nabla \times (\nu \nabla \times \vec{A}) = -\sigma \dfrac{\partial \vec{A}}{\partial t} - \sigma \nabla \varphi \\ \nabla \cdot (-\sigma \dfrac{\partial \vec{A}}{\partial t} - \sigma \nabla \varphi) = 0 \end{cases}, \tag{4.31}$$

in conducting region V_1 and

$$\nabla \times (\nu \nabla \times \vec{A}) = \vec{J}_s. \tag{4.32}$$

in nonconducting region V_2. As illustrated in Fig. 2.1, two kinds of boundary conditions are typically encountered in low-frequency EM field computation, namely

$$\vec{n} \times \vec{A} = 0, \text{ on } S_B, \tag{4.33}$$

and

$$\vec{n} \times (\nu \nabla \times \vec{A}) = 0, \text{ on } S_H. \tag{4.34}$$

At the interface between conducting region and non-conducting region, the normal component of the induced eddy-currents are required to be vanishing

$$(-\sigma \frac{\partial \vec{A}}{\partial t} - \sigma \nabla \varphi) \cdot \vec{n} = 0, \text{ on } S_{12}. \tag{4.35}$$

The solution of (4.31)-(4.35) has attracted much attention during the past decades [A20-A23, A36, A41-A44]. As discussed in Chapter 2, if nodal finite elements are used to approximate the three components of the MVP $\vec{A}$, the numerical result is not satisfactory at material interfaces or shape corners of the problem domain. And the imposition of the Coulomb gauge condition by penalty technique results in an unacceptable error for problems involving different media of high contrast [A42]. In this thesis, the edge element is adopted to approximate $\vec{A}$. Supposing the solenoidality of the source current can be rigorously satisfied after spatial discretization, then (4.31) and (4.32) can be directly used for eddy-current problems without any gauge condition.

4.2.1. Finite Edge Element MVP Formulation

In this thesis, the tetrahedral element is used for the discretization of the problem domain V. For the MVP $\vec{A}$ on an element e as shown in Fig. 4.13, its edge element expression is

$$\vec{A}^e = \sum_{k=1}^{6} A_k^e \vec{N}^k, \tag{4.36}$$

where $\vec{N}^k$ is the edge element basis function which is defined by

$$\vec{N}^k = \vec{N}_{ij} = (N_i \nabla N_j - N_j \nabla N_i) l_{ij}. \tag{4.37}$$

where the k-th (k=1,2,…,6) edge $e(i,j)$'s two end points are denoted by i and j and the length of the edge l_{ij} is used to normalize the edge basis function as well as to make it dimensionless [D5]. As a result, the edge element basis function $\vec{N}_{ij}$ has the property

$$\vec{N}_{ij} \cdot \vec{e}_{ij} = 1, \tag{4.38}$$

where $\vec{e}_{ij}$ is the unit vector pointing from i to j.

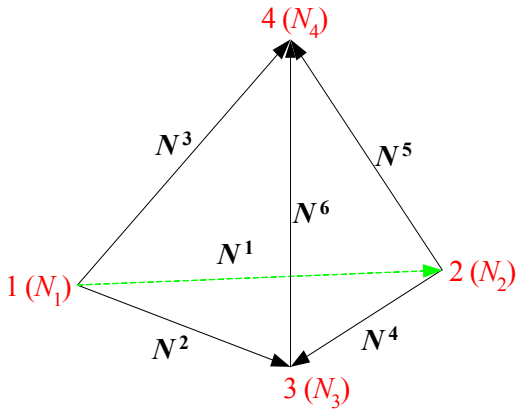

Fig. 4.13. The six edge element basis functions defined on an element e, the local edge directions are also indicated.

Besides the fact that the vector basis function $\vec{N}_{ij}$ has unit tangential component along the edge (i,j), it also has zero tangential component along all the other 5 edges of a tetrahedron. So the interpolation coefficients $\{A_k^e\}_{k=1}^6$ are the tangential component of the MVP along the k-th (or (i,j)-th) edge, namely

$$\int_{e(i,j)} \vec{A}^e \cdot dl = \int_{e(i,j)} \sum_{k=1}^{6} A_k^e \vec{N}^k \cdot dl = A_{ij}^e = A_k^e. \tag{4.39}$$

In the definition of the edge element basis function, N_i is the usual nodal element basis function on a tetrahedral element:

$$N_i = \frac{1}{6V_e}\left(p_i + q_i x + r_i y + s_i z\right), i = 1,2,3,4, \tag{4.40}$$

where V_e is the volume of the element *e*. These nodal basis functions have the Kronecker-delta property:

$$N_i(x_j, y_j, z_j) = \delta_{ij} = \begin{cases} 1, & i = j \\ 0, & i \neq j \end{cases}. \tag{4.41}$$

As shown in Fig. 4.13, the six edge basis functions within an element can be written as

$$\frac{\vec{N}^1}{l_{12}} = \frac{\vec{N}_{12}}{l_{12}} = N_1 \nabla N_2 - N_2 \nabla N_1 = N_1 \frac{1}{6V_e} \begin{pmatrix} q_2 \\ r_2 \\ s_2 \end{pmatrix} - N_2 \frac{1}{6V_e} \begin{pmatrix} q_1 \\ r_1 \\ s_1 \end{pmatrix}, \tag{4.42}$$

$$\frac{\vec{N}^2}{l_{12}} = \frac{\vec{N}_{13}}{l_{13}} = N_1 \nabla N_3 - N_3 \nabla N_1 = N_1 \frac{1}{6V_e} \begin{pmatrix} q_3 \\ r_3 \\ s_3 \end{pmatrix} - N_3 \frac{1}{6V_e} \begin{pmatrix} q_1 \\ r_1 \\ s_1 \end{pmatrix}, \tag{4.43}$$

$$\frac{\vec{N}^3}{l_{12}} = \frac{\vec{N}_{14}}{l_{14}} = N_1 \nabla N_4 - N_4 \nabla N_1 = N_1 \frac{1}{6V_e} \begin{pmatrix} q_4 \\ r_4 \\ s_4 \end{pmatrix} - N_4 \frac{1}{6V_e} \begin{pmatrix} q_1 \\ r_1 \\ s_1 \end{pmatrix}, \tag{4.44}$$

$$\frac{\vec{N}^4}{l_{12}} = \frac{\vec{N}_{23}}{l_{23}} = N_2 \nabla N_3 - N_3 \nabla N_2 = N_2 \frac{1}{6V_e} \begin{pmatrix} q_3 \\ r_3 \\ s_3 \end{pmatrix} - N_3 \frac{1}{6V_e} \begin{pmatrix} q_2 \\ r_2 \\ s_2 \end{pmatrix}, \tag{4.45}$$

$$\frac{\vec{N}^5}{l_{12}} = \frac{\vec{N}_{24}}{l_{24}} = N_2 \nabla N_4 - N_4 \nabla N_2 = N_2 \frac{1}{6V_e} \begin{pmatrix} q_4 \\ r_4 \\ s_4 \end{pmatrix} - N_4 \frac{1}{6V_e} \begin{pmatrix} q_2 \\ r_2 \\ s_2 \end{pmatrix}, \tag{4.46}$$

$$\frac{\vec{N}^6}{l_{12}} = \frac{\vec{N}_{34}}{l_{34}} = N_3 \nabla N_4 - N_4 \nabla N_3 = N_3 \frac{1}{6V_e} \begin{pmatrix} q_4 \\ r_4 \\ s_4 \end{pmatrix} - N_4 \frac{1}{6V_e} \begin{pmatrix} q_3 \\ r_3 \\ s_3 \end{pmatrix}. \tag{4.47}$$

From the equation that $\nabla \times (vA) = v\nabla \times A + \nabla v \times A$, and $\nabla \times (\nabla v) = 0$ for any scalar function *v*, the curl of $\vec{N}_{ij}$ is a constant vector within an element

$$\begin{aligned} \nabla \times \vec{N}_{ij} &= \nabla \times (N_i \nabla N_j - N_j \nabla N_i) l_{ij} = 2 \nabla N_i \times \nabla N_j l_{ij} \\ &= 2 \frac{1}{36V_e^2} \begin{pmatrix} q_i \\ r_i \\ s_i \end{pmatrix} \times \begin{pmatrix} q_j \\ r_j \\ s_j \end{pmatrix} l_{ij} = \frac{1}{18V_e^2} l_{ij} \begin{pmatrix} r_i s_j - s_i r_j \\ s_i q_j - q_i s_j \\ q_i r_j - r_i q_j \end{pmatrix}. \end{aligned} \tag{4.48}$$

For the eddy-current equation (4.31)-(4.35), the Galerkin weak form obtained by multiplying the two equations with arbitrary test function $\delta\vec{A}$, $\delta\varphi$ and then integrating by parts. For the term on the left-hand-side of the first equation of (4.31),

$$\begin{aligned}
&\iiint_{V_1} \delta\vec{A}\cdot\nabla\times(\nu\nabla\times\vec{A})dV \\
&= \iiint_{V_1} (\nabla\times\delta\vec{A}\cdot\nu\nabla\times\vec{A} - \nabla\cdot(\delta\vec{A}\times\nu\nabla\times\vec{A}))dV \\
&= \iiint_{V_1} \nabla\times\delta\vec{A}\cdot\nu\nabla\times\vec{A}dV - \iiint_{V_1} \nabla\cdot(\delta\vec{A}\times\nu\nabla\times\vec{A}))dV \\
&= \iiint_{V_1} \nabla\times\delta\vec{A}\cdot\nu\nabla\times\vec{A}dV - \oiint_{\partial V_1} \delta\vec{A}\times\nu\nabla\times\vec{A}\cdot\vec{n}dS
\end{aligned} \tag{4.49}$$

From the following equation

$$(\vec{F}\times\vec{G})\cdot\vec{T} = \vec{F}\cdot(\vec{G}\times\vec{T}), \tag{4.50}$$

one can easily see that

$$\delta\vec{A}\times\nu\nabla\times\vec{A}\cdot\vec{n} = \delta\vec{A}\cdot(\nu\nabla\times\vec{A}\times\vec{n}). \tag{4.51}$$

From the fact that the test function $\delta\vec{A}$ satisfies zero Dirichlet BC (4.33), the last boundary integration term of (4.49) vanishes.

For the second equation of (4.31), multiply both sides by $\delta\varphi$ and integrate by parts, one has

$$\begin{aligned}
&\iiint_{V_1} \delta\varphi\nabla\cdot(-\sigma\frac{\partial\vec{A}}{\partial t} - \sigma\nabla\varphi)dV \\
&= \iiint_{V_1} -\nabla\cdot(\delta\varphi(\sigma\frac{\partial\vec{A}}{\partial t} + \sigma\nabla\varphi))dV + \iiint_{V_1} \nabla\delta\varphi\cdot\sigma(\frac{\partial\vec{A}}{\partial t} + \nabla\varphi)dV \\
&= \iiint_{S_{12}} -(\delta\varphi(\sigma\frac{\partial\vec{A}}{\partial t} + \sigma\nabla\varphi))\cdot\vec{n}dS + \iiint_{V_1} \nabla\delta\varphi\cdot\sigma(\frac{\partial\vec{A}}{\partial t} + \nabla\varphi)dV \\
&= \iiint_{V_1} \nabla\delta\varphi\cdot\sigma(\frac{\partial\vec{A}}{\partial t} + \nabla\varphi)dV
\end{aligned}, \tag{4.52}$$

where the interface condition (4.35) is used.

Finally, the Galerkin weak form of the eddy-current problem (4.31)-(4.35) reads

$$\begin{cases}
\iiint_{V_1} \nabla\times\delta\vec{A}\cdot\nu\nabla\times\vec{A}dV + \iiint_{V_1} \delta\vec{A}\cdot\sigma(\frac{\partial\vec{A}}{\partial t} + \nabla\varphi)dV = 0 \\
\iiint_{V_1} \nabla\delta\varphi\cdot\sigma(\frac{\partial\vec{A}}{\partial t} + \nabla\varphi)dV = 0
\end{cases}, \tag{4.53}$$

$$\iiint_{V_2} \nabla\times\delta\vec{A}\cdot\nu\nabla\times\vec{A}dV = \iiint_{V_2} \delta\vec{A}\cdot\vec{J}_s dV. \tag{4.54}$$

They can be combined into a compact form as

$$\begin{cases} \iiint_V \nabla \times \delta\vec{A} \cdot \nu \nabla \times \vec{A} dV + \iiint_V \delta\vec{A} \cdot \sigma(\frac{\partial \vec{A}}{\partial t} + \nabla\varphi) dV = \iiint_V \delta\vec{A} \cdot \vec{J}_s dV \\ \iiint_{V_1} \nabla\delta\varphi \cdot \sigma(\frac{\partial \vec{A}}{\partial t} + \nabla\varphi) dV = 0 \end{cases}, \tag{4.55}$$

or

$$\begin{cases} (\nabla \times \delta\vec{A}, \nu \nabla \times \vec{A}) + (\delta\vec{A}, \sigma(\frac{\partial \vec{A}}{\partial t} + \nabla\varphi)) = (\delta\vec{A}, \vec{J}_s) \\ (\nabla\delta\varphi, \sigma(\frac{\partial \vec{A}}{\partial t} + \nabla\varphi)) = 0 \end{cases}. \tag{4.56}$$

The fully-discrete finite element scheme with backward Euler formula to discretize the temporal variable reads

$$\begin{cases} \frac{\sigma}{\Delta t}(\delta\vec{A}, \vec{A}^n) + (\nabla \times \delta\vec{A}, \nu \nabla \times \vec{A}^n) + \sigma(\delta\vec{A}, \nabla\varphi^n) = \frac{\sigma}{\Delta t}(\delta\vec{A}, \vec{A}^{n-1}) + (\delta\vec{A}, \vec{J}_s) \\ \sigma(\vec{A}^n, \nabla\delta\varphi) + \sigma\Delta t(\nabla\varphi^n, \nabla\delta\varphi) = \sigma(\vec{A}^{n-1}, \nabla\delta\varphi) \end{cases}, \tag{4.57}$$

where Δt is the time-step. In the following, the detailed computation of the element matrices and load vectors of (4.57) are given.

4.2.2. Computing the Element Matrices

In this thesis, the following notations are used for any tetrahedral element *e* in the mesh:

$$M_{AA}^e = (\delta\vec{A}, \vec{A})^e, \tag{4.58}$$

$$K_{AA}^e = (\nabla \times \delta\vec{A}, \nabla \times \vec{A})^e, \tag{4.59}$$

$$K_{AV}^e = (\delta\vec{A}, \nabla\varphi)^e, \tag{4.60}$$

$$K_{VA}^e = (\delta\nabla\varphi, \vec{A})^e, \tag{4.61}$$

$$K_{VV}^e = (\delta\nabla\varphi, \nabla\varphi)^e, \tag{4.62}$$

$$F^e = (\delta\vec{A}, \vec{J}_s)^e, \tag{4.63}$$

and M_{AA}, K_{AA}, K_{AV}, K_{VA}, K_{VV}, F denote the global matrices and RHS load vector.

The entries of the elemental matrices are given in the following:

(1) The (p,q)-th (p,q=1,2,…,6) entry of the element matrix M_{AA}^{e} is

$$
\begin{aligned}
&M_{AA}^{e}(p,q)=\int_{e}\vec{N}_{i1j1}\cdot\vec{N}_{i2j2}dxdydz\\
&=l_{i1j1}l_{i2j2}\int_{e}(N_{i1}\nabla N_{j1}-N_{j1}\nabla N_{i1})\cdot(N_{i2}\nabla N_{j2}-N_{j2}\nabla N_{i2})dxdydz\\
&=l_{i1j1}l_{i2j2}\int_{e}\begin{pmatrix}N_{i1}N_{i2}\nabla N_{j1}\cdot\nabla N_{j2}+N_{j1}N_{j2}\nabla N_{i1}\cdot\nabla N_{i2}-\\ N_{i1}N_{j2}\nabla N_{j1}\cdot\nabla N_{i2}-N_{j1}N_{i2}\nabla N_{i1}\cdot\nabla N_{j2}\end{pmatrix}dxdydz\\
&=\frac{l_{i1j1}l_{i2j2}}{36V_{e}^{2}}\int_{e}\begin{pmatrix}N_{i1}N_{i2}\begin{pmatrix}q_{j1}\\ r_{j1}\\ s_{j1}\end{pmatrix}\cdot\begin{pmatrix}q_{j2}\\ r_{j2}\\ s_{j2}\end{pmatrix}+N_{j1}N_{j2}\begin{pmatrix}q_{i1}\\ r_{i1}\\ s_{i1}\end{pmatrix}\cdot\begin{pmatrix}q_{i2}\\ r_{i2}\\ s_{i2}\end{pmatrix}-\\ N_{i1}N_{j2}\begin{pmatrix}q_{j1}\\ r_{j1}\\ s_{j1}\end{pmatrix}\cdot\begin{pmatrix}q_{i2}\\ r_{i2}\\ s_{i2}\end{pmatrix}-N_{j1}N_{i2}\begin{pmatrix}q_{i1}\\ r_{i1}\\ s_{i1}\end{pmatrix}\cdot\begin{pmatrix}q_{j2}\\ r_{j2}\\ s_{j2}\end{pmatrix}\end{pmatrix}dxdydz\\
&=\frac{l_{i1j1}l_{i2j2}}{6V_{e}}\int_{\hat{e}}\begin{pmatrix}N_{i1}N_{i2}\begin{pmatrix}q_{j1}\\ r_{j1}\\ s_{j1}\end{pmatrix}\cdot\begin{pmatrix}q_{j2}\\ r_{j2}\\ s_{j2}\end{pmatrix}+N_{j1}N_{j2}\begin{pmatrix}q_{i1}\\ r_{i1}\\ s_{i1}\end{pmatrix}\cdot\begin{pmatrix}q_{i2}\\ r_{i2}\\ s_{i2}\end{pmatrix}-\\ N_{i1}N_{j2}\begin{pmatrix}q_{j1}\\ r_{j1}\\ s_{j1}\end{pmatrix}\cdot\begin{pmatrix}q_{i2}\\ r_{i2}\\ s_{i2}\end{pmatrix}-N_{j1}N_{i2}\begin{pmatrix}q_{i1}\\ r_{i1}\\ s_{i1}\end{pmatrix}\cdot\begin{pmatrix}q_{j2}\\ r_{j2}\\ s_{j2}\end{pmatrix}\end{pmatrix}d\alpha_{1}d\alpha_{2}d\alpha_{3}\\
&=\frac{l_{i1j1}l_{i2j2}}{6V_{e}}\frac{1}{120}[(1+\delta_{i1i2})A+(1+\delta_{j1j2})B-(1+\delta_{i1j2})C-(1+\delta_{j1i2})D]
\end{aligned}
$$

where

$$
A=\begin{pmatrix}q_{j1}\\ r_{j1}\\ s_{j1}\end{pmatrix}^{T}\cdot\begin{pmatrix}q_{j2}\\ r_{j2}\\ s_{j2}\end{pmatrix},\ B=\begin{pmatrix}q_{i1}\\ r_{i1}\\ s_{i1}\end{pmatrix}^{T}\cdot\begin{pmatrix}q_{i2}\\ r_{i2}\\ s_{i2}\end{pmatrix},
$$

$$
C=\begin{pmatrix}q_{j1}\\ r_{j1}\\ s_{j1}\end{pmatrix}^{T}\cdot\begin{pmatrix}q_{i2}\\ r_{i2}\\ s_{i2}\end{pmatrix},\ D=\begin{pmatrix}q_{i1}\\ r_{i1}\\ s_{i1}\end{pmatrix}^{T}\cdot\begin{pmatrix}q_{j2}\\ r_{j2}\\ s_{j2}\end{pmatrix}.
$$

(2) The (p,q)-th (p,q=1,2,…,6) entry of the element matrix K_{AA}^{e} is

$$
K_{AA}^{e}(p,q)=\int_{e}\nabla\times\vec{N}_{i1j1}\cdot\nabla\times\vec{N}_{i2j2}dV=V_{e}\nabla\times\vec{N}_{i1j1}\cdot\nabla\times\vec{N}_{i2j2}
$$

where the curl of the edge element basis function is given by (4.48).

(3) The (p,l)-th (p=1,2,…,6; l=1,2,3,4) entry of the element matrix K_{AV}^{e} is

$$K_{AV}^{e}(p,l)=\int_e \vec{N}^{p}\cdot\nabla N_l dV=\int_e \vec{N}_{ij}\cdot\nabla N_l dV$$
$$=l_{ij}\int_e (N_i\nabla N_l\cdot\nabla N_j-N_j\nabla N_l\cdot\nabla N_i)dV$$
$$=l_{ij}\left(\frac{q_lq_j+r_lr_j+s_ls_j}{36V_e^2}\int_e N_i dV-\frac{q_lq_i+r_lr_i+s_ls_i}{36V_e^2}\int_e N_j dV\right)$$
$$=l_{ij}\frac{(q_lq_j+r_lr_j+s_ls_j)-(q_lq_i+r_lr_i+s_ls_i)}{144V_e}$$

(4) The (l,p)-th (p=1,2,…,6; l=1,2,3,4) entry of the element matrix K_{VA}^{e} is given by

$$K_{VA}^{e}(l,p)=K_{AV}^{e}(p,l).$$

(5) The (i,j)-th i,j=1,2,3,4) entry of the element matrix K_{VV}^{e} is given by

$$K_{VV}^{e}(i,j)=\int_e \nabla N_i\cdot\nabla N_j dV$$
$$=\frac{q_iq_j+r_ir_j+s_is_j}{36V_e^{\,2}}V_e \qquad .$$
$$=\frac{q_iq_j+r_ir_j+s_is_j}{36V_e}$$

Unlike tradition nodal finite elements, the global edge orientation must be taken into account in the global assembly process [A7]. If the local edge orientation is opposite to the global one, one should put a negative sign to the corresponding element matrix entries for assembling. At last, the matrix form of the fully-discrete finite element scheme with backward Euler formula for the temporal derivative can be expressed as

$$\begin{bmatrix}\frac{\sigma}{\Delta t}M_{AA}+\nu K_{AA} & \sigma K_{AV}\\ \sigma K_{VA} & \Delta t\sigma K_{VV}\end{bmatrix}\begin{bmatrix}A^n\\ \varphi^n\end{bmatrix}=\begin{bmatrix}\frac{\sigma}{\Delta t}M_{AA}\\ \sigma K_{VA}\end{bmatrix}A^{n-1}+\begin{bmatrix}F^n\\ 0\end{bmatrix}. \qquad (4.64)$$

4.2.3. Generating the Source Field

In practice, to make the resultant linear system consistent and hence the solution of which converges fast using iterative solvers, the RHS vector must be in the range of the left hand side stiffness matrix [A45]. The key issue is to make sure that the applied excitation current is divergence free in the discrete level. Numerically, since only the values of current density on the Gaussian quadrature points are taken into

account, it is hard to ensure the zero divergence of the source current after discretization and hence the consistency of the resultant linear equation system.

To overcome this problem, one can introduce a current vector potential $\vec{T}_0$, also called the source field [A46], whose curl is the applied current density $\vec{J}_0$ in the coil region,

$$\vec{J}_0 = \nabla \times \vec{T}_0. \tag{4.65}$$

The source field $\vec{T}_0$ can be computed by the Biot-Savart law, which is however too computationally expensive to use. Alternatively the source field can be purely non-physical [D12-D15], besides this fictitious field can be made to be compactly supported [D16].

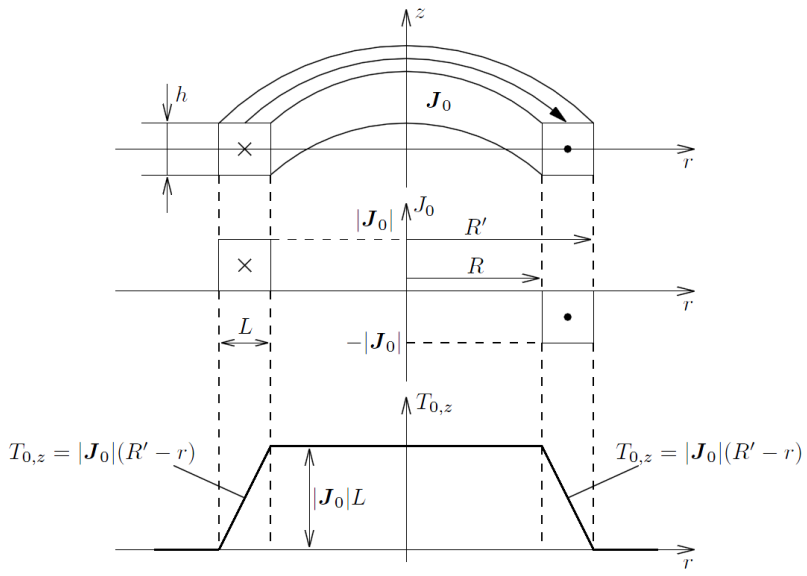

Fig. 4.14. Illustration of the current vector potential T_0 for stranded circular coil.

For stranded circular-shaped coil placed in parallel with the *x*-*y* place, we have the following analytical expression [A36] of the vector potential $\vec{T}_0 = [0, 0, T_{0,z}]$

$$T_{0,z} = \begin{cases} |\vec{J}_0|(R'-R), r < R \\ |\vec{J}_0|(R'-r), R \le r \le R', \\ 0, r > R' \end{cases} \tag{4.66}$$

which is shown in Fig. 4.14. It is noted that the support of this source field is a simply-connected region comprising the conductor. Another commonly used coil is

the race-track-shaped coil, as shown in Fig. 4.15, the source field $\vec{T}_0$ for which can be given analytically [A28]. For rectangular coil as shown in Fig. 4. 16, analytical source field is also available [D17].

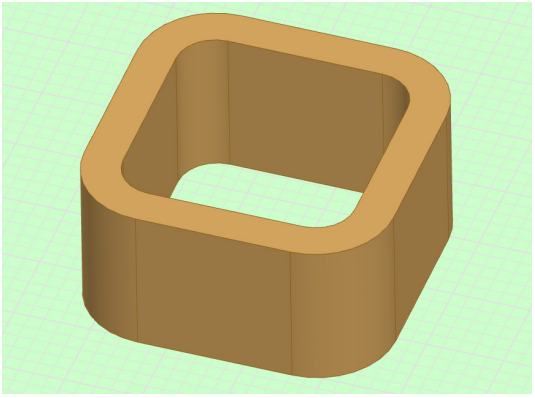

Fig. 4.15. Illustration of the race-track-shaped coil.

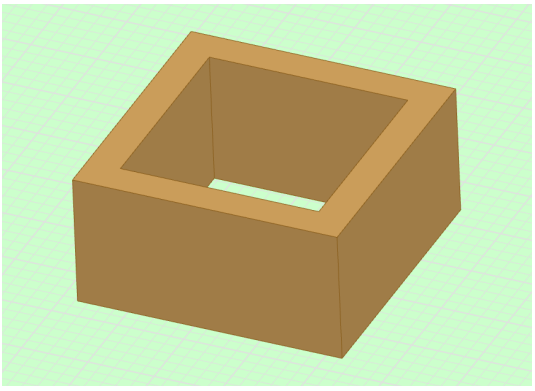

Fig. 4.16. Illustration of the rectangular coil.

For arbitrarily shaped stranded coil with given current density $\vec{J}_0$, the following variational equation can be solved in the conducting region V_c to determine the source field $\vec{T}_0$:

$$\iiint_{V_c} \nabla \times \delta\vec{T} \cdot \nabla \times \vec{T}_0 dV = \iiint_{V_c} \nabla \times \delta\vec{T} \cdot \vec{J}_0 dV. \tag{4.67}$$

Note that the above equation is symmetric and compatible [D18], because the current density is projected to the curl of edge element space [A46]. For arbitrarily shaped solid coil, the following variational equation can be solved in the conducting region V_c to determine the source field $\vec{T}_0$:

$$\iiint_{V_c} \frac{1}{\sigma} \nabla \times \delta\vec{T} \cdot \nabla \times \vec{T}_0 dV = 0, \tag{4.68}$$

with appropriate boundary conditions [A46].

4.2.4. Handling Nonlinear Materials

Since the electric conductivity is piecewisely constant in the conductors, the only nonlinear part is contained in the curl-curl operator. In this section the Newton-Raphson scheme for the nonlinear magnetostatic problem

$$\nabla \times (\nu \nabla \times \vec{A}) = \vec{J}_s, \tag{4.69}$$

is derived in details.

Suppose the resultant nonlinear algebraic equation system is $F(A)=p$, then the k-th equation reads ($e(i)$ is an element in the mesh and there are totally NE elements)

$$F_k = \sum_{i=1}^{NE} \int_{e(i)} \nu(\|\nabla \times \vec{A}\|)(\nabla \times \vec{N}_k \cdot \nabla \times \vec{A}) dV, \tag{4.70}$$

which is obtained by testing with the k-th global edge basis function. For the unknown vector potential $\vec{A}$, it is expanded under the edge element basis functions as:

$$\vec{A} = \sum_{i=1}^{NEdge} A_i \vec{N}_i, \tag{4.71}$$

where $\vec{N}_i$ is the i-th edge basis function and A_i is the tangential component along the i-th edge.

The elemental Jacobian matrix reads (g, h are integer indices)

$$\begin{aligned} J_{gh}^e = \frac{\partial F_g}{\partial A_h} &= \int_e \nu \frac{\partial}{\partial A_h}(\nabla \times \vec{N}_g \cdot \nabla \times \vec{A}) dV + \int_e \frac{\partial \nu}{\partial A_h}(\nabla \times \vec{N}_g \cdot \nabla \times \vec{A}) dV \\ &= \int_e \nu(\nabla \times \vec{N}_g \cdot \nabla \times \vec{N}_h) dV + \int_e \frac{\partial \nu}{\partial A_h}(\nabla \times \vec{N}_g \cdot \nabla \times \vec{A}) dV \end{aligned} \tag{4.72}$$

where the first term in the above equation can be calculated easily. For the second term, it can be computed as

$$\begin{aligned} &\frac{\partial \nu}{\partial A_h} = \frac{\partial \nu}{\partial B} \frac{\partial \sqrt{(\nabla \times \vec{A}, \nabla \times \vec{A})}}{\partial A_h} \\ &= \frac{\partial \nu}{\partial B} \frac{1}{2\sqrt{(\nabla \times \vec{A}, \nabla \times \vec{A})}} \frac{\partial (\nabla \times \vec{A}, \nabla \times \vec{A})}{\partial A_h} \\ &= \frac{\partial \nu}{\partial B} \frac{1}{2B} (2\nabla \times \vec{A}, \frac{\partial (\nabla \times \vec{A})}{\partial A_h}) = \frac{\partial \nu}{\partial B} \frac{1}{B} (\nabla \times \vec{A}, \frac{\partial (\nabla \times \vec{A})}{\partial A_h}) \\ &= \frac{\partial \nu}{\partial B} \frac{1}{B} (\nabla \times \vec{A}, \nabla \times \vec{N}_h) \end{aligned} \tag{4.73}$$

where

$$\frac{\partial \nu}{\partial B} = \frac{\partial (H / B)}{\partial B} = \frac{\partial H / \partial B \cdot B - H}{B^2}. \tag{4.74}$$

As in the 2D nonlinear magnetic field case, the derivative $\partial H / \partial B$ and H for given B can be approximated by spline function.

As a simple example, an artificial nonlinear magnetostatic problem is solved using the developed edge element program. The artificial solution is taken as

$$\begin{cases} \vec{A} = [0, 0, e^{x+y} / \sqrt{2}]^T \\ \nu(\| B \|) = e^{x+y} / \sqrt{2} \\ \vec{J}_s = [0, 0, -2e^{2x+2y}]^T \end{cases}, \tag{4.75}$$

where the nonlinear B-H relationship is given by

$$\| B \| = 2^{1/4} \sqrt{\| H \|}. \tag{4.76}$$

When using the Newton-Raphson iteration scheme, the convergence rates are given in Table 4.3, where about first-order rate of convergence of the magnetic flux density vector $\vec{B}$ can be observed. It should be noted that since the divergence of the MVP $\vec{A}$ is not specified in (4.75), the solution of $\vec{A}$ is not unique so there is no order of accuracy can be observed. It is very different from the 2D case.

Number of nodes	2294	14338	105172
L^2 error of $\vec{A}=[A_x,A_y,A_z]^T$	1.795E-001	2.062E-001	2.208E-001
	1.907E-001	2.002E-001	2.193E-001
	2.031E-001	2.557E-001	2.793E-001
L^2 error of $\vec{B}=[B_x,B_y,B_z]^T$	2.702E-002	1.494E-002	7.520E-003
	2.790E-002	1.503E-002	7.565E-003
	2.601E-002	1.403E-002	7.052E-003

Table 4.3. L^2 Error of MVP $\vec{A}$ and magnetic flux density $\vec{B}$.

Number of nodes	2294	14338	105172
L^2 error of $\vec{A}=[A_x,A_y,A_z]^T$	1.201E-003	5.379E-004	2.561E-04
	1.204E-003	5.266E-004	2.531E-04
	1.784E-003	7.478E-004	3.353E-04
L^2 error of $\vec{B}=[B_x,B_y,B_z]^T$	2.660E-003	1.478E-003	8.120E-04
	2.769E-003	1.491E-003	8.059E-04
	2.550E-003	1.387E-003	7.417E-04

Table 4.4. L^2 Error of MVP $\vec{A}$ and magnetic flux density $\vec{B}$.

4.2.5. Benchmark Numerical Examples

A. TEAM Workshop Problem 20

TEAM Workshop Problem 20 is a 3-D magnetostatic benchmark problem and its definition can be found in [D19]. The geometry of TEAM problem 20 consists of a steel center pole, surrounded by a coil with 381 windings of stranded copper wire, which is excited by a direct current. The magnetic circuit is completed by a yoke made of the same sort of steel as the center pole. In Figs. 4.17-19, the plan view, front view and 3D view of the geometry of the problem are given, where the length unit is mm. The magnetic flux density vector in the magnetic circuit using the 3D edge element solver is shown in Fig. 4.20, where the finite element mesh is shown in Fig. 4.21.

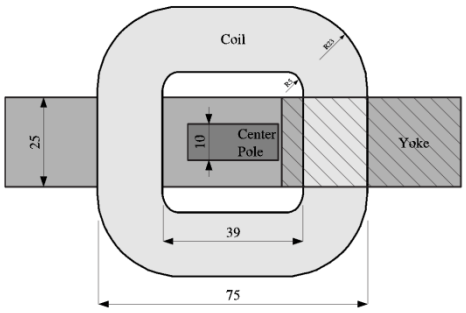

Fig. 4.17. Plan View of TEAM 20 Geometry.

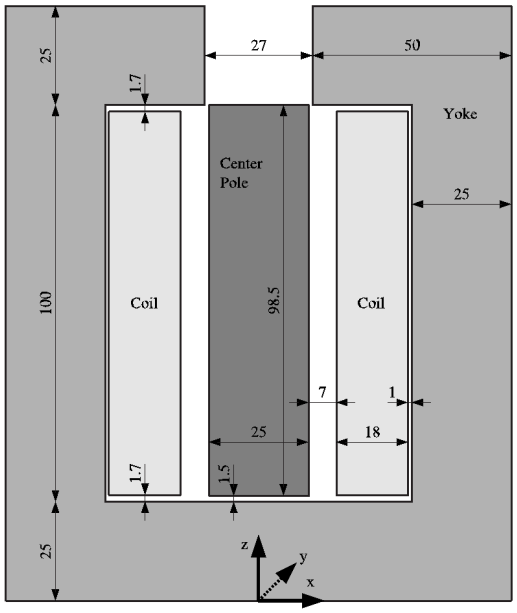

Fig. 4.18. Front View of TEAM 20 Geometry (Length Unit: mm).

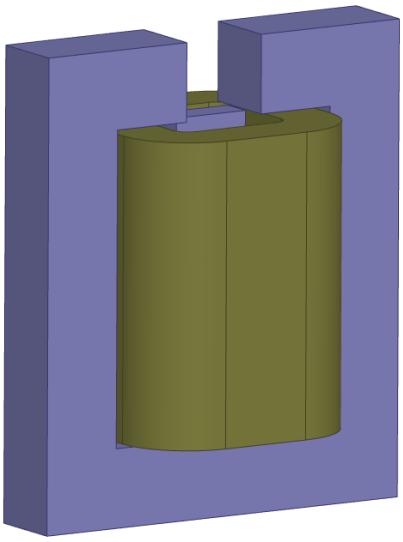

Fig. 4.19. 3D View of TEAM 20 Geometry.

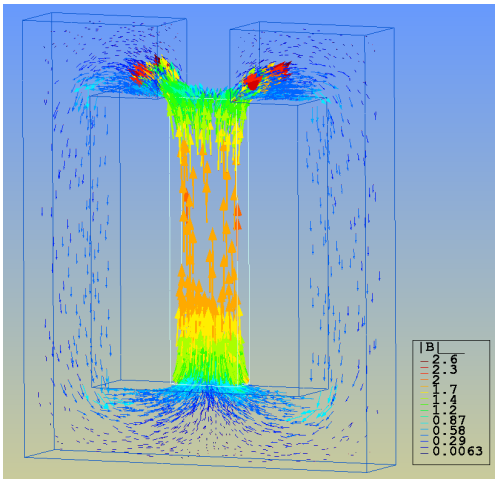

Fig. 4.20. Magnetic flux density vector in the center pole and the yoke, when the current in the coil is 4500A.

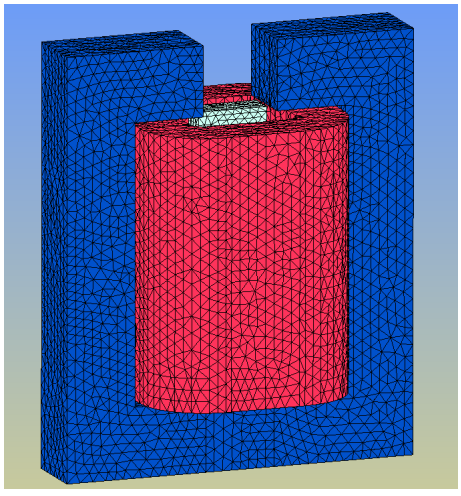

Fig. 4.21. Finite element mesh of the problem.

To check the accuracy of the developed edge element solver, the forces acting on the center pole with different DC excitations are computed using the Maxwell stress tensor method [D20] and compared with the measured results. In Fig. 4.22, the finite element mesh of the center pole and one layer of elements surrounding the pole for force computation are shown. In Table 4.5, the z-component of the force *Fz* on the center pole is listed when the excitation current is 1000AT, 3000AT, 4500AT and 5000AT. It can be seen that the numerical results are close to the measured data.

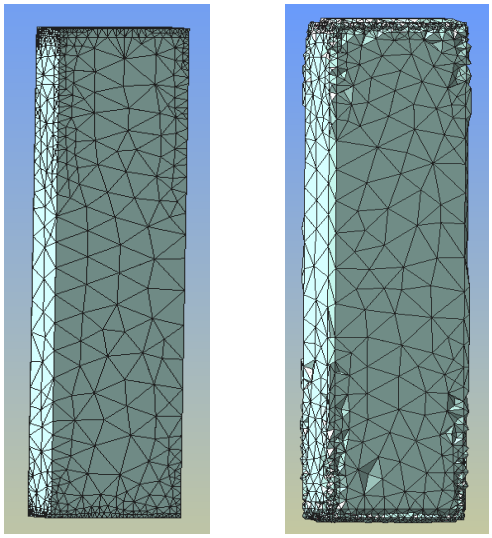

Fig. 4.22. Left: Mesh for the center pole; Right: Center pole mesh with the one layer of elements surrounding it for force computation by the Maxwell stress tensor method.

DC Excitations (AT)	Numerical results (N)	Measured Results (N)
1000	8.08	8.1
3000	56.5	54.4
4500	77.3	75.0
5000	82.5	80.1

Table 4.5. Force *Fz* acting on the center pole with different DC excitations.

B. TEAM Workshop Problem 7

As the second benchmark, the TEAM Workshop problem 7 [D21, D22] is solved in the time domain using the 3D edge element solver. In Figs. 4.23-4.25, the plan, front and full 3D views of the geometry are given, where the length unit is mm. It consists of a racetrack shaped coil (square coil with 200mm of width, 100mm of

height, 50/25mm of maximum/minimum radius at the corner) driven by a time harmonic current (amplitude I = 2742AT, frequency = 50Hz) over an asymmetrical conductor (a square plate of 294mm of width and 19mm of thickness) with a hole (108mm × 108 mm). The conductivity of the aluminum conductor is 3.526×10^7S/m.

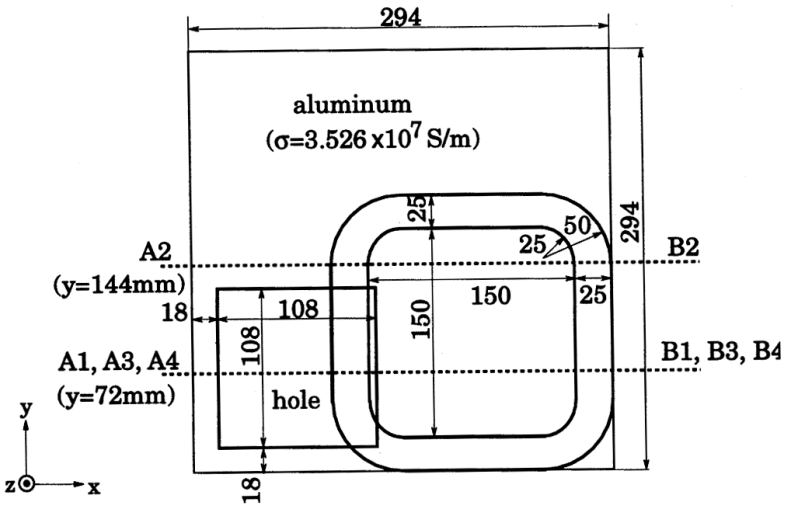

Fig. 4.23. Plan view of TEAM 7 geometry.

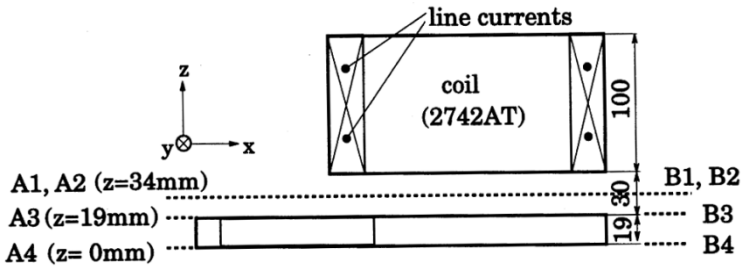

Fig. 4.24. Front view of TEAM 7 geometry.

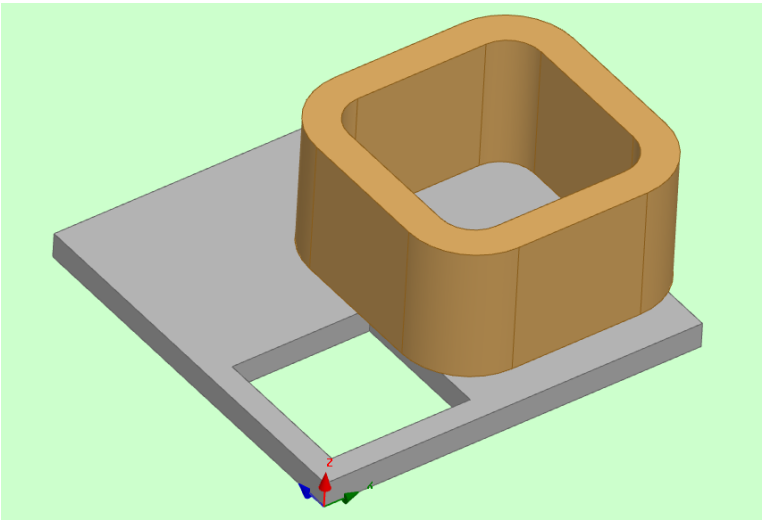

Fig. 4.25. 3D view of TEAM 7 geometry.

The TEAM workshop problem 7 is solved in the time-domain using the Backward-Euler time-discretization scheme (4.64) and the CVP representation of the source current density. The size of the problem domain is taken to be 800mm × 800mm × 600mm, and homogeneous boundary condition (4.33) is applied to the boundary of the cuboid. The FE time-stepping is computed to T= 0.025s from zero initial value, where the time step is $dt=5\times10^{-4}$s. The numerical result and the measured result of the z-component of the magnetic flux density along the line from A1 to B1 is shown in Fig. 4.26. The induced eddy-current in the aluminum conductor is also given in Fig. 4.27. In the computation, all the linear matrix equations are solved by the GMRES solver with a Gauss-Seidel preconditioner.

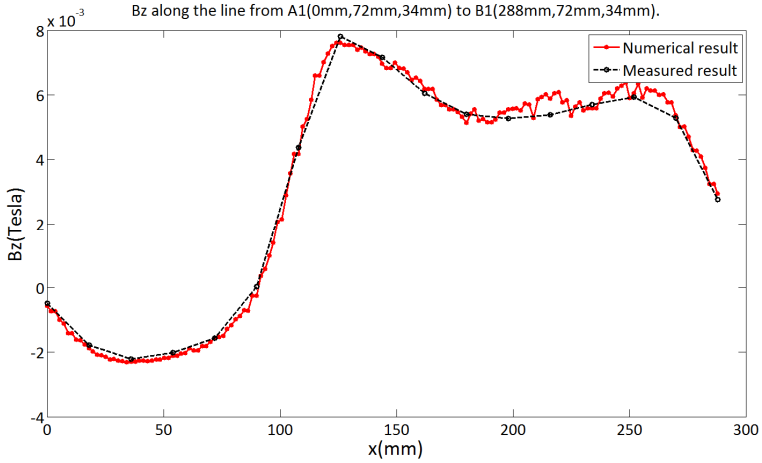

Fig. 4.26. Bz along the line from (0mm,72mm,34mm) to (288mm,72mm,34mm).

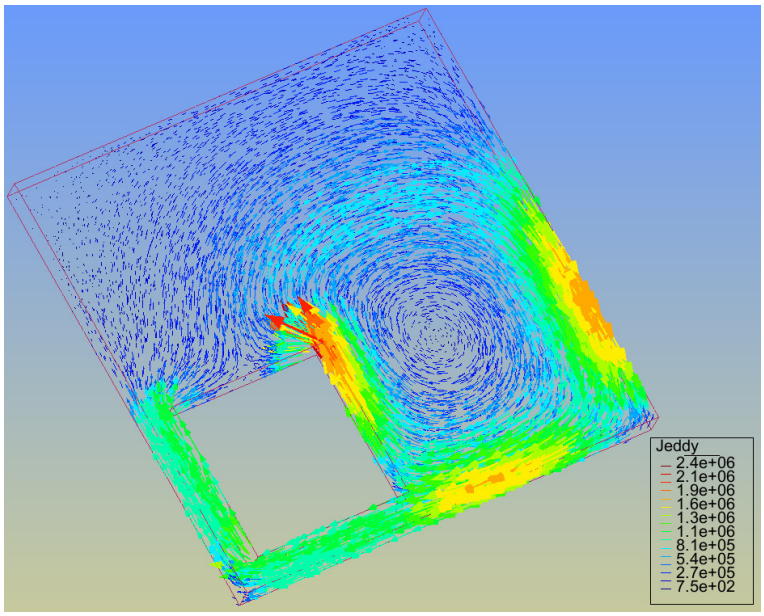

Fig. 4.27. Vector plot of the eddy current induced in the aluminum plate at time T= 0.025s, where the time step is $dt=5\times10^{-4}$s.

C. A skin-effect problem with voltage excitation

In the third example, the developed 3D edge element code based on the MVP formulation is used to solve a skin-effect problem with voltage excitation in the time-domain. The problem considered is shown in Fig. 4.28(a), where a sinusoidal voltage excitation is applied to the upper end terminal of the conductor while the lower end terminal of the conductor is grounded, i.e., the helical solid coil is excited by an alternating voltage as sin(*wt*).

The solid coil is made of copper with electric conductivity 5.8×10^{7}S/m. The diameter of the coil is 3mm, and the dimensions of the problem domain is 40mm$\times$ 40mm$\times$35mm. One finite element mesh of the helical coil is shown in Fig. 4.28(b). In the computation, the linear matrix equations are solved by the GMRES solver with a Gauss-Seidel preconditioner.

To check the accuracy of the developed 3D edge element code, the software package ANSYS Maxwell 3D is used for comparison for the same problem with the same problem settings. A global quantity, which is the total current in the solid conductor, defined as

$$I=-\iint_{S}\sigma(\frac{\partial\vec{A}}{\partial t}+\nabla\varphi)\cdot dS, \tag{4.77}$$

is calculated for each time-step.

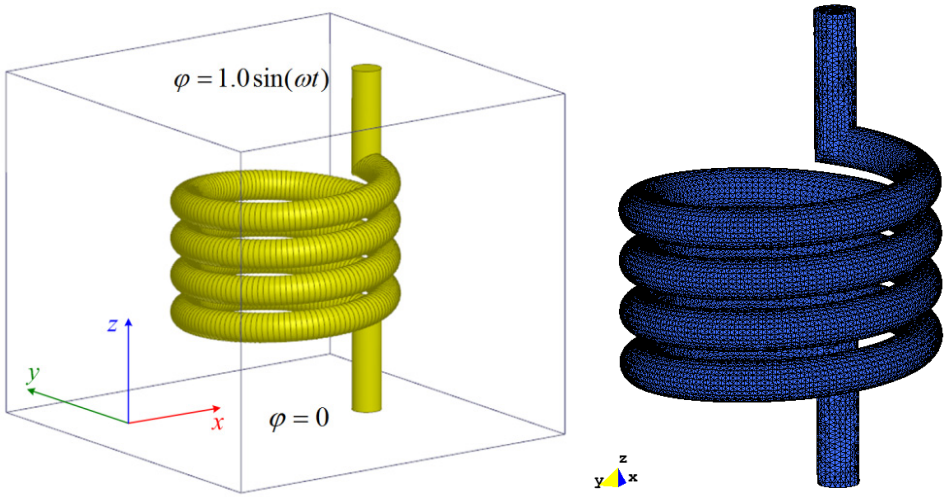

(a) (b)

Fig. 4.28 (a) The problem domain. (b) The finite element mesh of the solid conductor.

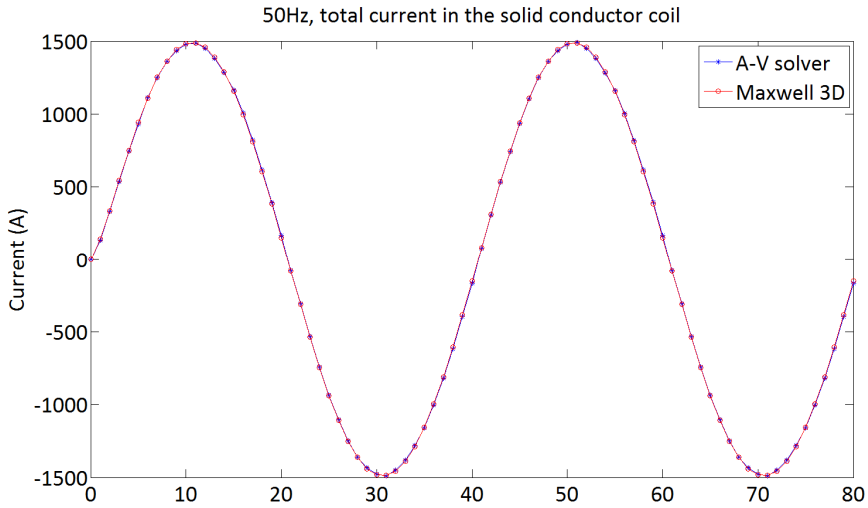

Fig. 4.29. The total current in the solid conductor for the first 80 time-steps with sinusoidal voltage excitation at a frequency of 50Hz.

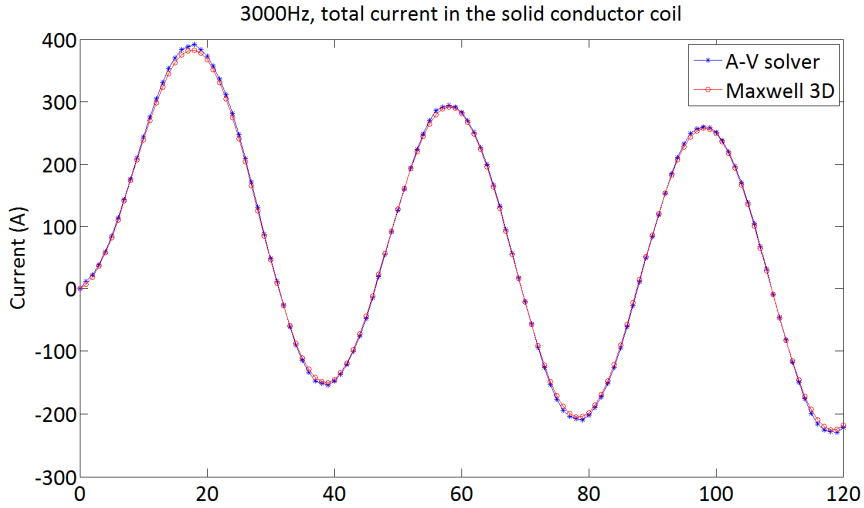

Fig. 4.30. Total current in the solid conductor for the first 120 time-steps with sinusoidal voltage excitation at a frequency of 3000Hz.

The total current in the conductor versus time when the voltage excitation frequency f is 50Hz and 3000Hz are given in Figs. 4.29 and 4.30 respectively with a uniform time-step dt=1/f/40s, where one can see that the two results are very close to each other. Besides, one can clearly see that the total current in the solid conductor decreases when the frequency rises due to skin-effect. Besides, at a frequency of 3000Hz, both the skin effect and the proximity effect can be clearly seen in the conductor as shown in Fig. 4.31.

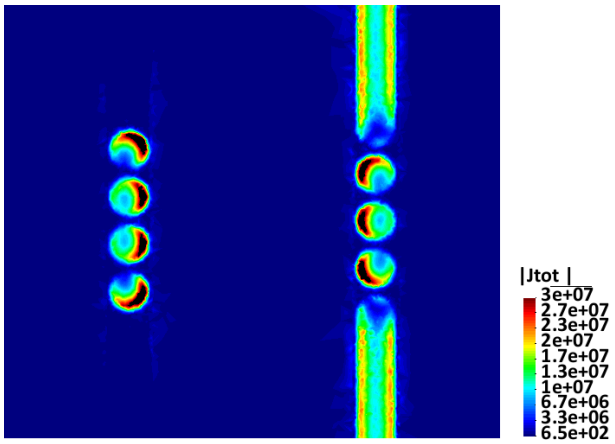

Fig. 4.31. The magnitude of the total current density in the conductor. Both the skin effect and the proximity effect can be clearly seen with the frequency of the excitation voltage to be 3000Hz.

D. A simple transformer

In the last example, a transformer with complex geometry, as shown in Fig. 4.32, is analyzed using the 3D A-V potential formulation solver. For this example, the primary winding and the secondary winding are both solid conductors with electric conductivity 1.0×10^{6}S/m. The iron core is linear with relative permeability 1000. The radius of the primary winding conductor is 10mm and the problem domain is of size 500mm × 200mm × 400mm.

Take the excitation frequency to be f=50Hz and use a uniform time-step dt=1/f/40s, the magnetic flux density vector in the iron core the total current density vector in the primary winding at 10 time-steps later are given in Fig. 4.33 and Fig. 4.34 respectively.

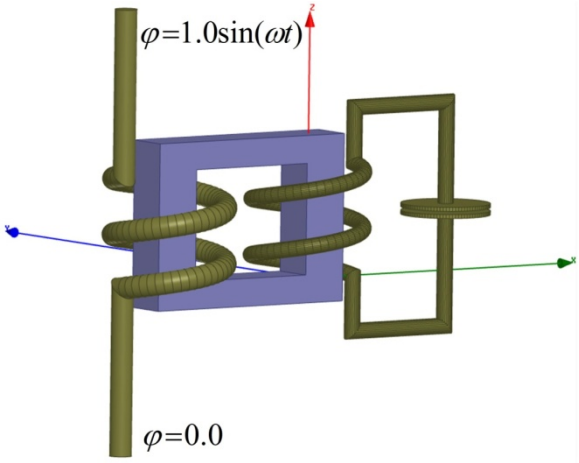

Fig. 4.32. The geometry of the studied transformer with AC voltage excitation.

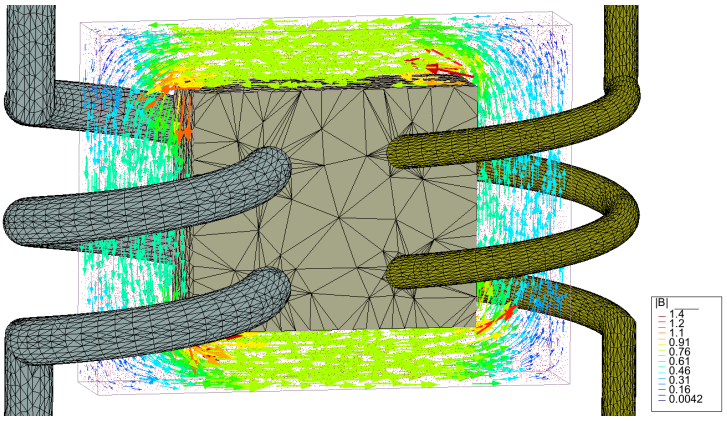

Fig. 4.33. Magnetic flux vector in the iron core with constant permeability 1000 at 10 time-steps later.

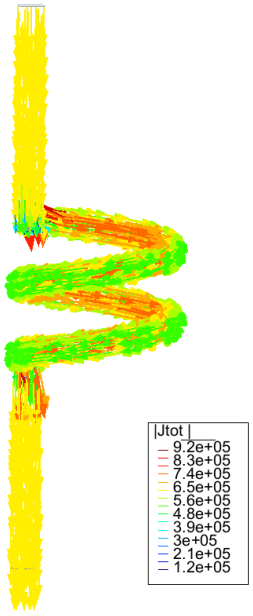

Fig. 4.34. Current density vector in the primary winding at 10 time-steps later.

The total current in the primary winding is also studied under two cases. For the first case, the secondary winding is open-circuited by adding a thin airgap to the conductor. For the second case, the secondary winding is short-circuited by replacing the airgap with conducting material. The total current in the primary conductor within 120 time-steps are calculated and plotted for the two cases. For comparison, the results with the commercial software package ANSYS Maxwell 3D are plotted together. One can see that the numerical results using A-V edge element solver are very close to that obtained by the Maxwell 3D solver, where a MSP formulation is used.

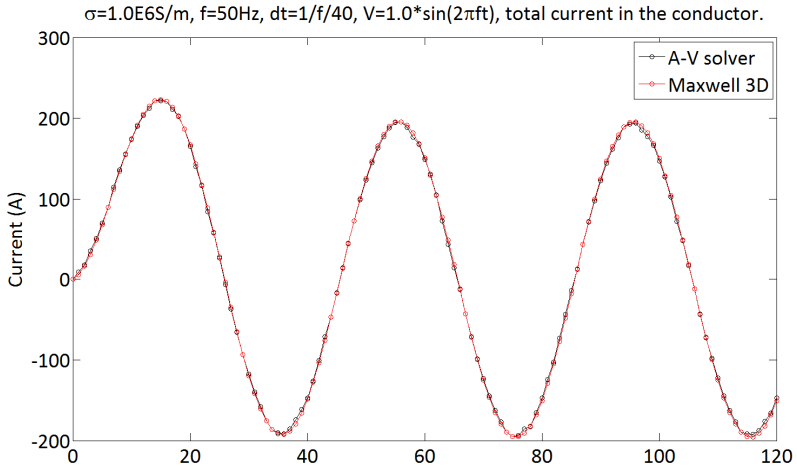

Fig. 4.35. Total current in primary conductor, when the secondary winding is open-circuited, compared with ANSYS Maxwell 3D.

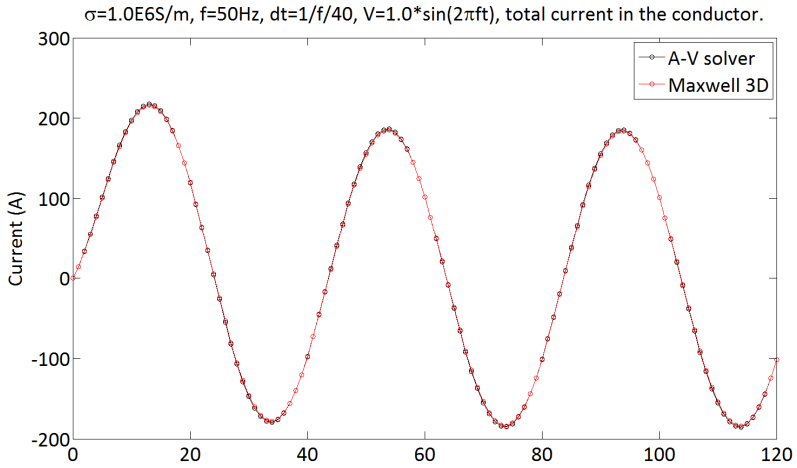

Fig. 4.36. Total current in the primary winding, when the secondary winding is short-circuited, compared with ANSYS Maxwell 3D.

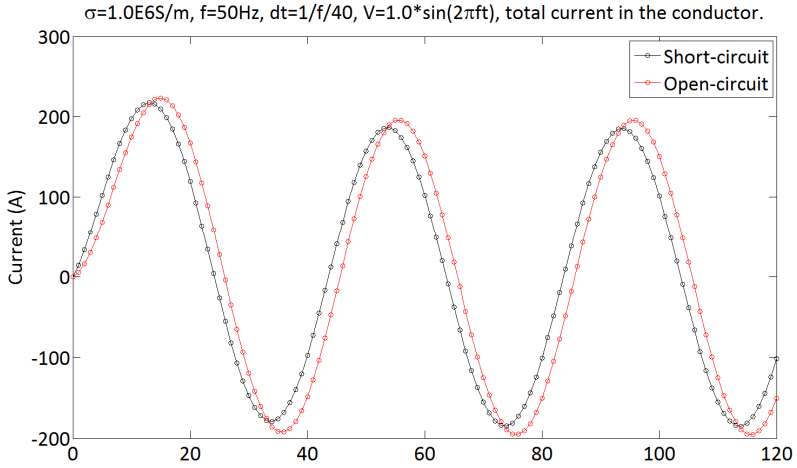

Fig. 4.37. Comparison of the observed total current when the secondary winding is short-circuited or open-circuited.

4.2.6. A Low-frequency Approximation to the Maxwell Equations Simultaneously Considering Inductive and Capacitive Effects in the Time-domain

Electric motors driven by power electronics are widely used nowadays as modern inverters can modulate their output waveforms flexibly to reduce the power loss in the electric machines. However, these inverters also create new problems to researchers because of their high speed switching operations and repetitive steep rising or falling of the pulse-width-modulation (PWM) waveforms. The presence of high-frequency signals also makes the transient simulation study of the motor much more complicated [D23-D26].

For inverter-fed electrical machines, where the machine windings are exposed to higher harmonic field components originating from the fast-switching inverter via the connecting cable, capacitive effects become relevant in addition. The common-mode voltage caused by the inverter in combination with the dielectric insulation of the machine windings gives rise to common-mode currents at higher frequencies [D27]. To simultaneously study the coupled inductive and capacitive effects, one can solve the ungauged potential formulation of the full wave Maxwell system:

$$\begin{cases} \nabla\times\left(\nu\nabla\times\vec{A}\right)+\sigma\dfrac{\partial\vec{A}}{\partial t}+\sigma\nabla\varphi+\varepsilon\dfrac{\partial}{\partial t}\left(\dfrac{\partial\vec{A}}{\partial t}+\nabla\varphi\right)=\vec{J}_s \\ \nabla\cdot\left(-\sigma(\dfrac{\partial\vec{A}}{\partial t}+\nabla\varphi)-\varepsilon\dfrac{\partial}{\partial t}\left(\dfrac{\partial\vec{A}}{\partial t}+\nabla\varphi\right)\right)=0 \end{cases} . \tag{4.78}$$

There are other full-wave Maxwell potential formulations proposed by researchers, such as the ghost-field-gauged MVP formulation [D28] and the Coulomb-gauged version [D29, D30]. Because there are more DoFs of the method proposed in [D28] and the current continuity equation is not explicitly specified (and thus maybe improper to be adopted to obtain physically correct solutions) [D29, D30], recently in [D31] a stable formulation was proposed in frequency domain to consider simultaneously the inductive and capacitive effects. In the formulation of [D31], the full wave Maxwell system is solved in the frequency domain, the term $\omega^2\varepsilon\vec{A}$ is dropped. It is reasonable when the frequency of the excitation is relatively low [D32].

In this thesis, the following MVP formulation in time-domain for analyzing fields considering simultaneously the inductive and capacitive effects reads

$$\begin{cases} \nabla\times\left(\nu\nabla\times\vec{A}\right)+\sigma\left(\frac{\partial\vec{A}}{\partial t}+\nabla\varphi\right)+\varepsilon\frac{\partial}{\partial t}\left(\nabla\varphi\right)=\vec{J}_s \\ \nabla\cdot\left(-\sigma\left(\frac{\partial\vec{A}}{\partial t}+\nabla\varphi\right)-\varepsilon\frac{\partial}{\partial t}\left(\nabla\varphi\right)\right)=0 \end{cases} \tag{4.79}$$

After spatial discretization, the semi-discrete scheme reads

$$\begin{cases} \nu K\vec{A}+\sigma M\frac{d\vec{A}}{dt}+\sigma K_{AV}\varphi+\varepsilon K_{AV}\frac{d\varphi}{dt}=rhs, \\ \sigma K_{VA}\frac{d\vec{A}}{dt}+\sigma K_{VV}\varphi+\varepsilon K_{VV}\frac{d\varphi}{dt}=0. \end{cases} \tag{4.80}$$

Finally, the fully-discrete scheme using backward Euler time-stepping is

$$\begin{bmatrix} \nu K+\frac{\sigma}{\Delta t}M & \sigma K_{AV}+\frac{\varepsilon}{\Delta t}K_{AV} \\ \frac{\sigma}{\Delta t}K_{VA} & \sigma K_{VV}+\frac{\varepsilon}{\Delta t}K_{VV} \end{bmatrix}\begin{bmatrix} A^n \\ \varphi^n \end{bmatrix}=\begin{bmatrix} \frac{\sigma}{\Delta t}M & \frac{\varepsilon}{\Delta t}K_{AV} \\ \frac{\sigma}{\Delta t}K_{VA} & \frac{\varepsilon}{\Delta t}K_{VV} \end{bmatrix}\begin{bmatrix} A^{n-1} \\ \varphi^{n-1} \end{bmatrix}+\begin{bmatrix} rhs \\ 0 \end{bmatrix}. \tag{4.81}$$

To test the developed computer program, a capacitor with alternating voltage excitation is numerically solved in the time-domain, as shown in Fig. 4.38. The radius of the upper terminal of the iron conductor is 1mm; the radius and height of the cylindrical dielectric are 5mm and 0.5mm respectively. The conductivity of the iron conductor is 10^6S/m.

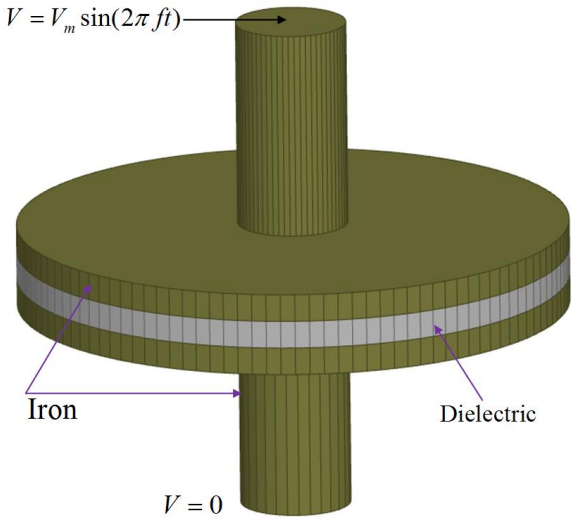

Fig. 4.38. The capacitor with alternating voltage excitation.

When the excitation peak voltage V_m=1000V, f=10^4Hz, the relative permittivity of the dielectric $\varepsilon_r = 10^4$, the total terminal current versus time-steps is given in Fig. 4.39, where a uniform time-step is used and there are 40 time-steps within a period.

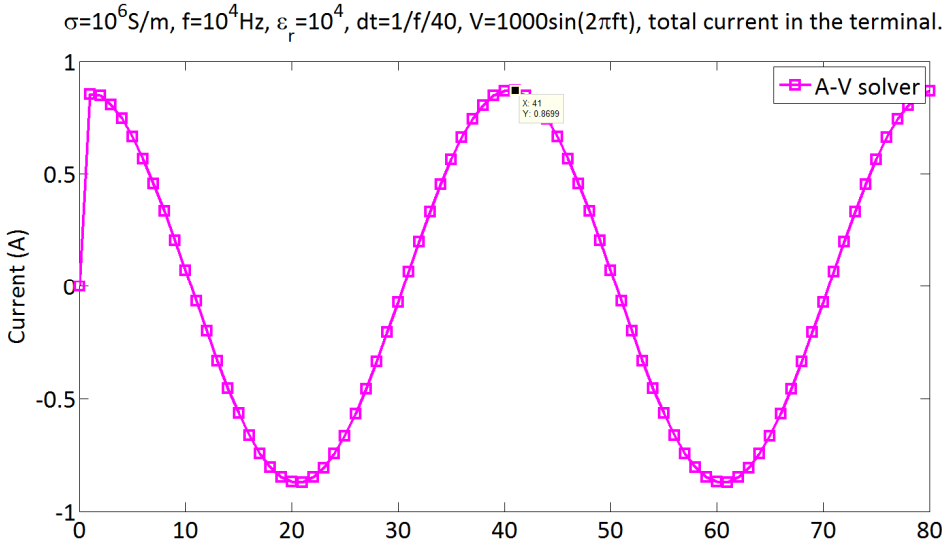

Fig. 4.39. Terminal total current flowing out of the terminal of the parallel capacitor.

For the capacitor considered, one can easily calculate the expected current as

$$\begin{aligned} I &= C\frac{dV}{dt} = \frac{\varepsilon_r \varepsilon_0 S}{d}\frac{dV}{dt} \\ &= \frac{10^4 \varepsilon_0 \pi (0.005)^2}{0.0005} \cdot 1000 \cdot 2\pi \cdot 10^4 \cos(2\pi \cdot 10^4 t), \\ &\approx 0.87 \cos(2\pi \cdot 10^4 t) \end{aligned} \tag{4.82}$$

which can be observed from Fig. 4.39, where the peak current is 0.8699A and the current is of cosine wave form. Other parameters are also chosen to test the code, it is further observed that the total current varies linearly with both the frequency of the excitation and the relative permittivity of the dielectric. So the potential formulation (4.79)-(4.81) is validated.

4.2.7. Coupling EM Field with External Circuit

For all the numerical examples given above, the source excitations such as the current density or the ESP are all explicitly specified for the conductors. Actually, as long as all currents inside the stranded conductors and all solid conductor voltage

drops are known, no extra unknowns have to be added to the system of equations. In practice, EM devices are usually connected through their terminals to external circuits [A32, B2, B3, D15, D33-D35]. As a result, the current or the ESP can't be directly applied as source terms. The analysis of the EM fields driven by circuits requires the coupling of FEM with electric circuit analysis to make it possible for the designers to perform system level simulation.

Based on the observed skin effect in the windings, two conductor models are mainly used:

(1) Thin (filamentary or stranded) conductors: windings are composed of many turns of thin wire, thus specifying the distribution of the current density vector $\vec{J}$. Stator windings in most electric machines fall under this category. For such conductors, induced eddy currents can be, and typically are neglected. For the case of thin conductors, the stranded conductors are included in the non-conducting region. And the transient analysis of coupled field-circuit equations can be viewed as a sequence of magnetostatic analysis coupled to the circuit equations via the specification of the current density vector $\vec{J}$.

For a 2D conducting region composed of N filamentary turns distributed uniformly over an area S and carrying uniform current i per turn, so the current density across the coil section is uniform and can be expressed as

$$J = Ni / S. \tag{4.83}$$

For 3D stranded conductors, the current density vector can be expressed as

$$\vec{J} = \vec{t}_0 \frac{N}{S} i. \tag{4.84}$$

where $\vec{t}_0$ is the unit vector along the coil direction or the current flow direction. For 3D field analysis, to get a solenoidal and uniformly distributed current density in an arbitrarily-shaped coil is not an easy task [D14, D36, D37]. In practice, the usage of inhomogeneous current density distribution obtained by solving the Laplace equation within conductor windings is also feasible [D38, D39]. As shown in [D39], the values calculated by using inhomogeneous current density distribution are nearly equal to those by the conventional method. Furthermore, the results by using inhomogeneous current density distribution are also in good agreement with the experiments.

(2) Thick (massive or solid) conductors: windings are typically made of solid conducting bars such as the cage rotor bars of induction machines. In solid conductors, induced eddy currents must be considered, which results in a nonuniform distribution of current density vector $\vec{J}$. For a massive conductor with conductivity σ, the current density vector is given by

$$\vec{J} = -\sigma(\frac{\partial \vec{A}}{\partial t} + \nabla\varphi). \tag{4.85}$$

In 2-D, $\nabla\varphi$ is constant over the conductor length and is directly related to the voltage drop along the conductor. The total current i in a solid conductor can be found by integrating the current density in (4.79) over the cross-sectional surface of the conductor, i.e.

$$i = -\iint_S \sigma(\frac{\partial \vec{A}}{\partial t} + \nabla\varphi) \cdot d\vec{S}. \tag{4.86}$$

Equations for circuits composed of resistors, inductors, capacitors, and voltage and current sources can be generated automatically using loop or nodal analysis [A11], or using graph-theoretic techniques [D40, D41]. If the machine contains only stranded conductors, loop analysis is generally applied where the unknowns in the circuit part are loop currents; and if it contains only solid conductors, then nodal analysis is preferred where the unknowns in the circuit part are nodal potentials. For devices that contain both solid and stranded conductors, the circuit equations are generally established using the technique of modified nodal analysis, which avoids current and voltage transformations.

For stranded conductors, the induced back-EMF are mostly used as the bridge to link the magnetic field domain with the electric circuit domain [D33, D42-D44]. For solid conductors connected with electric circuits, as has been shown in [D45], the voltage of a conductor with skin effect can be prescribed by specifying on the electrodes in addition to setting the tangential component of to zero there. So it is convenient to set the terminal voltage as the bridge for field-circuit coupling.

The field-circuit coupling problem is illustrated in Fig. 4.40, where the finite element part is connected with the external circuit with inductance L_e and resistance R_e. In this thesis, six kinds of excitations, which are most frequently encountered, are considered, namely,

(A) Solid conductor with voltage source;

(B) Solid conductor with total current source;

(C) Solid conductor with external circuit source;

(A') Stranded conductor with current source;

(B') Stranded conductor with known voltage source;

(C') Stranded conductor with external circuit source.

For (A) and (A'), there is no need for field-circuit coupling. For (B), one can introduce one DoF *Vs*, the terminal voltage difference, for each conductor. For (C), one can introduce two DoFs *Vs* and *I* for each conductor. For (B') and (C'), one needs to introduce the current as one extra DoF.

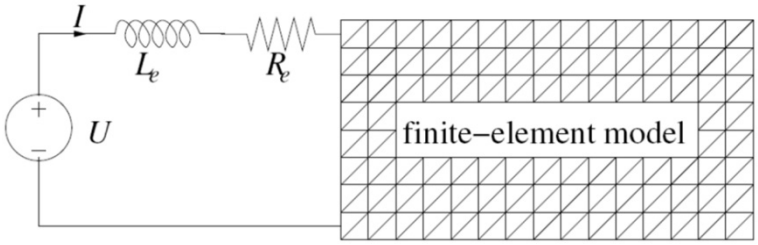

Fig. 4.40. Illustration of the field-circuit coupling problems.

For case (B) where solid conductors with total current excitation, one can introduce one DoF *Vs* for each conductor, and the fully-discrete finite element scheme reads

$$\begin{bmatrix} \nu K + \dfrac{\sigma M}{\Delta t} & \sigma K_{AV} + \dfrac{\varepsilon K_{AV}}{\Delta t} & 0 \\ \dfrac{\sigma}{\Delta t} K_{VA} & \sigma K_{VV} + \dfrac{\varepsilon K_{VV}}{\Delta t} & 0 \\ \cdots & \cdots & \cdots \end{bmatrix} \begin{bmatrix} A^n \\ \varphi^n \\ V_s^n \end{bmatrix} = \begin{bmatrix} \dfrac{\sigma M}{\Delta t} & \dfrac{\varepsilon K_{AV}}{\Delta t} & 0 \\ \dfrac{\sigma K_{VA}}{\Delta t} & \dfrac{\varepsilon K_{VV}}{\Delta t} & 0 \\ \cdots & 0 & 0 \end{bmatrix} \begin{bmatrix} A^{n-1} \\ \varphi^{n-1} \\ V_s^{n-1} \end{bmatrix} + \begin{bmatrix} 0 \\ 0 \\ I \end{bmatrix}, \quad (4.87)$$

where the last equation is discretized from (4.86). Take Fig. 4.41 for example, the upper coil terminal is supposed to be with equal-potential V_s^n and the lower terminal is supposed to be grounded. In fact, it is only the voltage difference that matters. For the boundary condition of each node on the upper terminal, the global coefficient matrix of (4.87) should be modified as

$$\begin{bmatrix} 1 & 0 & 0 & 0 & -1 \\ 0 & 1 & 0 & 0 & -1 \\ 0 & 0 & 1 & 0 & -1 \\ 0 & 0 & 0 & 1 & -1 \\ \cdots & & & & \end{bmatrix} \begin{bmatrix} \varphi^n \\ V_s^n \end{bmatrix} = \begin{bmatrix} 0 \\ 0 \end{bmatrix}. \tag{4.88}$$

For the lower coil terminal, the Dirichlet BC is treated in the traditional way.

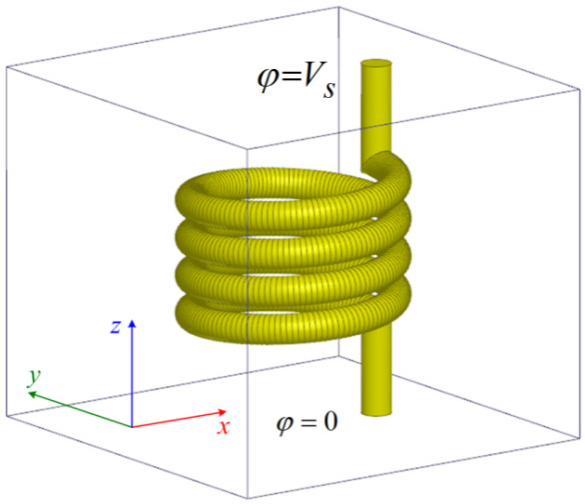

Fig. 4.41. Helical coil example for illustration of the field-circuit coupling.

As an example, the helical coil shown above is excited with total current $I = 100\sin(2\pi \cdot 50t)$, as shown in Fig. 4.42. The computed upper terminal voltage is given in Fig. 4.43, which is the same as using the commercial software Maxwell 3D.

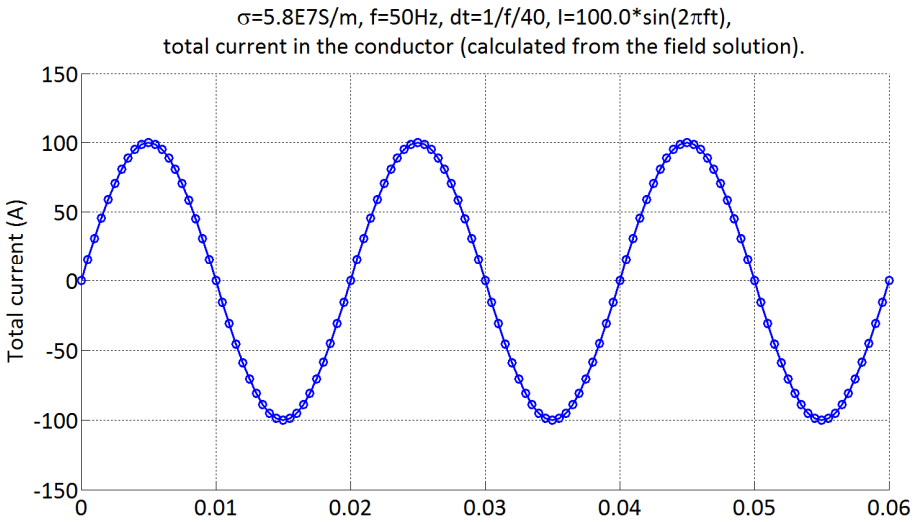

Fig. 4.42. Total current excitation to a solid conductor, the current is obtained by post-processing the field solution.

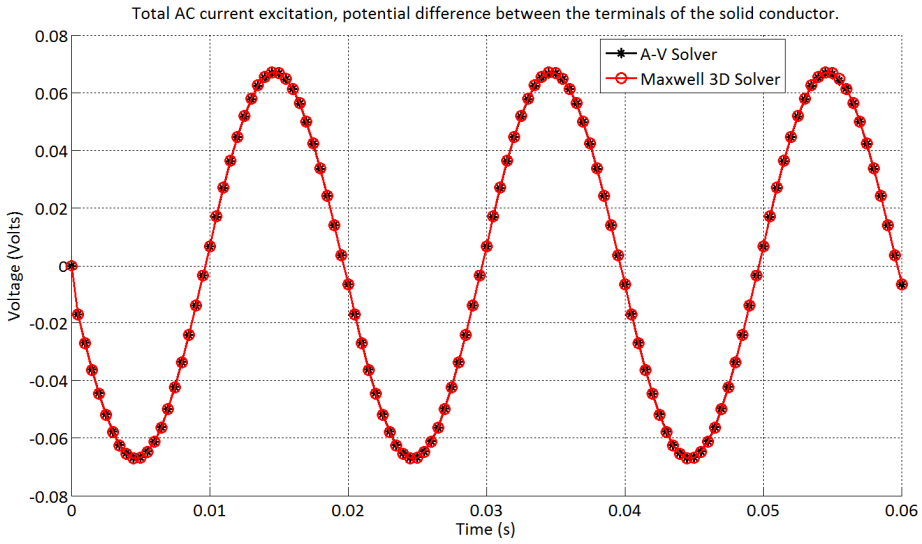

Fig. 4.43. Total current excitation to a solid conductor, the upper terminal voltage of the conductor which is extracted from field-circuit coupled model.

For case (C) where solid conductors with external circuit excitation, one can introduce two DoFs *Vs* and *I* for each conductor, and the fully-discrete finite element scheme reads

$$\begin{bmatrix} \nu K + \dfrac{\sigma M}{\Delta t} & \sigma K_{AV} + \dfrac{\varepsilon K_{AV}}{\Delta t} & 0 & 0 \\ \dfrac{\sigma}{\Delta t} K_{VA} & \sigma K_{VV} + \dfrac{\varepsilon K_{VV}}{\Delta t} & 0 & 0 \\ \cdots & \cdots & 1 & 0 \\ 0 & 0 & R_e + \dfrac{L_e}{\Delta t} & 1 \end{bmatrix} \begin{bmatrix} A^n \\ \varphi^n \\ I^n \\ V_s^n \end{bmatrix}$$

$$= \begin{bmatrix} \dfrac{\sigma M}{\Delta t} & \dfrac{\varepsilon K_{AV}}{\Delta t} & 0 & 0 \\ \dfrac{\sigma K_{VA}}{\Delta t} & \dfrac{\varepsilon K_{VV}}{\Delta t} & 0 & 0 \\ \cdots & 0 & 0 & 0 \\ 0 & 0 & \dfrac{L_e}{\Delta t} & 0 \end{bmatrix} \begin{bmatrix} A^{n-1} \\ \varphi^{n-1} \\ I^{n-1} \\ V_s^{n-1} \end{bmatrix} + \begin{bmatrix} 0 \\ 0 \\ 0 \\ U \end{bmatrix}, \tag{4.89}$$

where the last equation is discretized from the voltage balance equation

$$U = Vs + R_e I + L_e \frac{dI}{dt}. \tag{4.90}$$

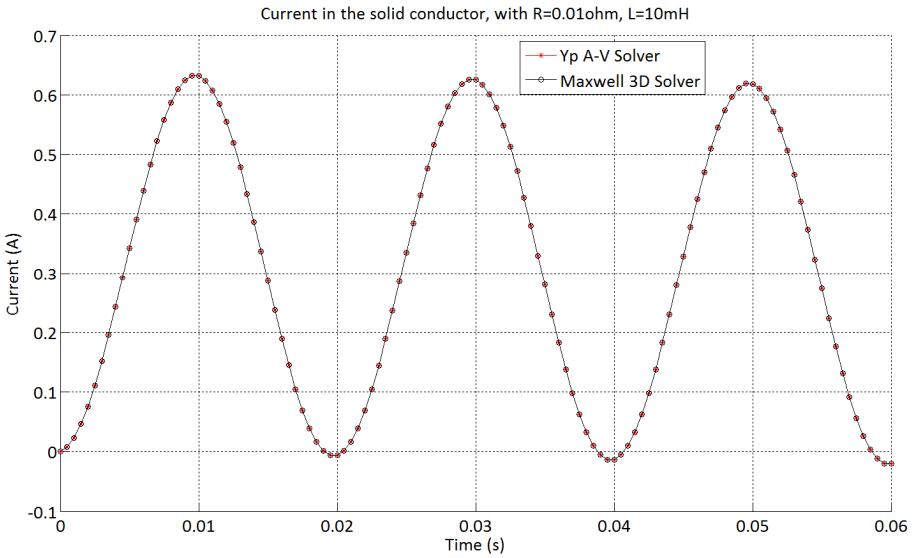

Fig. 4.44. Total current in the solid conductor as shown in Fig. 4.41 when it is connected to an external circuit with parameters R_e=0.01ohm, L_e=10mH, and $U = \sin(2\pi \cdot 50t)$.

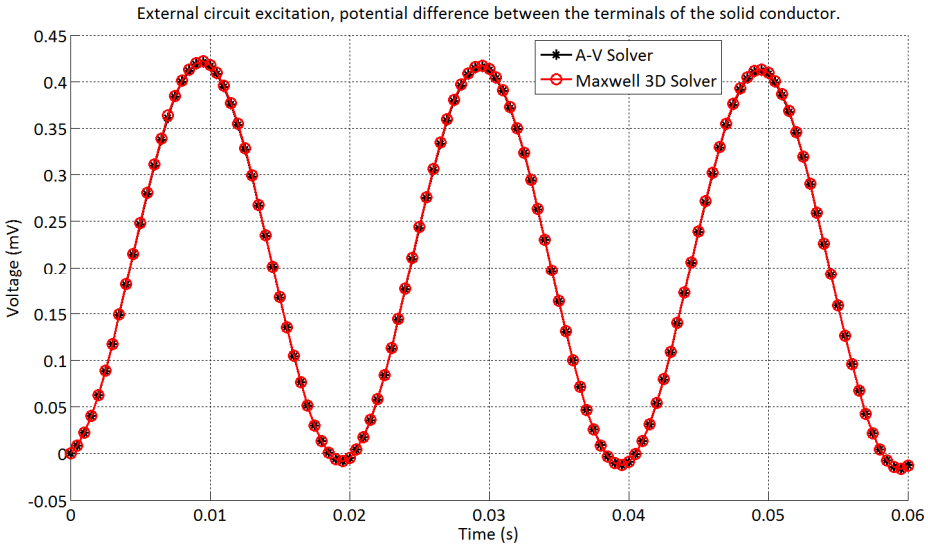

Fig. 4.45. Coil terminal potential of the solid conductor as shown in Fig. 4.41.

For case (B') and (C') where stranded conductors with voltage or external circuit excitation, one needs to introduce the current as one extra DoF, and the fully-discrete finite element scheme reads

$$\begin{bmatrix} \nu K + \dfrac{\sigma M}{\Delta t} & \sigma K_{AV} + \dfrac{\varepsilon K_{AV}}{\Delta t} & \cdots \\ \dfrac{\sigma}{\Delta t} K_{VA} & \sigma K_{VV} + \dfrac{\varepsilon K_{VV}}{\Delta t} & \cdots \\ \cdots & 0 & \cdots \end{bmatrix} \begin{bmatrix} A^n \\ \varphi^n \\ I^n \end{bmatrix} = \begin{bmatrix} \dfrac{\sigma M}{\Delta t} & \dfrac{\varepsilon K_{AV}}{\Delta t} & 0 \\ \dfrac{\sigma K_{VA}}{\Delta t} & \dfrac{\varepsilon K_{VV}}{\Delta t} & 0 \\ \cdots & 0 & 0 \end{bmatrix} \begin{bmatrix} A^{n-1} \\ \varphi^{n-1} \\ I^{n-1} \end{bmatrix} + \begin{bmatrix} 0 \\ 0 \\ U \end{bmatrix}. \quad (4.91)$$

where the last equation is discretized from the voltage balance equation for stranded conductors with resistance R_0

$$U = \frac{d\psi}{dt} + (R_0 + R_e)I + L_e \frac{dI}{dt}, \quad (4.92)$$

and the flux linkage ψ is given by

$$\psi = \frac{N}{S} \iiint_{V_c} \vec{A} \cdot \vec{t}_0 \mathrm{d}V . \quad (4.93)$$

The numerical example is similar to that in [D46], where the induced back-EMF in a stranded coil with voltage excitation is solved using the formulation (4.91). The problem setting is shown in Fig. 4.46, where the cylindrical plate above the coil can be made of air, aluminum or iron. The thickness of the plate is 1cm and its radius is 8cm. The inner and outer radius of the coil are 5cm and 6cm respectively, the height of the coil is 1cm. The stranded winding resistance is taken to be 1Ohm, and the number of turns is 100. The applied voltage excitation is $U = \sin(2\pi \cdot 50t)$.

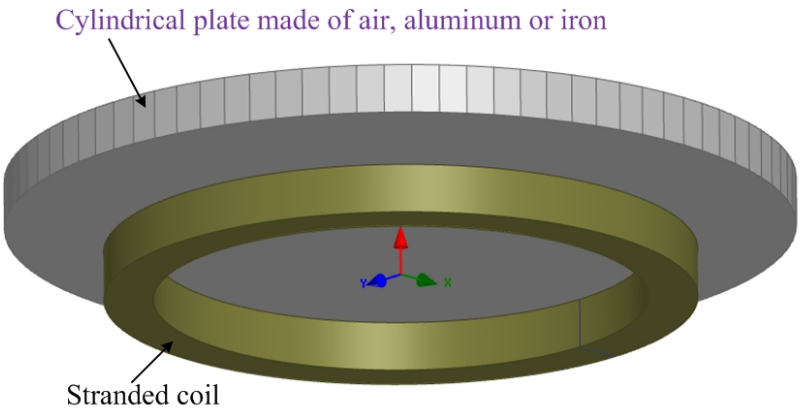

Fig. 4.46. The numerical example for testing the field-circuit coupling with stranded conductor.

The plate above the coil can be air, aluminum or iron, so there are three cases to be tested:

(1) Air plate, $\sigma = 0, \mu = \mu_0$;

(2) Aluminum plate, $\sigma = 3.8 \times 10^7 \text{S/m}, \mu = \mu_0$;

(3) Iron plate, $\sigma = 3.8 \times 10^5 \text{S/m}, \mu = 1000\mu_0$.

The numerical results of the induced back EMF in the stranded coil are given in Figs. 4.47-4.49 respectively, where the numerical results obtained using ANSYS Maxwell 3D are also given for comparison. It can be noticed that the results obtained using formulation (4.91) are very close to that of the Maxwell 3D.

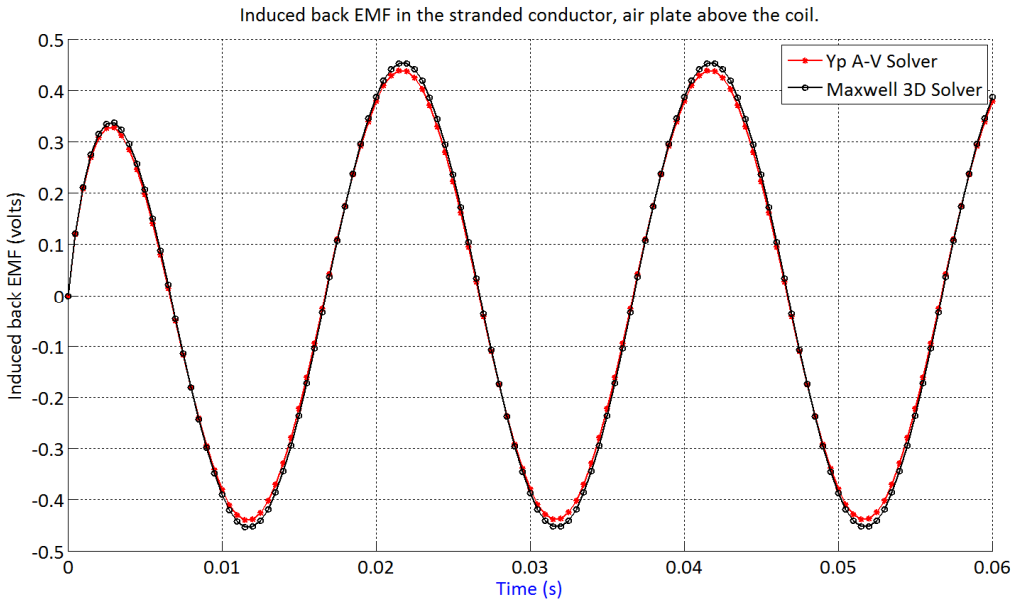

Fig. 4.47. Test (1), induced back EMF in the stranded coil, air plate above the coil.

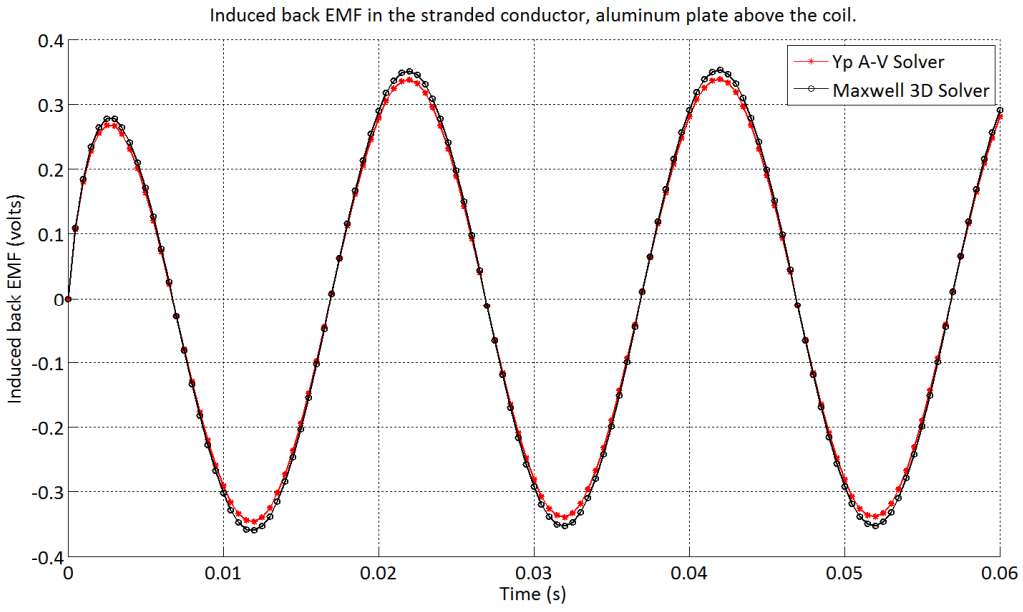

Fig. 4.48. Test (2), induced back EMF in the stranded coil, aluminum plate above the coil.

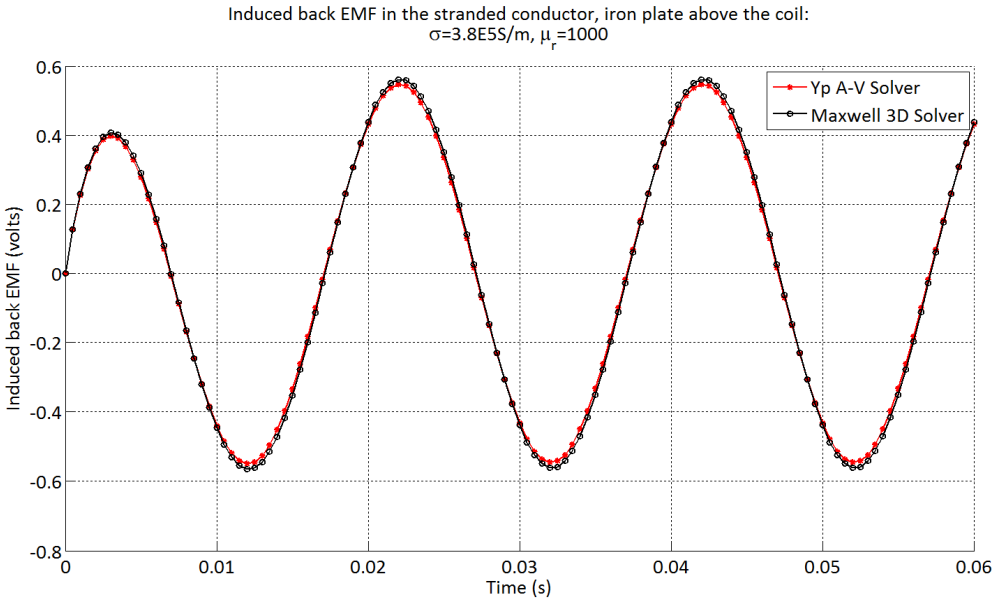

Fig. 4.49. Test (3), induced back EMF in the stranded coil, iron plate above the coil.

4.3. Summary

In this chapter, the 2D FEM for magnetostatic and transient field computation is fully described. Second-order nodal elements are used to discretize the MVP *A*. The nonlinear material is handled using the Newton-Raphson iteration. The rotational movement of the rotor is handled using the slave-master technique, where a matching boundary condition is applied at the sliding surface between the rotor and stator. For transient eddy-current fields, a time-stepping process is needed. The backward Euler time-discretization scheme is adopted in this thesis since it is absolutely stable.

For the solution of the magnetic vector potential in 3D space, since the component-wise solution method by nodal element present large error at air-iron interface, nowadays the edge element is widely used to discretize vector variables. All the three components of the MVP are viewed as a whole and the tangential component along the mesh edges are set to be the unknowns to solve. The detailed finite element formulation of 3D edge element for static and transient EM fields are presented. Extensive numerical examples are given to validate the developed code. A

novel solver for analyzing problems with both conductive and capacitive effects are developed and validated. Formulations for field-circuit coupled problems are also given and verified by numerical experiments.

4.4. References-Part D

[D1] S. L. Ho, and W. N. Fu, "Review and further application of finite element methods in induction motors," *Electric Machines and Power Systems*, Taylor & Francis, vol.26, no.2, pp. 111-125, 1998.

[D2] S. L. Ho, H. L. Li, W. N. Fu, and H. C. Wong, "A novel approach to circuit-field-torque coupled time stepping finite element modeling of electric machines," *IEEE Trans. Magn.*, vol.36, no.4, pp. 1886-1889, Jul. 2000.

[D3] W. N. Fu, S. L. Ho, H. L. Li, and H. C. Wong, "A versatile finite element model of electric machines," *Electric Power Components and Systems*, Taylor & Francis, vol. 31, no. 10, pp. 941-966, Oct. 2003.

[D4] F. Hecht, O. Pironneau, J. Morice, FreeFem++, http://www.freefem.org/.

[D5] J. M. Jin, *The Finite Element Method in Electromagnetics*. New York: John Wiley & Sons, 1993.

[D6] T. A. Davis, "Algorithm 832: UMFPACK V4.3-an unsymmetric-pattern multifrontal method," *ACM Transactions On Mathematical Software*, vol. 30, no. 2. pp. 196-199, Jun. 2004.

[D7] O. Schenk, Pardiso [Online]. Available: http://www.computational.unibas.ch /computer_science/people/schenk/software/.

[D8] R. Barrett, M. Berry, T. Chan, J. Demmel, J. Donato, J. Dongarra, V. Eijkhout, R. Pozo, C. Romine, and H. van der Vorst, Templates for the Solution of Linear Systems: Building Blocks for Iterative Methods. SIAM, Philadelphia, 1994.

[D9] TEAM Optimization Benchmark 25 [Online]. Available: http://www.compumag. org/jsite/team.html.

[D10] H. D. Gersem, "Spectral-element method for high-speed rotating cylinders," *COMPEL: Int. J. Computat. Math. Elect. Electron. Eng.*, vol. 28, no. 3, pp. 730-740, 2009.

[D11] TEAM workshop problem 30 A-three-phase induction motor problem [Online]. Available: http://www.infolytica.com/en/applications/ex0035/.

[D12] P. Dular, F. Henrotte, A. Genon, and W. Legros, "A generalized source magnetic field calculation method for inductors of any shape," *IEEE Trans. Magn.*, vol. 33, no. 2, pp. 1398-1401, Mar. 1997.

[D13] Y. L. Menach, S. Clénet, and F. Piriou, "Numerical model to discretize source fields in the 3D finite element method," *IEEE Trans. Magn.*, vol. 36, no. 4, pp. 676-679, Jul. 2000.

[D14] Z. Badics, and Z. J. Cendes, "Source field modeling by mesh incidence matrices," *IEEE Trans. Magn.*, vol. 43, no. 4, pp. 1241-1244, Apr. 2007.

[D15] S. Schops, H. D. Gersem, and T. Weiland, "Winding functions in transient magneto-quasistatic field-circuit coupled simulations," *COMPEL: Int. J. Computat. Math. Elect. Electron. Eng.*, vol. 32, no. 6, pp. 2063-2083, 2013.

[D16] O. Bíró, and Kurt Preis, "Generating source field functions with limited support for edge finite-element eddy current analysis," *IEEE Trans. Magn.*, vol. 43, no. 4, pp. 1165-1168, Apr. 2007.

[D17] S. R. H. Hoole, Finite Elements, Electromagnetics and Design, Elsevier Science, 1st edition, Jun. 1995.

[D18] Z. Ren, "Influence of R.H.S. on the convergence behaviour of the curl-curl equation," *IEEE Trans. Magn.*, vol. 32, no. 3, pp. 655-658, 1996.

[D19] T. Nakata, N. Takahashi, and H. Morishige. "Summary of results for problem 20 (3-D static force problem)," *COMPEL*, vol. 14, No. 2/3, pp. 57-75, 1995.

[D20] Z. Ren, "Comparison of different force calculation methods in 3D finite element modelling," *IEEE Trans. Magn.*, vol. 30, no. 5, pp. 3471-3474, Sep. 1994.

[D21] W. Zheng, Z. Chen, and L. Wang, "An adaptive finite element method for the H-ψ formulation of time-dependent eddy current problems," *Numer. Math.*, vol. 103, pp. 667-689, 2006.

[D22] K. Fujiwara, and T. Nakata, "Results for benchmark problem 7," *COMPEL*, vol. 11, pp. 335-344, 1990.

[D23] E. Persson, "Transient effects in application of PWM inverters to induction motors," *IEEE Trans. Ind. Appl.*, vol. 28, no. 5, pp. 1095-1101, Sep./Oct. 1992.

[D24] H. A. Toliyat, G. Suresh, and A. Abur, "Simulation of voltage stress on the inverter fed induction motor winding supplied through feeder cable," IEEE Industry Applications Society Annual Meeting, New Orleans, Louisiana, October 5-9, pp. 143-150, 1997.

[D25] J. M. Erdman, R. J. Kerkman, D. W. Schlegel, and G. L. Skibinski, "Effect of PWM inverters on AC motor bearing currents and shaft voltage," *IEEE Trans. Ind. Appl.*, vol. 32, no. 2, pp. 250-259, Mar./Apr. 1996.

[D26] J. Adabi, F. Zare, A. Ghosh, and R. D. Lorenz, "Calculations of capacitive couplings in induction generators to analyse shaft voltage," *IET Power Electron.*, vol. 3, no. 3, pp. 379-390, 2010.

[D27] P. Mäki-Ontto, and J. Luomi, "Induction motor model for the analysis of capacitive and induced shaft voltages," *Proc. IEEE Int. Conf. Electr. Mach. Drives*, May 2005, pp. 1653-1660.

[D28] W. Schoenmaker, and P. Meuris, "Electromagnetic interconnects and passives modeling: software implementation issues," *IEEE Trans. Comput. Aided Des.*, vol. 21, no. 5, pp. 534-543, May 2002.

[D29] R. Hiptmair, F. Kramer, and J. Ostrowski, "A robust Maxwell formulation for all frequencies," *IEEE Trans. Magn.*, vol. 44, no. 6, pp. 682-685, Jun. 2008.

[D30] J. Ostrowski, R. Hiptmair, F. Krämer, J. Smajic, and T. Steinmetz, "Transient full Maxwell computation of slow processes," *Scientific Computing in Electrical Engineering SCEE 2010*, pp. 87-95, 2012.

[D31] S. Koch, H. Schneider, and T. Weiland, "A low-frequency approximation to the Maxwell equations simultaneously considering inductive and capacitive phenomena," *IEEE Trans. Magn.*, vol. 48, no. 2, pp. 511-514, Feb. 2012.

[D32] B. Doliwa, H. D. Gersem, T. Weiland, and T. Boonen, "Optimised electro-magnetic 3d field solver for frequencies below the first resonance," *IET Science, Meas. Technol.*, vol. 1, no. 1, pp. 53-56, Jan. 2007.

[D33] C. Golovanov, Y. Marechal, and G. Meunier, "3D edge element based formulation coupled to electric circuits," *IEEE Trans. Magn.*, vol. 34, no. 5, pp. 3162-3165, Sep. 1998.

[D34] O. Bíró, K. Preis, G. Buchgraber, and I. Ticar, "Voltage-driven coils in finite-element formulations using a current vector and a magnetic scalar potential," *IEEE Trans. Magn.*, vol. 40, no. 2, pp. 1286-1289, Mar. 2004.

[D35] G. Meunier, Y. L. Floch, and C. Guérin, "A nonlinear circuit coupled t-t_0-ϕ formulation for solid conductors," *IEEE Trans. Magn.*, vol. 39, no. 3, pp. 1729-1732, May 2003.

[D36] C. Im, H. Kim, and H. Jung, "Novel technique for current density distribution analysis of solidly modeled coil," *IEEE Trans. Magn.*, vol. 38, no. 2, , pp. 505-508, Mar. 2002.

[D37] D. N. Dyck, and J. P. Webb, "Solenoidal current flows for filamentary conductors," *IEEE Trans. Magn.*, vol. 40, no. 2, pp. 810-813, Mar. 2004,

[D38] J. A. A. Santos, J. P. A. Bastos, and N. Sadowski, "Using Laplace's equation for defining magnetizing current densities for 3D analysis with edge elements," *IEEE Trans. Magn.*, vol. 35, no. 3, pp. 1179-1182, May 1999,

[D39] Keiji Iwata, and Housei Hirano, "Magnetic field analysis by edge elements of magnetic components considering inhomogeneous current distribution within conductor windings," *IEEE Trans. Magn.*, vol. 42, no. 5, pp. 1549-1554, May 2006.

[D40] H. D. Gersem, R. Mertens, U. Pahner, R. Belmans, and K. Hameyer, "A topological method used for field-circuit coupling," *IEEE Trans. Magn.*, vol. 34, no. 5, pp. 3190-3193, Sep. 1998.

[D41] H. D. Gersem, K. Hameyer, and T. Weiland, "Field-circuit coupled models in electromagnetic simulation," *Journal of Computational and Applied Mathematics*, vol. 168, pp.125-133, 2004.

[D42] T. Nakata, N. Takahashi, K. Fujiwara, and A. Ahagon, "3-D finite element method for analyzing magnetic fields in machines excited from voltage sources," *IEEE Trans. Magn.*, vol. 24, no. 6, pp. 2582-2584, Nov. 1988.

[D43] T. Dreher, and G. Meunier, "3D modeling of electromagnets fed by alternating voltage sources", *IEEE Trans. Magn.*, vo1.29, no.2, pp.1341-1344, Mar. 1993.

[D44] Koji Tani, Takashi Yamada, and Yoshihiro Kawase, "Dynamic analysis of linear oscillatory actuator driven by voltage source using FEM with edge elements

and 3-D mesh coupling method ," *IEEE Trans. Magn*, vol. 36, no. 4, pp. 1830-1836, Jul 2000.

[D45] O. Bíró, P. Böhm, K. Preis, and G. Wachutka, "Edge finite element analysis of transient skin effect problems," *IEEE Trans. Magn.*, vol. 36, no. 4, pp. 835-839, Jul. 2000.

[D46] P. J. Leonard, and D. Rodger, "Voltage forced coils for 3D finite-element electromagnetic models," *IEEE Trans. Magn.*, vol. 24, no. 6, pp.2579-2581, Nov. 1988.

CHAPTER 5

ADAPTIVE FINITE ELEMENT METHODS

5.1. Introduction to AFEMs And Error Estimates

Adaptive finite element methods (AFEMs) are indispensable in the numerical computation of engineering magnetic field nowadays [E1-E8]. Indeed, AFEMs can obtain solutions with the desired accuracy and lower degrees of freedom (DoFs) and hence saving computing time. Generally, the AFEMs can be classified into three categories, including the *h*-refinement [E9-E17], *p*-refinement [E18-E20] and *r*-refinement [E21-E25] methods. These methods can also be used in combination with each other, such as the *h*-*r*-refinement [E21], *h*-*p*-method [E26, E27] and so on.

In the *h*-refinement AFEM, the same type of finite elements (FEs) are being used continuously but their sizes are changed. In the *p*-refinement method, the order of the polynomial basis functions is increased adaptively but the mesh element size is kept to be unchanged. For the *r*-refinement, the number of mesh nodes and elements are kept constant, but the nodes are repositioned to areas where needed to enhance the resolution.

Of all the AFEMs, the local *h*-refinement method is usually simpler and hence widely used. As is well known, a suitable computational mesh with well-distributed mesh nodes and elements with good quality factor is a key factor for getting accurate finite element solution. One key isse is how to determine the regions where needed to insert the nodes in order to balance or evenly distribute the numerical error of the FE solution, which can be done by a local *a* posterior error estimate procedure from the computed numerical solution. For all other AFEMs, the *a* posterior error estimate is also the most important technical issue to be addressed. It is the error estimator that mostly determines the efficiency of the AFEMs.

For the *h*-type AFEM, the *a* posteriori error estimation is to obtain an estimated numerical error from the existing FE solution for each element, which plays an important role in guiding the mesh refinement procedures. The ideal error estimator should be asymptotically accurate and effective in use, computationally simple and

robust with regard to a wide range of applications. Hitherto, fellow researchers have proposed many error estimators, such as the norm of the gradient of the solution [E1], the jump in the normal derivative at element edges [E1], the error of the constitutive relations [E2-E6], the energy-based method [E7] and recently the magnetic flux line method [E8]. Other error estimators in literature mainly include the recovery-type [E9-E15] and residual-type [E16, E17].

The idea of the recovery-type error estimators is to recover or reconstruct the potential, the gradient or the flux value to a higher accuracy than the ones obtained directly from the FE solution. This recovery process can be obtained only by postprocessing the FE solution and the improved solutions are then used as the exact solutions. The most well known recovery type error estimator is the ZZ error estimator proposed by Zienkiewicz and Zhu [E9], which is based on flux recovery by solving local least square problems over discrete patches. The method is relatively easy to incorporate into a finite element code and is independent of the problem formulation. In practice, the reconstruction process can be replaced by an averaging technique using the superconvergent points to obtain the improved nodal gradient values. This recovery process is simple if linear FEM is used [E13], however it becomes more complicated for high order finite elements [E13, E15] and for interface problems [E10, E14].

The residual-type error estimator can be further classified into the explicit type and implicit type [E28]. The explicit error estimator involves a direct computation of the elemental residuals and jumps at the element boundaries for finding the error in the energy norm. In the implicit error estimate, one needs to solve a local Dirichlet or Neumann problem on one element (element residual method) or a patch of elements (subdomain residual method), and it is more time consuming and more expensive than the recovery-type error estimators. Furthermore, to get accurate error estimate, the boundary conditions for the local problem must be carefully prescribed [E16, E17].

In the following sections, first a novel convenient error estimator is proposed for magnetostatic field computation using second-order nodal FEs. Then an adaptive DoFs FEM is proposed to accelerate the nonlinear iteration process in the solution of magnetostatic problems. At last, the proposed adaptive DoFs FEM is also used to

transient eddy-current field analysis, where the DoFs can be dynamically changing within each time-step.

5.2. AFEM for Magnetostatic Problems

To ensure the accuracy of the FE solution for magnetostatic problems, adaptive mesh refinements are usually needed to get a series of more and more accurate numerical solutions converging to the exact solution. This can be done in a standard SOLVE-ESTIMATE-MARK-REFINE way [E29]. In practice, the linear FEM is usually not accurate enough to resolve the magnetic field and second order FEM is necessary nowadays. Besides, the presence of material discontinuities is very common in engineering magnetic field problems. Considering the afore-mentioned difficulties encountered for the *a* posteriori error estimate process for high order FEM as well as for problems with material interface, a novel estimator for the second-order elements is proposed in this section for second-order nodal FEs. Several numerical examples are given to show the effectiveness of the proposed error estimator.

5.2.1. A Proposed Error Estimator

For numerical computation of engineering magnetic field problems, the linear FEM with piecewise linear basis functions for solving the magnetic potential A is usually inadequate, as only piecewisely constant magnetic flux density on each element can be obtained. In most applications, it is necessary to use second-order or quadratic FEs. For each triangular element $e = \Delta ijk$ in the mesh T of the problem domain, denote A^e as the quadratic FE solution and A_i, A_j, A_k as the nodal values of A^e on that element. From the three nodal values A_i, A_j, A_k, it is easy to construct a linear interpolation function A_{ijk} on the same element. Then the proposed error estimator is computed by the L^2 norm of A^e and A_{ijk} to give the elemental error $\varepsilon^e = \|A^e - A_{ijk}\|$, which is very easy to compute and simple to implement.

The reason for the proposed error estimator lies in the fact that if the exact solution belongs to the quadratic polynomial space, then the FEM solution is actually the exact solution and thus this error estimator gives the exact L^2 error when

approximating the exact solution by linear interpolation. It is simple in practice and is expected to work in more general cases.

After calculating the error indicators for each element *e* in the mesh, certain percentages of the triangular elements in the mesh with the largest error indicators are then refined. The adaptive refinement process is done several times until some termination conditions are satisfied. The elements can be refined either by bisection, trisection, regular refinement or their combinations. The bisection method is to add a middle point to the longest side of the triangle. The trisection method is to add a point to the centroid of the triangle. Regular refinement is to divide the triangle into four similar sub-triangles by adding three middle nodes to all their edges. These methods can be separately used or mixed together to produce satisfactory mesh node distribution.

In this thesis a unified implementation to allow for arbitrary refinement type is used. Firstly, a subroutine is needed to mark the refinement type for each element with the largest estimated errors. This can be done by introducing an integer flag to indicate the refinement type for each element. For example, 1 is used for do nothing, 2 for bisection, 3 for trisection and 4 for regular refinement to the element. For all elements marked for refinement, another two subroutines, one for adding nodes and the other for Delaunay diagonal swapping, would suffice to perform the adaptive *h*-refinement process.

5.2.2. Numerical Examples

A. An Artificial Numerical Example

The proposed method is first applied to an artificial numerical example which is a steady state Poisson problem with constant diffusion coefficient

$$-\Delta u = f\,, \tag{5.1}$$

on the unit square with the homogeneous Dirichlet boundary condition. The analytical solution is chosen to be

$$u = xy(1-x)(1-y)e^{-1000[(x-0.5)^2+(y-0.117)^2]}, \tag{5.2}$$

and the right hand side function *f* is calculated by substituting (5.2) to (5.1). Note that the solution *u* has a rapid variation around the point (0.5, 0.117). The ideal

computational mesh should have much more nodes which are concentrated around that point.

The initial mesh composing of 16 elements is shown in Fig. 5.1(a). The adaptively refined mesh using the proposed error estimator containing 756 elements is shown in Fig. 5.1(b), where it is refined 12 times from the mesh shown in Fig. 5.1(a) and each time 30% of the elements are refined using the bisection mesh refinement method. The equipotential lines and the surface plot of the FEM solution u_h are shown in Fig. 5.1(c) and Fig. 5.1(d), respectively (with absolute L^2 error 9.66×10^{-7}), where it is clearly seen that the solution has been sharply resolved by the adaptive FEM.

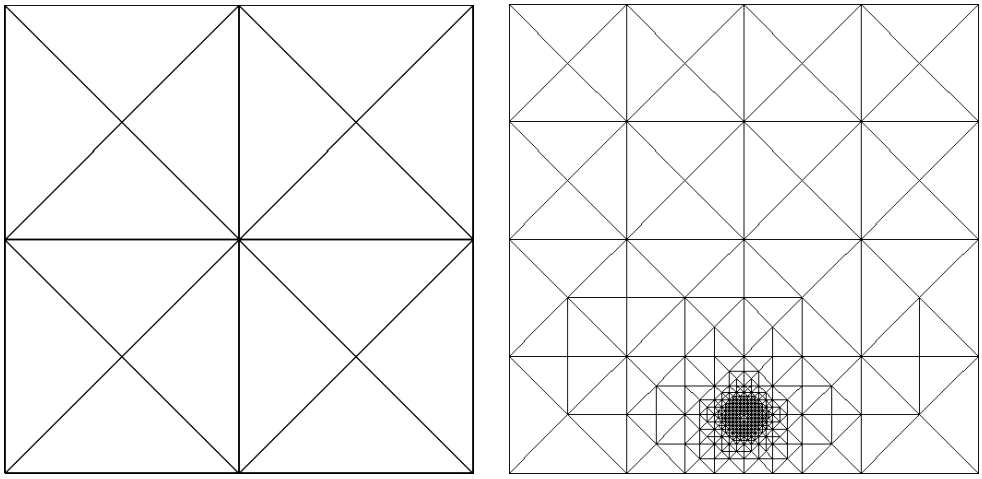

(a) (b)

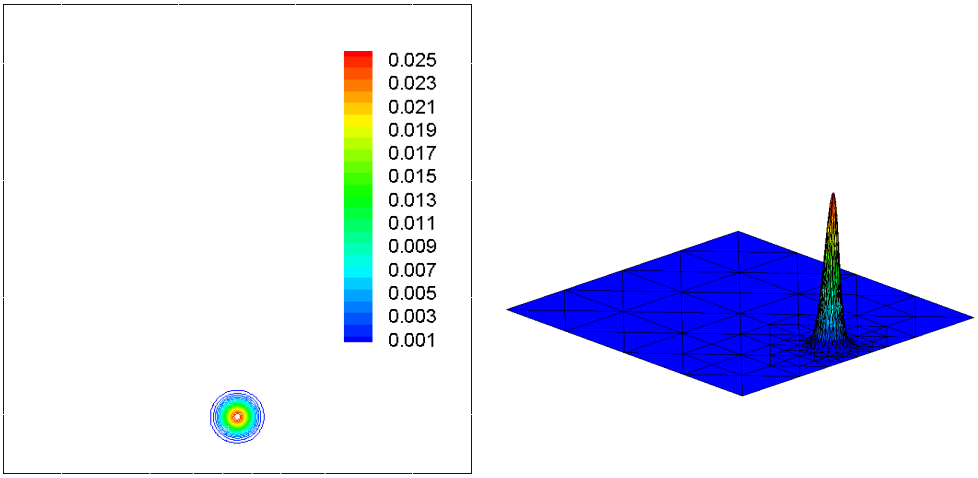

(c) (d)

Fig. 5.1. (a) The initial mesh. (b) The FE mesh after 12 times refinement (with 756 elements). (c) The equipotential lines of the solution u. (d) Surface plot of the FEM solution.

To check the effectiveness of the proposed error estimator, the ZZ error estimator which is widely used in engineering computation is used for comparison. In Fig. 5.2, the same problem computed by FEM with uniform mesh refinement and by AFEM using different error estimators are shown, where the red line is obtained by using the exact error measured in the L^2 norm of the FEM solution to the analytical solution given in (2). From the figure one can see the proposed error estimator which is simple in implementation is effective in use.

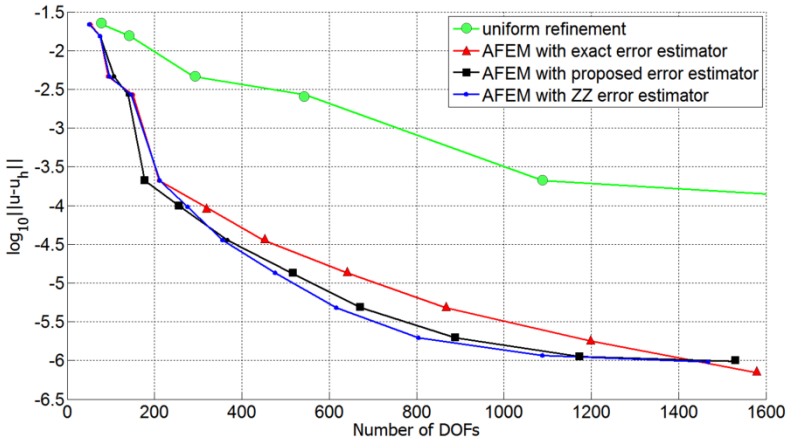

Fig. 5.2. Numerical error of the FEM solution computed on the mesh by uniform refinement (green line) and by AFEM with different error estimators, thereby highlighting the accuracy of the AFEM.

B. An Example where the Problem Domain Contains Multiple Materials

In the second example, the magnetic potential distribution in a magnetic device is solved. The device composes of a permanent magnet (PM) with H_c=8.38×10^{5}A/m and its polarization is along the x axis, two blocks made of ferromagnetic iron material with μ_r=1000 and surrounded by air with μ_r=1.

The problem setting is as follows. In Fig. 5.3(a), the black region is the PM, the two blue subdomains are the ferromagnetic blocks and the other is the air. On the left boundary of the problem domain, the homogeneous Neumann condition is used and on the other three boundaries the homogenous Dirichlet condition A=0 is prescribed.

In Fig. 5.3(b) the initial coarse mesh is shown. In Fig. 5.3(c) the adaptive mesh after 8 times using the proposed error estimator (30% of the elements in the mesh are refined each time) and the bisection refinement method is shown. The computed

magnetic potential is shown in Fig. 5.3(d). From Fig. 5.3(c) and Fig. 5.3(d) one can see clearly that the mesh nodes are concentrated in the region where the equipotential lines are dense. So the proposed *a* posteriori error estimator can also work with problems containing more than one material conveniently.

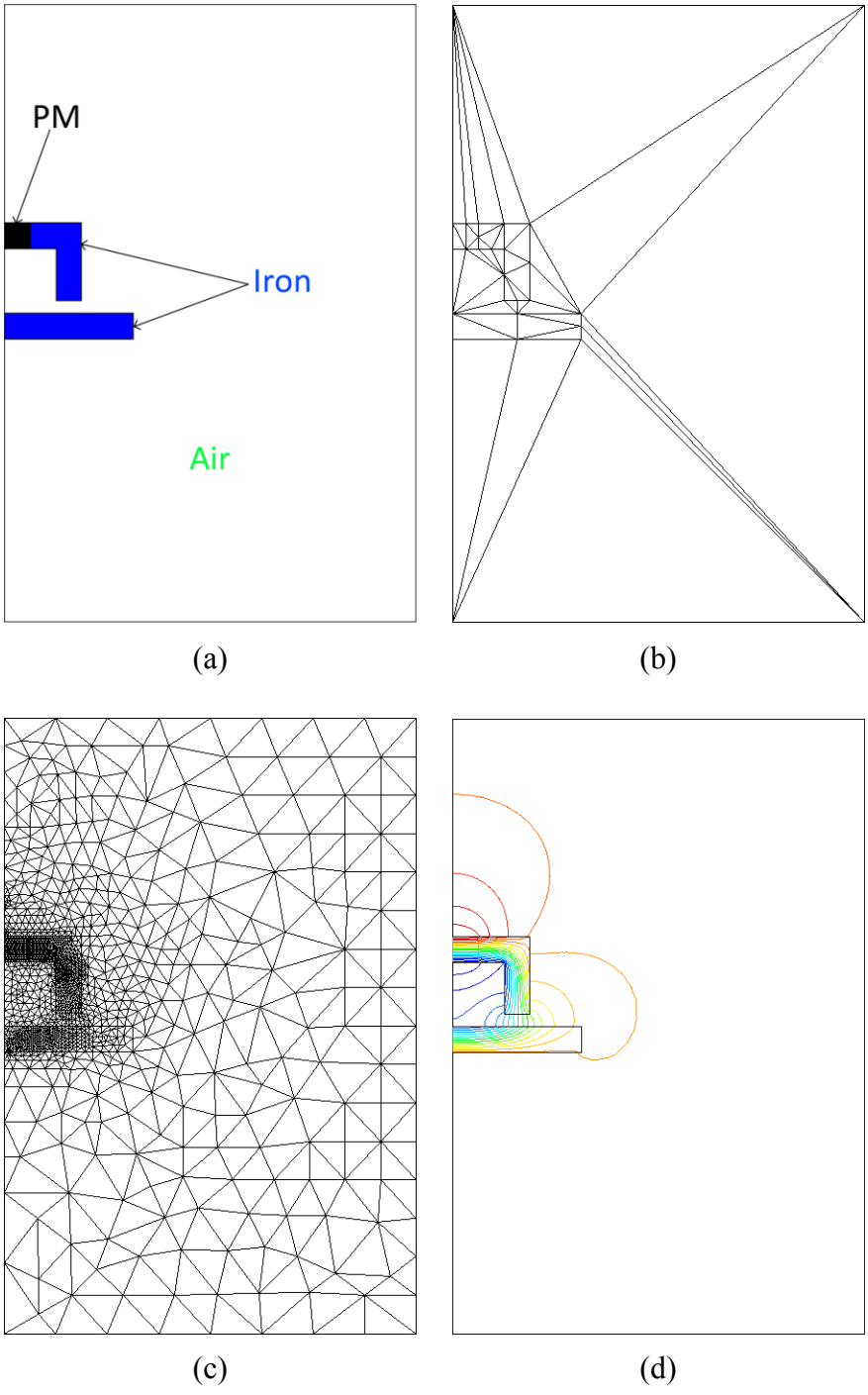

Fig. 5.3. (a) The material composition of the problem. (b) The initial mesh. (c) The adaptive mesh after 8 refinements (30% of the elements in the mesh are refined each time). (d) The equipotential lines of the solution.

5.3. Adaptive DoFs FEM

The AFEMs for static problems use successively refined meshes to achieve a solution with high accuracy. For time-dependent problems or nonlinear problems, there are multiple static problems to be solved, either in each time-step or each nonlinear iteration step. As a result, it is usually necessary to adapt the mesh by both refinement or coarsening. However, it is difficult and tedious to simultaneously refine or coarsen the mesh [E30-E32]. In this section a novel adaptive DoFs FEM for nonlinear and transient magnetic field analysis is proposed. To illustrate the basic idea, first-order linear triangular elements are considered only. Generalization of the proposed AFEM to high-order elements and quadrilateral meshes is straightforward.

The proposed method incorporates functions of both mesh refinement and mesh coarsening. Instead of explicitly eliminating unnecessary nodes in the mesh, the proposed mesh coarsening algorithm only needs a single mesh. The procedure is to apply constraints to those DoFs with small estimated error. This process avoids solution interpolation errors due to changes from a fine mesh to a coarse mesh and can be implemented readily. The slave-master technique is adopted to eliminate the constrained DoFs in the linear system, which has the same effect as mesh coarsening. Unlike the usual slave-master technique applied to multiple meshes, it is generalized to be applicable within only one set of mesh. Implementation details of the algorithm are presented and numerical examples are tested to showcase the effectiveness of the proposed method.

5.3.1. Algorithm to Adapt the DoFs

The key idea is to use the longest edge bisection method [C16-C18] for adaptive mesh refinement and record the mesh refinement process. All the nodes in the initial coarse mesh is set as master nodes, and the nodes later inserted to the middle of the edges are set as slave nodes, with their master nodes to be the two ends of the corresponding edges. Based on the error estimate, if the DoF associated with a slave node is to be eliminated from the unknowns list, an algebraic condition is applied there to reduce the total number of DoFs.

The AFEM using adaptive DoFs is both applicable to the numerical computation of static magnetic fields involving nonlinear materials [E33] and transient eddy-current problems [E34]. For nonlinear magnetostatic problems, the resultant algebraic matrix equation is nonlinear, which is usually successively linearized by the Newton-Raphson (NR) method. For static linear problems, the NR algorithm terminates after one nonlinear iteration step. This means both linear and nonlinear problems can be unified in formulation, the only difference is that iterations are needed for nonlinear materials to converge. For transient problems, a linear or nonlinear field needs to be solved for each time-step in a time-stepping process. Since the smallest computation unit is to advance the problem to a linear iteration step, all the adaptive techniques are therefore focused for linear problems in the following discussions.

A. Error Estimator and Adaptive Mesh Refinement Method

For each AFEM computation of transient problems, the FE solution is first solved before the error estimator is extracted. The mesh adaptation method is then invoked to adjust the mesh according to estimated errors. Mesh nodes are either added to those elements with larger error or removed from the mesh if the error of the surrounding elements is small enough.

As for the error estimator, the ZZ estimator [E9] is used in this work. Although the ZZ estimator is computed for the mesh elements, the nodal errors can be obtained by averaging these errors on the surrounding elements. For the mesh refinement method, the edge bisection method is adopted as mentioned above. A simple mesh refinement example by the bisection algorithm is show in Fig. 5.4(a)-(b).

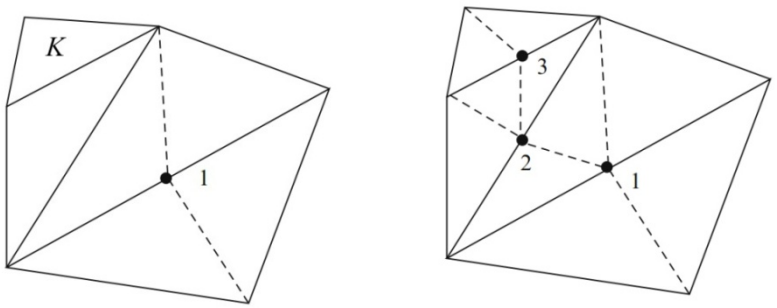

(a) (b)

Fig. 5.4. (a) The initial mesh, element *K* is marked to be refined. (b) The final refined mesh using the longest edge bisection algorithm.

B. Imposing Constraints to Slave DoFs

When it is necessary to remove unwanted DoFs and decrease the number of unknowns in the FE computation, which is very useful in transient field analysis, one choice is to perform mesh coarsening by explicitly deleting some nodes from the mesh [E30]. Realization of this procedure is however complicated in computer implementation. Besides, the mesh data have to be modified frequently and a solution projection process from the old mesh to the new mesh is also needed. Such procedure may also introduce noise to the solutions.

In this thesis, the proposed mesh coarsening process is effectively realized in an implicit manner, that means, the actual mesh coarsening function is not executed. The mesh data do not need to be updated repeatedly when performing the coarsening function. Besides, the proposed mesh coarsening method is also solution-projection-free and thus there are neither solution data transition noises nor other related errors.

The core idea for mesh coarsening is to coarsen the FE space or remove the unknowns associated with the mesh nodes without deleting the nodes from the mesh explicitly. This can be done by introducing a constraint equation for each node to be removed from the mesh. That is, if a node is to be removed from the unknowns list in accordance to the error estimator, an algebraic equation which is obtained from the variational principle, instead of the original FE equation, is applied to constrain the solution value on that node as explained below.

In the implementation of the former edge bisection mesh refinement algorithm, the newly added nodes are inserted into the rear of the node list of the initial mesh one by one. Thus the coordinates of a new node S, and potentially the solution value of S, are dependent on those of the two nodes in the initial mesh referred as M_1 and M_2. If the solution around S varies smoothly and if it is also to be eliminated from the unknowns list, the following algebraic equation is applied

$$u_S = \frac{u_{M_1} + u_{M_2}}{2}. \tag{5.3}$$

C. Node Data Structure in the Adaptive DoF Algorithm

To facilitate the management of the master DoFs and slave DoFs, a data structure of the mesh node is proposed and described as follows. For any node in the FE mesh,

its data members consist of its coordinates (x, y), its geometric Id (*Id*) in the whole node list, its DoF Id (*dofId*) which indicates whether it is a slave node (*dofId* = 1 if the node is a regular node; *dofId* = -1 if the node is a slave node), its global equation Id (*eqId*) in the equation list (*eqId* = 0 if the node is a slave node), as well as the two master nodes' geometric Id m_1 and m_2 (m_1 and m_2 are set to be 0 for non-slave DoFs).

As a simple example, for the initial mesh and the refined mesh of a unit square shown in Figs. 5.5(a) and 5.5(b), where the node with Id = 25 is set to be a slave node, the settings for all the data members of the nodes are given in Table 5.1. In summary, there is one slave node with Id = 25 in the mesh and there are totally 41 nodes in the mesh, which means there are 40 unknowns to be solved.

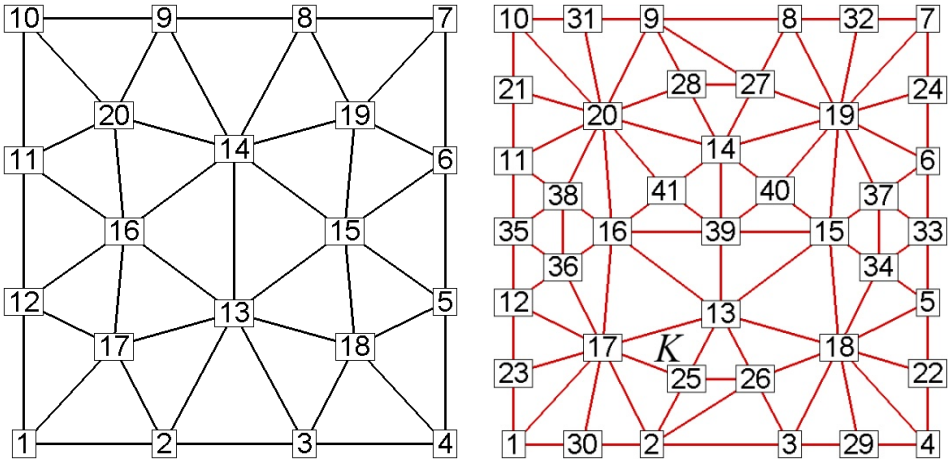

(a) (b)

Fig. 5.5. (a) The initial mesh (20 nodes). (b) The refined mesh using the longest edge bisection algorithm (41 nodes).

Id	*dofId*	*eqId*	m_1	m_2	x	y
1	1	1	0	0	0.0	0.0
2	1	2	0	0	0.3333	0.0
…	…	…	…	…	…	…
20	1	20	0	0	0.2143	0.7719
21	1	21	10	11	0.0	0.8333
22	1	22	4	5	1.0	0.1667
23	1	23	1	12	0.0	0.1667
24	1	24	6	7	1.0	0.8333
25	-1	0	2	13	0.4167	0.1535
26	1	25	3	13	0.5833	0.1535
…	…	…	…	…	…	…
41	1	40	14	16	0.3690	0.5965

Table 5.1. Settings of the data members for all nodes shown in Fig. 5.5(b).

D. Method to Modify the Element Matrix

In principle, after performing traditional element analysis process, the algebraic constrain equation (5.3) can be incorporated into the global FE equation in a global manner as stated in [E35]. However such algorithm cannot be implemented readily because the resulting global matrix operations require a lot of memory and is computationally very expensive. To ensure the proposed method is useful in practice, the constraint equation (5.3) should be realized at an element analysis level with little overhead. Fortunately, with the help of the following node data structure, equation (5.3) can be assembled into the global matrix easily and conveniently.

In this section, the proposed DoF constraining algorithm is briefly reviewed to illustrate how element matrix is modified in order to produce the correct global matrix equation for the solution of the remaining active DoFs in the coarsened FE space. Since the adaptive mesh coarsening is done by imposing constraints to those nodes with sufficiently small estimated numerical errors, the triangular element K in the FE mesh generally consists of both master nodes and slave nodes. Moreover, the DoFs defined on the latter are not present in the list of unknowns. In other words, all the DoFs $\{u_K\}$ involved in an element K can be classified either into the slave DoFs $\{u_S\}$ or the master DoFs $\{u_M\}$. All the master DoFs associated with all the three nodes of element K include the master DoFs in K $\{u_M\}$ as well as the 'active' master DoFs of $\{u_S\}$ which are outside $\{u_K\}$ [E36].

For simplicity, the three-node linear triangular element is taken to illustrate the slave DoFs elimination idea. High order FEs can be treated in a similar manner. In the element analysis process of element K, the traditional element matrix S_e of size 3×3 is computed first. For the master DoFs $\{u_M\}$ in element K, the entries in the modified element matrix $\widetilde{S}_e$ corresponding to them are invariant. The main technique is to calculate the element entries corresponding to the slave DoFs $\{u_S\}$ in the modified element matrix and distribute their contributions to the global FE equation correctly. This can be done by properly modifying the traditional element matrix and global assembly process.

As shown in the following example, by using the proposed data structure of the mesh node, the DoF constraining algorithm proposed in this work can be realized

readily in an element level without adjusting the global matrix profile for the slave DoFs [E35]. The method used to remove slave DoFs is basically the same as that used in [A37, E37], where the element matrix transformation method is used to address the matching condition on the circular sliding interface between the rotor mesh and stator mesh.

In this work, it is shown that the idea of element matrix transformation in [A37, E37] can be used within only a single mesh to remove the unused DoFs. Besides, the resultant modified element matrices using the method are symmetrical. As a simple example of the proposed DoF constraining algorithm, the procedure to modify the element matrix and the element right hand side (RHS) using the transformation matrix is shown below.

For element K as shown in Fig. 5.5(b) which has nodes with Ids {25, 13, 17}, the node with Id 25 is a slave node and it is constrained by $u_{25} = (u_2+u_{13})/2$. It can be seen that the following relationship between $\{u_K\} = \{u_{25}, u_{13}, u_{17}\}$ and the set of all master DoFs for $\{u_K\}$ (in this case is the set $\{u_2, u_{13}, u_{17}\}$) is satisfied:

$$\begin{Bmatrix} u_{25} \\ u_{13} \\ u_{17} \end{Bmatrix} = \begin{bmatrix} 1/2 & 1/2 & 0 & 0 \\ 0 & 0 & 1 & 0 \\ 0 & 0 & 0 & 1 \end{bmatrix} \begin{Bmatrix} u_2 \\ u_{13} \\ u_{13} \\ u_{17} \end{Bmatrix} \triangleq T \begin{Bmatrix} u_2 \\ u_{13} \\ u_{13} \\ u_{17} \end{Bmatrix}. \tag{5.4}$$

Then the element matrix S_e (of size 3×3) is transformed into a 4×4 matrix

$$\tilde{S}_e = T^T S_e T\,, \tag{5.5}$$

and the element RHS vector f_e (of size 3×1) is transformed into a 4×1 vector

$$\tilde{f}_e = T^T f_e\,. \tag{5.6}$$

Subsequently the transformed matrix (5.5) and the transformed RHS vector (5.6) are assembled into the global matrix and the global RHS vector, respectively, where the global row and column indices are the global equation indices corresponding to $\{u_2, u_{13}, u_{13}, u_{17}\}$. It is not difficult to see from (5.5) that by using this matrix transformation method, the symmetry property of the original system will be upheld. For general cases (quadrilateral meshes, higher order FEs, higher-dimensional problems), the element matrix and RHS can be assembled in the same way. After

solving the resultant global FE equation, the solution for the slave DoF u_{25} can be recovered by averaging its master solution values u_2 and u_{13} according to (5.3).

E. Method for Handling Multiple-level Slave Nodes

In successive mesh refinement processes, the meshes of all the refinement steps are hierarchical. As a result, a slave node to be removed from the DoF list can be a multiple-level slave node, whose master nodes are slave nodes of some nodes in a higher level mesh. In other words, a slave node may depend on the master nodes of different hierarchy levels. In this case the node data structure as introduced above can be slightly modified to account for this problem.

By denoting l as the mesh node hierarchy number, set l=0 for the initial mesh nodes and l=1 for the nodes inserted in the first mesh refinement. Then for a multiple-level slave DoF, the transformation matrix T in (5.4) can be calculated in the similar way as that for the single-level slave DoF. Here all the master nodes of a multiple-level slave node S are found recursively and then sorted according to their hierarchy number l as $\{\{M^0\}, \{M^1\}, ...,\{M^L\}\}$, where L is the maximum refinement level and the set $\{M^l\}$ denotes all l-level master nodes for the slave node S. Then the algebraic constraint equation

$$u_S = \sum_{l=0}^{L} \sum_{M \in \{M^l\}} \frac{u_M}{2^{l+1}}, \tag{5.7}$$

is imposed for u_S.

5.3.2. Validating the Proposed Algorithm

In this section, two simple examples are used to validate the proposed algorithm, including artificial problems with linear function solution and polynomial solution.

A. A very simple example

To check the DoF constraining algorithm, the first example is to solve the Poisson equation with exact solution $u=x+y$. For this example, the solution contour lines are parallel and uniformly distributed, it is very easy to see whether the slave DoFs are correctly handled. The mesh is shown in Fig. 5.5(b), and the nodes with Id greater than 20 are set as slaves. There are 21 constraints hence only an equation with

20 unknowns needs to be solved. From Fig. 5.6(b), it can be seen that the contour lines is the same as Fig. 5.6(a) without any slave DoF.

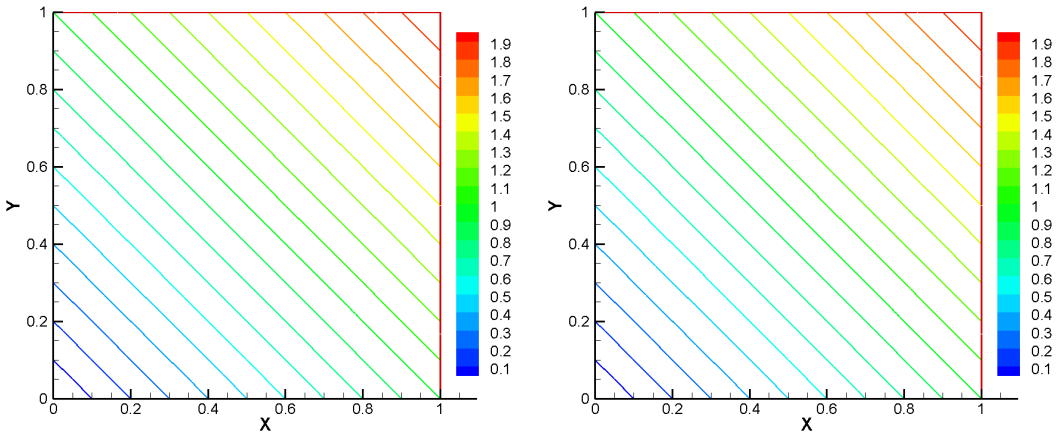

(a) (b)

Fig. 5.6. (a) The solution contour lines without slave DoF. (b) The solution contour lines with 21 slave DoFs.

B. A Linear Poisson Problem

In this example, the problem is a Poisson problem with exact solution to be

$$u = xy(1-x)(1-y). \tag{5.8}$$

To check the algorithm, the nodes in the mesh shown in Fig. 5.5(b) with Id greater than 20 are set as slaves. The L^2 error of the numerical solution obtained using the mesh shown in Fig. 5.5(a) is calculated as 8.16×10^{-3}, while the L^2 error calculated on the mesh as shown in Fig. 5.5(b) with 20 constraints is 7.74×10^{-3}. Note that the result is reasonable, because the meshes shown in Fig. 5.5(a) and Fig. 5.5(b) are nested, the corresponding finite element spaces are also nested.

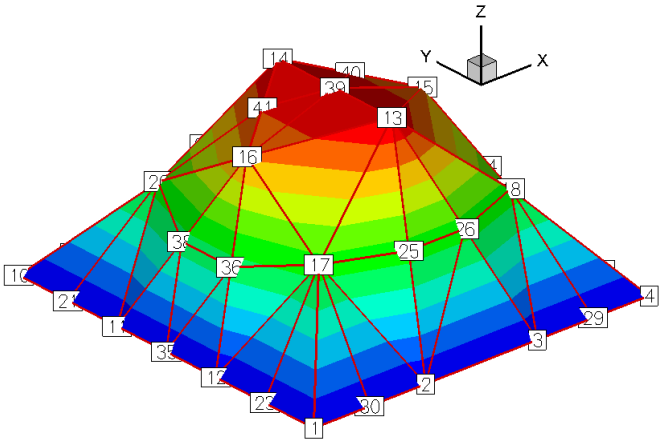

Fig. 5.7. The solution surface plot with 21 slave DoFs (41 nodes in the mesh).

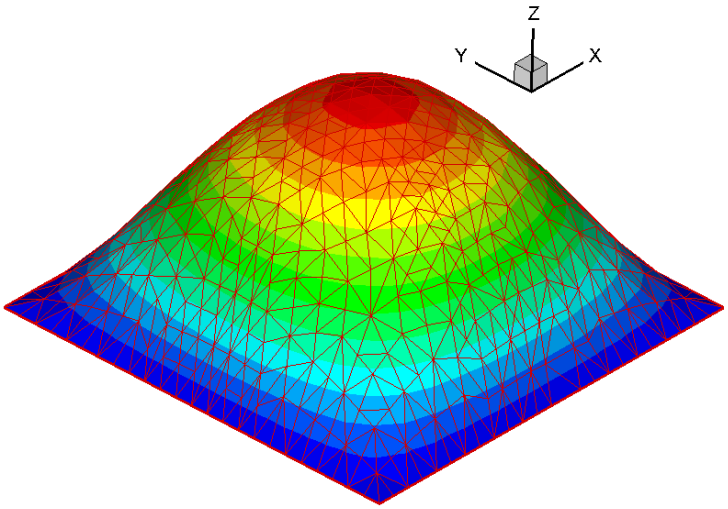

Fig. 5.8. The solution surface plot with 300 slave DoFs (598 nodes in the mesh).

The surface plot of the calculated solution on the mesh as shown in Fig. 5.5(b) with 20 constraints is shown in Fig. 5.7. When there are 300 slave nodes in a mesh having 598 nodes, the solution contour plot is shown in Fig. 5.8, where the L^2 error of the solution is accuracy is 5.714×10^{-4}. Hence the correctness of the DoF constraining algorithm is validated.

5.3.3. Application to Nonlinear Static Problems

To check the usefulness of the algorithm for engineering problems, the TEAM workshop problem 25 [D9] is solved using the proposed AFEM. The problem domain and the *B-H* curve for the nonlinear material are shown in Fig. 5.9 (a) and Fig. 5.9(b) respectively. The computed potential lines and the dofId plot of the mesh nodes are shown in Figs. 5.10(a) and 5.10(b) respectively, where there are totally 6246 nodes in the mesh.

In the computation, the NR iteration process terminates after 7 times iteration with the relative residual error 1.7×10^{-5}. During each NR iterative step, there are about 4900 unknowns to be solved in the linearized equation, hence about 1350 DoFs are constrained. It is estimated that roughly about 20% of the CPU time can be saved using the proposed adaptive finite element algorithm than using traditional FEM. Furthermore, it is not difficult to see that the proposed technique can be also directly applied to transient field analysis.

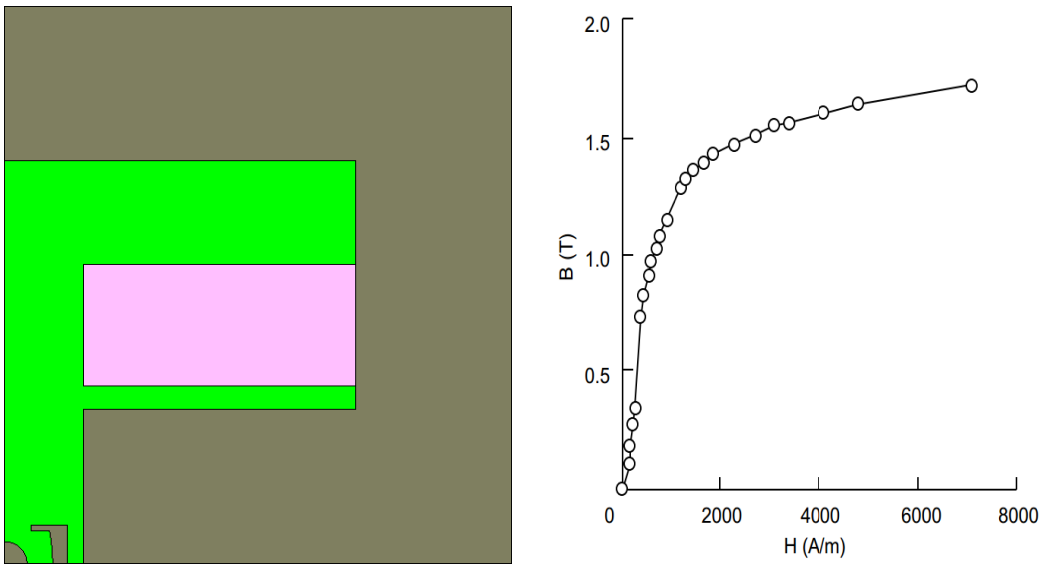

(a) (b)

Fig. 5.9. (a) The computational domain of the TEAM workshop problem 25. (b) The B-H curve for the nonlinear material.

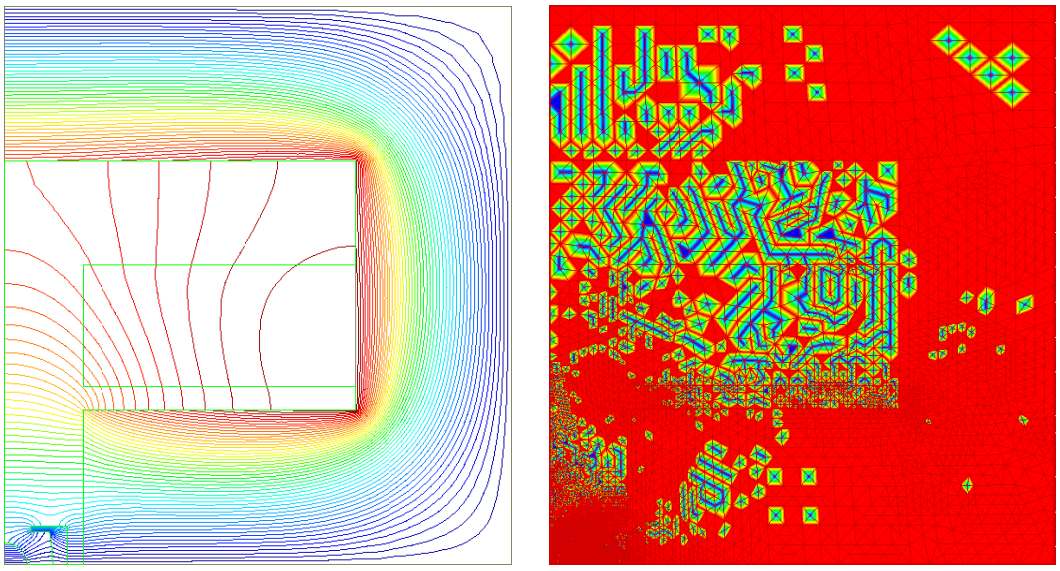

(a) (b)

Fig. 5.10. (a) The computational magnetic equi-potential lines. (b) The computational mesh and the plot of the dofId for each node (red-master nodes, blue-slave nodes).

5.3.4. Application to Transient FE Time-stepping Process

A. An Artificial Example

For the first example, a quasi-stationary transient problem with a time-dependent RHS source function, which is conterclockwisely rotating, is solved using the

proposed adaptive DoFs algorithm to show its effectiveness. The equation to be solved reads

$$-\Delta u(x,y,t) = e^{-500(\vec{x}-\vec{x}_c(t))^2}, \tag{5.9}$$

where

$$\vec{x}_c(t) = (0.5+0.3\cos(t), 0.5+0.3\sin(t)), \tag{5.10}$$

and homogeneous Dirichlet boundary condition

$$u(x,y,t) = 0, (x,y) \in \partial\Omega, \tag{5.11}$$

is applied on the boundary of the domain $\Omega = [0,1]^2$. The problem (5.9)-(5.11) is then solved for $t \in [0, 2\pi]$ with a uniform time step $\Delta t = \pi / 20$, where only one mesh containing 4331 nodes is used and the adaptive DoFs algorithm is applied for each time step. The numerical solution contour figures and the DoF distribution figures are shown Figs. 5.11(a)-5.11(h) at four selected time instants, namely, $t = 0$, $t = \pi/2$, $t = \pi$ and $t = 3\pi/2$.

From Figs. 5.11(a)-5.11(h) one can see that the proposed adaptive DoFs algorithm can dynamically track the peak of the solution in a fixed mesh. The DoFs are kept in the region where the solution varies rapidly while in smooth region they are removed by imposing constraints. For all the selected 4 time instants, There are about 1400 slave DoFs for each time step and about 30% computational time is saved, when compared to traditional FEM. It is also easy to adapt the DoF in each time step for the proposed adaptive DoFs, when compared to the adaptive method used in [E32], for time-dependent problems.

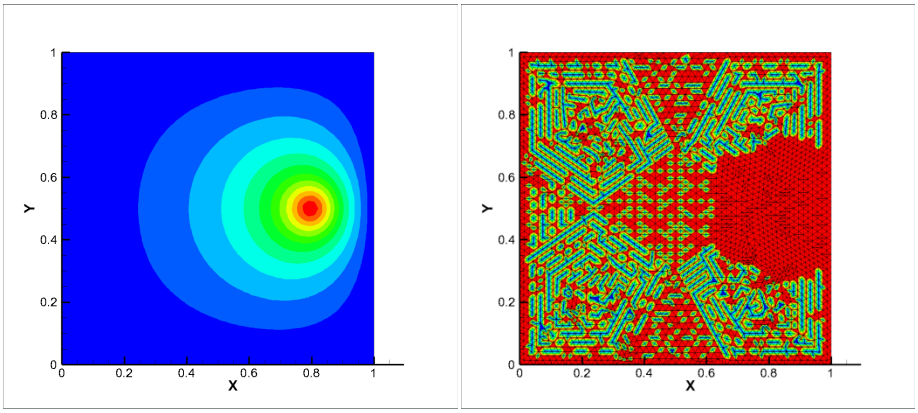

(a) (b)

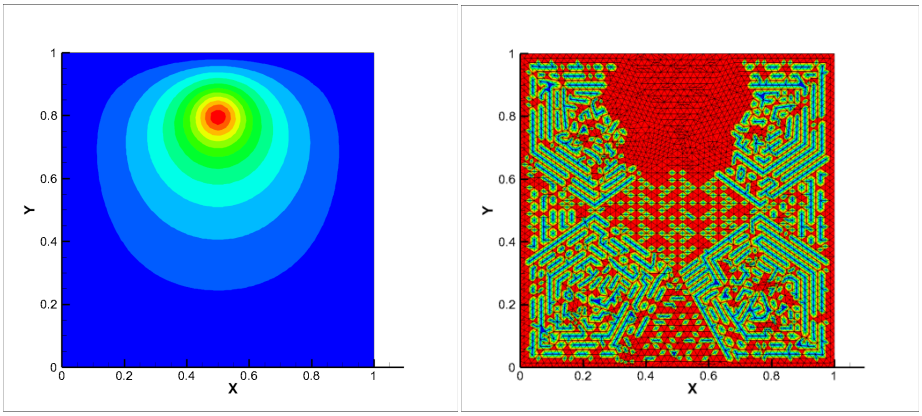

(c) (d)

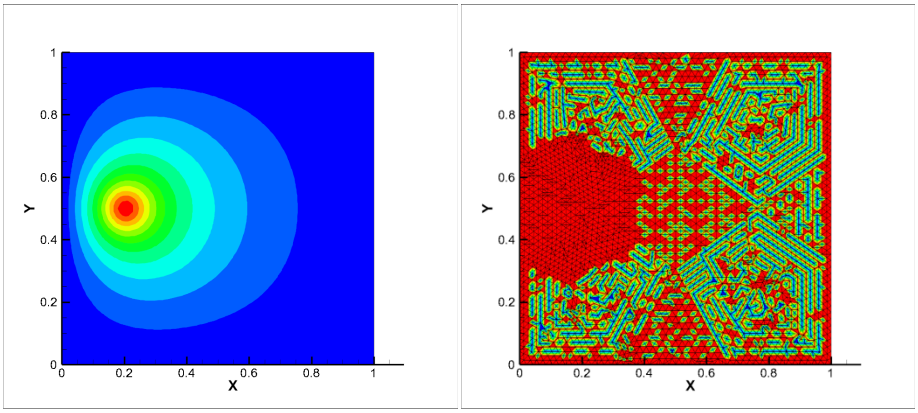

(e) (f)

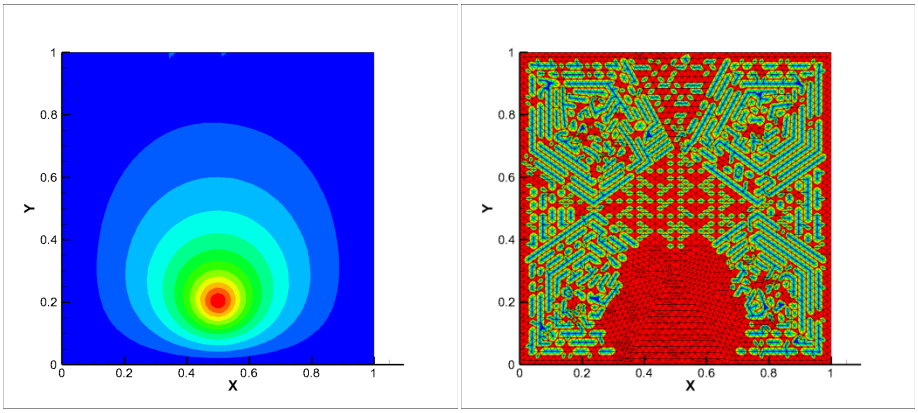

(g) (h)

Fig. 5.11. (a) The solution contour plot at t=0. (b) The computational mesh and the dofId at t=0 (1385 slave DoFs). (c) The solution contour plot at t= π/2. (d) The computational mesh and the dofId at t= π /2 (1413 slave DoFs). (e) The solution contour plot at t= π. (f) The computational mesh and the dofId at t=π (1392 slave DoFs). (g) The solution contour plot at t=3 π/2. (h) The computational mesh and the dofId at t=3 π/2 (1412 slave DoFs). For Figs. (b), (d), (f) and (h), the red color means master nodes and blue color means slave nodes.

B. Accelerating the Steady-state Solution Process in Time-domain

The proposed adaptive DoFs FEM can be applied to accelerate the calculation of the steady-state solution in time-domain. In [E38], the authors have proposed four novel techniques to accelerate the transient analysis process to reach the steady-state using time-stepping FEM. The adaptive DoFs FEM can be another choice to do this.

For illustration, the above TEAM workshop problem 30A [D11] is used as an example to calculate the transient torque curve versus time when the rotor rotates at 1200rad/s. Before the induction motor reaches its steady-state, the transition process is usually not important since the steady-state performance is mainly concerned. In the numerical computation, a coarse mesh is first used at the beginning of the time stepping by using the proposed multiple-level DoFs constraining algorithm.

For this example, two-level slave nodes are applied (5804 DoFs in the FE equation) when the average dc component of the solution $|X_{dc}(t)| \geq 10^{-6}$ [E38]. When $|X_{dc}(t)| < 10^{-6}$, the solution is close to the steady-state, the mesh containing 14538 nodes is used to continue the time-stepping process. By using the adaptive DoFs FEM and the initial coarse mesh technique by setting multiple-level DoFs, the steady-state toque is calculated as -2.1257Nm, which is almost identical with the result given in [A35]. The transient torque curve versus time is given in Fig. 5.12. At last, the total computing time for this example is reduced to about 48% of that needed for traditional FEM, which showcases the effectiveness of the proposed adaptive DoFs FEM when used to compute the steady-state solutions.

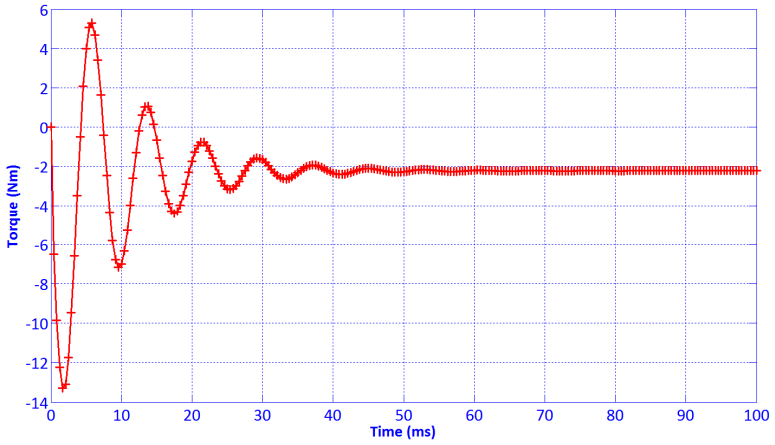

Fig. 5.12. The torque of the rotor versus time for TEAM workshop problem 30A, where the rotor speed is 1200rad/s.

5.4. Summary

AFEMs are very useful numerical techniques that can be used to get more accurate results given the same DoFs or attain the same accuracy with less DoFs. In this chapter, an error estimator was proposed that is very effective to use for problems with multiple materials. The effectiveness of this error estimator is also compared with classical ones. Then an adaptive DoFs FEM was proposed where only one set of mesh is used in the whole computation process, which can be applied to each nonlinear iteration step or each time-step for transient field analysis. Numerical examples are presented to illustrate the advantages of the proposed method.

5.5. References-Part E

[E1] Z. J. Cendes, and D. N. Shenton, "Adaptive mesh refinement in the finite element computation of magnetic fields," *IEEE Trans. Magn.*, vol. MAG-21, no. 5, pp. 1811-1816, Sep. 1985.

[E2] S. Y. Hahn, C. Calmels, G. Meunier, and J. L. Coulomb, "A posteriori error estimate for adaptive finite element mesh generation," *IEEE Trans. Magn.*, vol. 24, no. 1, pp. 315-317, Jan. 1988.

[E3] A. Raizer, G. Meunier, and J. L. Coulomb, "An approach for automatic adaptive mesh refinement in finite element computation of magnetic fields," *IEEE Trans. Magn.*, vol. 25, no. 4, pp. 2965-2967, Jul. 1989.

[E4] J. F. Remacle, P. Dular, F. Herotte, A. Genon, and W. Legros, "A posteriori error estimation and adaptive meshing using error in constitutive relation," *IEEE Trans. Magn.*, vol. 32, no. 3, pp. 1369-1373, May 1996.

[E5] J. F. Remacle, C. Geuzaine, P. Dular, H. Hedia, and W. Legros, "Error estimation based on a new principle of projection and reconstruction," *IEEE Trans. Magn.*, vol. 34, no. 5, pp. 3264-3267, Sep. 1998.

[E6] D. P. Labridis, "Comparative presentation of criteria for adaptive finite element mesh generation in multiconductor eddy-current problems," *IEEE Trans. Magn.*, vol. 36, no. 1, pp. 267-280, Jan. 2000.

[E7] D. Ladas, V. Mazauric, G. Meunier, O. Chadebec, M. Ebene-Ebene, Y. Marechal, and P. Wendling, “An energy based approach of electromagnetism applied to adaptive meshing and error criteria,” *IEEE Trans. Magn.*, vol. 44, no. 6, pp. 1246-1249, Jun. 2008.

[E8] S. Matsutomo, S. Noguchi, and H. Yamashita, “Adaptive mesh generation method utilizing magnetic flux lines in two-dimensional finite element analysis,” *IEEE Trans. Magn.*, vol. 48, no. 2, pp. 527-530, Feb. 2012.

[E9] O. C. Zienkiewicz, and J. Z. Zhu, “A simple error estimator and adaptive procedure for practical engineering analysis,” *Int. J. Numer. Meth. Eng.*, vol. 24, pp. 337-357, 1987.

[E10] E. Q. Hu, X. Z. Chen, and K. D. Zhou, “A new posteriori error estimate and adaptivity approach for electromagnetic field finite element computations,” *Proc. CSSE*, Mar. 1997, vol. 17, no. 2, pp. 78-83.

[E11] J. B. Li, D. X. Xie, and X. M. Liu, “A posteriori error estimation and adaptive mesh refinement controlling in finite element analysis of 3-D steady state eddy current field,” *IEEE Trans. Magn.*, vol. 46, no. 8, pp. 3500-3503, Aug. 2010.

[E12] A. B. Diaz-Morcillo, J. V. Balbastre, and L. Nuno, “New recovery error indicator for adaptive finite element analysis on waveguiding structures,” *IEEE Trans. Microw. Theory Tech.*, vol. 51, no. 5, pp. 1467-1475, May 2003.

[E13] G. Maisano, S. Micheletti, S. Perotto, and C. L. Bottasso, “On some new recovery-based a posteriori error estimators,” *Comput. Methods Appl. Mech. Eng.*, vol. 195, pp. 4794-4815, 2006.

[E14] Z. Q. Cai, and S. Zhang, “Recovery-based error estimator for interface problems: Conforming linear elements,” *SIAM J. Numer. Anal.*, vol. 47, no. 3, pp. 2132-2156, 2009.

[E15] Z. Q. Cai, and S. Zhang, “Flux recovery and a posteriori error estimators: Conforming elements for scalar elliptic equations,” *SIAM J. Numer. Anal.*, vol. 48, no. 2, pp. 578-602, 2010.

[E16] T. L. Horvath, and F. Izsak, “Implicit a posteriori error estimation using patch recovery techniques,” *Central Eur. J. Math.*, vol. 10, no. 1, pp. 55-72, 2012.

[E17] P. Fernandes, P. Girdinio, P. Molfino, and M. Repetto, “An enhanced error estimator procedure for finite element field computation with adaptive mesh refinement,” *IEEE Trans. Magn.*, vol. 26, no. 5, pp. 2187-2189, Sep. 1990.

[E18] M. M. Ilic, A. Z. Ilic, and B. M. Notaros, “Efficient large-domain 2-D FEM solution of arbitrary waveguides using *p*-refinement on generalized quadrilaterals,” *IEEE Trans. Microw. Theory Tech.*, vol. 53, no. 4, pp. 1377-1383, Apr. 2005.

[E19] J. P. Webb, and B. Forghani, “Adaptive improvement of magnetic fields using hierarchal tetrahedral finite elements,” *IEEE Trans. Magn.*, vol. 30, no. 5, pp. 3511-3514, Sep. 1994.

[E20] M. M. Gavrilovic, and J. P. Webb, “A port element for *p*-adaptive S-parameter calculation,” *IEEE Trans. Magn.*, vol. 35, no. 3, pp. 1530-1533, May 1999.

[E21] P. J. Capon, and P. K. Jimack, “On the adaptive finite element solution of partial differential equations using *h*-*r*-refinement,” Technical Report, Apr. 1996.

[E22] R. E. Bank, and R. K. Smith, “Mesh smoothing using a posteriori error estimates,” *SIAM J. Numer. Anal.*, vol. 34, no. 3, pp. 979-997, 1997.

[E23] S. Dufour, G. Vinsard, B. Laporte, and R.Moretti, “Mesh improvement in 2-D eddy-current problems,” *IEEE Trans. Magn.*, vol. 38, no. 2, pp. 377-380, Mar. 2002.

[E24] R. Boussetta, T. Coupez, and L. Fourment, “Adaptive remeshing based on a posteriori error estimation for forging simulation,” *Comput. Methods Appl. Mech. Eng.*, vol. 195, pp. 6626-6664, 2006.

[E25] J. Lang, W. M. Cao, W. Z. Huang, and R. D. Russell, “A two-dimensional moving finite element method with local refinement based on a posteriori error estimates,” *Appl. Numer. Math.*, vol. 46, pp. 75-94, 2003.

[E26] P. D. Ledger, and S. Zaglmayr, “hp-Finite element simulation of three-dimensional eddy current problems on multiply connected domains,” *Comput. Methods Appl. Mech. Eng.*, vol. 199, no. 49-52, pp. 3386-3401, 2010.

[E27] P. D. Ledger, “*hp*-Finite element discretisation of the electrical impedance tomography problem,” *Comput. Methods Appl. Mech. Eng.*, vol. 225-228, pp. 154-176, 2012.

[E28] T. Gratsch, and K. J. Bathe, “A posteriori error estimation techniques in practical finite element analysis,” *Comput. Struct.*, vol. 83, pp. 235-265, 2005.

[E29] G. Chen, H. Zhu, T. Cui, Z. Chen, X. Zeng, and W. Cai, "ParAFEMCap: A parallel adaptive finite-element method for 3-D VLSI interconnect capacitance extraction," *IEEE Trans. Microw. Theory Tech.*, vol. 60, no. 2, pp. 218-231, Feb. 2012.

[E30] K. Yamazaki, S. Watari, T. Saeki, and Y. Sugiura, "Adaptive finite element meshing at each iterative calculation for electromagnetic field analysis of rotating machines," *Electr. Eng. Japan*, vol. 164, no. 3, pp. 78-91, 2008.

[E31] J. Lang, and D. Teleaga, "Towards a fully space-time adaptive FEM for magnetoquasistatics," *IEEE Trans. Magn.*, vol. 44, no. 6, pp. 1238-1241, Jun. 2008.

[E32] S. A. Funken, D. Praetorius, and P.Wissgott, "Efficient implementation of adaptive P1-FEM in Matlab," *Comput. Meth. Appl. Math.*, vol. 11, no. 4, pp. 460-490, 2011.

[E33] Yanpu Zhao, S. L. Ho, and W. N. Fu, "A novel adaptive mesh finite element method for nonlinear magnetic field analysis," *IEEE Trans. Magn.*, vol. 49, no. 5, pp. 1777-1780, May 2013.

[E34] Yanpu Zhao, S. L. Ho, and W. N. Fu, "An adaptive degrees-of-freedom finite-element method for transient magnetic field analysis," *IEEE Trans. Magn.*, vol. 49, no. 12, pp. 5724-5729, Dec. 2013.

[E35] Lecture notes, in Ch. 8, sec. Multi-freedom Constraints I [Online]. Available: http://www.colorado.edu/engineering/cas/courses.d/IFEM.d/IFEM.Ch08.d/IFEM.Ch08.pdf

[E36] S. C. Chang, and T. W. Lin, "Constrain relation implementation for finite element analysis from an element basis," *Adv. Eng. Software*, vol. 10, no. 4, pp. 191-194, 1988.

[E37] S. L. Ho, S. X. Niu, W. N. Fu, and J. Zhu, "A convenient mesh rotation method of finite element analysis using sub-matrix transformation approach," *IEEE Trans. Magn.*, vol. 48, no. 2, pp. 303-306, Feb. 2012.

[E38] W. N. Fu, S. L. Ho, and P. Zhou, "Reduction of computing time for steady-state solutions of magnetic field and circuit coupled problems using time-domain finite-element method," *IEEE Trans. Magn.*, vol. 48, no. 11, pp. 3363-3366, Nov. 2012.

CHAPTER 6

NUMERICAL METHODS FOR PROBLEMS WITH HIGH SPEED MOVING CONDUCTORS

6.1. Field Analysis in High-speed Moving Conductors

Solid rotors are commonly found in induction motors and magnetic brakes [F1-F4]. For these rotors with cylindrical shape, the material configuration and property of the rotor are invariably constant along the rotational direction. If the Lagrangian formulation is used to model rotational movement, one has to generate multi-meshes in the meshing process and special techniques are needed to match the solution on the interface between the stator and the rotor of these devices [F5-F8]. To enhance the accuracy of the numerical solution of the magnetic fields between the stator and the rotor, recently a novel slave-master technique which has more slave modes than the master nodes on the sliding surface is proposed [F9].

To overcome the difficulties when using multiple meshes to model motion in the Lagrangian formulation, it is preferable to use the Eulerian formulation, where only a fixed mesh is needed for the modeling of eddy-current phenomena to include motion effects in cylindrical solid rotors. In the Eulerian description of motion, the potential formulation of the eddy-current equation for these devices including motional effect can be expressed in time-domain as [F3]

$$\sigma\partial_t A + \nabla\cdot(\vec{f}(A) - \nu(|\nabla\times A|)\nabla A) = J_s,\ \ (\vec{x},t)\in\Omega\times(0,T_f], \tag{6.1}$$

together with the homogeneous Dirichlet boundary condition

$$A|_{\partial\Omega} = 0, \tag{6.2}$$

and the initial condition

$$A|_{t=0} = A_0(\vec{x}). \tag{6.3}$$

where $\partial\Omega$ is the boundary of the problem domain Ω; T_f is the stopping time of the analysis; A is the axial component of the magnetic vector potential; σ is the electric conductivity of the conductor; $\vec{v}$ is the velocity of the rotor; ν is the magnetic reluctivity; the excitation term J_s is the current density of the applied source.

The above eddy-current equation is of elliptic-parabolic type, where in the insulating regions with $\sigma = 0$, the magnetic field will respond instantaneously to the excitation, while such response takes some time in conducting regions with $\sigma > 0$ due to the presence of induced eddy currents. When the rotor rotates at high speeds, in the conducting region with positive conductivity, the governing equation is a convection-diffusion equation with dominated convection coefficient. It is well-known that the solutions of this type of equations usually contain sharp and narrow transition layers which may also evolve with time [F5-F8].

In order to well resolve these local layers effectively, it is too computationally time-consuming and wasteful to use uniformly refined meshes and a much better choice is to track the sharp layers by concentrating the mesh nodes in layers with sharp changes and dynamically reposition the mesh nodes to track these layers with time. This is usually referred as the moving mesh method [F10]. However, an extra governing equation, referred as the moving mesh partial differential equation (MMPDE) to determine the motion of the mesh nodes, has to be solved besides the physical equation concerned. In [E30] the adaptive mesh finite element method, which allows for adaptive mesh refinement as well as mesh coarsening for transient magnetic field analysis, is adopted. However this is too complicated to implement in software. In this thesis, three numerical methods are proposed to capture the thin eddy-current layers efficiently, including the (adaptive) Discontinuous Galerkin Method (DGM), the Characteristic Galerkin Finite Element Method (CGFEM) and the Operator Splitting Method (OSM).

6.2. Discontinuous Galerkin Method

During the past decades, the discontinuous Galerkin (DG) method for the numerical solution of hyperbolic partial differential equations (PDEs), and related local discontinuous Galerkin (LDG) method for parabolic PDEs and elliptic PDEs, are recognized to be effective numerical tools to address time-dependent or steady-state convection-dominated problems [F11-F13]. Moreover, these methods can be realized for adaptive algorithms easily [F13]. For second order convection-diffusion problems,

the LDG method can treat the convective term effectively by suitably defining the numerical fluxes in the scheme. The main feature of the LDG method is that it requires no continuity across interelement boundaries. For convection dominated problems, the LDG method is a good choice because the upwinding stabilization mechanism has been built naturally into the method by the definition the numerical fluxes.

6.2.1. Some Notations

For convenience of discussion and without loss of generality, only two-dimensional (2-D) problems are considered and the notations adopted are introduced here. Define the *k*-th order discontinuous finite element space as

$$V_h = \{u \in L^2(\Omega) : u|_K \in P^k(K), \forall K \in T_h\}, \tag{6.4}$$

where Ω is the problem domain which is a bounded region in R^2; T_h is a mesh triangulation of the domain Ω; h is the maximum mesh element diameter of the triangulation.

Taking any two neighboring elements K^+ and K^- from T_h, then for the common edge $e = \partial K^+ \bigcap \partial K^-$, $\vec{n}^+$ and $\vec{n}^-$ are, respectively, the unit outward normal vectors pointing out to K^+ and K^- at any point of e as shown in Fig. 6.1. Denote by E_h the set of interior edges of the mesh T_h. Let $w^{\pm}$ be the respective trace of w from the interior of $K^{\pm}$. Define $\{\{\cdot\}\}$, $[[\cdot]]$ be the average value and jumping value of related function at $x \in e$

$$\begin{aligned} &\{\{u\}\} = (u^+ + u^-)/2, \quad \{\{\vec{q}\}\} = (\vec{q}^+ + \vec{q}^-)/2 \\ &[[u]] = u^+\vec{n}^+ + u^-\vec{n}^-, \quad [[\vec{q}]] = \vec{q}^+ \cdot \vec{n}^+ + \vec{q}^- \cdot \vec{n}^- \end{aligned}, \tag{6.5}$$

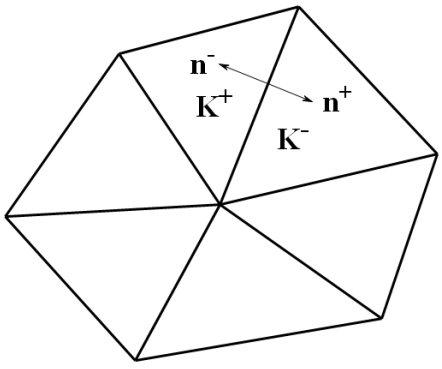

Fig. 6.1. Illustration of the mesh notations for the DG method.

6.2.2. LDG Method for A Steady-state Eddy-current Problem

In this section, the formulation of a LDG method is presented for a steady state eddy-current problem including motion effect, for which the control equation reads

$$\begin{aligned} &\Omega : \nabla^2 u + \nabla \cdot \vec{f}(u) + k_c^2 u = 0 \\ &\partial\Omega : u = g \end{aligned} . \tag{6.6}$$

To adopt the LDG method for numerical solution, the PDE in (6.6) is first rewrote into the mixed form as

$$\begin{cases} \vec{q} = \nabla u \\ \nabla \cdot \vec{q} + \nabla \cdot \vec{f}(u) + k_c^2 u = 0 \end{cases}, \tag{6.7}$$

The LDG scheme for (6.7) reads [F14]

$$\begin{cases} \int_K \vec{q}_h \cdot \vec{w} dV + \int_K u_h \nabla \cdot \vec{w} dV = \int_{\partial K} \hat{u}_h \vec{w} \cdot \vec{n} ds \\ \int_K \vec{q}_h \cdot \nabla v dV + \int_K \vec{f}(u_h) \cdot \nabla v dV - \int_K k_c^2 uv dV \\ = \int_{\partial K} v \hat{q}_h \cdot \vec{n} ds + \int_{\partial K} v \hat{f} \cdot \vec{n} ds \end{cases}, \tag{6.8}$$

for any $(\vec{w}, v) \in V_h^2 \times V_h$, where $\hat{u}_h$, $\hat{q}_h$ and $\hat{f}$ are the numerical fluxes which are defined by

$$\begin{aligned} \hat{f} \cdot \vec{n} &= \frac{1}{2}(\vec{f}(u^-) \cdot \vec{n} + \vec{f}(u^+) \cdot \vec{n} - \beta[[u]]) \\ \hat{q}_h &= \{\{\vec{q}_h\}\} - C_{11}[[u_h]] - \vec{C}_{12}[[\vec{q}_h]] \\ \hat{u}_h &= \{\{u_h\}\} + \vec{C}_{12}[[u_h]] \end{aligned} , \tag{6.9}$$

in the interior of the domain and by

$$\begin{aligned} &\hat{q}_h = \vec{q}_h^{\,+} - C_{11}(u_h^+ - g)\vec{n}, \text{on } \partial\Omega \\ &\hat{u}_h = g, \text{on } \partial\Omega \end{aligned} , \tag{6.10}$$

on the boundary of the domain Ω, where β is an estimation of the biggest eigenvalue of the Jacobian $(\partial / \partial u)\vec{f} \cdot \vec{n}$, $C_{11} = O(1/h)$ and $\vec{C}_{12}$ is a vector in R^2 of Euclidean length 1/2. The definition of the numerical flux $\hat{f} \cdot \vec{n}$ on $\partial\Omega$ can be found in [1]. In this thesis the numerical flux $\hat{f}$ is simply the local Lax-Friedrichs numerical flux and it can also take up other forms [F14].

The TEAM workshop problem 9 [F15, F16] is solved as a further verification of the proposed methodology. The geometry of this problem consists of an infinite

nonferromagnetic material with a 28 mm diameter cylindrical bore in it. A single loop of 24 mm in diameter moves inside the bore and carries a current of 1 A. The magnetic conductivity of either material is $\sigma = 5.0\times10^6$ S/m. The quantity of interest is the magnetic flux density along the line L_a of r = 13 mm illustrated in Fig. 6.2 at different velocities of v = 0, 10, 100 m/s.

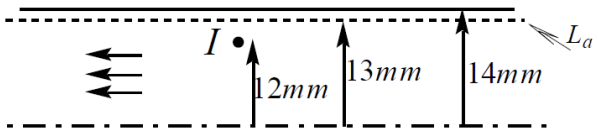

Fig. 6.2. Illustration of TEAM problem 9.

The mathematical model of this problem is a steady state axisymmetric problem. Due to rotational symmetry along the axis of the cylindrical bore, the constituent vector of function $\vec{A}$ only has the ϕ-component A_ϕ. For simplicity A_ϕ is denoted as A, and the reduced two-dimensional problem can be expressed in its Euler formulation in cylindrical coordinates (r,ϕ,z) [F16, F17]:

$$-\frac{\partial}{\partial r}\left(\frac{1}{\mu r}\frac{\partial (rA)}{\partial r}\right)-\frac{1}{z}\left(\frac{1}{\mu}\frac{\partial A}{\partial z}\right)+\sigma v\frac{\partial A}{\partial z}=J_\phi, \tag{6.11}$$

where μ is the magnetic permeability of the media, and J_ϕ is the ϕ-component of the applied current source density.

In this thesis, the diameter of the circular cross section of the current loop is taken as 1 mm, because in our numerical computation the results are almost not affected by this value. The rectangular solution domain in (r, z) plane is taken to be [0 mm, 70 mm] in the r-direction, and [-200 mm, 200 mm] in the z-direction as in [F15]. The rectangular mesh used for the LDG computation is shown in Fig. 6.3 (a), where a total number of 50×50 mesh points are used and of which 10×10 mesh points are located in the loop cross section domain where the source current density exists.

The equal magnetic potential lines for the LDG solution of A in (10) with v = 0 m/s is shown in Fig. 6.3 (b). The r- and z- components of $B=\nabla\times A$ of the LDG solution on the line L_a shown in Fig. 6.2 are given in Fig. 6.4 (a) and 6.4 (b), respectively. It can be seen clearly that the numerical solutions agree well with the experimental results.

The LDG method can cope with large velocities as well. The numerical results for the current loop moving at velocity of v = 10 m/s and v = 100 m/s are illustrated in Fig. 6.3 (c) and 6.3 (d) for the equal potential lines of A. In Fig. 6.5 and Fig. 6.6, the r- and z- components of B are shown and it can be seen that the LDG solutions agree very well with the experimental data for these high speed velocity cases.

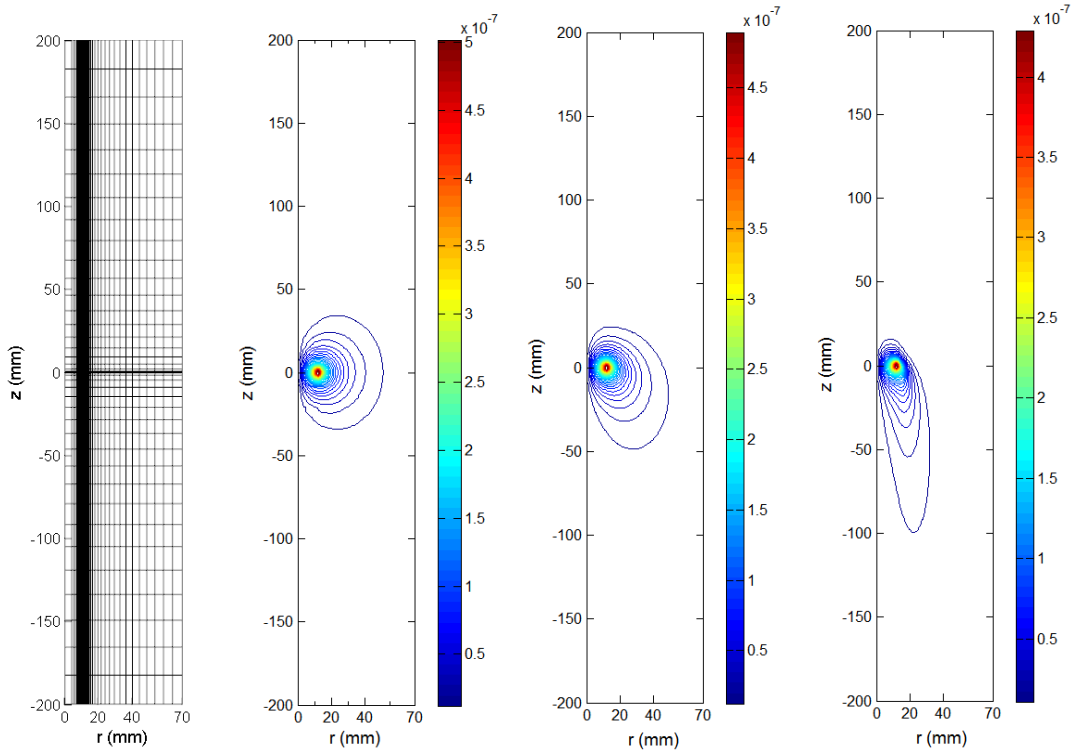

(a) (b) (c) (d)

Fig. 6.3. (a) The mesh for LDG computation. (b) The equal potential lines of A at v = 0 m/s. (c) The equal potential lines of the LDG solution of A at v = 10 m/s. (d) The equal potential lines of the LDG solution of A at v = 100 m/s.

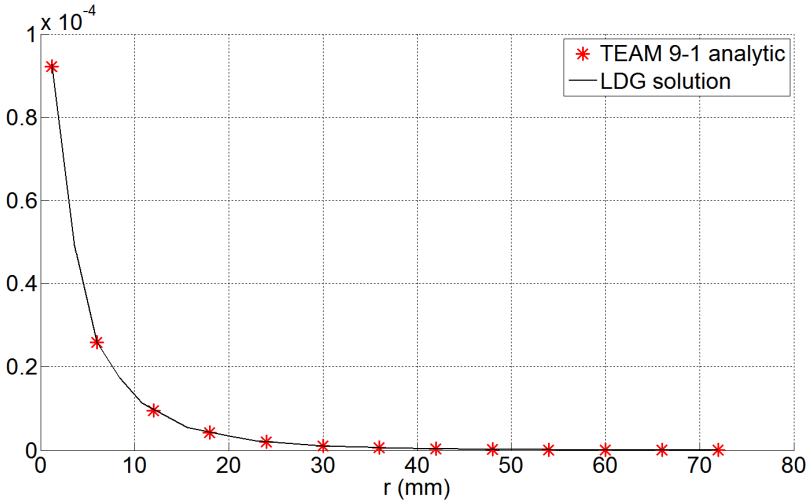

(a)

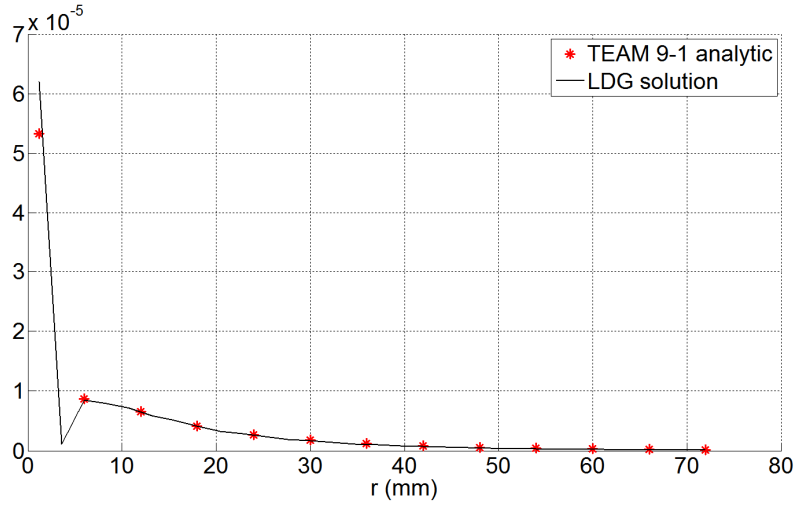

(b)

Fig. 6.4. (a) The *r*- component of B on L_a of the LDG solution for $v = 0$ m/s. (b) The *z*- component of B on L_a of the LDG solution for $v = 0$ m/s.

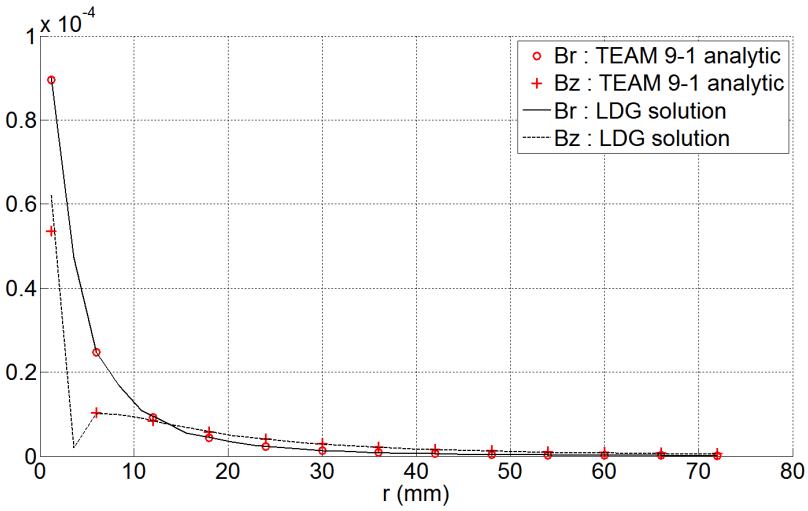

Fig. 6.5. The *r*- and z- components of B on L_a of the LDG solution for $v = 10$ m/s.

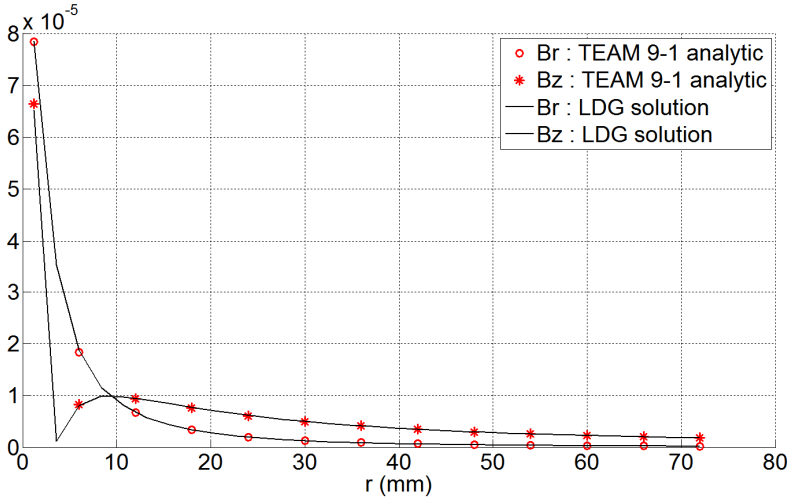

Fig. 6.6. The *r*- and z- components of B on L_a of the LDG solution for $v = 100$ m/s.

6.2.3. The DGM for Eddy-current Problems

The definition of the DG scheme for time-dependent eddy-current equation (6.1) is following the same way given in [F18]. Let A_h be the DG approximation of the unknown magnetic potential A in the space V_h, then multiply (4) by an arbitrary test function v_h in the same space V_h and integrate by parts, the semi-discrete DG formulation can be obtained as follows

$$\left(\sigma\frac{\partial A_h}{\partial t}, v_h\right)_\Omega + a_\varepsilon(A_h(t), v_h) + b(A_h(t), v_h) = L(A_h(t), v_h), \tag{6.12}$$

where the definitions of the operators $a_\varepsilon(u,w)$, $b(u,w)$ and $L(u,w)$ are given by

$$\begin{aligned} a_\varepsilon(u,w) = &\sum_{K\in T_h}\int_K \nu\nabla u\cdot\nabla w dV + \sum_{e\in E_h}\frac{m_0}{|e|^{n_0}}\int_e [[u]][[w]]ds - \\ &\sum_{e\in E_h}\int_e \{\{\nu\nabla u\}\}[[w]]ds + \varepsilon\sum_{e\in E_h}\int_e \{\{\nu\nabla w\}\}[[u]]ds \end{aligned}, \tag{6.13}$$

$$b(u,w) = -\sum_{K\in T_h}\int_K \vec{f}(u)\cdot\nabla w dV + \sum_{e\in E_h}\int_e \hat{u}[[w]]ds, \tag{6.14}$$

$$L(u,w) = \int_\Omega J_s(u)\cdot w dV, \tag{6.15}$$

where $|e|$ is the length of the edge e, $\hat{u}$ is the upwind convective flux which can also take other forms as given by [F11], m_0=1 and n_0=1 are stabilization parameters. In this thesis the parameter ε is set to be 1 and the resultant DG scheme is actually a non-symmetric interior penalty Galerkin method.

The nonlinear reluctivity in the DG formulation can be solved using traditional Newton-Raphson iteration method. At the starting time t=0, the initial value given by (6) is projected onto the DG space V_h. For time discretization of (9), the backward Euler scheme is used.

6.2.4. Adaptive DGM for Transient Field Analysis

For transient eddy-current problems, to capture the sharp solution fronts accurately and try to equi-distribute the numerical error on each element, each triangular element may be refined or coarsened according to the estimated elemental

errors at each time-step. In this thesis the elemental error estimator given in [E30] is used to determine how to adapt the mesh.

Suppose ξ_K is the calculated elemental error indicator, then every N time-steps later (N=30), the mesh is adapted in the following way: for each mesh adaption, first all the error indicators are sorted in an ascending order and then 30% of the elements with the largest errors are marked to be refined while 10% of the elements with the smallest errors are marked to be de-refined. In order to prevent the mesh from changing too drastically, the 1-irregulerity rule is enforced to maintain the quality of the mesh, where the refinement level number of any two edges in the same triangular element are not greater than 1 [F19].

For algorithm implementation, the parent-children mesh data structure for the nonconforming adaptive mesh is adopted. In computation, if an element K_1 is labeled to be refined, then this element itself is deactivated and its four children elements K_{11}, K_{12} K_{13}, and K_{14} are activated and vice versa, see Fig. 6.7. A sample nonconforming mesh with hanging nodes is also shown in Fig. 6.8.

After obtaining the new mesh, the solution on the old mesh is then projected onto the new mesh to continue the time-stepping computation process. To enhance the stability of DG scheme for convection-dominated problems, the slope limiter is also used to adjust the obtained numerical solution at each time-step [F20].

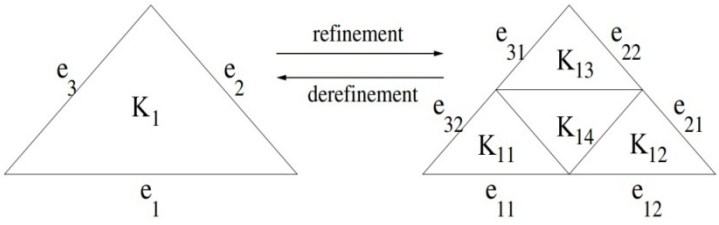

Fig. 6.7. A simple example illustrating the refinement and de-refinement operations.

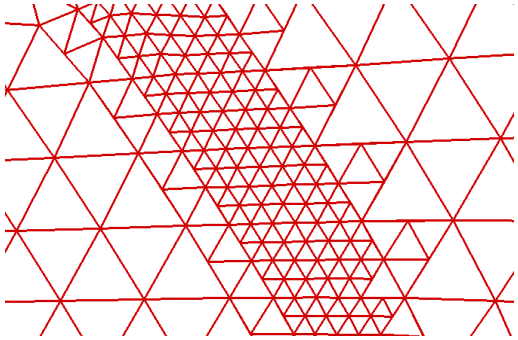

Fig. 6.8. A sample nonconforming mesh.

6.2.5. Application to TEAM Workshop Problem 30

A benchmark problem with a moving interface is solved by using the adaptive DG method. The problem domain is [-1,1]×[-1,1] and the control equation is given by

$$\frac{\partial u}{\partial t}+\frac{\partial}{\partial x}\left(\frac{u^2}{2}\right)+\frac{\partial}{\partial y}\left(\frac{u^2}{2}\right)=\frac{1}{\mathrm{Re}}\left(\frac{\partial^2 u}{\partial x^2}+\frac{\partial^2 u}{\partial y^2}\right), \tag{6.16}$$

The exact solution is given by the following equation

$$u(x,y,t)=\frac{1}{2}\{1-\tanh[\frac{\mathrm{Re}}{4}(x+y-t)]\}\,. \tag{6.17}$$

Take Re=1000 and compute to T_f=1.0, the meshes and the corresponding solution at t=0, t=0.5 and t=1.0 by using P^2 DG basis functions are shown in Figs. 6.9-6.11. From them one can clearly see that the sharp moving interfaces at different time instants have been well-resolved.

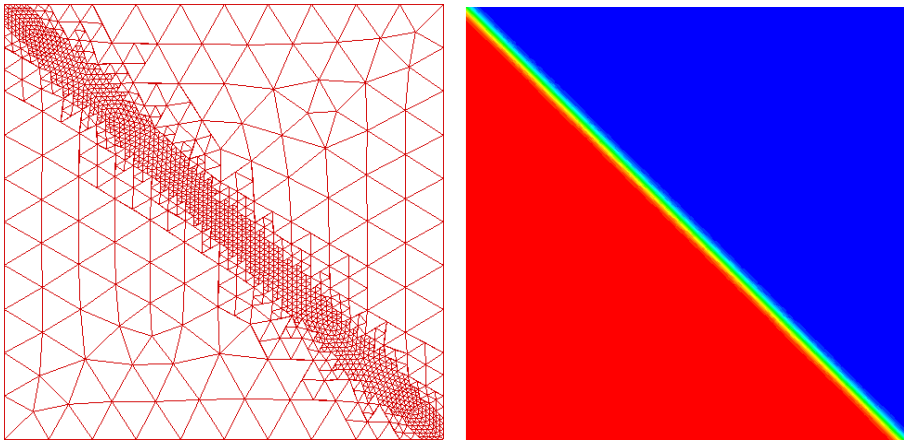

(a) (b)

Fig. 6.9. Adaptive mesh and solution contour at t=0.

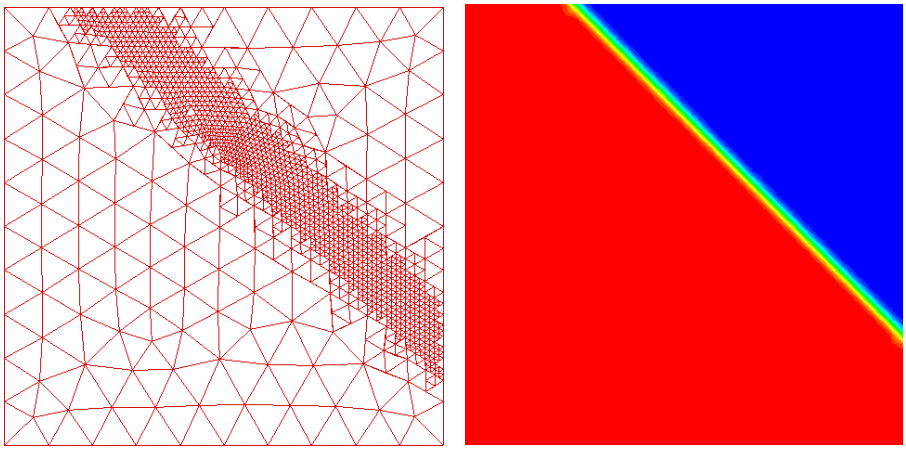

(a) (b)

Fig. 6.10. Adaptive mesh and solution contour t=0.5.

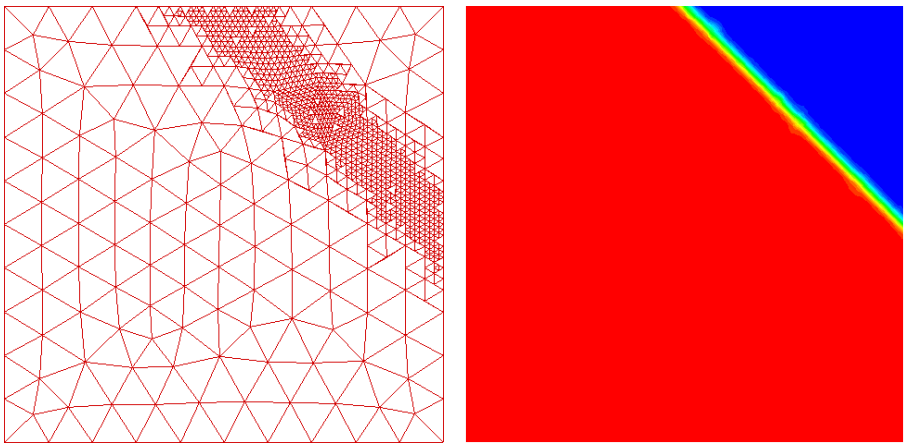

(a) (b)

Fig. 6.11. Adaptive mesh and solution contour t=1.0.

Select different rotation speeds, the magnetic fields are computed and the torque is also calculated to T_f=100ms for both problems. The torque errors of the DG method (P^2 DG basis functions are used and about 3700 nodes in the mesh) between the analytical values are shown in Fig. 6.12 and Fig. 6.13, respectively. For comparison, the results given in [A35] using the traditional FEM are used as reference solutions. Once can clearly see that when the rotor is rotating at high speeds, the torque calculated by using the adaptive DG method is more accurate than using the FEM.

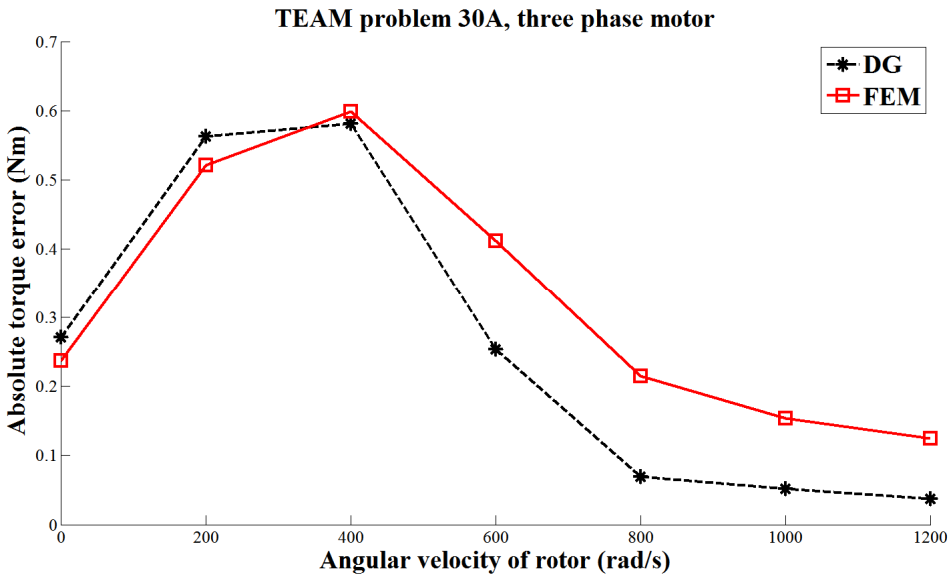

Fig. 6.12. Torque errors of the three-phase motor of the TEAM workshop problem 30A using DG and FEM for different rotor speeds.

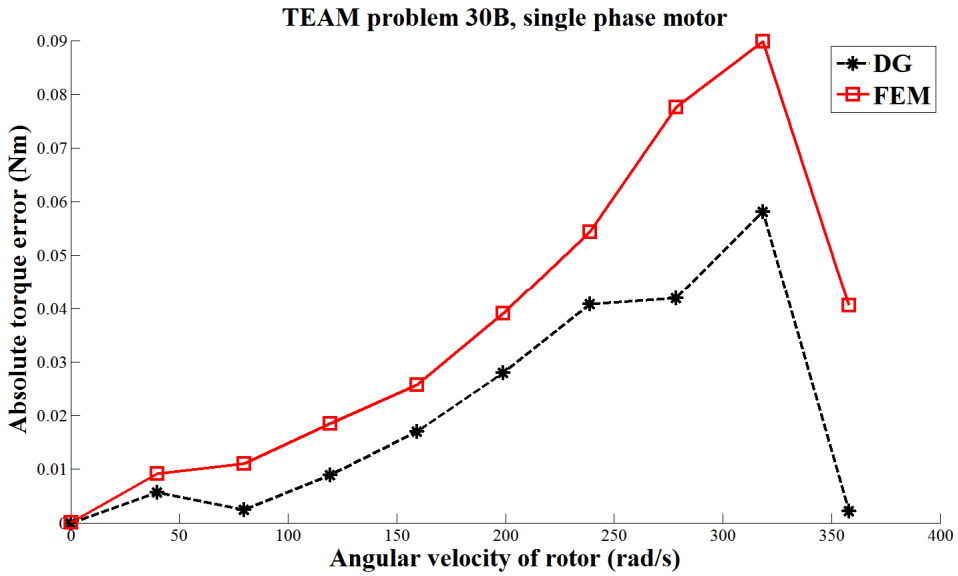

Fig. 6.13. Torque errors of the single-phase motor of the TEAM workshop problem 30B using DG and FEM for different rotor speeds.

6.3. Characteristic Galerkin Finite Element Method

In this section the Characteristic Galerkin Method (CGFEM), which needs only minor modification to the widely used FEM formulation, is used for the numerical solution of transient eddy-current problems with high rotor speed. Numerical experiments are also carried out to illustrate the effectiveness of CGFEM.

6.3.1. Introduction to CGFEM

CGFEM combines the FEM for spatial discretization and the backward-Euler method for temporal discretization of the time-dependent convection-diffusion problem defined in (6.1). To introduce the scheme of the CGFEM, suppose the convection term has the following form

$$\vec{f}(A) = \vec{v}A = (v_x A, v_y A), \tag{6.18}$$

then the weak problem of (6.1) is to find a solution A in the trial space U

$$\int_\Omega \sigma \frac{\partial A}{\partial t} w d\vec{x} + \int_\Omega \sigma \vec{v} \cdot \nabla A w d\vec{x} + \int_\Omega \nu \nabla A \cdot \nabla w d\vec{x} = \int_\Omega J_s w d\vec{x}\,, \tag{6.19}$$

for any test function w in the test space U at any time t.

For all numerical methods, an important issue is to define the unknowns to be solved and establish the algebraic linear equation of the original problem. For CGFEM, to define the unknowns, the domain Ω is divided into a set of triangular elements containing N nodes at which the degrees of freedom (DoFs) are defined. In the following numerical computation process, the equations of (1)-(3) are solved in the N-dimensional finite element space U_N, which is a subspace of U to which U_N converges when N approaches infinity. The unknown function A can be represented in the approximation space U_N as

$$A = \sum_{i=1}^{N} A_i(t)\varphi_i \,, \tag{6.20}$$

where $\{\varphi_i\}_{i=1}^{N}$ are the basis functions of U_N.

For any time t>0, one substitutes (5) into (4) and, assuming it is valid for each of the basis functions $\{\varphi_i\}_{i=1}^{N}$, then a system of ordinary differential equations (ODEs) consisting of N components is obtained as follows

$$M\frac{d\vec{A}(t)}{dt} + K\vec{A}(t) = \vec{F}(t)\,, \tag{6.21}$$

where $\vec{A}(t) = \{A_1(t), A_2(t), ..., A_N(t)\}^T$ is the column vector of all unknown nodal values (at t=0, $\vec{A}(0)$ is calculated from the initial condition (3)), M is the mass matrix, K is the stiffness matrix and $\vec{F}(t)$ is the source vector.

To discretize the ODEs (5) for the temporal variable t, a uniform time step size $\Delta t = T/N_t$ is used and the time levels are given by $t^n = n\Delta t$, n=1, 2, …, N_t. In practical engineering computations, the backward Euler scheme which is unconditionally stable is widely used and which reads

$$M\frac{\vec{A}^n - \vec{A}^{n-1}}{\Delta t} + K\vec{A}^n = \vec{F}^n\,. \tag{6.22}$$

Based on the method of characteristics, the main idea of the CGFEM is to adopt a backward tracing method by looking at which point, moving along the characteristics starting from $t=t_{n-1}$, that reaches the mesh node $\vec{x}$ at time level $t=t_n$. For the model equation (1), in order to solve for the solution of A at the n-th time level A^n, the first two terms of (1) are approximated by [F21, F22]

$$\sigma \frac{\partial A}{\partial t}|_{t^n} + \sigma \vec{v} \cdot \nabla A|_{t^n} \approx \sigma \frac{A^n - A^{n-1} \circ X^{n-1}}{\Delta t}, \tag{6.23}$$

where the symbol "$\circ$" is an operator which has similar meaning as the composite function and

$$X^{n-1}(\vec{x}) = \vec{x} - \vec{v}(t_{n-1}, \vec{x})dt \approx \vec{X}(t_{n-1}; t_n, \vec{x}), \tag{6.24}$$

is an Euler explicit approximation of the characteristics $\vec{X}(t; t_n, \vec{x}), t \in [t_{n-1}, t_n]$ is determined by

$$\begin{aligned} &\frac{d\vec{X}(t; t_n, \vec{x})}{dt} = \vec{v}(t, \vec{X}(t; t_n, \vec{x})) \\ &\vec{X}(t_n; t_n, \vec{x}) = \vec{x} \end{aligned}, \tag{6.25}$$

In short, it is noted that the characteristic curve $\vec{X}(t; t_n, \vec{x})$ is composed of the departure point at time t of a particle that arrives at mesh node $\vec{x}$ at time t_n. Finally, the CGFEM scheme for updating the solution from the (n-1)-th time to n-th time reads

$$\int_\Omega \sigma \frac{A^n - A^{n-1} \circ X^{n-1}}{\Delta t} w d\vec{x} + \int_\Omega \nu \nabla A^n \cdot \nabla w d\vec{x} = \int_\Omega J_s{}^n w d\vec{x}, \tag{6.26}$$

for any test function w in the finite element space U_N.

6.3.2. Application to An Artificial Problem

In this section, the performance and effectiveness of the CGFEM method are illustrated by several examples.

Firstly, a convection-diffusion problem, defined on the half unit circle with a large Peclet number (the convection coefficient is p=1000 and the diffusive coefficient is 1.0), is solved using the CGFEM. The control equation of the example is

$$\frac{\partial A}{\partial t} - p\frac{\partial A}{\partial x} - \frac{\partial^2 A}{\partial x^2} - \frac{\partial^2 A}{\partial y^2} = 0, \text{ in } \Omega = \{(x, y) \mid x^2 + y^2 < 1, y > 0\}, \tag{6.27}$$

the boundary conditions are

$$A(\vec{x}, t) = 1, \text{ on } \Gamma_1 = \{(x, y) \mid x^2 + y^2 = 1, y \geq 0\}, \tag{6.28}$$

$$\frac{\partial A(\vec{x}, t)}{\partial y} = 0, \text{ on } \Gamma_2 = \{(x, y) \mid -1 < x < 1, y = 0\}, \tag{6.29}$$

and the initial condition is A=0.

With a maximum mesh size of 1/30, the computed solution using the CGFEM at stopping time $1/p$ is shown in Fig. 6.14 (a). In Fig. 6.14 (b), the numerical result on the diameter is also shown. It can be seen that the boundary and internal layers of the solution have been well-resolved by CGFEM without oscillation. It is noted that if Standard Galerkin FEM (SGFEM) is used, the mesh size needs to be about 1/1000 (about two million nodes in the mesh) to ensure there is no spurious oscillation in the computed solution [F23]. It is obviously advantageous to use CGFEM rather than SGFEM for convection-dominated problems, as much less computer resource is needed by the former.

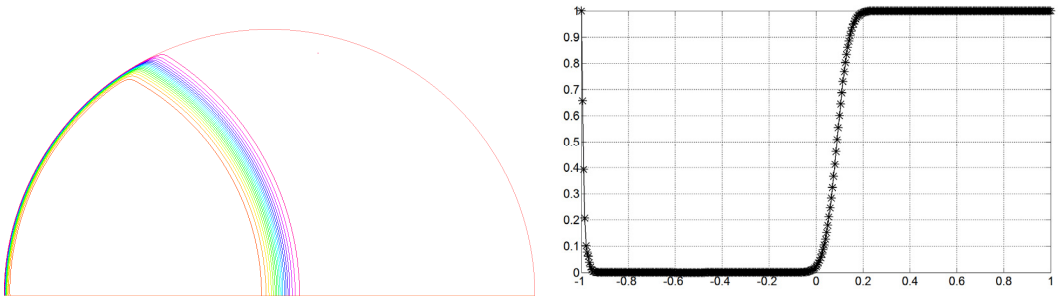

(a) (b)

Fig. 6.14. (a) The contour lines of the numerical solution at time T=1/1000 with p=1000. (b) The numerical solution on the diameter of the unit circle.

In the second example, the Peclet number is increased to an extremely large value of p=4000. Figs. 6.15(a)-(b) show the numerical results at stopping time 1/4000 with a maximum mesh size 1/100. It can be seen that the CGFEM still works well to produce non-oscillatory solution. From Figs. 6.14(a) and 6.15(a), it can be seen that as the Peclet number increases, the boundary and internal layers become thinner and thinner. Actually, it is these steep fronts appearing in convection-dominated problems that undermines the efficiency of SGFEM. However CGFEM still works well for convection-diffusion problems with large Peclet numbers and relatively small DOFs. Indeed, it is believed that the proposed method can efficiently and accurately solve problems with dominated convection terms.

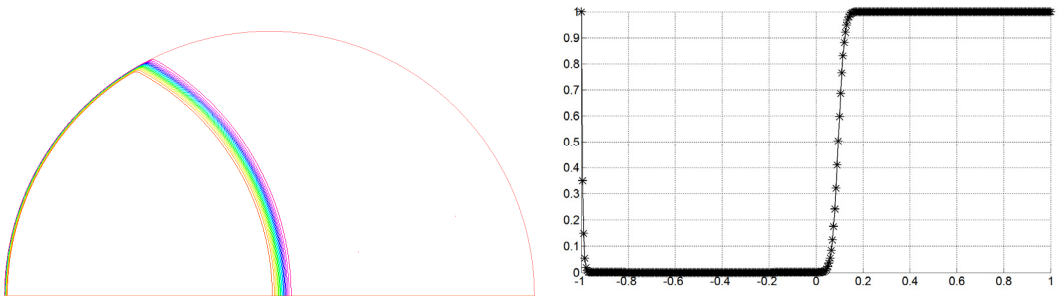

(a) (b)

Fig. 6.15. (a) The contour lines of the numerical solution at time T=1/4000 with p=4000. (b) The numerical solution on the diameter of the unit circle.

6.3.3. Application to TEAM Workshop Problem No. 30

For eddy-current problems when the rotor rotates at high speeds, the problems are convection-dominated. CGFEM can also be used to address the steep fronts effectively in the solution. The third example is a benchmark problem, the TEAM workshop problem 30A. The problem definition is given in Fig. 4.11, which is a three-phase induction motor with a solid rotor rotating at different speeds [D11].

The physical parameters (electric conductivity, magnetic permeability, applied source current density) are given in Fig. 4.11. The winding in the stator is excited at a frequency of 60 Hz. The rotor is made of steel (with electric conductivity σ =1.6×10^{6}S/m) and aluminum (with electric conductivity σ =3.72×10^{7}S/m), with the steel rotor surrounded by the aluminum rotor. The stator steel is laminated and its conductivity is assumed to be σ =0.

The problem is solved using CGFEM when the rotor rotates at a high angular speed of ω =1200rad/s counterclockwisely (the corresponding linear speed is calculated by $\vec{v}$ =[v_x,v_y]=[- ωy, ωx]). In this case, the maximum Peclet number is about 1683, and about ten thousand nodes are probably needed in the mesh if the SGFEM is used to obtain the non-oscillatory numerical solution. However, if CGFEM is used, only 829 nodes are enough and the computational mesh is shown in Fig. 6.16(a). Hence the computational effort for the CGFEM is much smaller than that of the SGFEM. To check the accuracy of the CGFEM, the rotational torque is also calculated and found to be -2.14476Nm, while the torque found by using SGFEM

(which has 20,000 nodes in the mesh) is -2.12514Nm [A35]. Since the analytical value is -2.24966Nm [A35], it is clear that CGFEM is more accurate even on a coarse mesh.

In the time-stepping analysis, at t=0, a static magnetic field is firstly computed to provide the initial values [A37]. Let $T_0=2\pi/\omega$, then the numerical solutions using CGFEM on the mesh as shown in Fig. 6.16(a) at t=0, $T_0/4$, $T_0/2$, $3T_0/4$ are given in Figs. 6.16(b)-6.16(e), respectively. Numerical results again show that CGFEM can generate good solutions for eddy-current problems at high rotor speed.

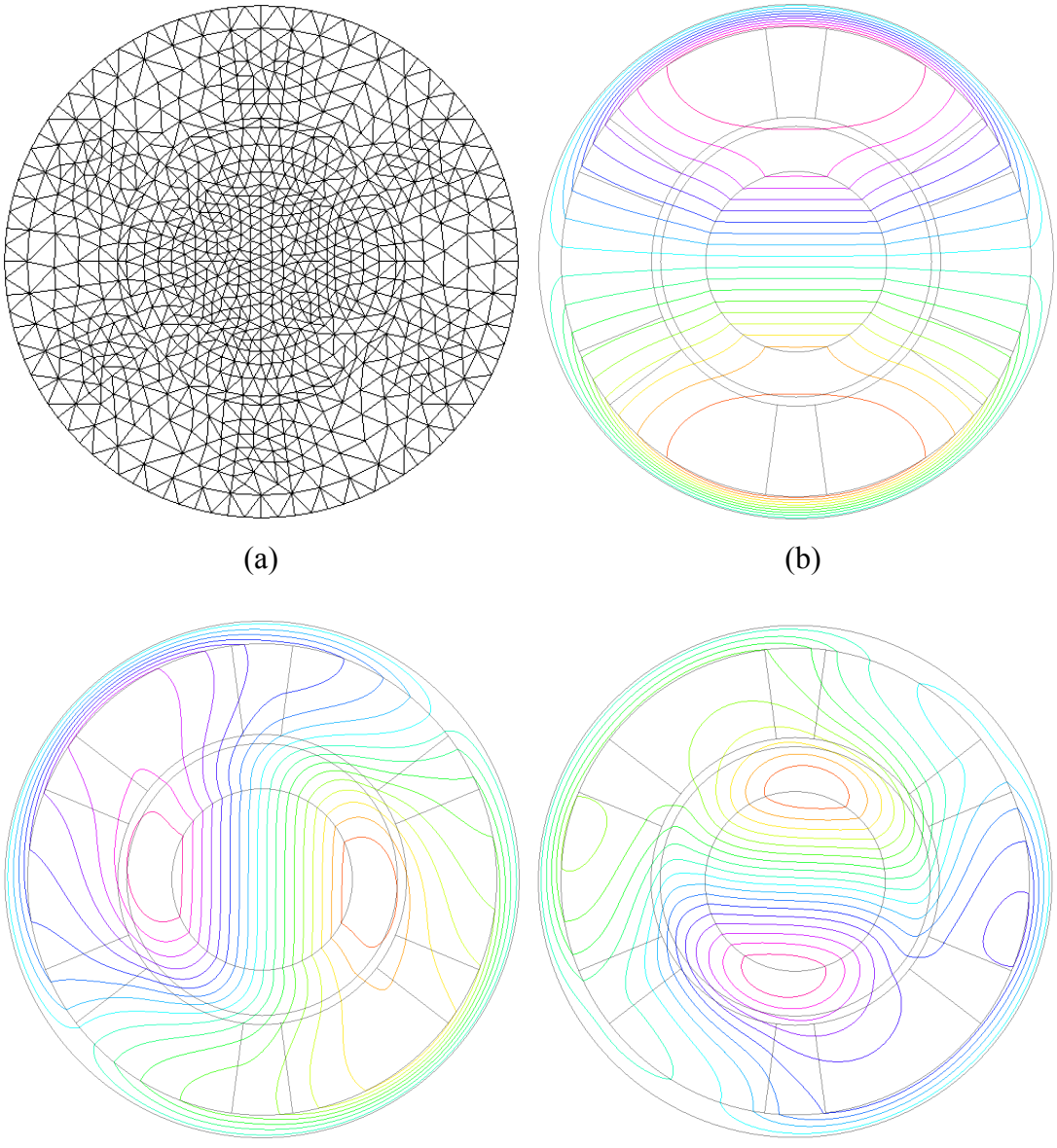

(a) (b)

(c) (d)

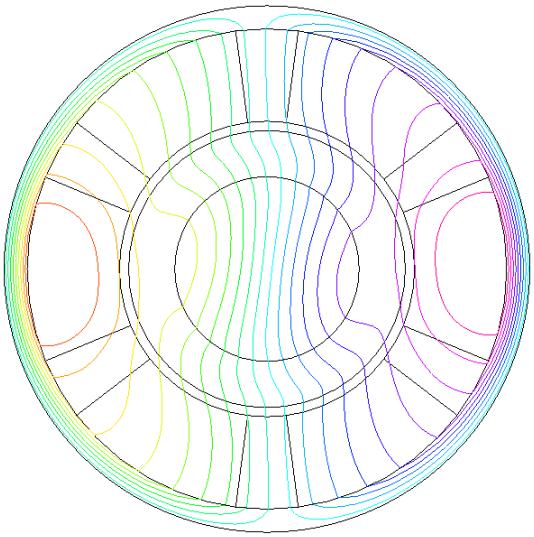

(e)

Fig. 6.16. (a) Mesh for TEAM workshop problem 30A with 829 nodes. (b) Initial solution of the magnetic potential A at t=0. (c) The solution A at time $t=T_0/4$, a quarter of period later. (d) The solution A at time $t=T_0/2$, a half period later. (e) The solution A at time $t=3T_0/4$.

6.4. Operator Splitting Method

In this section the operator splitting finite element method (OSFEM) [F24-F26] is proposed for numerically solving the transient eddy-current problem that may include high-speed rotation of a solid rotor. The motivation of the OSFEM is to isolate the convection part and diffusion part of the eddy-current equation to be solved. It is a divide-and-conquer strategy where the time evolution is split into partial steps to separate the effects of convection and diffusion in order to combine modern methods developed for hyperbolic equations and that for the parabolic equations readily. Moreover, it has also been reported that OSFEM is even superior to upwinding algorithms [F26].

To evaluate the performance and accuracy of OSFEM, an artificial example with extremely large convection coefficient is first calculated. Then two benchmark transient eddy-current field problems, the TEAM workshop problems 30A and 30B [A35], are used to test the accuracy of the method further. Numerical results show that

the solution obtained using the OSFEM is non-oscillatory even for convection dominated cases. Besides, the calculated torque values are more accurate using OSFEM when compared to those obtained using SGFEM. Consequently one concludes that the OSFEM can solve eddy-current problems with high-speed rotating conductors efficiently and accurately.

6.4.1. Introduction to Operator Splitting Method

In the OSFEM, the convective and diffusive terms of the original convection-diffusion equation are solved separately in each time step [F24, F25]. Suppose the time interval [0, T] has been divided into N equal sub-intervals with a time-step dt such that $0=t_0<t_1<\ldots<t_N=T$. For (6.1) and (6.18), the operator splitting method is to first solve the convective part which is a hyperbolic problem

$$\frac{\partial A}{\partial t}+\vec{v}\cdot\nabla A=0, t\in(t_{i-1},t_i),\ i=1,2,...,N\ , \tag{6.30}$$

with homogeneous Dirichlet boundary condition and initial condition $A(\vec{x},t_{i-1})=A_{h,i-1}$. $A_{h,i}^{1/2}$ denotes the computed solution of (6.30). The diffusive part of (1) reads

$$\sigma\frac{\partial A}{\partial t}-\frac{\partial}{\partial x}(\nu\frac{\partial A}{\partial x})-\frac{\partial}{\partial y}(\nu\frac{\partial A}{\partial y})=J_s, t\in(t_{i-1},t_i), i=1,2,...,N\ , \tag{6.31}$$

with homogeneous Dirichlet boundary condition and initial condition $A(\vec{x},t_{i-1})=A_{h,i}^{1/2}$ is then solved. The calculated solution is denoted as $A_{h,i}$.

As illustrated for the OSFEM scheme described above, in each time-step, the eddy-current equation (6.1) and (6.18) is split into two simple sub-problems. The pure convection problem (6.30) can be solved by using either analytical methods or any numerical method available for first order hyperbolic equations. The pure diffusion problem (6.31) can be solved by SGFEM with good stability and high accuracy. Hence the OSFEM is simple in idea and also easy to implement.

6.4.2. Application to TEAM Workshop Problem No. 30

To check the accuracy of the OSFEM, the electromagnetic torque of the rotor is calculated when it rotates at high speeds. The formulation for calculating the torque is

based on the Maxwell stress tensor method [D20]. All the computations are calculated to the stopping time of T=100ms for both the TEAM Problem 30A and 30B. The SGFEM solution in the time domain using A,V-A formulation numerical results reported in [A35] is used for comparison.

For TEAM Problem 30A, when the rotor rotates at different speeds, the torque values obtained by using OSFEM and SGFEM versus the analytical ones [F27] are given in Table 6.1. There are 2990 nodes in the mesh for OSFEM and there are about 20,000 nodes in the mesh for SGFEM in the numerical computation process. From Table 6.1 it is clear that the OSFEM is more accurate even with a lesser number of DoFs than that of the SGFEM at high rotor speeds. For example, when the rotor rotates at a high speed of 600 rad/s, the steady torque obtained is -5.5363Nm by using the OSFEM. The accuracy is very satisfactory because the analytical one is -5.75939Nm. While the torque value obtained by using the SGFEM is -5.3482Nm.

When the rotor rotates at an even higher speed of 1200 rad/s, the calculated steady torque is -2.2239Nm using the OSFEM, while the torque value obtained using the SGFEM in time-domain is -2.1249Nm. All these are compared to the analytical value of -2.24996Nm. Again it is clear that the OSFEM is more accurate even with a less number of degrees of freedom. In Figs. 6.17 and 6.18, the torque of the rotor versus time is also shown when the rotor rotates at 600rad/s and 1200rad/s.

Rotor speed (rad/s)	Analytical (Nm)[F27]	OSFEM (Nm)	SGFEM (Nm)[A35]
0	3.825857	3.46526	3.5884
200	6.505013	5.97154	5.9835
400	-3.89264	-3.32115	-3.2941
600	-5.75939	-5.5363	-5.3482
800	-3.59076	-3.5510	-3.3763
1000	-2.70051	-2.6884	-2.5472
1200	-2.24996	-2.2239	-2.1249

Table 6.1. Numerical comparison of the torque values computed by OSFEM and SGFEM for TEAM problem 30A.

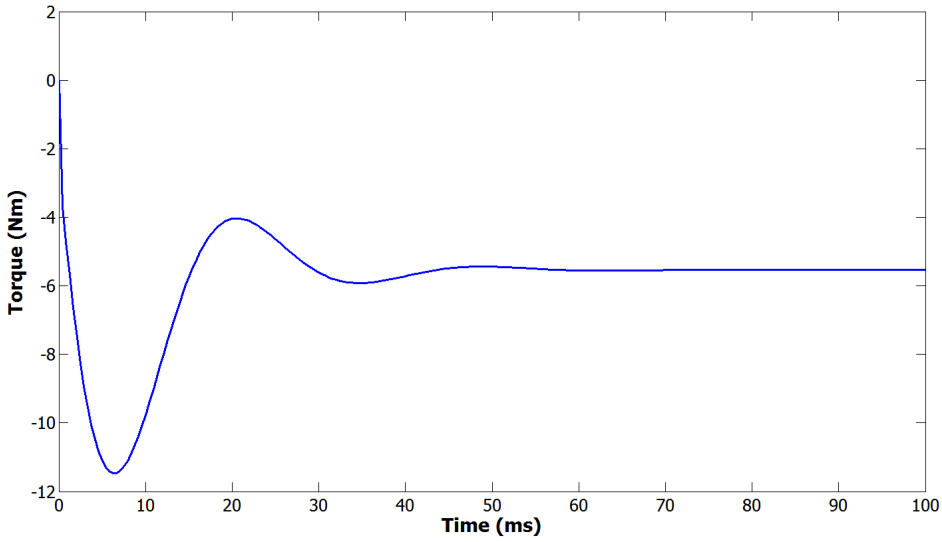

Fig. 6.17. The electromagnetic torque of the rotor versus time for TEAM workshop problem 30A. The rotor speed is 600rad/s.

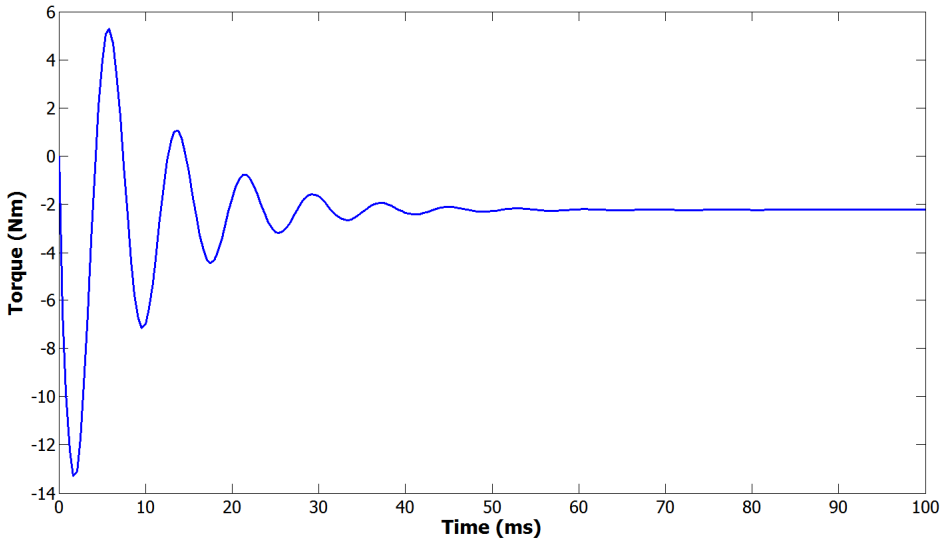

Fig. 6.18. The electromagnetic torque of the rotor versus time for TEAM workshop problem 30A. The rotor speed is 1200rad/s.

When the rotor rotates at different speeds, the torque-speed characteristics of the three-phase motor and the single-phase motor are given in Figs. 6.19 and 6.20, respectively. For comparison, the numerical results using *A*,*V*-*A* formulation in time-domain as given in [A35] are used as the SGFEM solution. One can again observe that the torque values calculated using the OSFEM is more accurate than using the SGFEM.

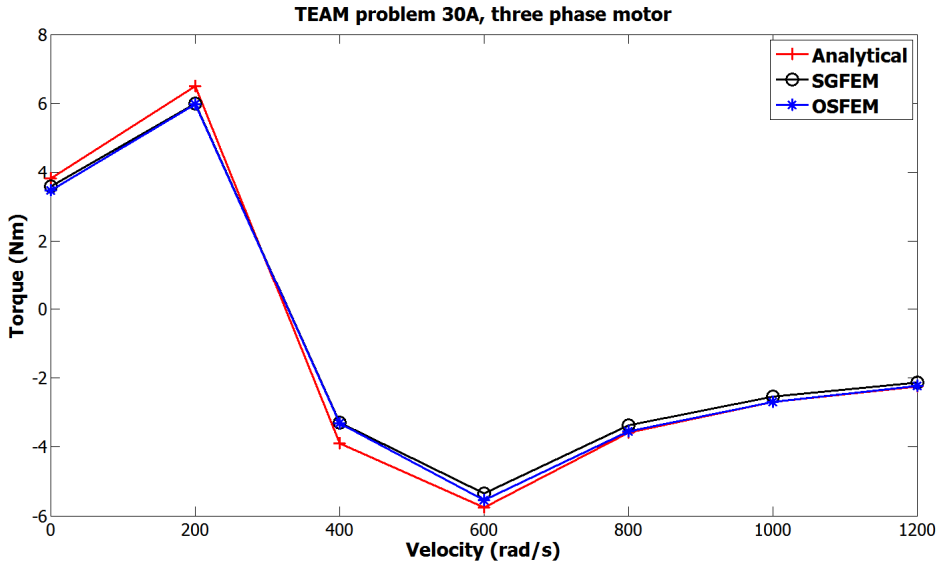

Fig. 6.19. Torque-speed characteristics of the three-phase motor of the TEAM workshop problem 30A.

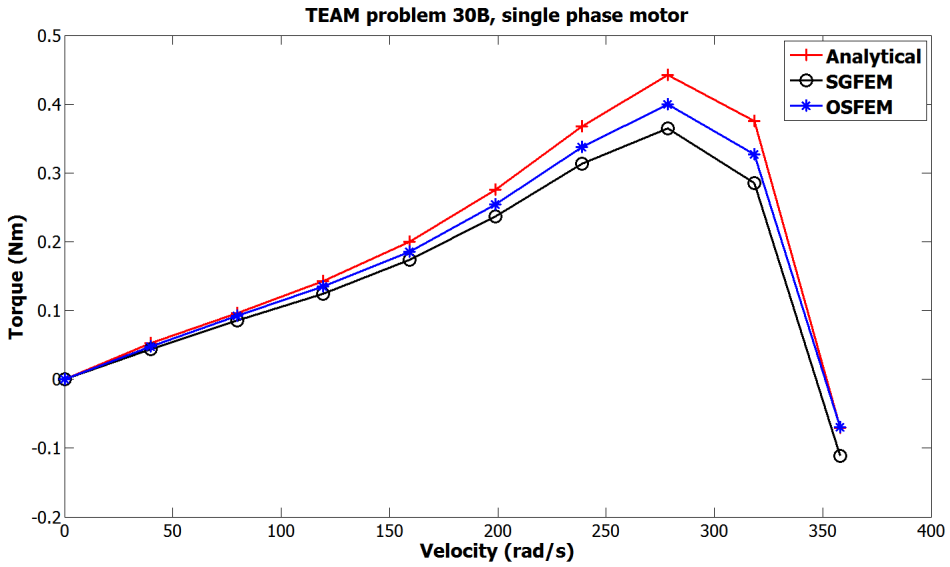

Fig. 6.20. Torque-speed characteristics of the single-phase motor of the TEAM workshop problem 30B.

6.5. Summary

The EM fields in high-speed moving conductors usually present thin eddy-current layers, the accurate solution of these fields needs special numerical techniques. In this chapter, three numerical methods were proposed to capture the thin eddy-current layers efficiently, including the (adaptive) DGM, the CGFEM and the OSM.

Benchmark TEAM workshop problems are solved by these methods and the classical FEM, numerical comparisons are carried out to show the accuracy and effectiveness of the proposed methods.

6.6. References-Part F

[F1] H. D. Gersem, H.V. Sande, and K. Hameyer, "Motional magnetic finite element method applied to high speed rotating devices," *COMPEL: Int. J. Computat. Math. Elect. Electron. Eng.*, vol. 19, no. 2, pp. 446-451, 2000.

[F2] H. D. Gersem, and K. Hameyer, "Finite element simulation of a magnetic brake with a soft magnetic solid iron rotor," *COMPEL: Int. J. Computat. Math. Elect. Electron. Eng.*, vol. 21, no. 2, pp. 296-306, 2002.

[F3] H. D. Gersem, "Spectral-element method for high-speed rotating cylinders," *COMPEL: Int. J. Computat. Math. Elect. Electron. Eng.*, vol. 28, no. 3, pp. 730-740, 2009.

[F4] H. D. Gersem, "Combined spectral-element, finite-element discretization for magnetic-brake simulation," *IEEE Trans. Magn.*, vol. 46, no. 8, pp. 3520-3523, Aug. 2010.

[F5] I. A. Tsukerman, "Overlapping finite elements for problems with movement," *IEEE Trans. Magn.*, vol. 28, no. 5, pp. 2247-2249, Sep. 1992.

[F6] A. Buffa, Y. Maday, and F. Rapetti, "Calculation of eddy currents in moving structures by a sliding mesh-finite element method," *IEEE Trans. Magn.*, vol. 36, no. 4, pp. 1356-1359, Jul. 2000.

[F7] P. Alotto, A. Bertoni, I. Perugia, and D. Schotzau, "Discontinuous finite element methods for the simulation of rotating electrical machines," *COMPEL*, *Int. J. Comput. Math. Electr. Electron. Eng.*, vol. 20, no. 2, pp. 448-462, 2001.

[F8] O. J. Antunes, J. P. A. Bastos, and N. Sadowski, "Using high-order finite elements in problems with movement," *IEEE Trans. Magn.*, vol. 40, no. 2, pp. 529-532, Mar. 2004.

[F9] H. L. Li, S. L. Ho, and W. N. Fu, “Precise magnetic field modeling techniques of rotary machines using transient finite-element method,” *IEEE Trans. Magn.*, vol. 48, no. 11, pp. 4192-4195, Nov. 2012.

[F10] R. Li, T. Tang, and P. W. Zhang, “Moving mesh methods in multiple dimensions based on harmonic maps,” *J. Computat. Phys.*, vol. 170, no. 2, pp. 562-588, 2001.

[F11] B. Cockburn and C. W. Shu, “Runge-Kutta discontinuous Galerkin method for convection-dominated problems,” *J. Sci. Comput.*, vol. 16, no. 3, pp. 173-261, Sep. 2001.

[F12] Q. Zhang, and Z.-L. Wu, “Numerical simulation for porous medium equation by local discontinuous Galerkin finite element method,” *J. Sci. Comput.*, vol. 38, no. 2, pp.127-148, 2009.

[F13] A. Dedner, and R. Klöfkorn, “A generic stabilization approach for higher order discontinuous Galerkin methods for convection dominated problems,” *J. Sci. Comput.*, vol. 47, pp. 365-388, 2011.

[F14] J. X. Qiu, B. C. Khoo, and C. W. Shu, “A numerical study for the performance of the Runge-Kutta discontinuous Galerkin method based on different numerical fluxes,” *J. Comp. Phys.*, vol. 212, pp. 540-565, 2006.

[F15] E. X. Xu, J. Simkin, and S. C. Taylor, “Streamline upwinding in a 3-D edge-element method modeling eddy currents in moving conductors,” *IEEE Trans. Magn.*, vol. 42, no. 2, pp. 667-670, Apr. 2006.

[F16] Y. Gan, J. J. Ruan, Y. Zhang, and W. P. Shuai, “Discussion of the TEAM9-1 problem and application of the hybrid finite element and finite volume method,” *Trans. China Electro-Techn. Soc.*, vol. 24, no. 1, pp. 1-7, 2009.

[F17] J. B. M. Melissen, and J. Simkin, “A new coordinate transform for the finite element solution of axisymmetric problems in magnetostatics,” *IEEE Trans. Magn.*, vol. 26, no. 2, pp. 391-394, Mar. 1990.

[F18] B. Riviere, Discontinuous Galerkin Methods for Solving Elliptic and Parabolic Problems: Theory and Implementation. Philadelphia, PA, USA: SIAM, 2008.

[F19] P. Solin, J. Cerveny, and I. Dolezel, “Arbitrary-level hanging nodes and automatic adaptivity in the hp-FEM,” *Math. Comput. Simul.*, vol. 77, no. 1, pp. 117-132, Feb. 2008.

[F20] W. Klieber, and B. Riviere, “Adaptive simulations of two-phase flow by discontinuous Galerkin methods,” *Comput. Methods Appl. Mech. Eng.*, vol. 196, nos. 1-3, pp. 404-419, Dec. 2006.

[F21] J. Kacur, “Solution of degenerate convection-diffusion problems by the method of characteristics,” *SIAM J. Numer. Anal.*, vol. 39, no. 3, pp. 858-879, 2001.

[F22] A. Quarteroni, and A. Valli, Numerical Approximation of Partial Differential Equations. New York: Springer-Verlag, 1994.

[F23] T. Ikeda, Maximum Principle in Finite Element Models for Convection-Diffusion Phenomena. Amsterdam, The Netherlands: North-Holland, 1983.

[F24] A. Quarteroni, and A. Valli, Numerical Approximation of Partial Differential Equations. New York: Springer-Verlag, 1994.

[F25] M. Remesikova, “Numerical solution of two-dimensional convection-diffusion-adsorption problems using an operator splitting scheme,” *Appl. Math. Computat.*, vol. 184, pp. 116-130, 2007.

[F26] D. Mishraa, K. Muralidhar, and P. S. Ghoshdastidar, “Computation of flow and heat transfer around a vertical discrete protruding heater using an operator-splitting algorithm,” *Numer. Heat Transfer, Part A: Appl.: Int. J. Computat. Meth.*, vol. 28, no. 1, pp. 103-119, 1995.

[F27] K. R. Davey, “Analytic analysis of single- and three-phase induction motors,” *IEEE Trans. Magn.*, vol. 34, no. 5, pp. 3721-3727, Sep. 1998.

CHAPTER 7

APPLICATION OF THE COUPLED METHOD IN OPTIMAL DESIGN OF EM DEVICES

7.1. Integrating FEM with Global Optimization Method

Electromagnetic (EM) devices such as permanent magnet (PM) motors are widely used in industry. Good designs of PM motors with high performance and high reliability can greatly reduce energy losses during the energy conversion process. Unfortunately, the motor design process is complicated and time consuming because the products are required to meet several special specifications under many design parameters [G1-G4]. To avoid the expensive prototyping, optimal design by use of computers is needed to find the best design before manufacturing. Mathematically, this is a multiobjective optimization problem to find the optimal solution to meet multiple performance parameters under constraints of the design variables. In practice, single objective optimization is the most popular, which can be also used to solve multiobjective optimization problems by using the weighed sum method [G5].

Of the optimal design problems, sizing [G1-G4] and shape optimization [G6-G10] is of paramount importance. With the fast increase of the computational ability of digital computers and thanks to the versatility of the finite element method (FEM) for field computation, the objective function values can be extracted from the numerical solution by postprocessing for a design with a set of chosen design parameters. In this process, FEM is much more widely used than analytical approach in order to get motor parameters, including machine parameters that can be computed by static field analysis (air-gap flux density that the PM and armature winding act on alone, no-load back electromotive force (EMF) and the thrust force in steady-state operation) and those must be computed by transient field analysis (torque, loss or the efficiency).

Nowadays, the combination of FEM with stochastic or evolutionary optimization solvers makes the field computation to be successfully extended to the design stage and greatly useful in the design phase of various EM devices [G1-G4, G6, G10]. To

combine the finite element (FE) solver with evolutionary optimization algorithms in the design optimization process, there are two ways available. Firstly, one can directly couple the optimization solver with the FE solver to compute the objective function values. One can initialize the stochastic optimization solver an generate an initial population of individuals, call the FE solver to get the objective function values for each individual and generate the new population again and again until the stopping criterion is met.

Another choice is to use the response surface method (RSM) [A54-A55, G4, G10] to reconstruct a relationship of the objective functions and the design variables through chosen design parameters and observed response data from the system by FE computation, then the optimization solver will find the global optimal solution from the response surface function instead of directly calling the FE solver to get the objective function values to save computational time. In the following section, the popular evolutionary algorithms widely used in industry is briefly reviewed. Optimal design examples are also solved using the developed remesh-free FEM and global optimal solvers.

7.2. Shape Optimization of A DC Magnet Device

In this section, an optimal shape design problem is solved using the FEM with the developed remesh-free mesh deformation technique and the Tabu Search Algorithm (TSA). The direct current (DC) magnet device is shown in Fig. 7.1, where the pole shape *AB* is to be optimized to generate a magnetic flux density as uniform as possible in the observation line *CD*. Due to symmetry, only the right half of the problem domain is illustrated. For this problem, the design variables are taken to be $\{x_0,\ y_0,\ r_0\}$ as shown in Fig. 7.2. The ranges of the design variables are $55\text{mm}<x_0<65\text{mm}$, $-55\text{mm}<y_0<-15\text{mm}$ and $18\text{mm}<r_0<60\text{mm}$. There are also additional two constraints of the design variables,

$$\begin{cases} y_A = r_0\sin(\pi\text{-acos}(x_0\text{-}50)/r_0)+y_0 \geq 5, \\ y_B = r_0\sin(\text{acos}(70\text{-}x_0)/r_0)+y_0 \geq 5. \end{cases} \tag{7.1}$$

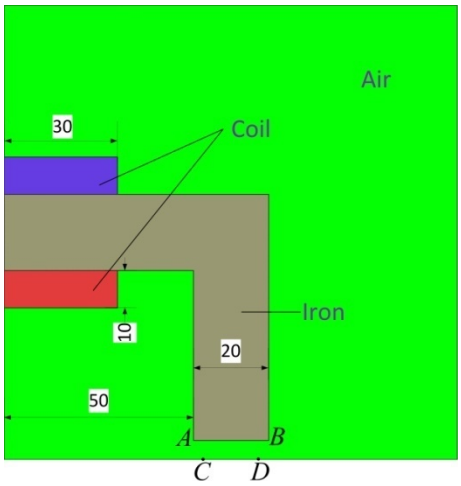

Fig. 7.1. An optimal shape design problem, where the shape of *AB* is to be optimized to generate uniform magnetic density on the line of *CD* in the center line of the airgap. The dimensions of the DC magnet is given in the unit of mm.

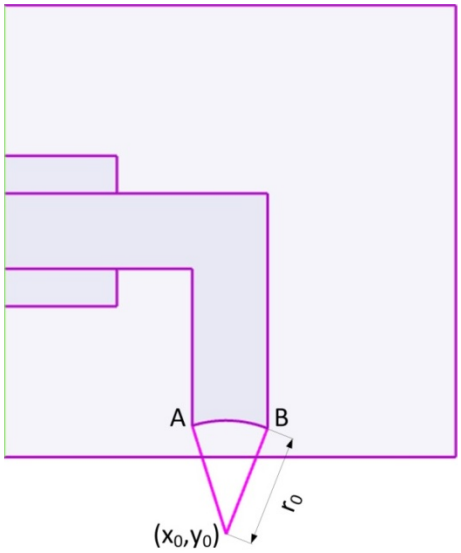

Fig. 7.2. The shape of *AB* is to be optimized with the design variables $\{x_0, y_0, r_0\}$.

In the shape design process, the mesh needs to be deformed according to the change of the design parameters. By using the developed remesh-free mesh deformation technique as stated in chapter 3, no mesh-regeneration is needed. One FE mesh is shown in Fig. 7.3(a), the initial boundary mesh is given in Fig.7.3(b). The deformed boundary mesh is shown in Fig. 7.3(c), and the final deformed mesh is given in Fig. 7.3(d). In Fig. 7.4, the enlarged view of the meshes before and after deformation are plotted together, where the original mesh is plotted with thick lines and the deformed mesh is plotted with thin lines. The arrows represent the nodal displacement vectors for each node in the mesh before deformation.

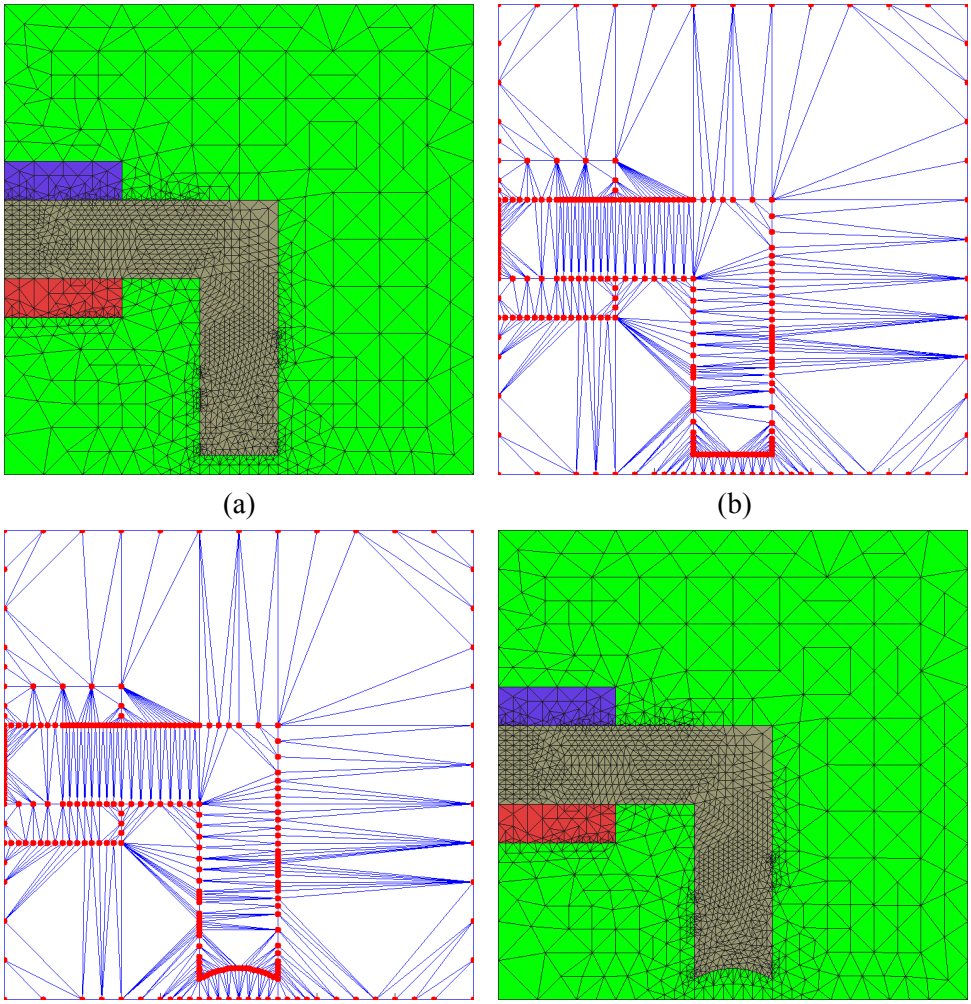

Fig. 7.3. (a) The FE mesh before deformation. (b) The boundary mesh with red dots indicating the boundary nodes. (c) The deformed boundary mesh. (d) The FE mesh after deformation.

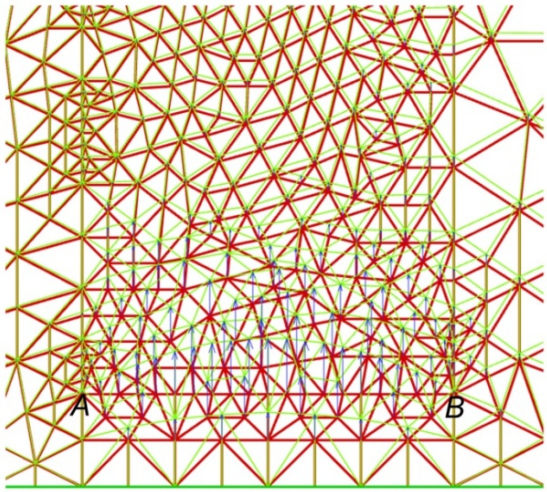

Fig. 7.4. Illustration of the nodal displacement vectors by using the remesh-free mesh deformation method.

The TSA is used to find the optimal solution. In the computation, the population size is taken to be 20 and the maximum iteration number is taken to be 200. The optimal solution is found to be $\{x_0$=60.1798mm, y_0=26.5629mm, r_0=36.1074mm$\}$ and the corresponding geometry is given in Fig. 7.5(a). The numerical solution on the optimal geometry is shown in Fig. 7.5(b). In Figs. 7.6(a) and 7.6(b), the magnetic flux density vector on the line *CD*, as indicated in Fig. 7.1, are given for an initial pole shape and the optimized shape, where one can see that the flux density is uniform and very close to the desired value of 0.04T by performing optimal design.

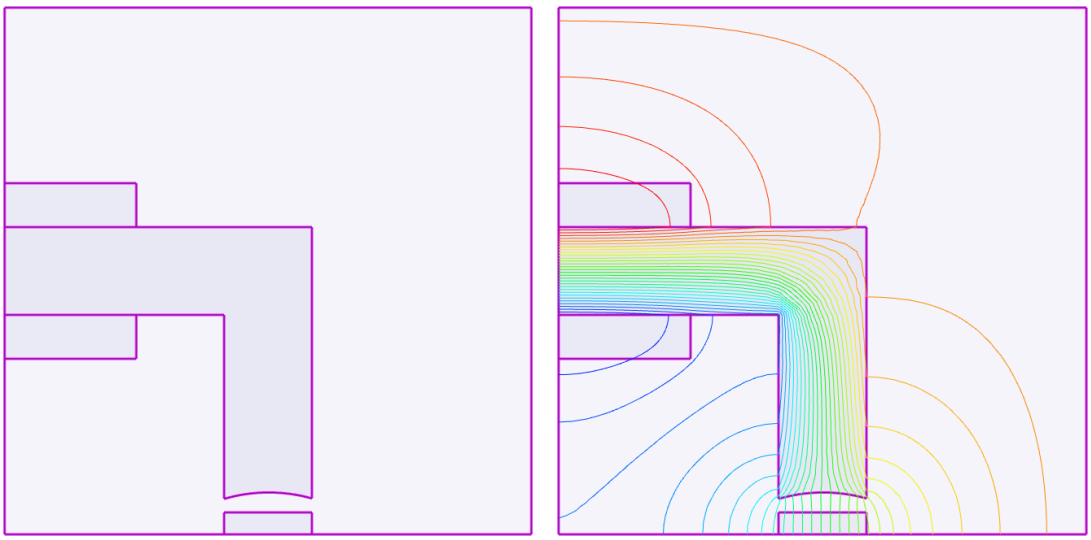

(a) (b)

Fig. 7.5. (a) The optimized pole shape. (b) The flux lines on the geometry with the optimal pole shape.

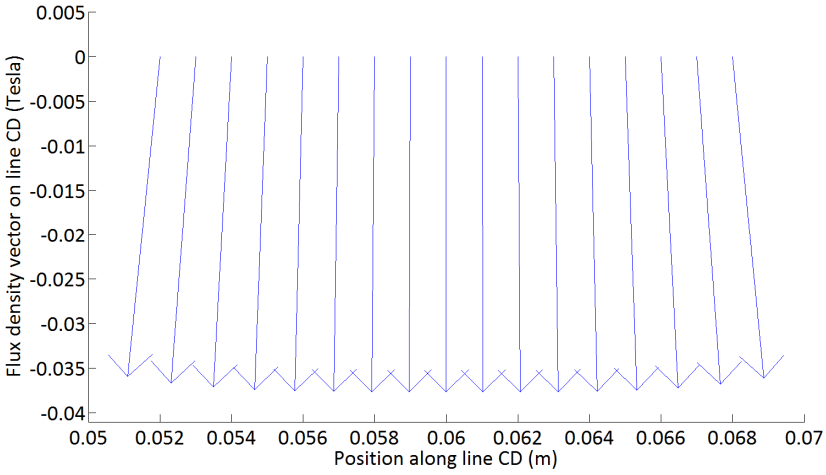

(a)

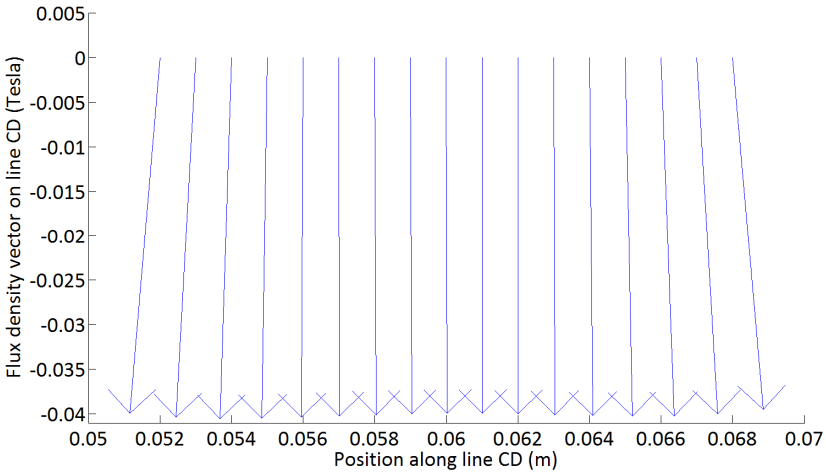

(b)

Fig. 7.6. (a) The magnetic flux density on the observation line *CD* for an initial pole shape. (b) The magnetic flux density on the observation line *CD* for the optimized pole shape.

7.3. A Benchmark 2D Sizing Design Problem

The remesh-free FEM coupled with evolutionary optimization method is applied to a nonlinear magneto-static benchmark sizing design problem, the TEAM Workshop Problem 25 [D9, G11, G12] as shown in Fig. 7.7, where the stranded coils carry a DC current excitation of 4253 Ampere-Turns (AT). The nonlinear *B-H* curve of the ferromagnetic pole piece is given in Fig. 4.6. Due to symmetry, one can solve the problem in one fourth of the whole problem domain, as shown in Fig. 7.7.

The objective is to optimize the shape of the die press to generate radially distributed magnetic flux density in the die mold. There are totally four sizing parameters $\{R_1, L_2, L_3, L_4\}$ to be optimized as illustrated in Fig. 7.8 (see also Fig. 4.4). The geometric constraints of the design parameters are given by 5mm$<R_1<$9.4mm, 12.6mm$<L_2<$18mm, 14mm$<L_3<$45mm and 4mm$<L_4<$19mm. The aim of the design optimization is to minimize the following objective function

$$W = \sum_{i=1}^{n} [(B_{xp_i} - B_{xo_i})^2 + (B_{yp_i} - B_{yo_i})^2], \tag{7.2}$$

where n is the number of specified points along the test line *e-f* (n=10); B_{xp} and B_{yp} are the respective computed x- and y- components of the magnetic flux density values along the line *e-f*; B_{xo} and B_{yo} are the desired value specified as B_{xo}=0.35cos(θ) (T), B_{yo}=0.35sin(θ) (T).

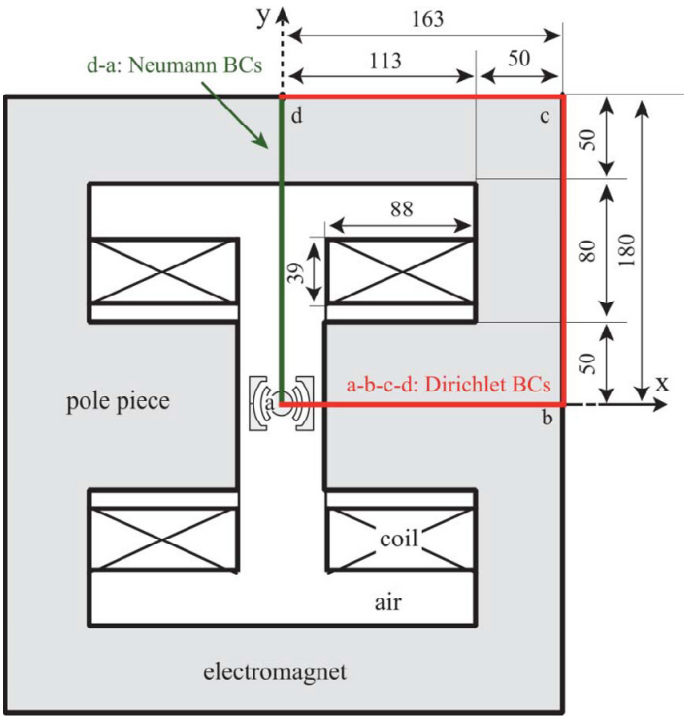

Fig. 7.7. Illustration of the whole model of the TEAM Workshop Problem 25.

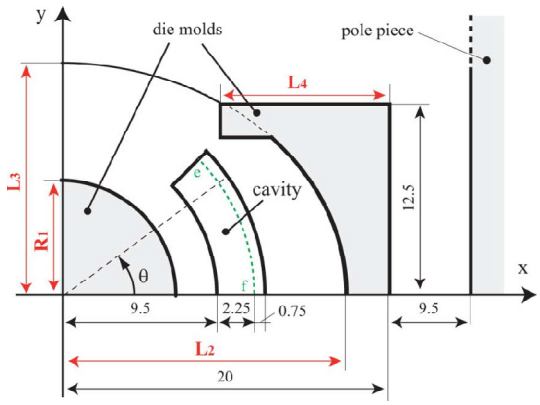

Fig. 7.8. Enlarged view of the die molds of TEAM Workshop Problem 25, the shape design parameters are R_1, L_2, L_3 and L_4.

The initial boundary mesh of the problem domain and the fine mesh after 5 adaptive refinements (30% elements in the mesh are refined each time) are shown in Figs. 7.9 (a)-(b), respectively. The RSM is adopted here to reconstruct the objective function and then the Differential Evolution Algorithm (DEA) is used to find the optimal solution. The design parameters are swept 10^4 times, with 10 sample values for each parameter.

Using the RSM and the DEA (Np=40, G_{max}=100), the optimal solution calculated is R_1=7.18mm, L_2=13.75mm, L_3=13.97mm, L_4=14.63mm with the optimal objective

function value $W_{opt}=1.43\times10^{-4}$, which is close to the results given in [G13]. The optimized shape of the device is shown in Fig. 7.10(a) and the computed flux line distribution are given in Fig. 7.10 (b), where one can see the radial distribution of the magnetic flux lines in the cavity region shown in Fig. 7.8.

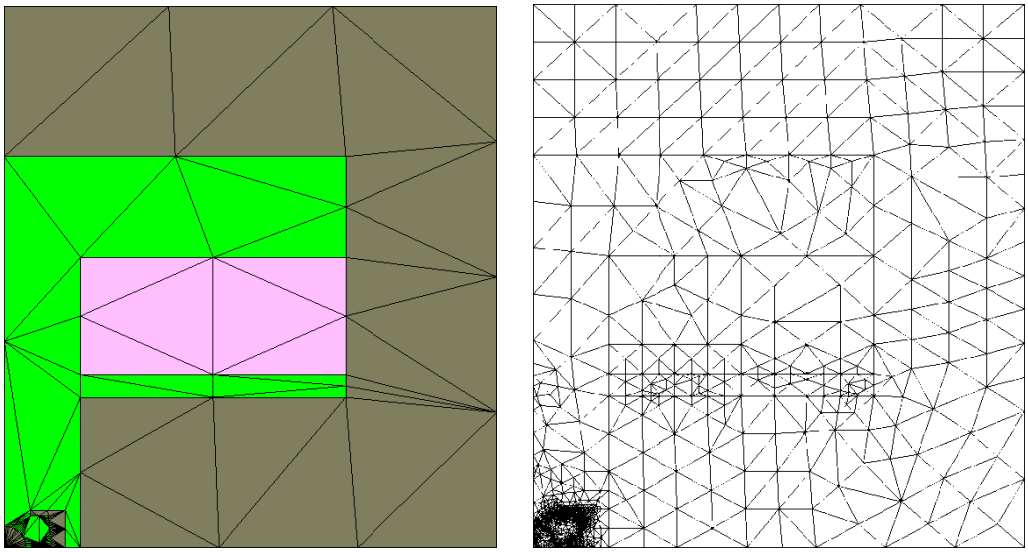

(a) (b)

Fig. 7.9. (a) Initial mesh for TEAM Workshop Problem 25 with shape parameters $\{R_1=7.2\text{mm}, L_2=15.3\text{mm}, L_3=29.5\text{mm}, L_4=11.5\text{mm}\}$. (b) The fine mesh obtained after 5 adaptive refinements.

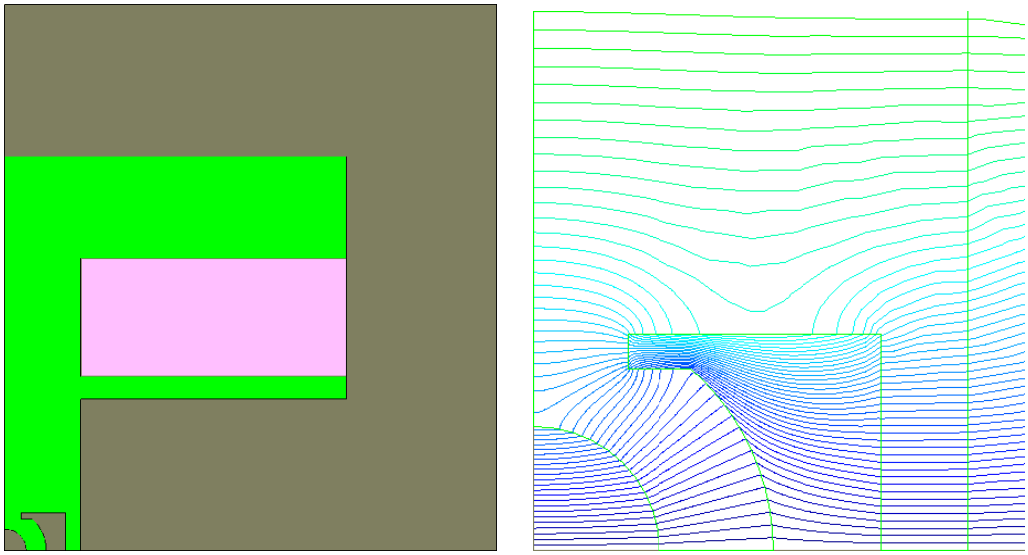

(a) (b)

Fig. 7.10. (a) TEAM Workshop Problem 25, optimal shape with $\{R_1=7.18\text{mm}, L_2=13.75\text{mm}, L_3=13.97\text{mm}, L_4=14.63\text{mm}\}$ by using the DE algorithm with RSM. (b) The equipotential lines in the domain with optimal mold shape.

7.4. A Practical PM Motor Sizing Design Problem

In this example, the geometrical parameters of a PM motor with 24 slots and 4 PM poles is optimized, aiming to maximize the magnetic flux of the windings. The design parameters are set to be the thickness of the PM p_1, the embrace ratio of the PM p_2 and the distance between slots or the width of the tooth of the stator p_3. There are totally three parameters $\{p\}=\{p_1, p_2, p_3\}$ to sweep for the design analysis, the constrains are 2 mm $\le p_1 \le$10 mm, 0.7 $\le p_2 \le$ 0.99, 4 mm$\le p_3 \le$6 mm. The initial geometry of the motor when p_1 = 3 mm, p_2 = 0.7, p_3 = 4 mm is given in Fig. 7.11 (a) and the corresponding initial mesh is shown in Fig. 7.11 (b). During FEM sweeping analysis, a constraint is imposed to keep the area of each slot unchanged at 72 mm^2.

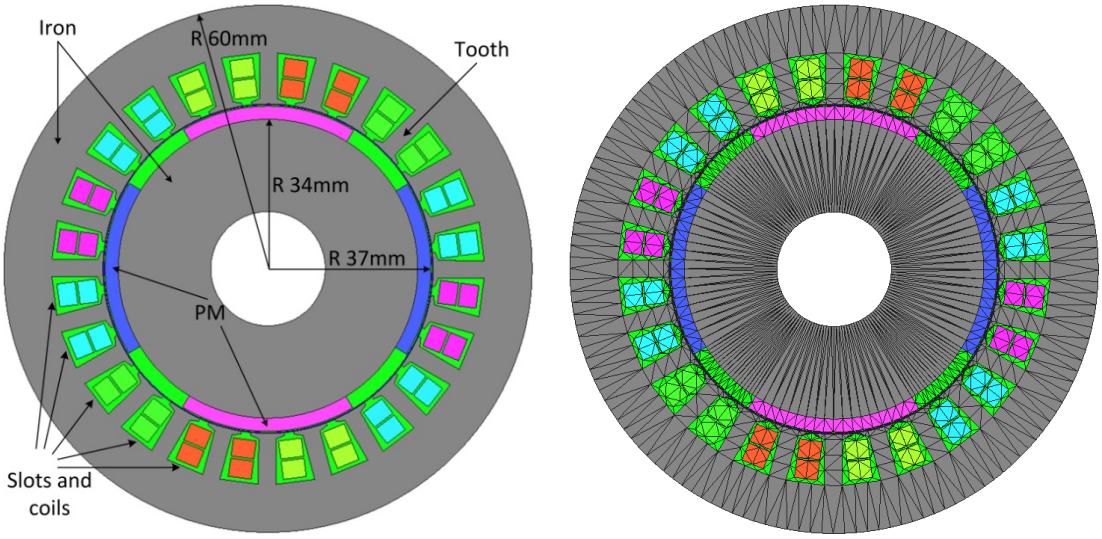

(a) (b)

Fig. 7.11. (a) The PM motor geometry with p_1 = 3 mm, p_2 = 0.7, and p_3 = 4 mm. (b) The corresponding initial boundary mesh of the PM motor.

In the optimal design process, the sizing parameters are changed in order to obtain the desired optimal solution to fulfill the objective. As an example, the mesh with p_1 = 3 mm, p_2 = 0.7, and p_3 = 4 mm is given Fig. 7.12 (a), and the deformed mesh when $p1$ is changed to 5mm is given in Fig. 7.12 (b). The x- and y-components of the nodal displacement vectors, which is the nodal position difference between the original mesh and the deformed mesh, are also given in Figs. 7.12 (c) and 7.12(d) respectively. The numerical solution of the magnetic vector potential A and the magnetic flux density $\boldsymbol{B}$ is also shown in Figs. 7.13 (a) and 7.13(b).

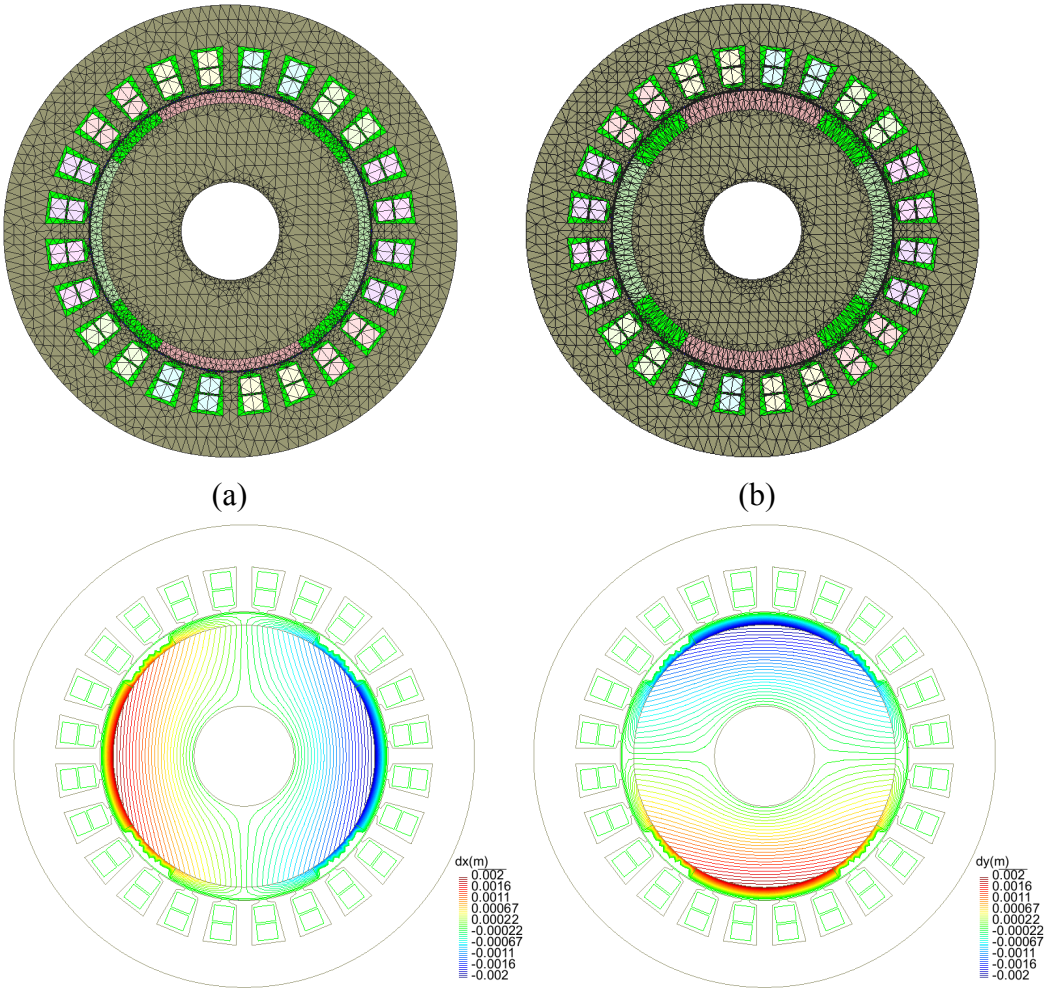

Fig. 7.12. (a) The mesh before deformation with p_1=3 mm, p_2=0.7, and p_3=4 mm. (b) The mesh after deformation with new design parameters p_1=5 mm, p_2=0.7, and p_3=4 mm. (c) The x-component of the nodal displacement vectors. (d) The y-component of the nodal displacement vectors.

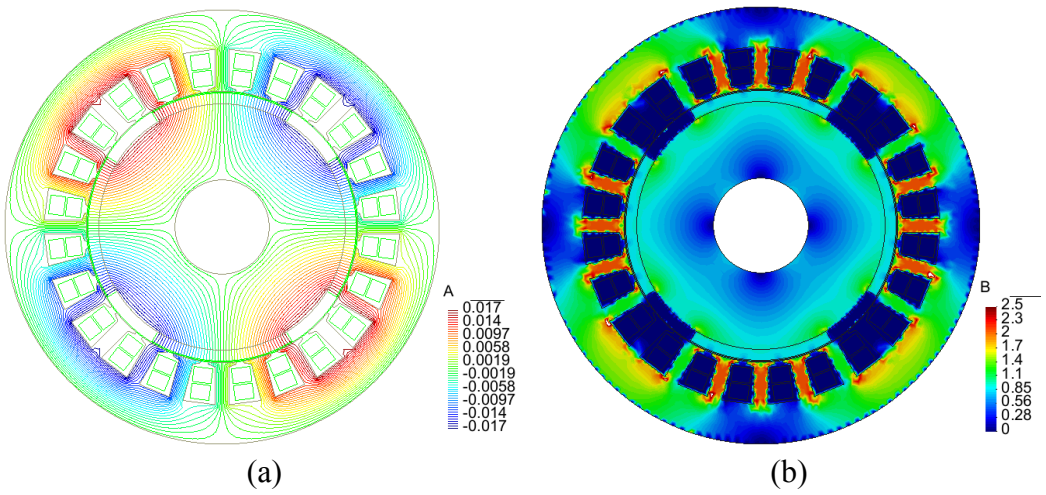

Fig. 7.13. (a) The computed magnetic flux contour lines. (b) The computed magnetic flux density.

For all the parameters in the sweeping analysis, uniform size steps are used to solve for the optimal design such that h_1 = 0.8 mm, h_2 = 0.2, h_3 = 0.01 mm for parameters p_1, p_2, and p_3, so there are totally 21×11×30 = 6930 times FEM computations. In our finite element parameter sweeping computation, it takes around 5.0 hours to obtain all the solutions. For each FEM computation of a set of chosen parameters, the time consumed on initial mesh generation and mesh refinement processes occupies about 30% of the total computational time. For classical methods for parameter sweeping analysis, where we have to generate the mesh again and again, it will take about 7.0 hours.

After obtaining the average magnetic flux values versus the sample parameters, it is found that the magnetic flux is essentially independent of the width of tooth p_3. The average magnetic flux values versus the thickness of the PM p_1 for various PM ratio p_2 is shown in Fig. 7.14. It can be seen that when $p_1 \approx 6$mm, $p_2 \approx 0.88$, and $p_3 \approx 6$mm, the approximate maximum magnetic flux of 22.0 mWb is obtained, and further enlargement of the volume of PM will produce hardly any magnetic flux increase.

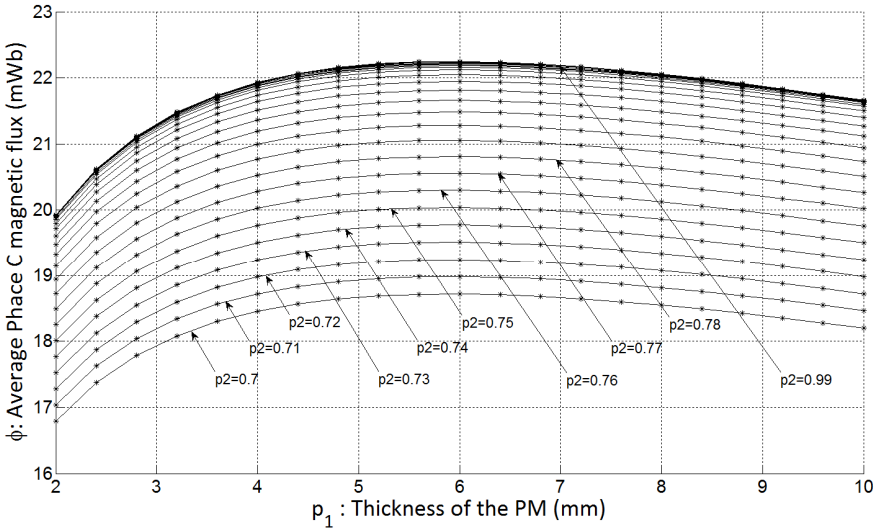

Fig. 7.14. Average phase magnetic flux versus p_1 and p_2.

7.5. A 3D Mesh Deformation Example

The developed remesh-free mesh deformation method in this thesis is applied to perform a sweeping of the design variable of an EM device, as shown in Fig. 7.15. The problem is the same as a 3D magnetostatic example of the commercial software

Maxwell 3D. In the sweeping process, the armature of the device will be rotated in center of a fixed point around the x-axis counterclockwisely. The range of the design variable α is $0^0 \le \alpha \le 5^0$.

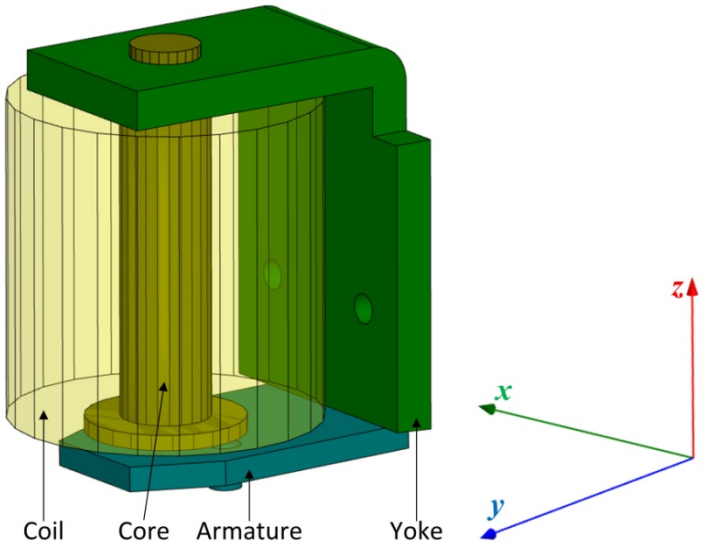

Fig. 7.15. The EM device where the armature is rotated around the x-axis.

The initial mesh with $\alpha = 0^0$ having 127,967 tetrahedral elements and 22,137 nodes is shown in Fig. 7.16(a). The deformed mesh with $\alpha = 5^0$ is given in Fig. 7.16 (b). It is noted that it costs about 85 seconds to generate the conforming mesh shown in Fig. 7.16(a) by the mesh generator. While it only costs 0.02 second to deform the mesh. So the mesh regeneration time is almost totally saved when using the remesh-free technique, compared with the traditional brute force sweeping method.

For the initial mesh, the mean quality factor (QF) of the elements is 0.7839, where the QF is defined as [G14]

$$QF = \frac{12(3V)^{2/3}}{\sum_{0 \le i < j \le 3} l_{ij}^{\,2}}, \tag{7.3}$$

where V is the signed volume of a tetrahedral element and $\{l_{ij}\}_{0 \le i < j \le 3}$ are the lengths of all its six edges. For the deformed mesh, the mean quality factor (QF) of the elements is 0.7786, so the quality of the mesh is still good. In Figs. 7.17(a) and 7.17(b), the contour plot of the absolute value of the displacement vectors and the vector plot of them are also given respectively. It can be seen that the modification of

the boundary interface nodes are diffused into the interior nodes of the armature object by the remesh-free mesh deformation method proposed in Chapter 3.

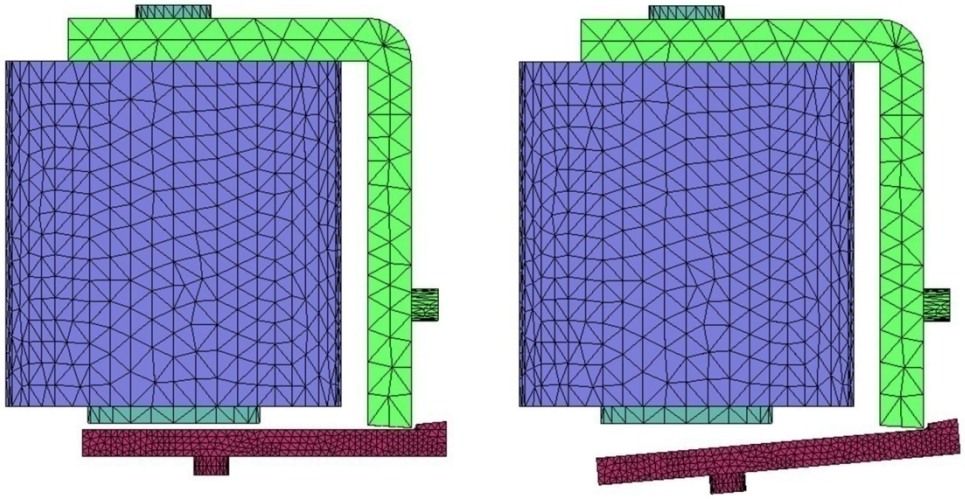

(a) (b)

Fig. 7.16. (a) The initial mesh when $\alpha = 0^0$. (b) The deformed mesh using the remesh-free mesh deformation method with $\alpha = 5^0$.

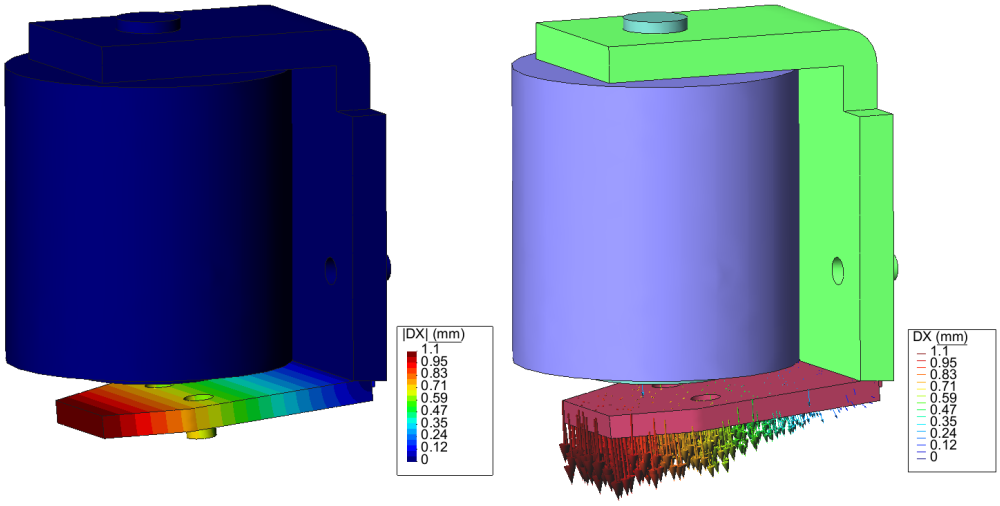

(a) (b)

Fig. 7.17. (a) The absolute value of the nodal displacement vectors. (b) The vector plot the nodal displacement vectors.

7.6. A Practical 3D Optimal Design Example

The developed remesh-free FEM is applied to optimize the geometrical sizes of an electromechanical levitation device to produce a maximum magnetic force per unit

volume of PM. The dimensions of the device are the same as those given in [G15], except that the device is extended along the z-axis to 10mm and a 3D test problem is thus formulated, as shown in Fig. 7.18(a). The volume of the PM is constrained to be $10^{-3}m^3$ and the airgap is 0.5mm. There are three geometry variables for designing, namely $\{p_1, p_2, p_3\}$, as illstrated in Fig. 7.18(b). The ranges of the design variables are $0<p_1<5$mm, $0<p_2<10$mm, $0<p_3<100$mm.

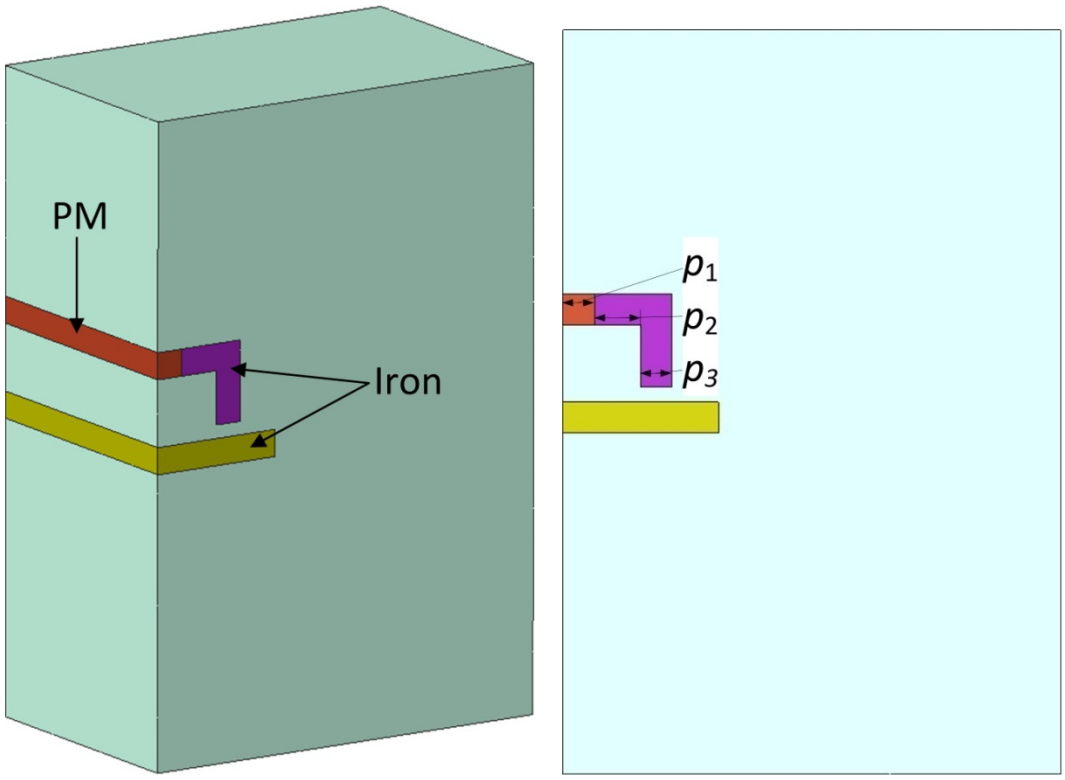

(a) (b)

Fig. 7.18. (a) Full 3D view of the PM magnet. (b) Front view of the 3D PM magnet, where the design parameters are also shown.

In the computation, 10^3 times of the parameters are swept and there are 10 sample values for each design parameter. Using the RSM and the DEA (N_p=40, G_{max}=100), the optimal solution is found to be [2.77 mm, 7.55 mm, 39.87 mm], and the corresponding objective function value is 1.25N, which is close to the results given in [G15].

The mesh in Fig. 7.19(a) is generated when p_1=1mm, p_2=1.5mm and p_3=1mm, and the deformed mesh using the proposed remesh-free method is shown in Fig.

7.19(b). The nodal displacement vectors are also shown in Figs. 7.20(a) and 7.20(b). To morph the mesh shown in Fig. 7.19(a) having 140,159 tetrahedral elements and 25,710 nodes, which costs about 90s to make, only 0.022s is needed to deform it by applying the remesh-free mesh deformation technique proposed in Chapter 3.

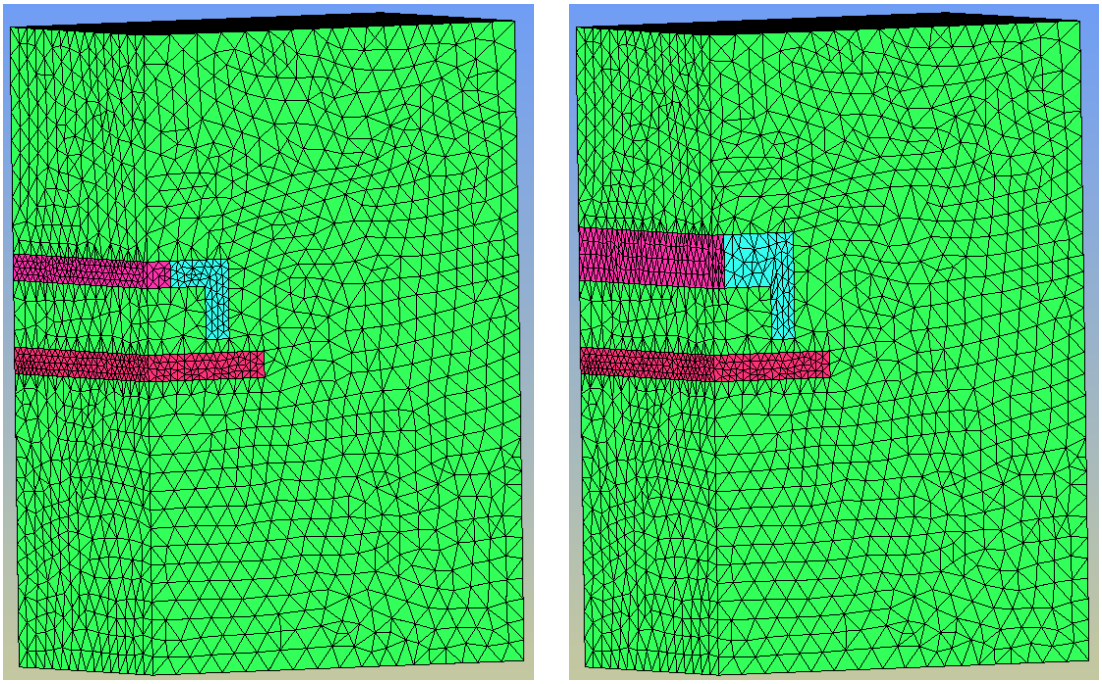

(a) (b)

Fig. 7.19. (a) 3-D computational mesh when p_1=1mm, p_2=1.5mm and p_3=1mm. (b) 3-D deformed mesh when p_1=0.5mm, p_2=2mm and p_3=1mm.

The solution of the magnetic flux density on the mesh shown in Fig. 7.20(a) is given in Fig. 7.21, where the magnetic vector potential formulation with edge element basis functions is used. The homogenous Neumann boundary condition is imposed on the symmetric plane x=0, and the homogenous Dirichlet boundary conditions are imposed for all other boundary surfaces. For each FE computation, it takes about 30s to solve the field solution. As it costs about 90s to make the boundary conforming mesh each time for the conventional method, it is clear that the total computational time elapsed in the optimal design process is greatly saved when the developed remesh-free FE technique is adopted.

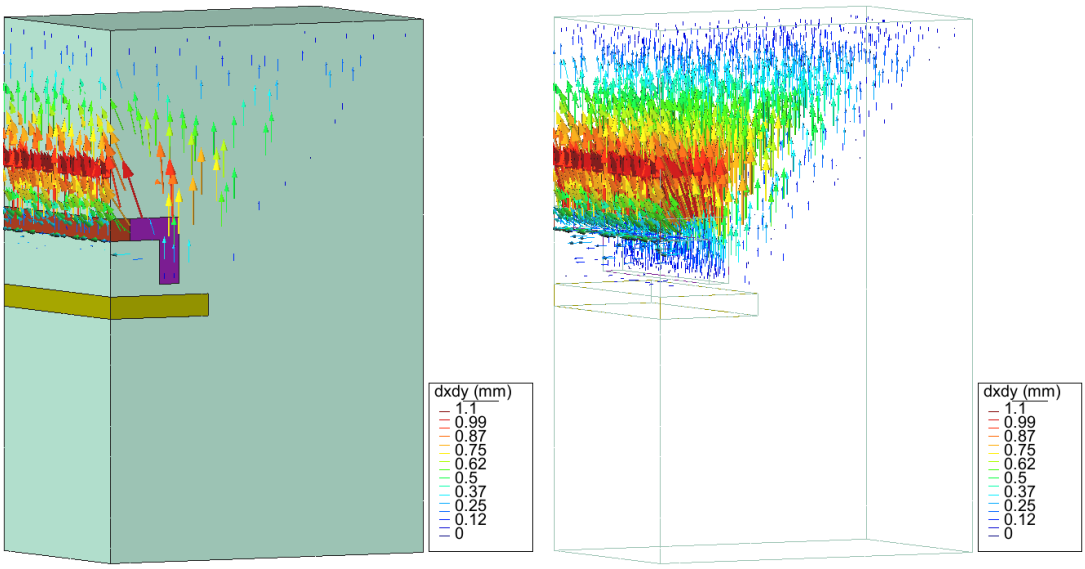

(a) (b)

Fig. 7.20. (a) Nodal displacement vectors on the surface of the domain. (b) Nodal displacement vectors in the interior of the domain.

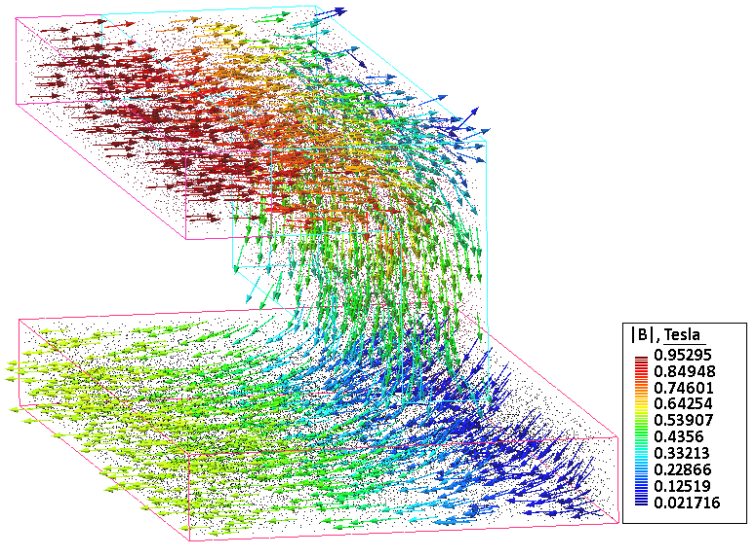

Fig. 7.21. Magnetic flux density in the PM and iron regions, where the FE mesh is the one shown in Fig. 7.19(a).

7.7. Summary

In this chapter, several optimal design problems, including 2D and 3D examples, are solved using the developed remesh-free FEM. Benchmark test examples are solved using the developed method and the numerical results are compared with the

analytical ones, they are shown to be similar to each other and hence validated the developed optimal design package. The developed method can be also used to practical optimal shape design and optimal sizing design problems. For example, the shape the pole piece of a DC magnet is optimized to produce uniform magnetic fields in the targeted region. In another example, several sizing parameters of a PM motor is optimized to produce maximum magnetic flux in the *C* phase. 3D optimal design problems can also be solved using the developed method efficiently.

7.8. References-Part G

[G1] N. Bianchi, and S. Bolognani, "Design optimisation of electric motors by genetic algorithms," *IEE Proc.-Electr. Power Appl.*, vol. 145, no. 5, pp. 475-483, Sep. 1998.

[G2] T. Ohnishi, and N. Takahashi, "Optimal design of efficient IPM motor using finite element method," *IEEE Trans. Magn.*, vol. 36, no. 5, pp. 3537-3539, Sep. 2000.

[G3] K. Yamazaki, and H. Ishigami, "Rotor-shape optimization of interior-permanent-magnet motors to reduce harmonic iron losses," *IEEE Trans. Ind. Electron.*, vol. 57, no. 1, pp. 61-69, Jan. 2010.

[G4] N. Baatar, H. Yoon, M. Pham, P. Shin, and C. Koh, "Shape optimal design of a 9-pole 10-slot PMLSM for detent force reduction using adaptive response surface method," *IEEE Trans. Magn.*, vol. 45, no. 10, pp. 4562-4565, Oct. 2009.

[G5] R. Timothy Marler, and Jasbir S. Arora, "The weighted sum method for multi-objective optimization: new insights," *Struct. Multidisc. Optim.*, vol. 41, pp. 853-862, 2010.

[G6] J. Chun, M. Kim, H. Jung, and Sun-Ki Hong, "Shape optimization of electromagnetic devices using immune algorithm," *IEEE Trans. Magn.*, vol. 33, no. 2, pp. 1876-1879, Mar. 1997.

[G7] D. Lukáš, and Ostrava, "On solution to an optimal shape design problem in 3-dimensional linear magnetostatics," *Applications of Mathematics*, vol. 49, no. 5, pp 441-464, Oct. 2004.

[G8] J. Ryu, Y. Yao, C. Koh, and Y. Shin, "3-D optimal shape design of pole piece in permanent magnet MRI using parameterized nonlinear design sensitivity analysis," *IEEE Trans. Magn.*, vol. 42, no. 4, pp. 1351-1354, Apr. 2006.

[G9] K. Yamazaki, and Y. Kanou, “Shape optimization of rotating machines using time-stepping adaptive finite element method,” *IEEE Trans. Magn.*, vol. 46, no. 8, pp. 3113-3116, Aug. 2010.

[G10] P. S. Shin, S. H. Woo, and C. S. Koh, “An optimal design of large scale permanent magnet pole shape using adaptive response surface method with Latin hypercube sampling strategy,” *IEEE Trans. Magn.*, vol. 45, no. 3, pp. 1214-1217, Mar. 2009.

[G11] P. Bettini, R. Specogna, and F. Trevisan, “A discrete geometric approach to solving 2-D non-Linear magnetostatic problems,” *IEEE Trans. Magn.*, vol. 46, no. 8, pp. 3049-3052, Aug. 2010.

[G12] S. L. Ho, N. N. Chen, and W. N. Fu, “A moving mesh embedded algorithm in finite element method for optimal design of electromagnetic devices,” *IEEE Trans. Magn.*, vol. 47, no. 10, pp. 2947-2950, Oct. 2011.

[G13] P. G. Alotto, C. Eranda, B. Brandstatter, G. Furntratt, C. Magel, and G. Molinari, “Stochastic algorithms in electromagnetic optimization,” *IEEE Trans. Magn.*, vol. 34, no. 5, pp. 3674-3684, Sep. 1998.

[G14] A. Liu, and B. Joe, “Relationship between tetrahedron shape measures,” *BIT Numerical Mathematics*, vol. 34, no. 2, pp. 268-287, 1994.

[G15] Shuangxia Niu, Yanpu Zhao, S. L. Ho, and W. N. Fu, “A parameterized mesh technique for finite element magnetic field computation and its application to optimal designs of electromagnetic devices,” *IEEE Trans. Magn.*, vol. 47, no. 10, pp. 2943-2946, Oct. 2011.

CHAPTER 8

CONCLUSIONS AND FUTURE WORK

In this thesis, a novel fast remesh-free finite element method (FEM) for optimal design of electromagnetic (EM) devices is investigated and the computer program is developed. The 2D parameterized algorithm and 3D remesh-free mesh deformation method are proposed and implemented in C++. Benchmark and practical optimal design problems are solved using the developed method to verify its effectiveness. The mesh re-generation time can be almost totally saved in the mesh deformation process using the proposed method, which hence greatly reduce the time needed when solving optimal design problems.

For the proposed fast remesh-free mesh deformation methods, it is effective to use in most optimal sizing or shape design problems. However there may be inverted elements in case of very large shape changes of the geometry under consideration, which makes the finite element solution process invalid. A future work to totally remove this disadvantage is to develop an overlapping finite element technique which is still valid even for overlapping mesh with inverted elements.

Practical engineering optimal design problems are solved using the developed remesh-free FEM combined with evolutionary optimization algorithms and the response surface methodology (RSM). Global optimization methods including Genetic Algorithm (GA), Taboo Search Algorithm (TSA),Particle Swarm Optimization (PSO) and Differential Evolution Algorithm (DEA) are coupledwith FEM program to find the best design. Further improvements can be investigated to try to reduce the number of sampling points without sacrificing the accuracy of the optimal result, adaptive RSMs can be helpful to this end.

2D nodal FEMand 3D edge element-based FEM are developed in C++ to analyzeEM fields in devices.The developed time stepping FEM with Newton-Raphson iteration for nonlinearmaterials, slave-mastertechnique for rotational movement andfield-circuit coupling technique is used to analyze practical problems. The developed program is verifiedfor benchmark problems and compared with the

numerical solutions obtained by the commercial software ANSYS Maxwell.

A low-frequency approximation to the Maxwell equations simultaneously considering inductive and capacitive effects in the time-domain is developed using 3D edge elements. A parallel-plate capacitor is analyzed using the developed code to check its correctness. In the future work, more engineering applications can be solved by the proposed solver where eddy-current solvers are not accurate enough or they are unable to resolve the coupled inductive and capacitive effects.

A novel error estimator, which is very convenient to use, is proposed to estimate the error of the numerical solution. It is effective when the solution domain contains multiple materials, which is very common in practical magnetic field analysis. Besides, a novel adaptive Degrees of Freedom (DoFs) FEM is proposed for the first time and it can be applied to static nonlinear problems and transient time-domain field computation. The implementation details of the algorithm is presented and numerical examples are given to show its usefulness in accelerating the transient field analysis without sacrificing the accuracy. To further accelerate the optimal design process, reduced basis method (RBM) or other model order reduction methods can be investigated to shorten the numerical simulation time for a design.

To solve quasi-magneto-static problems with high-speed moving conductors, which presents thin eddy-current layers, the adaptive discontinuous Galerkin method (DGM), characteristic Galerkin method (CGM) and operator splitting method (OSM) are proposed. Numerical examples are given to show their advantages over traditional FEM. The generalization of these proposed methods from 2D to 3D problems can be investigated in a further study.

In reality, the magnetic field and the thermal field are coupled together for practical EM devices. The optimal design process should consider this thermal effect to obtain the true optimal solution. The key for magnetic-thermal field coupling is how to model the energy dissipation from the magnetic field side as the heat source in the thermal field side. Since the thermal field is a scalar field, the developed computer code can account for this with minimal modification. The coupling of magnetic field and thermal field can be considered in a future study.